Proceedings

of the International Conference

**The multi-messenger astronomy:
gamma-ray bursts, search for electromagnetic counterparts
to neutrino events and gravitational waves**

7-14 October 2018.
Nizhnij Arkhyz (SAO RAS) and Terskol (BNO INR RAS)

Труды

Международной конференции

**Астрономия быстрого реагирования: гамма-всплески,
электромагнитное отождествление нейтринных событий и источников
гравитационных волн**

Content

4

Conference participants

Preface

The new modern field of multi-messenger astronomy aims at the study of astronomical sources using different types of "messenger" particles: photons, neutrinos, cosmic rays and gravitational waves. Topicality of this direction is confirmed by many conferences all over the world.

The international conference on this urgent topic was held in Russia for the third time. The success of the first workshop "Quark Phase Transition in Compact Objects and Multimessenger Astronomy: Neutrino Signals, Supernovae and Gamma-Ray Bursts" held in October 2015 and the second conference "SN 1987A, Quark Phase Transition in Compact Objects and Multimessenger Astronomy" held in October 2017 persuaded the organizers that such meetings arranged in locations of unique Russian Observatories – Special Astrophysical Observatory of RAS (SAO RAS), Baksan Neutrino Observatory of Institute for Nuclear Research of RAS (BNO INR RAS) and the International Observatory Peak Terskol – are well needed.

The conference's scientific program covers a wide range of problems of the modern astrophysics including that of existence of quantum-chromodynimic (QCD) phase transition and matter states at high temperatures and densities. Such conditions are likely to be achievable only in astrophysical objects – collapsars of stellar mass, the objects whose formation is related with collapse and explosion of hot and dense cores of massive stars observable as gamma-ray bursts and supernovae. Solution of such problems demands development of methods combining optical astronomical observations and experiments with neutrino telescopes, cosmic-ray recording sets and detectors of gravitational waves.

The Conference program will also include talks and discussion on the THESEUS (Transient High-Energy Sky and Early Universe Surveyor) mission concept, being developed by a large International collaboration involving also SAO and BNO. THESEUS aims at exploiting high-redshift gamma-ray bursts for getting unique clues to the Universe and, being an unprecedentedly powerful machine for the detection, accurate location and redshift determination of all types of gamma-ray bursts (long, short, high-z, under-luminous, ultra-long) and many other classes of transient sources and phenomena, at providing a substantial contribution to multi-messenger astrophysics and time-domain astronomy. Under these respects, THESEUS will show a beautiful synergy with the large observing facilities of the future, like E-ELT, TMT, SKA, CTA, ATHENA, in the electromagnetic domain, as well as with next-generation gravitational-waves (aLIGO/ aVirgo, KAGRA, ILIGO, Einstein Telescope, LISA) and neutrino detectors, thus enhancing importantly their scientific return. Moreover, it will also operate as a flexible IR and X-ray observatory, thus providing an even larger involvement of the scientific community.

Results of three years search for the ^{213}Po half-life variations

E.N.Alexeev[1], Yu.M.Gavrilyuk[1], A.M.Gangapshev[1,3], A.M.Gezhaev[1], V.V.Kazalov[1], V.V.Kuzminov[1,3,*], S.I.Panasenko[2], S.S.Ratkevich[2]

[1]Institute for Nuclear Research of the RAS, 60-th October Anniversary Prospect, 7a, Moscow 117312, Russia; e-mail: bno_vvk@mail.ru

[2]V.N.Karazin Kharkiv National University, pl. Svobody 4, Kharkiv 61022, Ukraine

[3]H.M.Berbekov Kabardino-Balkarian State University, Chernyshevsky St., 173, Nalchik 360004, Russia

Abstract   Description of the TAU-3 installation intended for long-term monitoring of the half-life value $T_{1/2}$ of the ^{213}Po is presented. Isotope ^{229}Th is used as a source of the mother's chain. The methods of measurement and processing of collected data are reported. Solar-daily variation with an amplitude $A_{So}=(5.3\pm1.1)\times10^{-4}$, lunar-daily variation with an amplitude $A_L=(4.8\pm2.1)\times10^{-4}$ and sidereal-daily variation with an amplitude $A_S=(4.2\pm1.7)\times10^{-4}$ were found as a results of a processing of the 622 days data series (July 2015 – March 2017). An averaged value of the ^{213}Po nuclei decay half-life was found to be to $T_{1/2}=3.705\pm0.001\mu$s. A half-life value data set with the week duration step was constructed for the 1177 days measurement time (July 2015 – September 2018). Features of the half-life time behavior were analyzed. Annular variation with an amplitude $A=(3.6\pm0.6)\times10^{-4}$ was found.

Keywords: Half-Life, ^{213}Po Nucleus, Daily and Annual Variations

1. Introduction

Experimental research of the ^{214}Po half-life (τ) time stabilities is carried out at the Baksan Neutrino Observatory of the INR RAS [1-3] since 2008. A half-life is defined as a result of an analysis of the decay curves constructed from a set of life-time values of separate nuclei of the isotope under consideration. Delays between a birth of the nuclear (β-particle from the ^{214}Bi decay + γ-quantum) and its decay (α-particle from the ^{214}Po decay) are measured to define this parameter.

Half-life value time sequences with different time steps are the objects for a subsequent analysis. The measurements (973 days) are performed at the TAU-2 low background facility placed in the underground low background laboratory DULB-4900 at a depth of 4900 m.w.e.. Further, time series of τ with different temporal steps are analyzed. According to data obtained at TAU-2, the averaged value of the ^{214}Po half-life is $\tau = 163.47 \pm 0.03$ µs. The annual variation with amplitude $A = (9.8 \pm 0.6)\times10^{-4}$, the solar-daily variation with amplitude $A_{So} = (7.5 \pm 1.2)\times10^{-4}$, the lunar-daily variation with amplitude $A_L = (6.9 \pm 2.0)\times10^{-4}$, and the sidereal daily variation with amplitude $A_S = (7.2 \pm 1.2)\times10^{-4}$ are detected in the series of τ values. Another pair of radioactive isotopes which have similar decay diagram but much smaller half-life of the daughter isotope was proposed to proof reality of the obtained

variations. The ^{213}Bi($T_{1/2}$ = 46 min) → ^{213}Po($T_{1/2}$ = 4.2 μs) [5] were choose as the pair. These isotopes are the daughter products in the ^{229}Th ($T_{1/2}$=7340 years) decay chain from the ^{237}Np series [6]. The results obtained for the data measured during 1177 days with such source are listed in the presented work.

2. The facility description

The construction of the TAU-3 facility with a ^{229}Th source is similar to that of TAU-2 [1]. It comprises a scintillation detector D1which is made of two disks d = 18 mm and h = 1 mm of a plastic scintillator (PS) glued together. The radiation source ^{229}Th ($T_{1/2}$ = 7340 years) positioned between the disks is the parent isotope for ^{213}Po. The test sample is manufactured at the Khlopin Radium Institute (St. Petersburg).

The source is precipitated from Th(NO$_3$)$_4$ salt solution on the surface of a LAVSAN film with h = 2.5 μm and covered by the same film pasted along the edge by the epoxy resin. The assembly is placed at the bottom of a case made of VM-2000 reflecting film open from one end. The case is put inside a stainless-steel rectangular case 9×23×140 mm, thickness 0.5 mm. The open end of the case is connected with the bottom of a 2.5-mm stainless-steel cylinder with d = 44 mm, and h = 160 mm. Inside the cylinder, there is a high-speed FEU-87 photomultiplier monitoring PS. The signal is taken from the FEU anode load through the matching circuit and is supplied via the cable (50 Ohm) to the first entry of the registering unit. Detector D1 is placed in the 15-cm Pb protective layer in a gap with h = 10 mm between two scintillation detectors NaI(Tl) 150×150 mm (detector D2) in a low-background box of the DULB-4900 underground low-background laboratory [6]. Signals from the anodes of two photomultipliers of the D2 detector are amplified by charge-sensitive preamplifiers, summed, and supplied to the second, starting entry of the registering unit. The registering facility comprises a LA-n10-12 PCI digital oscilloscope (DO) integrated with a PC, which is registering the waveform of pulses arriving from D1 and D2 in the online mode. The frequency of pulse digitization in DO is chosen as 100 MHz. The reading and recording are started by a pulse in the D2 channel. The record frame is 2048 temporal channels (10 ns per channel), including 256 channels of prehistory and 1792 channels of history. In Fig. 1, the decays of ^{213}Bi and ^{213}Po isotopes [5] are presented schematically. From Fig1a it follows that 66% of β decays of ^{213}Bi are transitions to the ground level, and 31% to the excited level with an energy of 440 keV. The decay of this level is accompanied by a γ quantum emission (26% per decay). The isotope ^{213}Po decays in 100% of cases with emission of an α particle with an
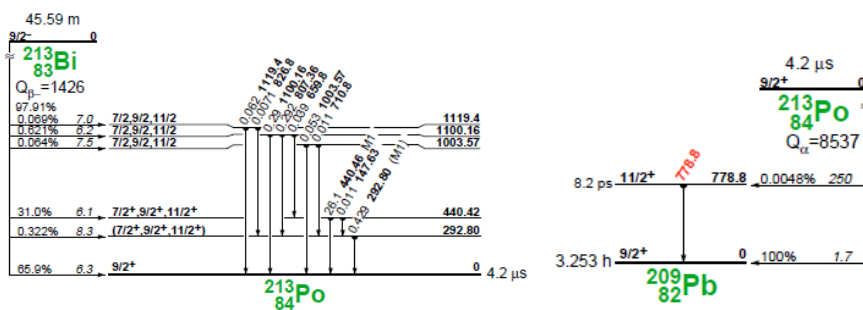
Fig.1. Decay schemes of ^{213}Bi (left) and ^{213}Po (right).

energy of 8537 keV. If the device registers all three particles released by the decay of the pair of isotopes, it is the event with three pulses. In this event, pulses coming from the γ quantum and β-particle coincide instantaneously, and the pulse from the α particle is delayed. In Fig. 2, one of the events (frames) stored by DO in the PC memory is displayed as an example. The pulse on the upper beam (1) is a γ quantum, the first pulse train on the lower beam (2) corresponds to a β particle, and the second one to an α particle. The observed triple coincidences considerably reduce the contribution of background events accompanying decays of the remaining isotopes in the chain of decays of ^{229}Th to the total counting rate of the facility.   The activity of ^{229}Th is ∼ 80 Bq. Alongside the main isotope there are small amounts of extraneous radioactive impurities in the specimen. The DO recording rate of the event started by D2 pulses with amplitudes of 380-500 keV was ∼27 s^{-1}.   The recording rate of useful events with parameters of all pulses corresponding to ^{213}Po decay was ∼ 18 s^{-1}. From Fig.2 it follows that signals from β- and α-particles are clusters of short subpulses with total duration of up to ∼ 1 μs, decreasing exponentially in frequency and amplitude.
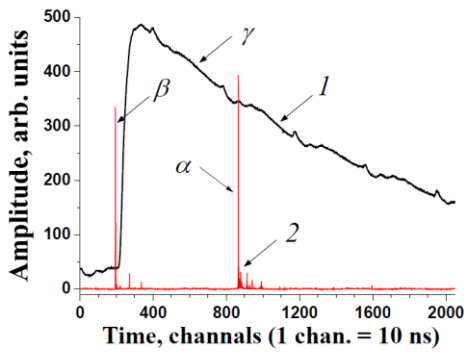
Fig2. An example of ^{213}Bi–^{213}Po pair decay event stored by DO in PC memory: (1) upper beam, a pulse from D2 detector (γ quantum), (2) lower beam, pulses from particle (start), and particle (stop) in D1 detector.
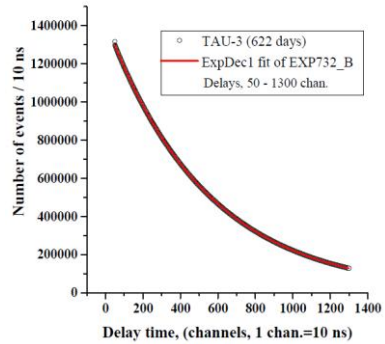
Fig3. Decay curve for ^{213}Po plotted by the data from TAU-3 device obtained over 622 days.

The clusters can overlap at small delays between particles; therefore, the processing program should consider the relation between the amplitudes of the first and subsequent subpulses in a cluster to unambiguously separate the delayed (β ⊗ α) coincidences. The delays between pulses in channel D1 are determined as the result of processing the recorded waveforms, and a decay curve of daughter isotope ^{213}Po is plotted for the chosen time interval. The half-life determination is based on this curve. The sequential time series of this magnitude is plotted.

3. Measurement results

Continuous measurements started at TAU-3 on July 9, 2015. The statistics for 622 days (March 2017) was processed at the beginning. In Fig. 3, the decay curve of the ^{213}Po isotope is given. The value of τ was obtained approximating the decay curve by function
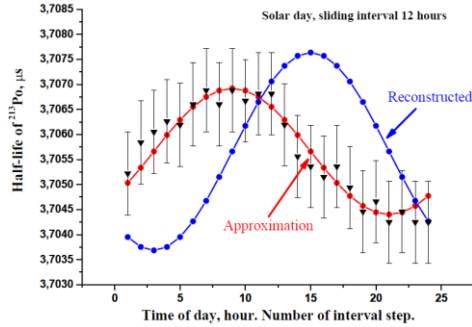
Fig4. *Dependence of ^{213}Po half-life on the time of solar day obtained by the method of interior moving average (triangles). Approximation by function $\tau(t) = \tau_0[1+3.4\times10-4sin\{2\pi/24(t-3)\}]$ (red curve). Restored dependence $\tau(t) = \tau_0[1+5.3\times10-4 \times \times sin\{2\pi/24(t-9)\}]$ (the blue dot-dashed curve).*
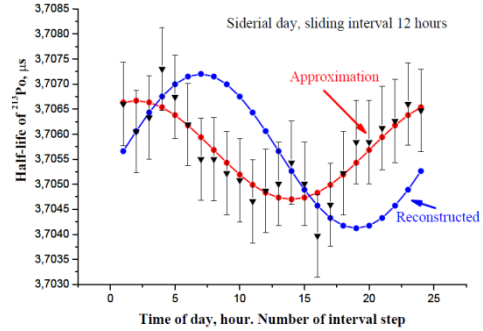
Fig5. *Dependence of ^{213}Po half-life on the time of sidereal day obtained by the method of interior moving average (triangles). Approximation by function $\tau(t)=\tau_0[1+2.7\times10-4sin\{(2\pi/24)(t-19)\}]$ (red curve). Restored dependence $\tau(t) = \tau_0[1+ 4.2\times10-4\times sin\{2\pi/24(t-1)\}$ (the blue dot-dashed curve).*

$F(t) = A\times exp[-\ln(2)t/\tau] + b$ using the minimum χ^2 test in the delay interval of 0.5-13.0 μs. It was found that $\tau = 3.705 \pm 0.001$ μs. The inner moving-average (IMA) method was used to search for a possible time variation of the τ-values. A time interval with the duration equal to about 0.5 of the expected periods is chosen to search for any harmonic component and the τ-value is determined for this interval. Then, the interval has shifted by one step and the procedure is repeated. In the studies of daily variations of the ^{213}Po half-life dependence on solar, sidereal, and lunar time, the length of the respective day was divided into 24 hours. The duration of a sidereal and lunar day in the standard solar time is 23 hours 56 minutes 4.09 s and 24 hours 50 minutes 28.2 s, respectively.

A period of 12 hours was chosen as an interval of averaging. The analysis of events was made as follows. We selected the events registered in the interval of 0-12 hours for the entire period study and determined the half-life values. After that, the interval was shifted by one hour and the procedure was repeated. The results of the search of the daily variation in solar time are given in Fig. 4. Here, the result of approximation of the daily half-life dependence by the function $\tau(t) =\tau_0[1 + A\times sin\{\omega(t + \varphi)\}]$ (the red curve) is displayed, where τ_0 is the mean half-life; $\omega = 2\pi/24$ h^{-1}; $A = 3.4\times10^{-4}$ is the amplitude; $\varphi = -3$ h is a phase shift of the initial point of the curve relative to 0 hours. The figure shows that the time dependence of the ^{213}Po half-life is well described by a sinusoidal function. The period found is 24 hours and the relative amplitude is 0.00034 half-lives. It is easy to show that the initial periodic dependence of time data has the same period (24 h), the amplitude is higher by the factor of $\pi/2$ and is shifted by 0.5 of the moving intervals ($0.25\times24 = 6$ h). The amplitude of the initial daily periodic dependence obtained from these data in solar time is $A_{So} = (5.3\pm1.1)\times10^{-4}$ (the blue dot-dashed curve).

In Fig. 5, the results of the search for a sidereal daily variation of the ^{213}Po half-life are displayed. The experimental data are approximated by the curve $\tau(t) = \tau_0[1 + A\times sin\{\omega(t + \varphi)\}]$ (the red curve) with the parameters $A = 2.7\times10^{-4}$ is amplitude; $\varphi = -19$ h is the phase shift of the curve initial point relative to 0 hours. The analysis of the restored initial dependence similar to the analysis made for the solar-daily wave shows the presence of a sidereal-daily wave with the relative amplitude $A_S=(4.2\pm1.7)\times10^{-4}$ (the blue dot-dashed curve). In Fig. 6, the

results of search for a lunar-daily variation of the ^{213}Po half-life are given.
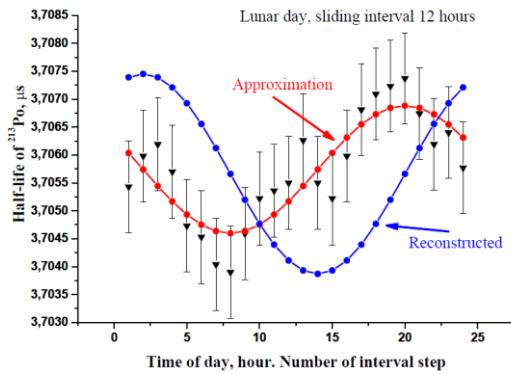
Fig6. Dependence of ^{213}Po half-life on the time of lunar day obtained by the method of interior moving average (triangles). Approximation by function
$\tau(t)=\tau0[1+3.1\times10-4sin\{2\pi/24(t-14)\}]$ *(the red curve). Restored dependence*
$\tau(t)=\tau0[1+4.8\times10-4sin\{2\pi/24(t-20)\}]$ *(the blue dot-dashed curve).*

The analysis of the restored initial dependence like the analysis made for the solar-daily wave shows the presence of a lunar-daily wave with relative amplitude $A_L = (4.8 \pm 2.1)\times 10^{-4}$ (blue dot-dashed curve). In Fig. 7, the time dependence of τ obtained from the decay curve for a weekly data set is presented. It is shown that τ increases with time, and that for a data set collected over 127 days, $\tau = (3.6998 \pm 0.0015)$ µs; for 320 days, $\tau = (3.6993 \pm 0.0014)$ µs; for 422 days $\tau = (3.7016 \pm 0.0011)$ µs, and for 622 days $\tau = (3.7053 \pm 0.0011)$ µs. The causes of such behavior of the τ parameter are not clear yet. It could be both an instrumental effect, for example, equipment ageing, and an unknown real physical effect. The presence of a pulse surge of data within the time interval comparable to a year in the series of weekly data hinders using the method of moving internal average for studies of the half-life annual variation.

The data collected during 1177 days (28 September 2018) allows us to suppose that the obtained trend has a shape of a logistic curve which can be done by an expression of $L=A_2+(A_1-A_2)/[1+(x/x_0)^P]$. The coefficients in the formula fitted the experimental data in the best way were found by the χ^2-method as $L=3.733+(3.700-3.733)/[1+(x/73.42)^{4.94}]$. The experimental data was normalized to the values of fitting curve. The results are shown in Fig.8 by points with error bars. This dependence was smoothed by a sliding averaging by the 26 points method at the ORIGIN 8.5 program. The result is shown in Fig.8 by the blue curve which contains the annular variation. This curve was approximated by a sine function $\tau(t)/\tau_0=1+2.3\times10^{-4}\times\sin((2\pi/365)\times(t-319))$ shown by red color in Fig.8. The amplitude of the functions is $A=(2.3\pm0.4)\times10^{-4}$. As mentioned above, this value was integrated over 26 points (the 0.5-year period) in the averaging process. A real value of the annular variation could be found by multiplying of sine amplitude by $\pi/2$ coefficient. This gives an amplitude of the variation equal to $A=(3.6\pm0.6)\times10^{-4}$.

4. Discussion

The results of a monitoring of the ^{213}Po half-life in the period July 2015 – September 2018 presented above show that this parameter undergoes solar-daily, sidereal-daily and lunar-daily variation with the amplitudes $A_{So}=(5.3\pm1.1)\times10^{-4}$, $A_S=(4.2\pm1.7)\times10^{-4}$ and $A_L=(4.8\pm2.1)\times10^{-4}$ respectively. These values coincide within the errors with those obtained in the ^{214}Po half-life values series. A search for the annular variations in the ^{213}Po data is complicated because of appearance of a nonperiodic unidirectional deviation of the half-life

values from the averaged one. The process became noticeable in the May - June 2016 data time range. The effect could be caused by the electronics aging
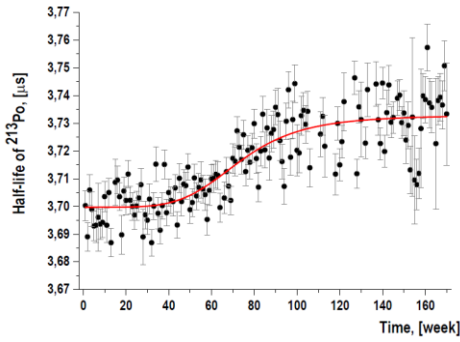
Fig7. *Time dependence of τ obtained from the decay curve for the weekly data set (time distance of measurements: July 9, 2015 – September 28, 2018). Trend shape L=3.733+(3.700-3.733)/[1+(x/73.42)$^{4.94}$] – the red curve.*
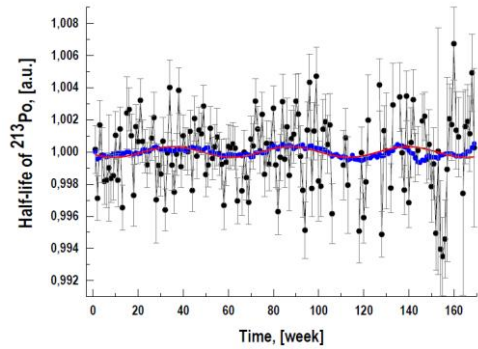
Fig8. *Time dependence of τ normalized on trend – the black dots. Time dependence of smoothed τ-values – the blue curve. Approximation by function τ(t)/τ$_0$=1+3.6×10^{-4}×sin((2π/365)×(t-319)) – the red curve.*

or some unknown physical factors. A length of the half-life series collected to the present moment is enough for estimation of the trend shape. Analysis of the dependence obtained from primary data normalization to the trend shape shows a presence of the annular variation with the amplitude $A=(3.6\pm0.6)\times10^{-4}$.

5. Conclusion

Description of the TAU-3 installation intended for long-term monitoring of the half-life value $T_{1/2}$ of the ^{213}Po is presented. The isotope ^{229}Th is used as a source of the mother's chain. The methods of measurement and processing of collected data are reported. Solar-daily variation with amplitude $A_{So}=(5.3\pm1.1)\times10^{-4}$, lunar-daily variation with amplitude $A_L=(4.8\pm2.1)\times10^{-4}$ and sidereal-daily variation with amplitude $A_S=(4.2\pm1.7)\times10^{-4}$ were found from treatment of the 622 days data series (July 2015 – March 2017). An averaged value of the ^{213}Po nuclei decay half-life was found to be equal to $T_{1/2}=3.705\pm0.001\mu s$. A half-life value data set with the week duration step was constructed for the 1177 days measurement time (July 2015 – September 2018). Features of the half-life time behavior were analyzed. The annular variation with the amplitude $A=(3.6\pm0.6)\times10^{-4}$ was found.

Acknowledgments

References

[1]   E.N. Alexeyev, V.V. Alekseenko, Ju.M. Gavriljuk, A.M. Gangapshev, A.M. Gezhaev, V.V. Kazalov,

V.V. Kuzminov, S.I. Panasenko, S.S. Ratkevich, S.P. Yakimenko. "Experimental test of the time stability of the half-life of alpha-decay 214Po nuclei" Astroparticle Physics, 46 (2013) 23-28.

[2] E. N. Alexeev, Yu. M. Gavrilyuk, A. M. Gangapshev, V. V. Kazalov, V. V. Kuzminov, S. I. Panasenko, S. S. Ratkevich. «Sources of the systematic errors in measurements of 214Po decay half-life time variations at the Baksan deep underground experiments» Physics of Particles and Nuclei, Volume 46, Issue 2, (2015), pp 157-165.

[3] E.N. Alexeev, Yu.M. Gavrilyuk, A.M. Gangapshev, V.V. Kazalov, V.V. Kuzminov, S.I. Panasenko, S.S. Ratkevich. "Results of a search for daily and annual variations of the 214Po half-life at the two-year observation period." Physics of Particles and Nuclei, 47(6), (2016), 986-994.

[4] Ju.M. Gavriljuk , A.M. Gangapshev , A.M. Gezhaev , V.V. Kazalov , V.V. Kuzminov , S.I. Panasenko, S.S. Ratkevich , A.A. Smolnikov , S.P. Yakimenko. "Working characteristics of the New Low-Background Laboratory (DULB-4900)" Nuclear Instruments and Methods in Physics Research A 729 (2013) 576–580.

[5] R.B. Firestone, "Table of Isotopes", CD ROM Edition, Version 1.0, March, 1996.

[6] Handbook edited by I.K.Kikoin "Tables of physical quantities" Moscow, Atomizdat, 1976

[7] E. N. Alexeev, Yu. M. Gavrilyuk, A. M. Gangapshev, A. M. Gezhaev, V. V. Kazalov, V. V. Kuzminov, S. I. Panasenko, S. S. Ratkevich. "Search for Variations of 213Po Half-Life" Physics of Particles and Nuclei, 2018, Vol. 49, No. 4, pp. 557–562.

The Transient High-Energy Sky and Early Universe Surveyor (THESEUS)

Lorenzo Amati[1] on behalf of the THESEUS international collaboration[2]

[1]*INAF - OAS Bologna, via P. Gobetti 101/1, Bologna, Italy; lorenzo.amati@inaf.it*

[2]*https://www.isdc.unige.ch/theseus/*

Abstract The Transient High-Energy Sky and Early Universe Surveyor (THESEUS) is a mission concept developed in the last years by a large European consortium and currently under study by ESA as one of the three candidates for next M5 mission (launch in 2032). As detailed in Amati et al. 2017 [1] and Stratta et al. 2017 [2], THESEUS aims at exploiting high-redshift GRBs for getting unique clues to the early Universe and, being an unprecedentedly powerful machine for the detection, accurate location (from ~arcmin to ~arcsec) and redshift determination of all types of GRBs (long, short, ~high-z, under-luminous, ultra-long) and many other classes of transient sources and phenomena, at providing a substantial contribution to multi-messenger time-domain astrophysics. Under these respects, THESEUS will show a beautiful synergy with the large observing facilities of the future, like E-ELT, TMT, SKA, CTA, ATHENA, in the electromagnetic domain, as well as with next-generation gravitational-waves and neutrino detectors, thus enhancing importantly their scientific return.

Keywords: THESEUS, Gamma-Ray Bursts, Early Universe, Gravitational Waves, Multi-Messenger Astrophysics

1. Introduction

The main feature of the modern astrophysics is the rapid development of multi-messenger astronomy. At the same time, relevant open issues still affect our understanding of the cosmological epoch (a few millions years after the "big-bang") at which first stars and galaxies start illuminating the Universe and re-ionizing the inter-galactic medium.

In this context, a substantial contribution is expected from the Transient High Energy Sky and Early Universe Surveyor (THESEUS), a space mission concept developed by a large European consortium including Italy, UK, France, Germany, Switzerland, Spain, Poland, Denmark, Czech Republic, Ireland, Hungary, Slovenia, ESA, with Lorenzo Amati (INAF, Italy) as a lead proposer. In May 2018 THESEUS was selected by ESA for a Phase 0/A study as one of the three candidates for theM5 mission within the Cosmic Vision program. End of Phase A and down-selection to one mission is expected for mid-2021, mission adoption for 2024 and launch in 2032. Details on the THESEUS science objectives, mission concept and expected performances are reported in Amati et al. 2018 [1], Stratta et al. 2018 [2] and on the THESEUS consortium website [3]. The Proceedings of the THESEUS Workshop 2017, held at INAF – Osservatorio di Capodimonte in Naples, Italy, are also available on the internet [4].

The program of the workshop covered such topics as THESEUS mission design and science objectives, probing the Early Universe with GRBs, multi-messenger and time domain astrophysics, the transient high energy sky, synergy with the next generation large facilities

(E-ELT, SKA, CTA, ATHENA, GW and neutrino detectors).

2. THESEUS scientific objectives

THESEUS is designed to vastly increase the discovery space of high energy transient phenomena over the entirety of cosmic history, whose modern concept is presented in Fig1.
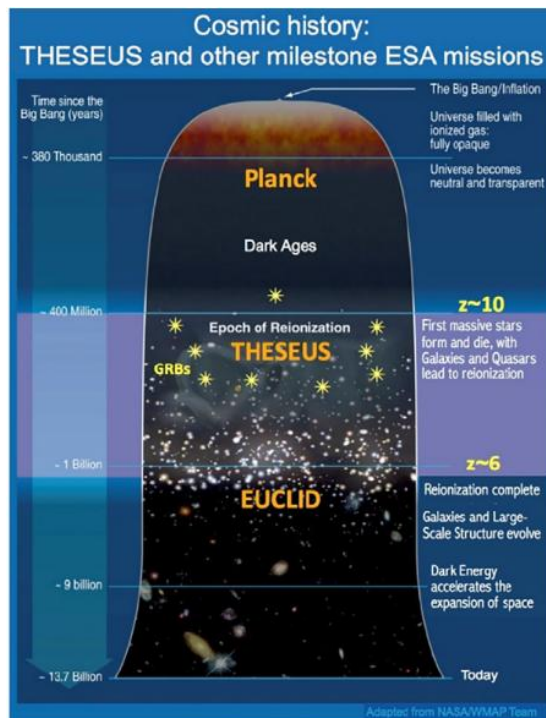
Fig1. *Gamma-Ray Bursts in the cosmological context and the role of THESEUS (adapted from a picture by the NASA /WMAP Science team).*

Because of their huge luminosities, mostly emitted in the X and gamma-rays, their redshift distribution extending at least to z ~9 and their association with explosive death of massive stars and star forming regions, GRBs are unique and powerful tools for investigating the early Universe: SFR evolution, physics of re-ionization, galaxies metallicity evolution and luminosity function, first generation (pop III) stars.

A statistical sample of high–z GRBs can provide fundamental information [1]:

- measure independently the cosmic star–formation rate, even beyond the limits of current and future galaxy surveys;
- directly (or indirectly) detect the first population of stars (pop III);
- the number density and properties of low-mass galaxies (Even JWST and ELTs surveys will be not able to probe the faint end of the galaxy Luminosity Function at high redshifts (z>8-10));
- the neutral hydrogen fraction;
- the escape fraction of UV photons from high-z galaxies;

- the early metallicity of the ISM and IGM and its evolution (Abundances, HI, dust, dynamics etc. even for very faint hosts. E.g. GRB 050730: faint host (R>28.5), but z=3.97, [Fe/H]=-2 and low dust, from afterglow spectrum (Chen et al. 2005; Starling et al. 2005).)

On the other side, a mission capable of substantially increase the rate of identification and characterization of high-z GRBs will also provide a survey of the high-energy sky for sof X-rays to gamma-rays with an unprecedented combination of wide Field Of View (FOV), source location accuracy and sensitivity below 10 keV. This features will give THESEUS the possibility of providing a substantial contribution also to time-domain astrophysics, in general, and in particular to the newly born and rapidly growing field of multi-messenger astrophysics. For instance, THESEUS will be able to provide detection, accurate location, characterization and possibly redshift measurement of electromagnetic emission (short GRBs, possible soft X-ray transient emission, kilonova emission in the near-infrared) from gravitational-wave sources like NS-NS or NS-BH mergers [2].

Indeed, THESEUS will be an unprecedentedly powerful machine for the detection, accurate location (from ~arcmin to ~arcsec) and redshift determination of all types of GRBs (long, short, high-z, under-luminous, ultra-long) and many other classes of transient sources and phenomena, at providing a substantial contribution to multi-messenger time-domain astrophysics.

THESEUS's capabilities in exploring the multi-messenger transient sky can be summarized as follow:

- Locate and identify the electromagnetic counterparts to sources of gravitational radiation and neutrinos, which may be routinely detected in the late '20s / early '30s by next generation facilities like aLIGO/aVirgo, eLISA, ET, or Km3NET;
- Provide real-time triggers and accurate (~1 arcmin within a few seconds; ~1'' within a few minutes) high- energy transients for follow-up with next-generation optical-NIR (E-ELT, JWST if still operating), radio (SKA), X-rays (ATHENA), TeV (CTA) telescopes; synergy with LSST;
- Provide a fundamental step forward in the comprehension of the physics of various classes of transients and fill the present gap in the discovery space of new classes of transients events.

LIGO, Virgo and partners make first detection of gravitational waves and light from colliding neutron stars.

THESEUS capabilities in these directions are:

- short GRB detection over large FOV with arcmin localization;
- Kilonova detection, arcsec localization and characterization;
- Possible detection of weaker isotropic X-ray emission.

4. THESEUS mission concept

THESEUS will be capable to achieve the exceptional scientific objectives summarized above thanks to a smart combination of instrumentation and mission profile. The mission will carry on-board two large FOV monitors covering simultaneously a 1sr FOV in the soft X-rays (0.3 – 5 keV) with unprecedented sensitivity and arcmin location accuracy) and several sr FOV form 2 keV up to 20 MeV, with additional source location capabilities of a few arcmin from 2 to 30 keV. Once a GRB or a transient of intereste is detected by one or both the monitors, the

TEHSEUS spacecraft will quickly slew to pint, within a few minutes, an on-board near infra-red telescope (70 cm class operating from 0.7 to 1.8 micron) to the direction of the transient, so to catch the fading NIR afterglow or, e.g., kilonova emission, localizing it a 1 arcsec accuracy and measuring its redshift through photometry and moderate resoluton spectroscopy.

The detailed description of THESEUS can be found in [1], [2] and [3]. The total view is presented in Fig2.
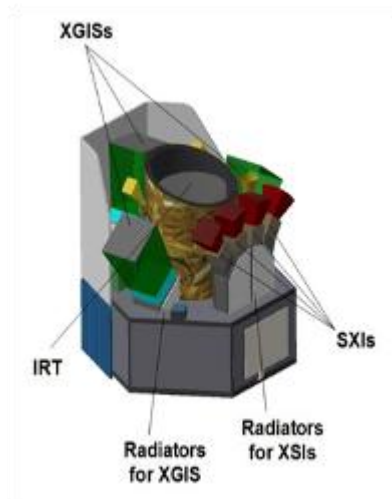
Fig2. THESEUS Satellite Baseline Configuration and Instrument suite accommodation

The main components are described below.

4.1. The Soft X-ray Imager (SXI) is led by UK

Soft X-ray Imager (SXI): a set of four sensitive lobster-eye telescopes observing in 0.3 - 5 keV band, total FOV of ~1sr with source location accuracy 0.5-1'. The appearance of the device can be seen in Fig3.
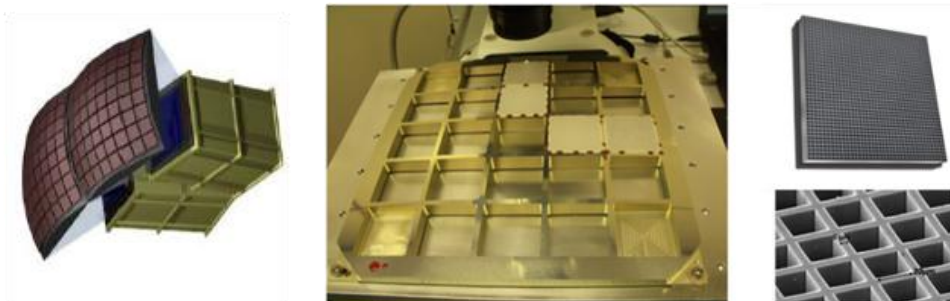
Fig3. *Left: the SXI optical elements. Middle: The SVOM MXT lobster eye optic aperture frame. Top right: A schematic of a single square pore MCP. Bottom right: A micrograph of a square pore MCP showing the pore structure. This plate has a pore size d = 20 μm and a wall thickness w = 6 μm.*
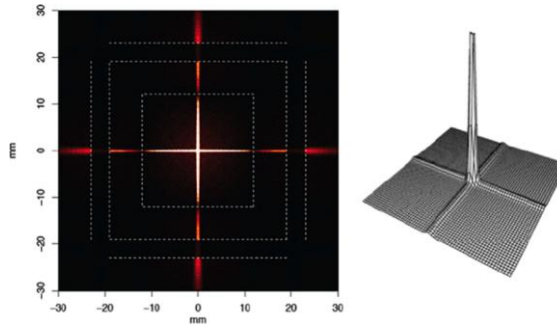
Fig4. *The point spread function of the SXI.*

4.2. The X-Gamma-rays imaging spectrometer (XGIS) – led by IT

X-Gamma rays Imaging Spectrometer (XGIS,): 3 coded-mask X-gamma ray cameras using bars of Silicon diodes coupled with CsI crystal scintillators observing in 2 keV – 10 MeV band, a FOV of ~2-4 sr, overlapping the SXI, with ~5' source location accuracy.
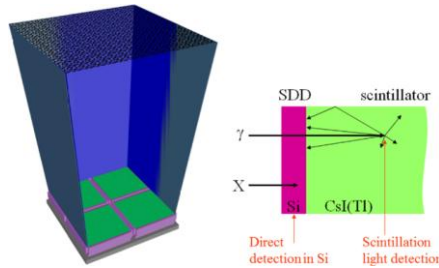
Fig5. *Left: Sketch of the XGIS Unit. Right: Principle of operation of the XGIS detection units: low-energy X-rays interact in Silicon, higher energy photons interact in the scintillator, providing an energy range covering three orders of magnitude. A pulse shape discriminator determines if the interaction has occurred in Si or in the crystal.*

3.3. The InfraRed Telescope (IRT) – led by FR

The InfraRed Telescope (IRT): a 0.7m class IR telescope observing in the 0.7 – 1.8 μm band, providing a 10′×10′ FOV, with both imaging and moderate resolution spectroscopy capabilities (→ redshift).
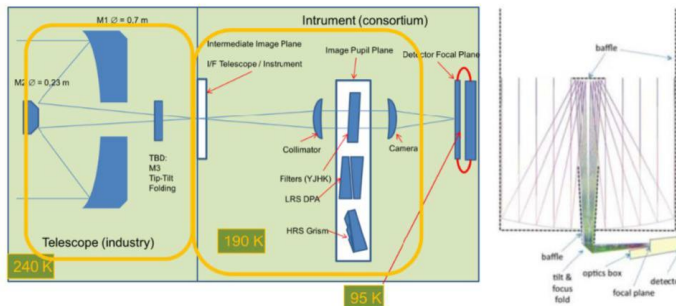
Fig6. *The IRT Telescope block diagram concept.*

The THESEUS total field of view is shown in Fig7.

Fig7. *Field of view of all instruments*

4. The main capabilities of THESEUS

THESEUS will have the ideal combination of instrumentation and mission profile for detecting all types of GRBs (long, short/hard, weak/soft, high-redshift), localizing them from a few arcmin down to arsec and measure the redshift for a large fraction of them (Fig. 8).
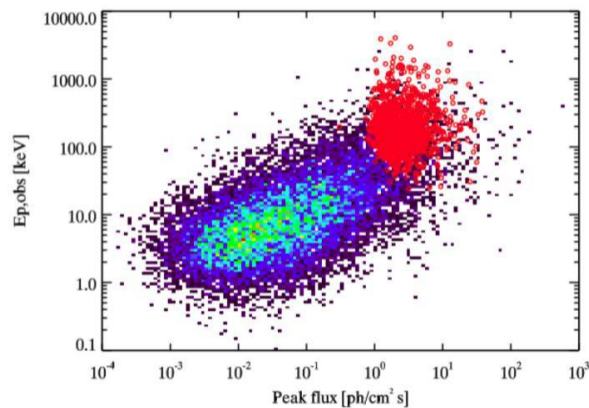
Fig8. GRB distribution in the peak flux – spectral peak energy (Ep) plane according to most recent population synthesis models and measurements (see [1] and references therein). For all the shown GRBs TEHSEUS will be able to provide detection, accurate location, characterization and measurement of redshift. The low-Ep – low peak flux region is populated by high-redshift GRBs (shown in dark blue, blue, light blue, green, yellow), a population inaccessible by current facilities, while the high Ep region highlighted with red points shows the region where most short GRBs will lay.

In addition the GRB prompt emission, THESEUS will also detect and localize down to 0.5-1 arcmin the soft X-ray short/long GRB afterglows, of NS-NS (BH) mergers and of many classes of galactic and extra-galactic transients. For several of these sources, THESEUS/IRT will provide detection and study of associated NIR emission, location within 1 arcsec and redshift.

The impact of these measurements for shedding light on the early Universe with GRBs is

represented in Fig. 9, where we show the expected number per year of GRBs detected, localized and with redshift measurement from THESEUS compared to the present situation achieved with the main efforts of the Swift, Konus-WIND, Fermi/GBM satellites and several on-ground robotic and large telescopes.
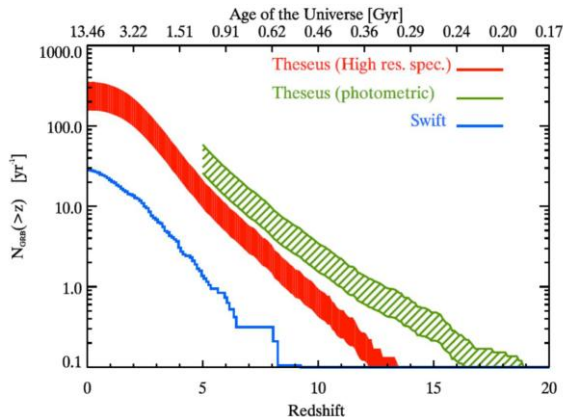
Fig9. The yearly cumulative distribution of GRBs with redshift determination as a function of the redshift for Swift and THESEUS. We note that these predictions are conservative in so far as they reproduce the current GRB rate as a function of redshift. However, with our sensitivity, we can detect a GRB of $E_{iso} \sim 10^{53}$ erg (corresponding to the median of the GRB radiated energy distribution) up to z = 12. Indeed, our poor knowledge of the GRB rate-SFR connection does not preclude the existence of a sizable number of GRBs at such high redshifts, in keeping with recent models of Pop III stars.

5. GW/multi-messenger and time-domain astrophysics.

As discussed in previous sections, GW transient sources that will be monitored in the e.m. domain by THESEUS include:

- NS-NS / NS-BH mergers:
  - collimated EM emission from short GRBs and their afterglows (rate of ≤ 1/yr for 2G GW detectors but up to 20/yr for 3G GW detectors as Einstein Telescope);
  - Optical/NIR and soft X-ray isotropic emissions from macronovae, off-axis afterglows and, for NS-NS, from newly born ms magnetar spindown (rate of GW detectable NS-NS or NS-BH systems, i.e. dozens-hundreds/yr).
- Core collapse of massive stars: Long GRBs, LLGRBs, ccSNe (much more uncertain predictions in GW energy output, possible rate of ~1/yr) ;
- Flares from isolated NSs: Soft Gamma Repeaters (although GW energy content is ~0.01%-1% of EM counterpart)

In particular, THESEUS will be able to detect, localize, characterize and measure the redshift for NS-NS / NS-BH mergers through the following channels:

- collimated on-axis and off-axis prompt gamma-ray emission from short GRBs;
- Optical/NIR and soft X-ray isotropic emissions from kilonovae, off-axis afterglows and, for NS-NS, from newly born ms magnetar spindown.

Thus, THESEUS will beautifully complement the capabilities of next generation GW detectors (e.g., Einstein Telescope, Cosmic Explorer, further advanced LIGO and Virgo,

KAGRA, etc.) by promptly and accurately localizing e.m. counterparts to GW signals form NS-NS and NS-BH mergers and measuring their redshift. These combined measurements will provide unique clues on the nature of the progenitors, on the extreme physics of the emission and, by exploiting simultaneous redshift (from e.m. counterpart) and luminosity distance (form GW signal modeling) of tens of sources, fully exploit multimessenger astrophysics for cosmology.

6. Time-domain astronomy and GRB physics

The unique capabilities of THESEUS, will also allow to provide relevant contributions to the more general field of time-domain astronomy and, of course, to GRB science. As a few examples, THESEUS will provide the astrophysical community with:

- survey capabilities of transient phenomena similar to the Large Synoptic Survey Telescope (LSST) in the optical: a remarkable scientific synergy can be anticipated;
- substantially increased detection rate and characterization of sub-energetic GRBs and X-Ray Flashes;
- unprecedented insights in the physics and progenitors of GRBs and their connection with peculiar core-collapse SNe.

7. Conclusions

THESEUS, under study by ESA and a large European collaboration with strong interest by international partners (e.g., US) will fully exploit GRBs as powerful and unique tools to investigate the early Universe and will provide us with unprecedented clues to GRB physics and sub-classes. This mission will also play a fundamental role for GW/multi-messenger and time domain astrophysics at the end of next decade, also by providing a flexible follow-up observatory for fast transient events with multi-wavelength ToO capabilities and guest-observer programs. THESEUS observations will thus impact on several fields of astrophysics, cosmology and even fundamental physics and will enhance importantly the scientific return of next generation multi messenger (aLIGO/aVirgo, LISA, ET, or Km3NET;) and e.m. facilities (e.g., LSST, E-ELT, SKA, CTA, ATHENA)

In addition, THESEUS scientific return will include significant Observatory Science, e.g.: study of thousands of faint to bright X-ray sources by exploiting the unique simultaneous availability of broad band X-ray and NIR observations; providing a flexible follow-up observatory for fast transient events with multi-wavelength ToO capabilities and guest-observer programs.

We would like to remark that THESEUS is also a unique occasion for fully exploiting the European leadership in time-domain and multi-messenger astrophysics and in key-enabling technologies (lobster-eye telescopes, SDD by INAF, INFN, FBK, Un.).

In conclusion, THESEUS will be a really unique and superbly capable facility, one that will do amazing science on its own, but also will add huge value to the currently planned new photon and multi-messenger astrophysics infrastructures in the 2020s to > 2030s.

References

[1]   L. Amati, P. O'Brien, D. Goetz et al., "The THESEUS space mission concept: science case, design and expected performances", Advances in Space Research, Vol.62, Iss. 1, 1 July 2018, Pages

191-244, DOI: 10.1016/j.asr.2018.03.010

[2] G. Stratta, R. Ciolfi, L. Amati et al., "THESEUS: a key space mission concept for Multi-Messenger Astrophysics", Advances in Space Research, Vol.62, Iss. 3, 1 August 2018, Pages 662-682, DOI: 10.1016/j.asr.2018.04.013

[3] http://www.isdc.unige.ch/theseus/

[4] https://www.isdc.unige.ch/theseus/2017-workshop-proceedings-2.html

Influence of accretion disk wind on the evolution of LMX outburst

A. L. Avakyan[1,2,*], K. L. Malanchev[1], G. V. Lipunova[1]

[1]*Sternberg Astronomical Institute of Lomonosov Moscow State University,*

Universitetskiy pr. 13, Moscow, 119234, Russia; artur_ava97@mail.ru

[2]*Faculty of Physics M.V.Lomonosov Moscow State University, Leninskie Gory, Moscow,*

119991 Russia

Abstract   From analysis of the light curves observed during outbursts of low-mass X-ray binaries it was found that viscosity parameter α, which characterizes the mass transport in the accretion disk within the framework of the Shakura-Sunyaev model, lies in the range of 0.2-1. However, simulations of the magnetorotational instability give values of α an order of magnitude smaller. In this work, we consider an additional source of matter transfer, namely, the wind from the disk surface. We calculate evolution of the disk taking into account the Compton-heated wind, which can decrease the value of α parameter derived from observations. As a result, we obtain the dependence of α on wind parameters. We show that the presence of wind can strongly affect the inferred value of α, as well as the entire evolution of the disk.

Keywords: Accretion, Accretion Disk, Compton-Heated Winds, Black Hole Physics, X-Ray Binary.

1. Introduction

A low mass X-ray binary (LMXB) consists of a neutron star or a black hole accreting matter from the other binary component, which usually fills its Roche lobe. In LMXB systems the donor is less massive than the compact object, and can be a main sequence star, a degenerate dwarf, or a red giant. The brightest part of the system is the accretion disk around the compact object. The orbital periods of LMXBs range from ten minutes to hundreds of days. LMXBs demonstrate repeating outbursts due to instability of disk or mass-transfer.

The matter, which transfers from the companion star, creates a cool quiescent disk. Accumulation of mass makes the disk temperature to rise. Thus, the temperature in the disk eventually reaches the value when hydrogen ionizes. The steep temperature dependence of opacity takes place in this temperature range, causing a thermal-viscous instability within the disk. During an outburst, a typical LMXB emits almost all of its radiation in X-rays, and typically less than one percent, in visible light, so LMXBs are among the brightest objects in the X-ray sky, but relatively faint in visible light.

Currently, about 18 LMXBs with a black hole are known in our Galaxy, identified by bright X-ray outbursts indicating rapid accretion episodes (see, for example, [1]). These outbursts last much longer and recur much less frequently than in many types of accreting white dwarfs, apparently due to the heating of the outer disk by X-rays emitted from the inner areas of the accretion flow.

It is believed that the magneto-rotational instability provides the physical mechanism underlying the angular momentum and mass transfer in accretion disks. The effective viscosity in the disks, usually parameterized using the α-viscosity prescription, determines the

efficiency of this transportation process. Physically, the α-viscosity parameter determines the viscous time of the accretion flow and, thus, according to the disk instability picture, is encoded in the decay profile of an outburst light curve. A disk with a higher viscosity, that is, with higher α, accretes mass during an outburst faster, reducing the decay time of an outburst.

Standard model of disk accretion [2] has introduced a dimensionless viscosity parameter $\alpha \lesssim 1$, which characterizes the angular momentum transfer. Analysis of the light curves observed during LMXB outbursts demonstrates that α lies in the range of ~ 0.2–1 [3, 4]. However, modern 3-D simulations of the magnetorotational instability give values an order of magnitude smaller: $\alpha \lesssim 0.1$ [5, 6, 7].

In this work, we consider an additional source of matter and angular momentum transfer, namely, a thermal wind [8]. In the presence of the wind, the outburst characteristic time decreases mimicking the effect of large α-viscosity parameter. Thus, high α inferred from observed light curves would correspond to a smaller α if the wind operates.

2. "Compton-heated" winds

Theoretical models of accretion disks and observational data indicate that emission from the disk center may irradiate the surface of the outer disk and thus affect the accretion flow. In the standard α-model of accretion disks, the disk "flares up" in thickness in the direction of large radii, which allows the surface to be exposed to a central source of luminosity.

The heating rate per particle is proportional to the radiation intensity, but at the same time the cooling rate in the disk depends on two-particle processes and, therefore, decreases with density, that is, away from the equatorial plane of the disk. When the density drops to a critical value, the radiation heating suppresses the cooling, and the gas is heated to a high temperature determined by the interactions between the particles and photons. For X-ray binaries and quasars, the central radiation is sufficiently hard so that the gas can be heated to temperatures in excess of 10^7K, predominantly via the Compton process [8].

Following [8], let us consider a disk illuminated by X-ray or EUV continuum. The disk thickness is determined by the ratio of the sound speed to the local Keplerian speed. Above this hydrostatic scale height, the irradiated gas must either be in the hot phase, $T = T_{IC}$, where T_{IC} is the inverse Compton temperature, or be in the process of heating toward T_{IC}. The notion of escape temperature can be introduced [2]: $T_g = GM\mu/kR_0$. A hydrostatic corona may exist, if T_{IC} is less that the escape temperature. This condition is satisfied inside the radius

$$R_{IC} = \frac{GM\mu}{kT_{IC}} = \frac{1.0\times10^{10}}{T_{IC8}}\left(\frac{M}{M_\odot}\right)cm \tag{1}$$

where $T_{IC8} = T_{IC}/10^8$ K [8].

Furthermore, in [2], a critical luminosity is proposed:

$$L_{cr} = \frac{1}{8}\left(\frac{m_e}{\mu}\right)^{1/2}\left(\frac{m_e c^2}{kT_{IC}}\right)^{1/2}L_{Edd} = 0.030T_{IC8}^{-1/2}L_{Edd} \tag{2}$$

where L_{Edd} is the Eddington luminosity. The ratio L/L_{cr} characterizes the effectiveness of the X-ray luminosity in overcoming gravity.

2.1. Oscillations

Instability takes place if the wind is driven by emission produced by accretion [9]. This instability leads to oscillations in the luminosity of the accretion disk, provided that the wind from the disk is strong enough. If the rate of mass loss due to wind $\dot{M}_{wind}$ is moderate in proportion to the central accretion rate $\dot{M}_a$ then the disk is stable and steady. But if $\dot{M}_{wind}$ is large enough, the flow in the disk is unstable, and the disk settles in the form of periodic oscillations [9].

3. Model

The evolution of the accretion disk is described by an equation of diffusion type [9]:

$$\frac{\partial \Sigma}{\partial t} = \frac{1}{4\pi} \frac{(GM_x)^2}{h^3} \frac{\partial^2 F}{\partial h^2} - W(h) \tag{3}$$

where Σ is the surface density of accretion disk, F is the viscous torque, $h = (GMr)^{1/2}$ is the specific angular momentum of the accreting matter, M_x is the mass of compact object, W is the function describing the wind action.

Initial and boundary conditions are required for a complete formulation of the problem of viscous evolution of a disk. In the case of accretion onto a black hole, the boundary condition at the inner boundary of the disk (corresponding to the last stable orbit) is the zero torque F. If the accretion disk is truncated by a magnetosphere of a neutron star or a young star, the internal boundary condition on F is determined by conditions at the magnetospheric boundary. Thus, in many cases, the problem has the internal boundary condition of the first kind, that is, a condition defined on the value of the unknown function. For the case of a black hole,

$$F(h_{in}, t) = 0 \tag{4}$$

The external boundary condition is important as well. In a binary system, the angular momentum is very effectively diverted by tidal forces from the outer boundary of the disk corresponding to h_{out}. Next, we assume that the mass inflow into the accretion disk proceeds only through its external boundary. Thus we obtain the boundary condition of the second kind:

$$\left(\frac{\partial F}{\partial h}\right)_{out} = \dot{M}_{out} \tag{5}$$

where $\dot{M}_{out}$ is the rate of matter inflow into the disk. Also we set the initial distribution of the viscous torque:

$$F(h,0) = F_0(h) , \tag{6}$$

which necessarily satisfies the boundary conditions.

We consider two types of the wind term in equation (3). In first case, for the function W we take a fitting formula for wind losses per unit area from [10] in the form:

$$W(h) = m_{ch} \times \left(\frac{1 + (0.125\xi/\eta)^2}{1 + (\eta^4(1 + 262\xi^2))^{-2}}\right)^{1/6} \times exp\left[-\left(1 - (1 + 0.25\xi^{-2})^{-1/2}\right)^2/2\xi\right] \tag{7}$$

where $m_{ch} = k_C \dot{M}_0/(\pi R_{out}^2)$ is the characteristic mass loss per unit area, k_C is a wind constant, $\dot{M}_0 = 2 \times 10^{18}$ g/s is the initial accretion rate on the compact object, $\xi = R/R_{IC}$ and $\eta = L/L_{cr}$. Here, we set the inflow of matter into the disk $\dot{M}_{out}$ equal to zero. The initial condition is chosen as the solution for the accretion disk at an outburst peak following Lipunova & Shakura   [11].

For the wind in the second case, we use a formula from Shields et al [9]:

$$W(h) = \frac{1}{2\pi}\left(\frac{C\dot{M}_a}{ln\,(R_{out}/R_w)R^2}\right) \quad , \tag{8}$$

where R_{out} is the accretion disk radius, R_w is the wind launching radius, and $C \equiv \dot{M}_{wind}/\dot{M}_a$. In this case, we take the initial condition in the form $F \sim \dot{M}_0 \times (h - h_{in})$, where $\dot{M}_0 = \dot{M}_{out}/(1 + C)$ and $\dot{M}_{out} = 10^{18}$ g/s. Wind exists only for $R > R_w$ otherwise $W(h)$ assumed to be zero.
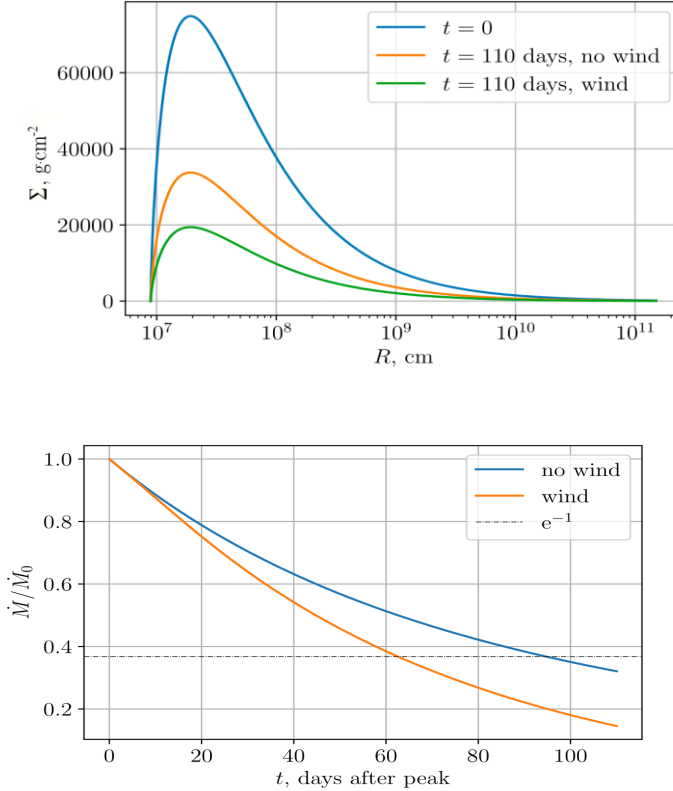
Fig1. *Evolution of accretion disk with and without wind described by equation (7).   The initial condition is fixed. Upper panel: surface density versus radius. Lower panel: accretion rate on the central object. Parameters are: Mx = 10 ×M⊙, outer disk radius Rout = 1.5×10¹⁴cm, kC = 3.*

4. Numerical method

Using an implicit difference scheme, we reduce the solution of differential equation (3) with the boundary conditions described in the previous section to the consequential solution of a system of algebraic equations at each time step, which is carried out by the sweep method. The implementation of the described scheme is performed using the program code FREDDI [3].

Code FREDDI calculates the evolution of the disk if it is completely ionized or if the cold front, beyond which the gas is not ionized, moves towards the center. The code is designed to simulate soft X-ray transients' light curves with fast rise and exponential decay.

The code was modified to include the wind influence on the accretion disk evolution.

5. Results

For the first type of wind (Eq. 7), dependences of the surface density on the distance from the center of the disk were calculated for different moments of time (Fig. 1, the upper panel). Dependences of the accretion rate on time, both with and without the wind, are shown in the lower panel of Fig.1.

Table1. Mass loss and change of the decay time due to wind

k_C	$\dot{M}_{wind}$, g/s	t_{exp}, days
0	0	94.7
0.1	8.2×10^{16}	92.9
0.3	2.46×10^{17}	89.6
1	8.2×10^{17}	80.6
3	2.46×10^{18}	62.6
10	8.2×10^{18}	39.6

Table 1 illustrates change of the decay time due to the wind effect. Here k_C is a parameter in the wind term $W(h) \sim k_C \times \dot{M}_0/(\pi R_{out}^2)$, $\dot{M}_0 = 2 \times 10^{18}, g/s$ is the initial (peak) accretion rate on the compact object, $\dot{M}_{wind}$ is the mass loss due to wind, t_{exp} is the time of the exponential decrease in accretion rate on the central object.

To verify our numerical method, we have compared results of our code with the results obtained earlier. An analytical solution for the structure of a supercritical disk with mass loss by Shakura and Sunyaev [8] was numerically successfully obtained. Also, we have reproduced the numerical results of the work of Shields et al. [9] for the accretion rate oscillations in the accretion disk with the Compton-heated wind. For this, we invoke the second type of wind (Eq. 8), which depends on the luminosity (the accretion rate on the central object). The evolution of the accretion rate is calculated (Fig. 2), which agrees well with the results presented by [9].
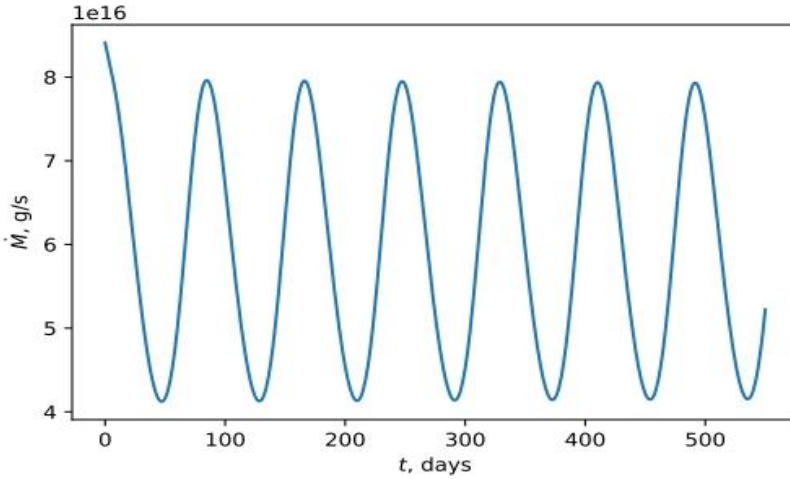
Fig2. *The time dependence of the central accretion rate for an accretion disk with wind (8) depending on the central luminosity. Here $R_w = 0.9 \times R_{out}$, $C = 15.8$. The graph clearly shows the occurrence of oscillations.*

6. Conclusion

Compton-heated winds lead to a mass loss from the disk and also remove angular momentum from it. Mass losses due to the wind can be of the order and sometimes even greater than the accretion rate onto the central object. Evidently, the winds are very significant for the accretion disk evolution if the mass loss in the wind reaches the order of the windless accretion rate. At the same time, the disk evolution speeds up remarkably.

We have verified our numerical method using the results of Shields et al [9]. Oscillations appear if the mass loss in the wind is an increasing function of the accretion rate onto the central object.

To sum up we note that a study of wind mechanisms is very important for understanding the time-dependent accretion disk behavior.

Acknowledgements

References

[1] B. E. Tetarenko, G. R. Sivakoff, C. O. Heinke, and J. C. Gladstone. WATCHDOG: A Comprehensive All-sky Database of Galactic Black Hole X-ray Binaries. , 222:15, Feb. 2016. doi:10.3847/0067-0049/222/2/15.

[2]   N. I. Shakura and R. A. Sunyaev. Black holes in binary systems. Observational appearance. , 24:337–355, 1973.

[3]   G. V. Lipunova and K. L. Malanchev. Determination of the turbulent parameter in accretion discs: effects of self-irradiation in 4U 1543-47 during the 2002 outburst. , 468:4735–4747, July 2017. doi: 10.1093/mnras/stx768.

[4]   V. F. Suleimanov, G. V. Lipunova, and N. I. Shakura. Modeling of non-stationary accretion disks in X-ray novae A 0620-00 and GRS 1124-68 during outburst. , 491:267–277, Nov. 2008. doi: 10.1051/0004-6361:200810155.

[5]   S. A. Balbus and J. F. Hawley. A powerful local shear instability in weakly magnetized disks. I - Linear analysis. II - Nonlinear evolution. , 376:214–233, July 1991. doi: 10.1086/170270.

[6]   S. Hirose, O. Blaes, J. H. Krolik, M. S. B. Coleman, and T. Sano. Convection Causes Enhanced Magnetic Turbulence in Accretion Disks in Outburst., 787:1, May 2014. doi: 10.1088/0004-637X/787/1/1.

[7]   R. G. Martin, C. J. Nixon, J. E. Pringle, and M. Livio. On the physical nature of accretion disc viscosity. arXiv e-prints, Jan. 2019.

[8]   [8] M. C. Begelman, C. F. McKee, and G. A. Shields. Compton heated winds and coronae above accretion disks. I Dynamics. , 271:70–88, Aug. 1983. doi:10.1086/161178.

[9]   G. A. Shields, C. F. McKee, D. N. C. Lin, and M. C. Begelman. Compton-heated winds and coronae above accretion disks. II - Instability and oscillations. , 306:90–106, July 1986. doi: 10.1086/164322.

[10] H. J. Cambier and D. M. Smith. Prototyping Non-equilibrium Viscous-timescale Accretion Theory Using LMC X-3. , 767:46, Apr. 2013. doi: 10.1088/0004-637X/767/1/46.

[11] G. V. Lipunova and N. I. Shakura. New solution to viscous evolution of accretion disks in binary systems. , 356:363–372, Apr. 2000.

Optical photometry and preliminary modeling of Type IIb Supernova 2017gpn

Elena A. Balakina[1,2,*], Maria V. Pruzhinskaya[1,3], Alexander S. Moskvitin[4], and Sergey I. Blinnikov[1,3,5,6]

[1] *Lomonosov Moscow State University, Sternberg Astronomical Institute, Universitetsky pr. 13, Moscow, 119234, Russia; buzm-ea@yandex.ru*

[2] *Lomonosov Moscow State University, Faculty of Physics, Leninskie Gory, 1-2, Moscow, 119234, Russia*

[3] *Space Research Institute, 84/32 Profsoyuznaya Street, Moscow, 117997, Russia*

[4] *Special Astrophysical Observatory RAS, Nizhnij Arhyz, 369167, Russia*

[5] *NRC "Kurchatov institute" - ITEP, B.Cheremushkinskaya 25, 117218 Moscow, Russia*

[6] *Kavli IPMU, University of Tokyo, Kashiwa, 277-8583, Japan*

Abstract   MASTER OT J033744.97+723159.0 (SN 2017gpn) was discovered in the error box of LIGO/Virgo alert G299232. The spectrum of SN 2017gpn is consistent with a Type IIb supernova. In this work we present the photometry of 20 epochs of observations performed with CCD photometer on the Zeiss-1000 telescope. The light curves in B and R filters were obtained. The multicolor light curves were also modeled numerically using the one-dimensional radiation hydrodynamical code STELLA.

1. Introduction

During follow-up inspection of the error box of the LIGO/Virgo alert G299232 on 2017 August 27.017, MASTER Global Robotic Net [7] discovered an optical transient named MASTER OT J033744.97+723159.0 [9], [10]. On 2017 September 6, M. Caimmi reported the discovery of a supernova with the 0.24-m telescope from Valdicerro Observatory [4]. The supernova received the IAU designation AT 2017gpn and was identified as MASTER OT J033744.97+723159.0.

On 2017 August 29, the spectrum of MASTER OT J033744.97+723159.0 was obtained with the Xinglong 2.16-m telescope of National Astronomical Observatory of China [11]. The object was classified as Type IIb Supernova (SN) by cross-correlating with a library of spectra (SNID, [3]). The spectra of SN IIb display hydrogen features at early phases with no evidence of helium. Helium features appear after about two weeks and they become stronger with time as the hydrogen features weaken rapidly. SN IIb has been proposed as an intermediate step between SN II and SN Ib [5]. The IIb Type supernovae arise from stars that have lost most of their hydrogen envelope because of powerful stellar winds or by interaction with a binary companion.

2. Observation and Data Reduction

We performed 20 epochs of observations (B and R filters) with CCD-photometer on the Zeiss-1000 telescope of the Special Astrophysical Observatory of the Russian Academy of Sciences.

All data were processed using the MIDAS software package of the European Southern Observatory (ESO). It includes standard image processing such as bias subtraction and flat field correction, removing the traces of cosmic particles, and stacking of individual frames into the summary image, but we did not make dark reduction as its influence was negligibly small. The line-of-sight reddening is adopted to be $E(B - V) = 0.017$ mag [12]. SN 2017gpn is located in ~0.039 degrees (> 20 kpc) from the center of the potential host galaxy NGC1343, so the galaxy's contamination is negligible.
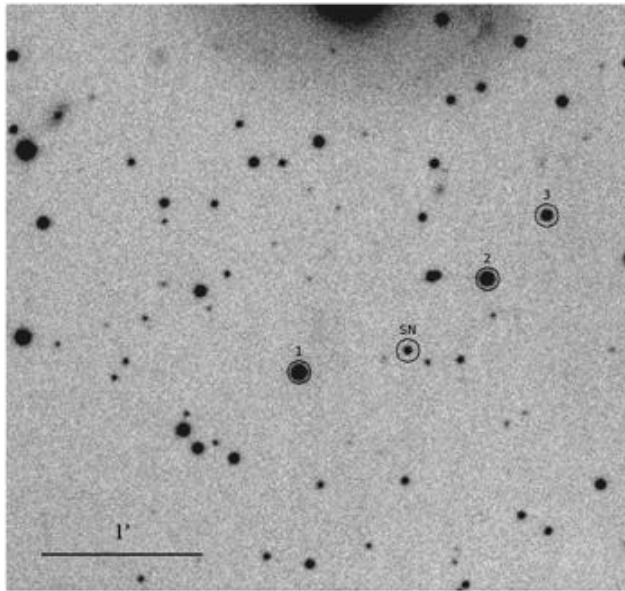
Fig1. The image of SN 2017gpn and its host galaxy obtained with the Zeiss-1000 telescope of SAO RAS.

3. Light curves

We performed the aperture photometry using standard procedures of ESO-MIDAS software package with an aperture diameter of four times the full width at half-maximum. The FWHM was measured for point sources at each epoch.

Since no Landolt or any other standard stars were available for this region, we used the Pan-STARRS magnitudes for comparison stars. The magnitudes of comparison stars were re-calculated from g, r, i to B, R with use of Lupton's transformation equations. For better modeling (see Sec. 4) the obtained light curves were also combined with publicly available data in B and R filters from the PIRATE robotic telescope [9]. The final light curves are shown in Fig. 2.
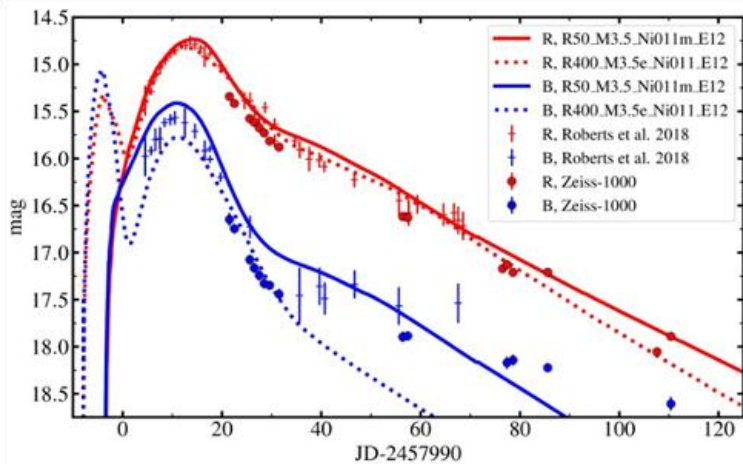
Fig2. *The results of modeling of SN 2017gpn (points are our data and crosses are the data taken from [9]). Our best-fit model is shown by solid lines (M =3.5 M⊙, R = 50 R⊙, E = 1.2 × 10⁵¹ erg, M_{56Ni} = 0.11 M⊙, mixed). For comparison the model with R = 400 R⊙ (M_{56Ni} = 0.11 M⊙, no mixing) is presented.*

3. Hydrodynamical Modeling

The numerical light curve modeling is performed with the one-dimensional multifrequency radiation hydrodynamical code STELLA. The full description of the code can be found in Blinnikov et al. [1], [2]; a public version of STELLA is also included with the MESA distribution [8].

In the current calculations we adopted 100 zones for the Lagrangian coordinate and 130 frequency bins. The main parameters we varied, were the pre-supernova star mass and radius, the energy of the explosion, the mass of synthesized nickel ^{56}Ni, and the mass of the resulting compact remnant. The compact remnant mass in the central part of the pre-supernova star with a fixed radius is treated as a point-like source of gravity that has a non-negligible influence on the expansion of the innermost layers of supernova ejecta. The ejecta of a supernova has the same chemical composition as a pre-SN star except for ^{56}Ni since STELLA does not calculate nucleosynthesis. The explosion is initiated by putting thermal energy into the innermost layers.

Our best-fit numerical model is shown by solid line in Fig. 2. The parameters of the model are: pre-SN mass M = 3.5 M⊙, pre-SN radius R = 50 R⊙, mass of hydrogen envelope M_{env} = 0.06 M⊙. The explosion energy is E = 1.2 × 10⁵¹ erg. The 0.11 M⊙ of ^{56}Ni is totally mixed through the ejecta. The compact remnant is a 1.41M⊙ neutron star. The parameters we found to be consistent with the results of hydrodynamical modeling of other typical Type IIb supernovae.

4. Discussion and Conclusions

Varying the model parameters. The parameters we found are consistent with the results of hydrodynamical modeling of other typical Type IIb supernovae. However, in different hydrodynamical models of SN IIb there is some variance in radius of pre-SN star (from 30-50 R⊙ to 700 R⊙, e.g., [1], [6], [13]). To check if it is possible to reproduce the observed

light curves of SN 2017gpn with a model of higher radius, we changed the radius in our best-fit model to R = 400 R$_\odot$ and variated the degree of ^{56}Ni mixing. By putting all the ^{56}Ni in the central part of ejecta, we were able to nearly reproduce the observed light curves (Fig. 2). This stresses the importance of ^{56}Ni mixing in such kind of studies.
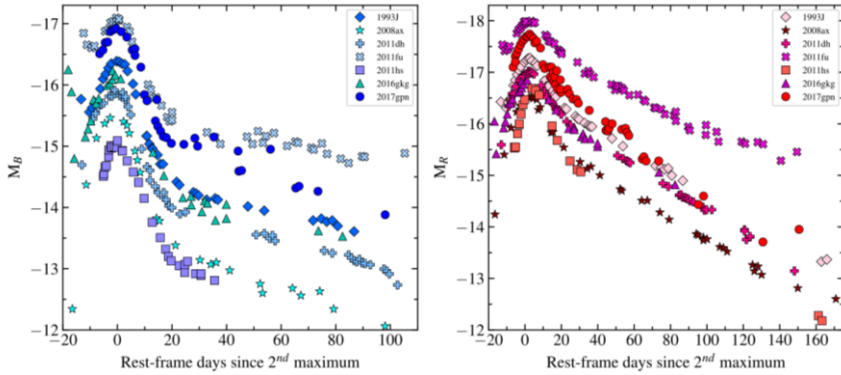
Fig3. *The classical light curves of Type IIb supernovae in B and R filters. The SN 2017gpn light curve is one of the brightest SNe IIb, its light curve behavior is similar to the others.*

Comparison with other SNe IIb. We also compared the resulting light curve with other classical and well-studied supernovae IIb light curves in B and R filters, this comparison is shown in Fig. 3. The shape of the light curve of SN 2017gpn is similar to the other typical SNe IIb light curves. Nevertheless, we noticed an interesting feature: SN 2017gpn is located rather far from its host galaxy, while the others are mainly exploded in spiral arms of their hosts (see Fig. 4).
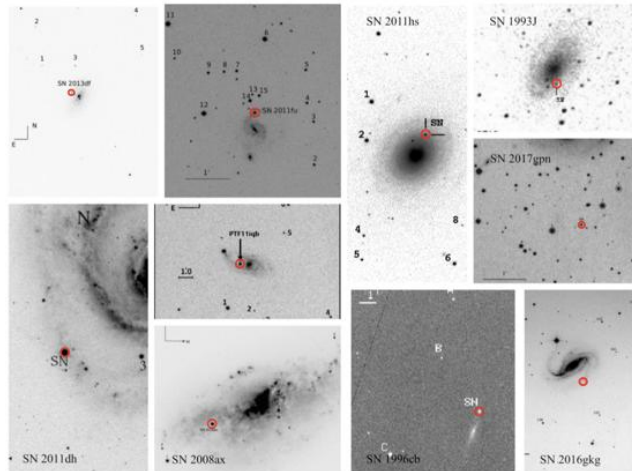
Fig4. *The location of classical Type IIb supernovae in their host galaxies.*

Connection with GW alert. By adopting the date of explosion from the models (Aug 20 for our best-fit model and Aug 16 for the model with R = 400 R$_\odot$), we can conclude that SN 2017gpn is unlikely to be connected to the LIGO/Virgo G299232 alert.

We obtained the multicolor light curve combining photometric data from Zeiss-1000 telescope of SAO RAS and the available data from the PIRATE telescope [9]. The light curves in B and R filters were modeled numerically using the one-dimensional radiation hydrodynamical code STELLA. We determined the values of the main parameters of the pre-supernova star, and these values are consistent with the results of hydrodynamical modeling of other typical Type IIb supernovae.

Acknowledgements

References

[1]   Blinnikov, S. I., Eastman, R., Bartunov, O. S., Popolitov, V. A., & Woosley, S. E. 1998, ApJ, 496, 454, doi: 10.1086/305375.

[2]   Blinnikov, S. I., Röpke, F. K., Sorokina, E. I., et al. 2006, A&A, 453, 229, doi: 10.1051/0004-6361:20054594.

[3]   Blondin, S., & Tonry, J. L. 2007, ApJ, 666, 1024, doi: 10.1086/520494.

[4]   Caimmi, M. 2017, Transient Name Server Discovery Report, 973.

[5]   Filippenko, A. V., Matheson, T., & Ho, L. C., 1993, ApJL, 415:L103.

[6]   Folatelli, G., Bersten, M. C., Kuncarayakti, H., et al. 2015, ApJ, 811, 147, doi: 10.1088/0004-637X/811/2/147.

[7]   Lipunov, V., Kornilov, V., Gorbovskoy, E., et al. 2010, Advances in Astronomy, 2010, 349171, doi: 10.1155/2010/349171.

[8]   Paxton, B., Schwab, J., Bauer, E. B., et al. 2018, ApJS, 234, 34, doi: 10.3847/1538-4365/aaa5a8.

[9]   Roberts, D., & Kolb, U. 2018, In: European Week of Astronomy and Space Science: RAS National Astronomy Meeting, 3-6 Apr 2018, Liverpool, UK.

[10]   Rui, L., Wang, X., Xiang, D., Lin, H., & Wang, H. 2017a, GRB Coordinates Network, Circular Service, No. 21780, #1 (2017/August-31), 21780.

[11]   Rui, L., Wang, X., Xiang, D., et al. 2017b, The Astronomer's Telegram, 10681.

[12]   Schlafly, E. F., & Finkbeiner, D. P. 2011, ApJ, 737, 103, doi: 10.1088/0004-637X/737/2/103.

[13]   Woosley, S. E., Eastman, R. G., Weaver, T. A., & Pinto, P. A. 1994, ApJ, 429, 300, doi: 10.1086/174319.

The study of coherent pulsations of optical emission of PSR J1023+0038 millisecond pulsar

Grigory Beskin[1,3,*], Sergey Karpov[1,2,3], Vladimir Plokhotnichenko[1], Yuri Shibanov[4], Dmitry Zyuzin[4]

[1]*Special Astrophysical Observatory, Nizhniy Arkhyz, Russia; beskin@sao.ru*

[2]*CEICO, Institute of Physics, Czech Academy of Sciences, Prague, Czech Republic*

[3]*Kazan Federal University, Kazan, Russia*

[4]*Ioffe Institute, Saint-Petersburg, Russia*

Abstract   We observed the PSR J1023+0038 millisecond redback pulsar in its accreting regime on two nights in Nov 2017 on Russian 6-m telescope with a high temporal resolution panoramic photometer-polarimeter in two-channel ("blue" and "red") setup. During 400 seconds of nearly 3 hours of total observations, we detected coherent optical pulsations in both color bands with 1.69 ms period, corresponding to the rotational period of neutron star known from radio data, with amplitudes of 2.1% ("red") and 1.3% ("blue"). Corresponding luminosity of pulsed component is about 10^{31} erg/s and may be caused by a synchrotron emission of electrons with moderate Lorentz factors close to a light cylinder during the interaction of accretion disk with ejected matter modulated with rotational period.

Keywords: Neutron Stars, Accretion Processes, Millisecond Pulsars, High Temporal Resolution

1. Introduction

The first millisecond radio pulsar PSR B1937+21 was discovered in 1982 [1], and its nature was immediately explained in view of the concept of neutron star rotation speed-up during the accretion of matter from a companion star in a compact binary system [2]. However, the first direct confirmation of this model came much later, after discovery in 1998 of a SAX J1808.4-3658 spinning-up pulsar in a low-mass binary system [3]. Finally, three systems were found to contain a neutron star transitioning from accretion to ejection stages – PSR J1023+0038 [4], XSS J12270−4859 [5], and PSR J1824−2452I [6]. The most interesting (and mysterious!) is a 1.69 ms period PSR J1023+0038 pulsar – the component of FIRST J102347.6+003841 binary, initially thought to be a cataclysmic variable detected by its radio emission [7]. To date, it was twice observed switching the stage – from accretion to ejection in 2003 [4] and back to accretion in 2013 [8]. This object is a "redback" compact binary with a 4.75 hour period, containing a 0.2 M⊙ G class normal component overflowing its Roche lobe, at a 1.37 kpc distance from the Earth [9]. X-ray and gamma-ray observations demonstrated the intensity variations with orbital period, interpreted as a manifestation of a shock wave at a collision region between pulsar wind and accreting matter [10]. Moreover, the X-ray emission was found to consist of three separate states – high (7 10^{33} erg/s), low (10^{33} erg/s) and flaring (10^{34} erg/s) with intensity variations on tens of seconds time scale, with state switching

occurring rapidly and sporadically [11]-[14]. Coherent X-ray pulsations with neutron star rotational period of 1.69 ms are detectable only in high state [15], [16], in contrast to the optical ones which was detected in flaring state too [16], [17]. In optical and infrared bands PSR J1023+0038 also displays sporadic activity on seconds to hours time scales [18], [21]. The minimal variability time scale of optical emission is as fast as fractions of seconds [22], [23], which is close to the characteristic time scales of variability due to matter fragmentation in propeller regime in MHD simulations [24]. The discovery of coherent optical pulsations synchronous with X-ray ones and having a characteristic double sinusoidal pulse shape during the accretion stage was an extremely important and unexpected result [16], [17]. It was suggested that these multi-wavelength pulsations may be caused by a synchrotron emission of electrons in the region of collision of pulsar wind with accretion flow [16].

In the present work we report on detection of periodic pulsations on neutron star rotation time scale simultaneously in two optical bands during our observations with the Russian 6-m telescope in Nov 2017, and discuss its nature.

2. Observations and results

We observed the PSR J1023+0038 millisecond pulsar, which is currently in accretion stage, on Nov 14 and 15, 2017, with the Russian 6-m telescope using a panoramic photometer-polarimeter in the dual-channel regime, using two MCP-based panoramic photon counters (the "red" one with the GaAs photocathode on 5640A effective wavelength, and the "blue" one with the multi-alcali photocathode on 4530A effective wavelength) to detect and register all photons in a $10'' \times 10''$ diaphragm around the object [25]. Total duration of observations was about 3 hours (1 hour at the first night, 2 hours at the second night), effective temporal resolution was 1 us. The times of arrival of every photon were converted to the Solar system barycenter, and then corrected for the orbital motion in the object binary system using the timing solution published in [26], adjusting the epoch of ascending node by 25.6 seconds by maximizing the phase-folding χ^2 analogous to the method using in [16], [27].

Time-resolved spectral analysis of the corrected data revealed a single 400 seconds long interval with significant (the peak significance is better than 10^{-16}) oscillations around rotational frequency of a neutron star. All other data intervals lack any peak there. Time-resolved phase folding using timing solution from [26] also revealed a single pulsed activity interval only (see Figure 1, Figure 2 and Figure 3).

Figure 4 shows the phase folded light curves in both colour bands over this time interval. The shape of folded light curves is nearly sinusoidal, in contrast with a two-peak one seen by [16], [17], [27]. Amplitudes of the pulsations after correction for the background flux contribution are A_R=2.1% in the "red" channel and A_B=1.3% in the "blue" band, with A_B/A_R = 0.61 (0.376 – 0.878 for 95% confidence interval), which, according to the optical spectrum of the object [16] and the throughput curves of channels, corresponds to absolute fluxes F_B=14.6±3 and F_R=6.8±2.6 microJansky. Therefore, for a distance to the object of 1.37 kpc [9], the optical luminosity of pulsed component is about 10^{31} erg/s with an accuracy of about 30%. Assuming the power law spectrum $F_\nu \sim \nu^{-\beta}$ for a pulsed component, its slope is β=3.5 (1.4 – 5.1 for the 95% confidence interval).
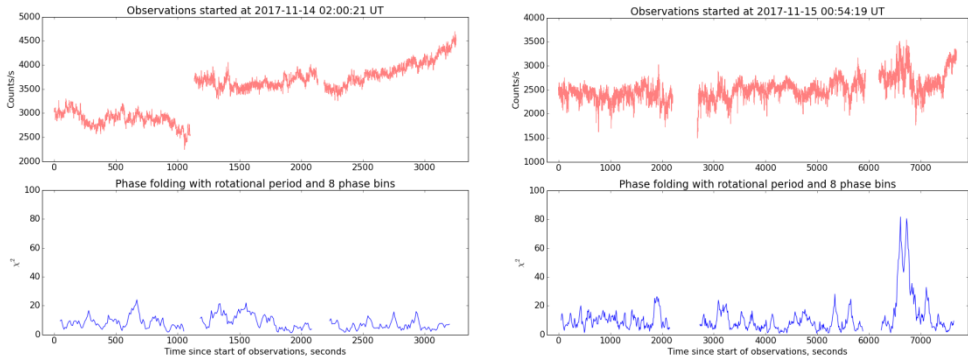
Fig1. Overall light curves for data from the "red" detector (up) and phase-folding χ² (down) using [26] timing solution in 100 s wide sliding windows. Left panel: data from the night on Nov 13, 2017. Right panel: data from the next night, Nov 14, 2017. Gaps separate continuous intervals of observations (data segments). Telescope pointing was adjusted between these observations, which explains the intensity jump on Nov 14. Only a single 400 seconds long interval in the last data segment contains significant pulsations on neutron star rotational period.
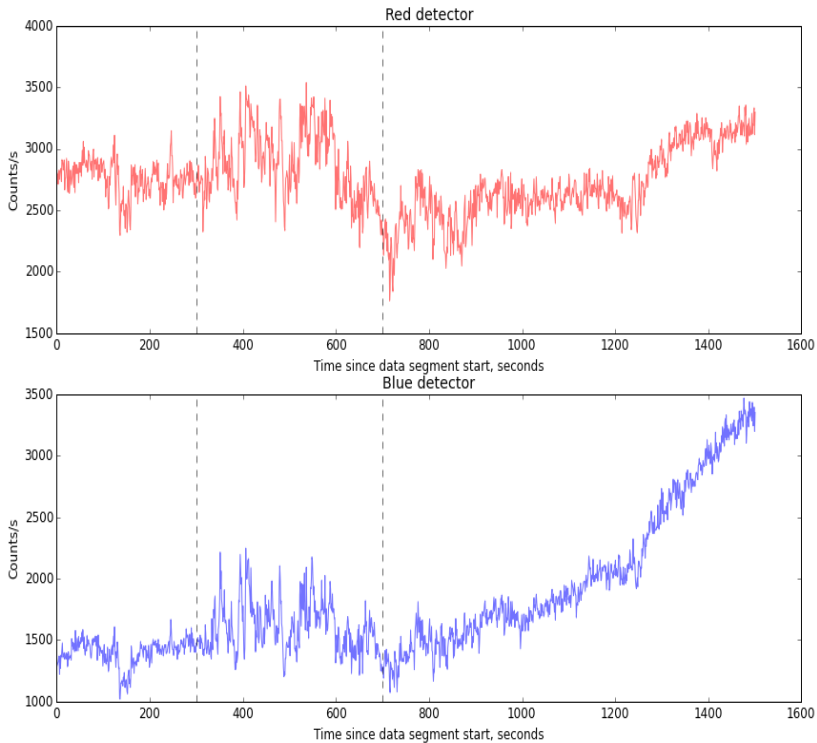
Fig2. Light curves in the "red" and "blue" channels during the data segment containing coherent optical pulsations on rotational time scale. 400 seconds long time interval when pulsations are evident is marked with vertical dashed lines. Flaring activity is evident during this interval, though such activity is also present on some other data segments lacking signs of coherent pulsations.
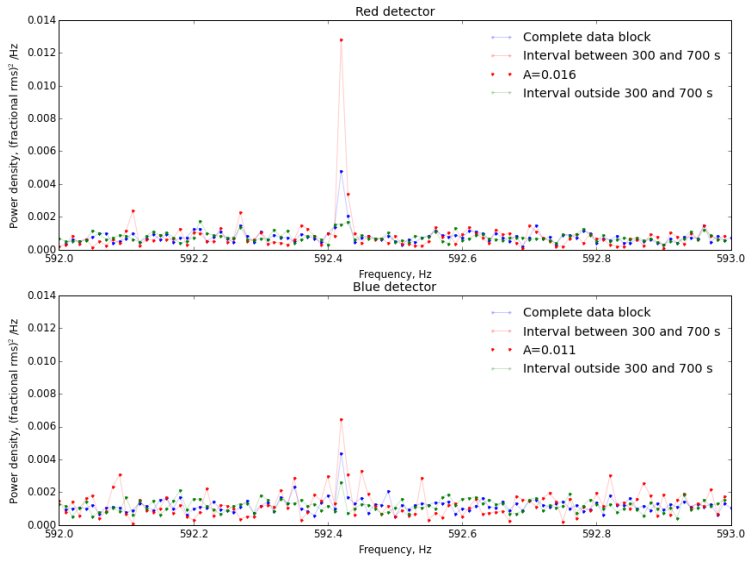
Fig3. *Periodograms of the "red" and "blue" channel light curves of a data segment shown in Figure 2. Shown are the ones for the whole segment (green), inside the activity interval (red) and outside it. The significance of the "red" channel peak inside the 400 seconds long activity interval is better than 10^{-16} after correction for the number of trial frequencies. There are no signs for any periodic oscillations outside the activity interval. The amplitudes listed for the peaks correspond to pure sinusoidal variations and are not corrected for the contribution of background emission (see the text for corrected ones).*
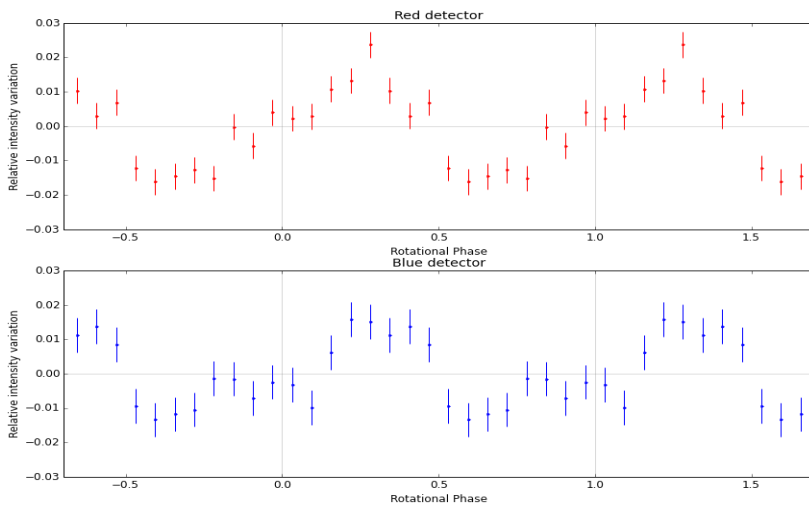
Fig4. *Folded light curves of a 400 seconds long interval containing coherent optical pulsations on rotational frequency in the "red" (upper panel) and "blue" (lower panel) channels. The intensities are not corrected for background text contributions (see the text for corrected amplitudes). The pulse shapes of different channels are similar and co-phased, and are close to sinusoidal shape, with no signs of a two-peaked shape reported by [16],[17],[27].*

3. Discussion and conclusions

In contrast to the results of other studies [16], [17], [27], the folded light curve in our observations tends to have a single-peaked, nearly sinusoidal shape. It is quite similar to the X-ray light curves of isolated radio pulsars, where the pulsations are driven by a relatively uniform thermal emission from polar caps heated by a flow of relativistic particles [28]. However, the estimate for brightness temperature corresponding to the peak fluxes in the pulses of PSR J1023+0038 is $T_b > 10^{11} F_\nu D^2 \nu^{-2} \tau^{-2} \approx 10^7 - 10^8$ K, where F_ν is a flux density in Janskys, D is the object distance in kpc, ν is the frequency in units of 10^{15} Hz, and τ is the characteristic time scale of a flux onset in milliseconds. Such large temperatures practically exclude the thermal origin of a pulsed emission, and suggests the non-thermal (synchrotron?) one [29]. On the other hand, [16] and [17] demonstrated that a large, about 10^{31} erg/s, optical pulsed emission can't be explained in neither the scenario of accretion onto neutron star pole, nor as a result of conversion of rotational energy. Finally, [17] suggested the generation of a two-peaked optical and X-ray emission as a result of collision of a pulsar wind with accretion disk, which leads to a shock wave formation and electron acceleration, and, consecutively, to synchrotron emission in a wide range of frequencies due to the motion of accelerated electrons in magnetic fields.

The coherent pulsations we see in our data are significantly different from those reported in [16], [17]. While having approximately the same position inside the binary (according to the time of passage of ascending node) and having comparable amplitudes of 1-2%, our phased light curve has a nearly sinusoidal single-peak shape, and the spectral slope of pulsed component ($\beta \sim 3.7$) is much softer than the multi-wavelength slope of $\nu F_\nu \sim \nu^{0.3}$ (β=0.7) seen in *high* mode [16] where the optical point was obtained in the white light. The lack of simultaneous X-ray data does not allow estimation of X-ray activity mode during our observations, but the interval of coherent optical pulsations (see Figure 2) is coincident with strong sporadic flaring events on a time scale of seconds to tens of seconds, especially evident in the "blue" band. The latter and a strong time correlation between the optical and X-ray flaring modes found in [16] motivate us to suppose that the system was likely in the *flaring* mode in X-rays as well. This may explain the differences in the spectral slope and the pulse shape. Indeed, the folded X-ray light curve in the *flaring* mode also shows pulsations with a quasi-sinusoidal pulse shape above 3 keV [12]. Albeit marginal (2σ significance), it is remarkably different from the clear double-peaked pulse profile in the high mode while it appears to be similar to what we see in the flaring optical state with much higher significance.

We suggest that the properties of coherent optical emission of PSR J1023+0038 we detected may be explained by synchrotron emission of relativistic electrons moving in a chaotic magnetic field just outside the light cylinder. These particles are accelerated in the current sheets during the reconnections of magnetic field lines in an outflow formed due to interaction of accretion disk with pulsar magnetosphere (the "propeller" regime) [24]. The parameters of this outflow are modulated with rotational period of neutron star, which causes the variations of the synchrotron emission with the same period. We may estimate the parameters of emission region in the following way. For a characteristic frequency of $\nu \sim 5 \cdot 10^{14}$ Hz, synchrotron energy loss timescale shorter than 0.25 of pulsar period, $\tau \sim 0.43$ ms, we get the Lorentz factor $\gamma < 50$ and $B > 1.5 \cdot 10^5$ Gauss (which is consistent with magnetic field strength close to the light cylinder). The single electron luminosity is L ~ 0.1 erg/s, which, for the pulsed component luminosity of 10^{31} erg/s, gives the number of emitting particles of 10^{32}. As the size of emission region is smaller than $c\tau \sim 10^7$ cm, the electron density is n $> 10^{10}$ cm^{-3}.

The results of MHD simulations of accretion/ejection processes onto neutron stars have

demonstrated that the process is highly non-stationary, and various parameters – matter density, outflow velocity and inhomogeneity, its luminosity, the structure and strength of magnetic fields – are strongly varying. However, our estimations do not contradict the values of parameters emerging in these simulations. On the other hand, the combination of parameters necessary for generation of coherent optical pulsations may happen sporadically. For example, when the density exceeds some threshold [30], the medium becomes opaque to a synchrotron radiation, and its intensity drops significantly. That may explain why the pulsations are detectable during the *flaring* mode – the chances to get a necessary combination of parameters are higher.

Finally, let's stress the importance of magnetic reconnections for acceleration of electrons that produce the observed optical emission. It seems that only this mechanism may lead to the formation of ensemble of electrons with such soft energetic spectrum, with the slope close to -8 [31] (which is necessary for generation of synchrotron spectrum with the slope of $\beta=3.5$).

Finally, our detection of the coherent optical pulsations with characteristics significantly different from those seen in [16], [17], [27] highlights the complex and non-stationary nature of the processes occurring in a binary system containing the transitional millisecond pulsar PSR J1023+0038.

Acknowledgements

References

[1] D.C. Backer, S.R. Kulkarni, C. Heiles, M.M. Davis and W.M. Goss. Nature, Nature 1982, 300, pp.615-618.

[2] M.A. Alpar, A.F. Cheng, M.A. Ruderman and J. Shaham, Nature 1982, 300, pp.728–730.

[3] G.S. Bisnovatyi-Kogan and B.V. Komberg. SvA 1974, 18, pp.217–221.

[4] A.M. Archibald A M et al. Science 2009, 324 1411–1414.

[5] C.G. Bassa et al. MNRAS 2014, 441, pp.1825–1830.

[6] A. Papitto et al. Nature 2013, 501, pp.517–520.

[7] Bond et al. PASP 2002, 114, pp.1359–1363.

[8] Stappers et al. ApJ 2014, 790, p.39.

[9] A.T. Deller et al. ApJ 2012, 756,   p.L25.

[10] J. Takata et al. ApJ 2014, 785, p.131.

[11] A. Patruno et al. ApJ 2014, 781, p.L3.

[12] Bogdanov et al. ApJ 2015, 806, pp.148-171.

[13] Campana et al. A&A 2016, 594, p. A31.

[14] Coti Zelati et al. A&A 2018, 611, id.A14, 12 pp.

[15] A.M. Archibald et al. ApJ 2015, 807, p.62.

[16] A. Papitto et al. ArXiv:1904.10433v1, 2019.

[17] F. Ambrosino et al. Nature Astronomy 2017, 1, pp.854-858.

[18] T. Shahbaz et al. MNRAS 2015, 453, pp.3461–3473.

[19] T. Shahbaz et al. MNRAS 2018, 477, 1, pp.566-577.

[20] Hakala and Kajava. MNRAS 2018, 474, 3, pp.3297-3306.

[21] Kennedy et al. MNRAS 2018, 477, 1, pp.1120-1132.

[22] Yu. Shibanov et al. Journal of Physics: Conf. Series 2017, 932, 012027.

[23] G. Beskin et al. In: Proceedings of The International Conference SN 1987A, Quark Phase Transition in Compact Objects and Multimessenger Astronomy, Terskol-Nizhnij Arkhyz, 2018, 24.

[24] M. Romanova et al. New Astronomy 2018, 62, pp.94–114.

[25] V. Plokhotnichenko et al. Astrophysical Bulletin 2009, 64, pp.308–316.

[26] A. Jaodand, A. et al. ApJ 2016, 830, p.122.

[27] L. Zampieri et al. ArXiv:1903.08930, 2019.

[28] V. Zavlin. Astrophys.Space Sci. 2007, 308, pp.297–307.

[29] G. Dulk. In: J.L.Linsky and Stencel R.E.(eds) "Cool stars, stellar systems, and the Sun". Lecture Notes in Physics, v/291, p.169.

[30] G.B. Rybicki and A.P. Lightman. "Radiative processes in astrophysics", 1979.

[31] M. Oka et al. Space Sci. Rev. 2018, 214, 82.

Electromagnetic Counterparts to Gravitational Waves and the case of GRB 170817A

Alberto J. Castro-Tirado[1,2,*], Youdong Hu[1], Binbin Zhang[3], and Vladimir Sokolov[4]

[1]*Instituto de Astrofísica de Andalucía (IAA-CSIC), P.O. Box 03004, E-18080 Granada, Spain; ajct@iaa.es*

[2]*Departmento de Ingeniería de Sistemas y Automática (Unidad Asociada al CSIC), Escuela de Ingeniería Industrial, Universidad de Málaga, Spain*

[3]*University of Nanjing, China*

[4]*Special Astrophysical Observatory (SAO-RAS), Zelenchuk, Karachai-Cherkessia, Russia*

Abstract We briefly report on detection of the first electromagnetic counterpart for GW 170817A. Thanks to it, the new Era of Gravitational Wave Astronomy has just been opened in 2017.

1. Introduction

The detection of gravitational waves (GWs) from a coalescing black hole binary system has been one of the major discoveries in this 21st century (Abbott et al. 2016) and will become more common from high energy celestial sources, cosmic explosions and astrophysical transients when a worldwide network of advanced versions of ground-based GW interferometers will become operational within the frequency range from 10 Hz to a few kHz within the coming years. Furthermore, the recent detection of the first GW counterpart at electromagnetic wavelengths (GW 170817) opened the new era of multi-messenger Astronomy in 2017. For the first time, this shed light on three open issues that remained obscure until that time: 1) electromagnetic counterparts can be detected for at least a fraction of GW alerts related to neutron stars (NS) mergers (Abbott et al. 2017 and references therein); 2) short duration gamma-ray bursts arise in these NS-NS mergers (see for instance Zhang et al. 2018) and 3) heavy elements (heavier than Fe) are produced in this sites due to the r-process nucleosynthesis (Pian et al. 2017).

2. Observational facts

Besides these superb discoveries reported in 2015-17 representing the first single accomplished direct test of general relativity, the detection of GWs allows to probe the inner regions of many astrophysical phenomena that are otherwise inaccessible to investigation and provide unique information on their emitters such as the two black holes (BH) merger for

GRB150914 or the NS-NS merger for the GW 170817. Other promising GW emitter candidates are the mergers of binary systems hosting two neutron stars or a NS-BH (Belczynski et al. 2008; Berger 2014) if they occur in the local Universe. The frequency of neutron star mergers is estimated at ~40 per year within 200 Mpc (Abadie et al. 2010; Singer et al. 2014; Kasliwal & Nissanke 2014).

The multi-wavelength imaging of a GW source is made extremely arduous by the size of the error areas expected to be returned by the interferometers. These are dozens to hundreds of square degrees, and only cameras with very large fields of view can cover entirely in one shot or with a small number of tiled pointings.

The monitoring of the confirmed NS-NS counterparts from early to late time is most essential, in order to properly sample the lightcurve and especially, monitor the evolving spectra. An NS-NS merger, accompanied by a short GRB first, and the emergence of so-called kilonova emission after, is expected to be accompanied by production of heavy r-process elements (Barnes & Kasen 2013; Bauswein et al. 2013) as seen in GW170817, and this translates into a transient signal that should peak hours after explosion at an expected optical absolute magnitude $M_v = 17$, and decrease thereafter with a timescale set by the diffusion time: the decline is faster for lower ejecta masses and higher energies.
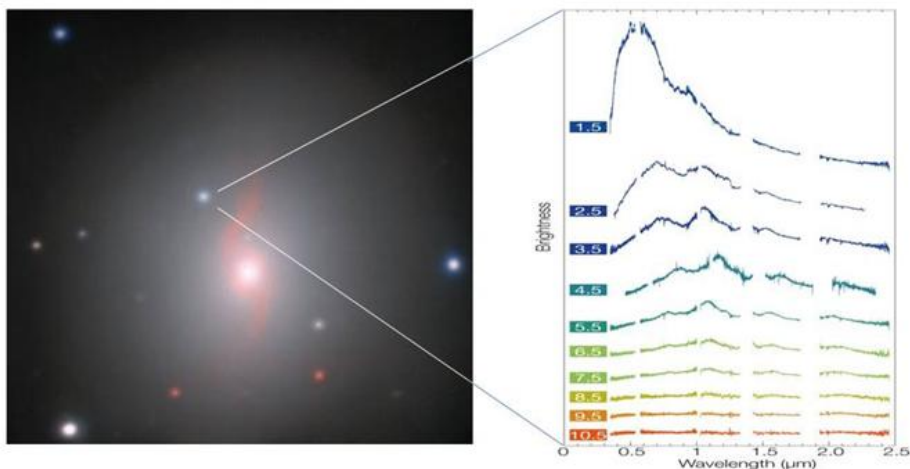
Fig1. *Left: The NGC 4993 galaxy at 40 Mpc including the optical counterpart to GW170817 following the short-duration gamma-ray burst GRB 170817A/ Right: the spectroscopic monitoring revealing the macronova (dubbed AT2017gfo) evolution for the first 11 days. From these observations, the existence of the r-process nucleosynthesis was inferred. As the ejecta expands, broad absorption-like lines appear on the spectral continuum, including atomic species produced by nucleosynthesis that occurs in the post-merger fast-moving dynamical ejecta and in two slower (0.05 times light speed) wind regions. Comparison with spectral models suggests that the merger ejected 0.03 to 0.05 solar masses of material, including high opacity lanthanides. Adapted from Pian et al. (including Castro-Tirado) 2017.*

The evolving spectra (complemented by NIR observations to properly model the kilonova Rayleigh-Jeans tail) is of utmost importance in order to search for the lanthanide-rich or lanthanide-free ejecta which may be present in heavy element production. Other candidates for GW in the range of frequencies accessible to ground based interferometers include also long GRBs (Corsi & Meszaros 2009), core-collapse supernovae (Ott et al. 2012; Muller et al. 2012),

newly born magnetars (Stella et al. 2005; Dall Osso et al. 2009), and magnetars (Corsi & Owen 2011; Abadie et al. 2011).
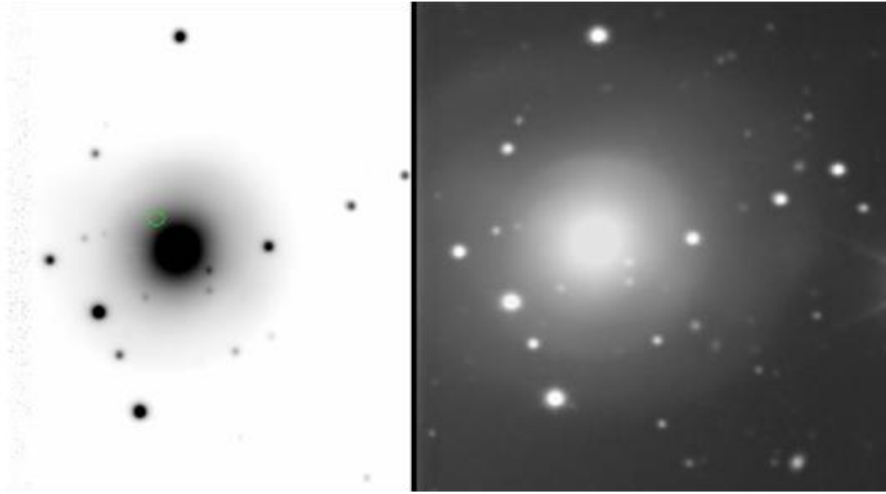
Fig2. NGC4993 (1200s, Sloan i'-band filter) was maged by the 10.4m GTC on 19 Jan 2018, ~5 months agfter the occurrence of GW 170817A. Left: the location of the NS-NS merger (the green circle) is shown. Right: the image has been processed to show the different stellat shells around the galaxy. Adapter from Pandey, Hu, Castro-Tirado et al. (2019).

3. Conclusions

The new Era of Gravitational Wave Astronomy has just been opened. With the advent of the forthcoming advanced LIGO-VIRGO Observing Run 3 (O3) in Apr 2019, the numbers of GW alerts will significantly increase. Coordinated multiwavelength efforts will shed light into the physics of compact objects mergers in the Universe.

Acknowledgements

References

[1]   Abbott, B. P. et al. 2016, Physical Review Letters, 116, 061102.

[2]   Abbott, B. P. et al. 2017, ApJL 848, 12

[3]   Abbott, B. P. et al. 2018,   http://adsabs.harvard.edu/abs/2018LRR....21....3A

[4]   Abadie, J., et al., 2010, ApJ, 734, L35.

[5]   Bauswein, A., et al., 2013, Physical Review Letters, 111, 131101.

[6] Barnes, J., & Kasen, D., 2013, ApJ, 775, 18.

[7] Belczynski, C., et al., 2008, ApJ, 682, 474.

[8] Berger, E., et al., 2013, ApJ, 774, L23.

[9] Berger, E., 2014, ARA&A, 52, 43.

[10] Castro-Tirado, A. J. et al., 2017, GCNC, 21624.

[11] Corsi, A., & Owen, B.J., 2011, Phys. Rev. D, 83, 104014.

[12] Dall ´Osso, S., et al., 2009, MNRAS, 398, 1869.

[13] Falta, D., et al., 2011, Phys. Rev. Lett., 106, 201103.

[14] Kasliwal, M., & Nissanke, S., 2014, ApJ, 789, L5.

[15] Mueller, E., et al., 2012, A&A, 537, 63.

[16] Ott, C., et al., 2012, Phys. Rev. D, 86, 024026.

[17] Pandey, S. B., Hu,Y.-D., Castro-Tirado, A.J. et al. 2019, MNRAS, in press (arXiv:1902.07900)

[18] Pian, E. et al. 2017, Nat 551, 67.

[19] Pankow, C. 2018, private   comm. at the LVC MIT Town Hall meeting, March 2018

[20] Perna, R. et al. 2018, MNRAS 477, 4228.

[21] Singer, L., et al., 2013, ApJ, 776, L34.

[22] Singer, L., et al., 2014, arXiv:1404.5623.

[23] Stella, L., et al., 2005, ApJ, 634, L165.

[24] Tanvir, N., et al., 2013, Nature, 500, 547.

[25] Zhang, B.-B. et al. 2018, Nat Co 8, id. 447.

Measurements of thermal neutron flux in underground laboratories, a standard proposal for the BSUIN project

Z. Dębicki, K. Jędrzejczak[*], M. Kasztelan, W. Marszał, J. Orzechowski, J. Szabelski, P. Tokarski

National Centre for Nuclear Research, Astrophysics Division, Cosmic Ray Laboratory,

28Pulku Strzelców Kaniowskich 69, 90-558 Lódź, Poland; kj@zpk.u.lodz.pl

Abstract One of the goals of the BSUIN project is to propose standard methods for the characterization of underground laboratories (UL). We have proposed scheme for thermal neutron flux measurement: simple and low-cost but still very reliable. A pilot measurements were made in mines in Freiberg (Germany) and Pyhasalmi (Finland). This work is still in progress, the final stage of the BSUIN project is planned for 2020.

Keywords: Underground Laboratory, Natural Neutron Flux, Cosmic Neutrino Measurements, Dark Matter Search

1. Introduction

The Baltic Sea Underground Innovation Network (BSUIN) project [1] is aimed at making the underground laboratories in the Baltic Sea region more accessible for innovation, business development and science by improving information about the underground laboratories, the operation, user experiences and safety. Potential beneficiaries of the project are various types of underground physics, such as neutrino measurements or dark matter searching. The BSUIN consortium comprises 14 members from eight Baltic Sea countries. Six underground labs are looking for new collaboration in the project. BSUIN is EU funded as a part of INTERREG Baltic Sea program [2].

The main topic of BSUIN Work Package WP2 (Characterization of Underground Laboratories) is the development of a standard for the characterization of underground laboratories. As part of WP2, National Centre for Nuclear Research (NCBJ, Poland) is the leader of activity WP2.2 (Natural radioactive background characterization). Therefore, we proposed a scheme for measuring the neutron background, built a test setup and carried out pilot measurements.

2. Minimal setup for thermal neutron flux measurements

We decided to consider what the simplest setup for thermal flux measurements should be. It is obvious that a setup containing many counters and sophisticated measuring electronics will give more reliable results than a smaller and simpler one, but in many cases it will be overkill, unnecessarily raising the complexity and cost of the measurement. We would like to propose a setup as simple as possible, but still able to measure thermal neutron flux in underground laboratories with sufficient reliability. In our opinion, the setup should have the following

features:

- to consist of at least two counters, so that the measurement uncertainty can be determined by comparing the results;
- the method of distinguishing real neutron recording from noise should exist;
- the presence of the operator during the measurements should not be necessary, which will make very long-term measurements easier.

So we built a test setup consisting of two helium counters and a simple data acquisition system.

2.1. Helium counter

In our implementation, we used two proportional helium counters of type ZDAJ NEM425A50.

The counter is made of a 50 cm long steel tube of diameter of 2.5 cm and is filled with helium-3 under pressure of 4 atm. and natural krypton under pressure of 0.5 atm.

This type of counter is a standard gas proportional counter, but filled with helium-3, which is a noble gas with high cross section for thermal neutrons capture. Charged products of the capture reaction $^{3}He(n,p)^{3}H$ poses 764 keV of released energy and are recorded by the proportional counter in the normal way. Therefore an amplitude spectrum recorded by the counter has a characteristic shape with a peak corresponding to 764 keV energy and a tail of smaller amplitudes for cases when one of the reaction products escaped from the active volume (it's a so-called "wall effect"). An example of amplitude spectrum, obtained with a relatively large flux of thermal neutrons is shown in Figure 1.
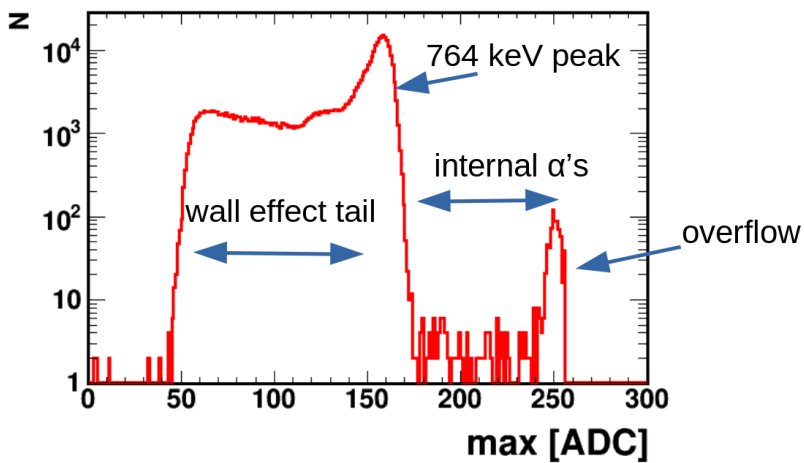
Fig1. Amplitude spectrum measured by the helium counter with an artificial neutron source. The 764 keV peak with tail is clearly visible.

2.2. Data acquisition system

The helium counter is a brilliant tool for neutron flux measuring because the distinction between neutrons and background signals is easy: you only need to recognize the 764 keV peak, so all you need is an amplitude spectrum. But in underground laboratories the neutrons flux from natural sources is usually very low, so noises negligible in normal conditions can

distort completely the shape of the spectrum. This is the reason why the pulse-shape analysis is necessary.

Our data acquisition system has been designed to save oscilloscope-like waveforms for all received signals. For each counter we use a simple device with a single channel ADC controlled by a microcontroller. The ADC samples the signal every 700ns, and after the trigger keeps 50 samples of the waveform. Every device is independent and self-triggered, powered and control by a PC computer via the USB port. Example waveform recorded for neutron is shown in Figure 2.
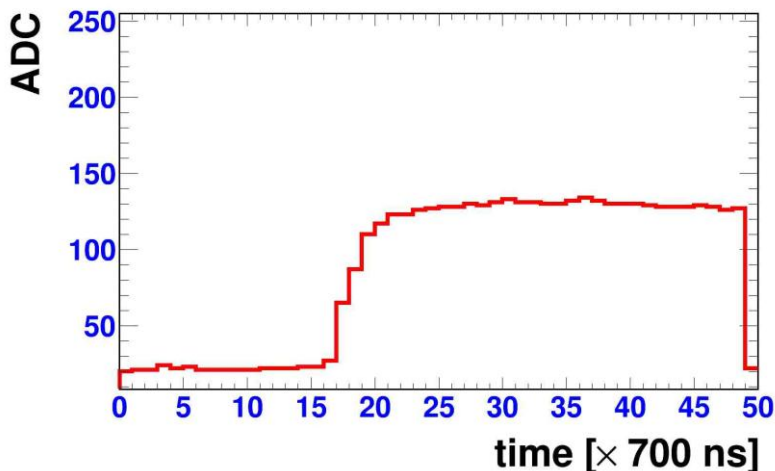
Fig2. An example of waveform registered for neutron

2.3.   Remote control

Because the setup consists of only two helium counters, data acquisition time must be relatively long (several weeks).   Such long presence of an operator would be very expensive so this forces the construction of the setup as remotely controlled. The setup of the main PC computer can be fully controlled via Internet using the ssh client or open source remote desktop program "Remmina"[4]. PC can be turned on and off by the standard Linux program "rtcwake", additionally, thanks to special PC power supply configuration, reset of all devices powered by USB is possible.

3. Data analysis

In our case data analysis was aimed at distinguishing neutrons from other signals recorded by helium counters. These "other signals:" can be divided into three groups:
- normal electronics noise – this type dominates at low amplitudes, but its intensity decreases exponentially with the increase in amplitude, so it rarely appears in the area of 764 keV peak.   The electronics noise intensity depends on the quality of the used electronics.
- alpha particles from counter's internal parts – helium counter parts contain natural radioactive isotopes that emit alpha particles. These particles travel random lengths

before they reach the active volume of the counter, which is why the recorded amplitude spectrum has a flat shape (shown in Figure 1). The shape of alpha signal is exactly the same as neutron signal, but alpha spectrum can be easily studied for amplitudes greater than the 764 keV peak and subtracted from the neutron spectrum.

- high voltage "sparks" – this type comes from the current flow on the surface of insulators in the high voltage connectors. Recorded pulses can have any kind of amplitude, so they mimic neutrons. Fortunately, the rise time for "sparks" is much shorter than for neutrons, so these two cases can be distinguished by pulse shape analysis.

A useful tool for pulse shape analyzing is the two-dimension histogram "rise time" versus "maximum pulse amplitude" shown in Figure 3 (in fact, in this figure "pulse maximum time" is shown instead of "rise time", but these times differ by a fixed value).
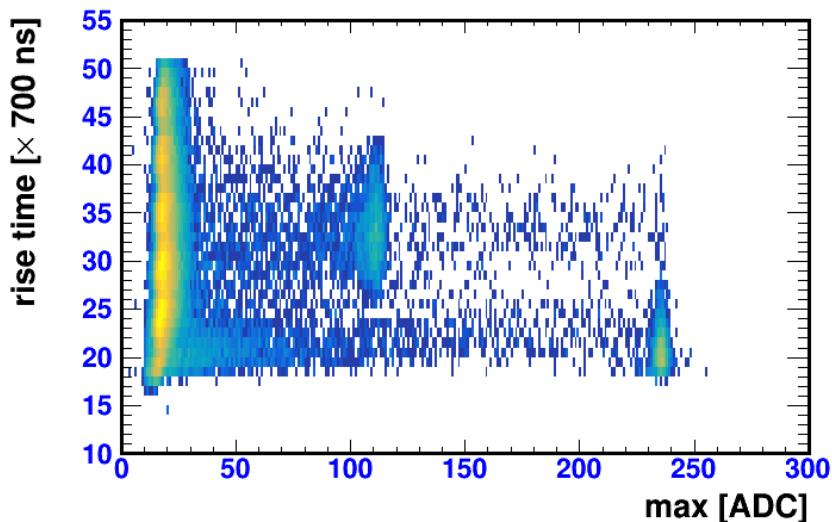
Fig3. Two dimension histogram "rise time" versus "maximum pulse amplitude"

The points in the histogram are arranged in a few distinct groups.

- The vertical band for amplitudes smaller than ~45 ADC corresponds to the normal electronics noise.
- The horizontal band for rise time smaller than ~29 ticks of time corresponds to high voltage "sparks".
- The remained vertical band with a clear stain at ~120 ADC and ~35 ticks of time corresponds to neutrons and alphas. The stain corresponds to peak 764 keV.

The impact of rejection of 'sparks' on the spectrum of amplitudes is shown in Figure 4.

Analysis like this allows us to determine the true frequency of neutron counts in the counters and after comparing with the MC simulation, determine the neutron flux.
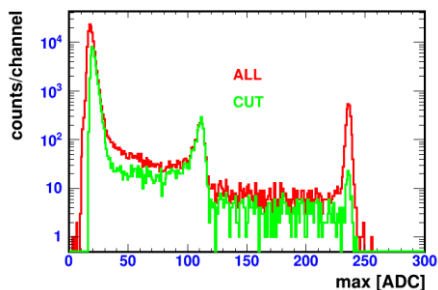
Fig4. *Amplitude spectrum   registered in Freiberg mine in Saxony (Germany) after 45.5 days of data acquisition . The red line marks the raw spectrum, the green line –   spectrum after subtraction of "sparks".*

4. Pilot measurements

To test the setup we have carried out measurements of the neutron flux in two mines: in Freiberg, Saxony (Germany) and in Pyhasalmi (Finland). These preliminary tests have shown that the setup is a useful tool for measuring neutron flux in the underground, but requires improvements and further tests.

4.1. Freiberg

Measurements were carried out at -250 m, in the network server room, near the "Reiche Zeche" shaft. The room was about 3x3x3 m, brick walls and a concrete ceiling.

The measurements were divided into two phases. In the first phase the setup consisted of two bare helium counters (as described above), and the measured results were used to determine the neutron flux. The registered amplitude spectrum for one of the counters is shown in Fig4, the thermal neutron flux calculated from the measurement results is equal to $(3.1 \pm 0.3) \cdot 10^{-6}$ cm^{-2}s^{-1}.

It is a rather high flux, but Reiche Zeche is an old silver mine, so a high level of natural radioactivity is expected. The first phase setup is shown in the Figure 5 on left panel.

Fig5. *Setup used in Freiberg   (Germany) in Reiche Zeche shaft Left: Bare counters for the first phase measurements. Right: Counters in borax shield for the second phase measurements.*

In the second phase of measurements the setup from the first phase was surrounded by a cover made of polyethylene bottles filled with technical borax. The shield decreased the neutron flux reaching the setup due to neutron capture by boron-10 contained in borax. The second phase setup is shown in the left panel of Figure 5.

The second phase was a test of the setup and the analysis method: the rate of neutron counts should decrease, but the rate of internal alpha particle rate should not. The measurement lasted 30 days and confirmed that the apparatus is working properly. The comparison of the first and second phase results is shown in Figure 6.
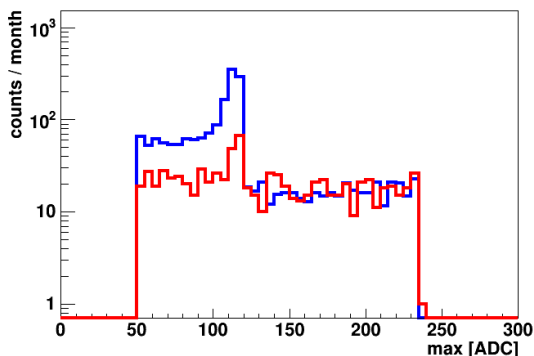
Fig6. Results obtained in Freiberg (Germany) in Reiche Zeche shaft. Comparison of the first (the blue line) and second (the red line) phase amplitude spectrum

4.2. Pyhasalmi

Measurements were carried out at -1444 m, in a special laboratory hall. The data acquisition system was similar to that used in Freiberg (with several improvements), but in this case the setup consisted of 10 bare helium counters. The data collection time was only about a week, which was enough due to the relatively high counting rate. Thermal neutron flux is probably 10 times greater than flux in Freiberg, but the data analysis is still in progress. The setup used in Pyhasalmi is shown in Figure 7.

Fig7. The setup used in Pyhasalmi (Finland)

5. Conclusion

As a part of the BSUIN project we have proposed a simple and low-cost but still very reliable scheme for thermal neutron flux measurement. Pilot measurements were made in mines in Freiberg (Germany) and Pyhasalmi (Finland). This work is still in progress, the final stage of the BSUIN project is planned for the year 2020.

Acknowledgements

References

[1]   http://bsuin.eu/

[2]   Interreg Baltic sea URL http://www.interreg-baltic.eu

[3]   Z. Dębicki et al 2019 J. Phys.: Conf. Ser.1181 012071

[4]   https://remmina.org/

Radiation properties of gamma-ray compact steep-spectrum sources

Shen-Shi Du[1], Hai-Ming Zhang[2], Ting-Feng Yi[3], Jin Zhang[4,*], En-Wei Liang[1]

[1]*Guangxi Key Laboratory for Relativistic Astrophysics, Department of Physics, Guangxi University, Nanning 530004, China*

[2]*School of Astronomy and Space Science, Nanjing University, Nanjing 210023, China*

[3]*Department of Physics, Yunnan Normal University, Kunming 650500, China*

[4]*National Astronomical Observatories, Chinese Academy of Sciences, Beijing 100012, China; jinzhang@bao.ac.cn*

Abstract   Three compact steep-spectrum sources (CSSs) have been detected by the *Fermi*/LAT. We collected their broadband SEDs from the literature and compared with two typical blazars, one BL Lacertae (BL Lac) and one flat spectrum radio quasar (FSRQ). The morphology of the broadband SEDs for the three CSSs is more analogous to FSRQs than BL Lacs. However, the multiband spectrum fitting may offer a complementary diagnostic clue of their gamma-ray emission production mechanisms and jet properties.

Keywords: Galaxies: Active, Galaxies: Jets, Radio Continuum: Galaxies, Gamma Rays: Galaxies

1. Introduction

So far, most confirmed extragalactic gamma-ray emission sources are blazars (Ackermann et al. 2015), for which the broadband spectral energy distributions (SEDs) are dominated by the jet emission and the jet direction points to the Earth. Blazars are divided into BL Lacertae (BL Lac) objects and flat spectrum radio quasars (FSRQs) according to their spectral features in the optical band. Generally, the observed SEDs of blazars are bimodal and can be well explained by the one-zone leptonic models; the synchrotron radiation and the inverse Compton (IC) scattering of relativistic electrons in the jets (Maraschi et al. 1992; Ghisellini et al.1996; Sikora et al.2009; Zhang et al. 2012, 2014, 2015).

Besides blazars, some other kinds of active galactic nuclei (AGNs) have also been detected by the *Fermi*/LAT, such as radio galaxies (RGs) and narrow-line Seyfert 1 (NLS1) galaxies (Ackermann et al. 2015). For both of them, the detected gamma-ray emission is also thought to be from the jet radiation. The SEDs of the GeV NLS1s are similar to blazars and can be well represented with the one-zone leptonic model. The jet properties of the GeV NLS1 galaxies are intermediate between FSRQ jets and BL Lac jets, but more analogous to FSRQ jets (Sun et al. 2015). According to the unification models for radio loud (RL) AGNs, BL Lacs are associated with FR I RGs, whereas FSRQs are usually linked with FR II RGs (Urry & Padovani 1995), i.e., RGs are the parent populations of blazars with large viewing angles and small Doppler factors. Although a more complex model with more parameters may produce a better fit to the

SEDs of some RGs (e.g., Tavecchio & Ghisellini 2014), the one-zone leptonic model is also used to reproduce the SEDs of RGs by many authors (Abdo et al. 2009a; Migliori et al. 2011; Fukazawa et al. 2015; Xue et al. 2017).

Another class of RL AGN, known as compact steep-spectrum sources (CSSs), is also detected in the GeV band by *Fermi*/LAT. The radio morphology of CSSs is typically characterized by fully developed radio lobes and by a small linear size (< 15 kpc; see O'Dea 1998 for a review). CSS is thought to be the first stage in the evolution of large extragalactic radio sources (e.g., Migliori et al. 2014). The radiation mechanisms and origin of the gamma-ray emission are useful to study many aspects of the physics of CSSs. Comparisons of broadband emission between CSSs with blazars may help to reveal the intrinsic connections among different RL AGNs.

2. The gamma-ray Emission CSSs

3C 286 also named B1328+307, at redshift of z = 0.849 (Cohen et al. 1977). The steep radio spectrum with a spectral index of α = -0.61 ($S_\nu \propto \nu^\alpha$) between 1.4 and 50 GHz with a turnover at about 300 MHz, below which it is flat till ~75 MHz (An et al. 2017). The source displays a primary core and a second lobe ~2.6 arcsec (19.4 kpc) to the south-west (Spencer et al. 1989; An et al. 2017). The radio emission at 15 GHz of this source is rather stable and no significant variation is observed in the past 10 years. The high polarization of the source has been detected in the radio band (Akujor & Garrington 1995). A compact bright nucleus associated with the radio core is also detected by the Hubble Space Telescope (deVries et al. 1997). Two compact components in the inner 10-mas region with comparable flux densities are resolved with the Very Long Baseline Interferometry (VLBI) and the more compact component showing an inverted spectrum with a turnover between 5 and 8 GHz may infer the core (An et al. 2017). A jet speed of ~0.5c and an inclination angle of ~48° are derived for 3C 286. The optical spectrum observed with the SDSS-BOSS clearly indicates that 3C 286 can be classified as a NLS1 (Berton et al. 2017). The source was detected in the 100 MeV−100 GeV energy range by *Fermi*/LAT (Ackermann et al. 2015).

4C+15.05 also known as NRAO 91 and PKS 0202+14. On the basis of [O III] λ3727 and [Ne I] λ3833 lines, the source was estimated to be located at z = 0.833 (Stickel et al. 1996), but a smaller redshift of z = 0.405 is reported by Perlman et al. (1998). Recently, Jones et al. (2018) suggested that the neutral hydrogen absorption feature of this source agrees very well with the value of z = 0.833. The mean spectral index of α = -0.33 between 400 MHz to 8 GHz is reported by (Herbig & Readhead 1992). This source displays a structure of a core and double lobes with a total projected size of ~1.3 kpc. A core-jet structure at pc-scale extends the projected size of ~25 pc at a position angle perpendicular to the kpc-scale structure (An et al. 2016). Different from 3C 286, the significant apparent superluminal motion of ~16c is detected (An et al. 2016). 4C+15.05 has been identified as a gamma-ray AGN with the EGRET, and later was detected by *Fermi*/LAT.

4C+39.23B located at photometric redshift of z = 1.18 (1.0-1.4) (Lilly 1989). The value of z = 1.21 was used in Law-Green (1995) and Roche et al. (1998). The spectral indices between 0.4 to 1.4 GHz and between 4.9 to 8.5 GHz are -0.3 and -1.02, respectively (Fanti et al. 2001). It is detected by *Fermi*/LAT and associated with J0824.9+3916 (Massaro et al. 2016). However, its gamma-ray association is doubtful and could arise from the nearby blazar 4C+39.23 (Migliori et al. 2016; An et al. 2017).
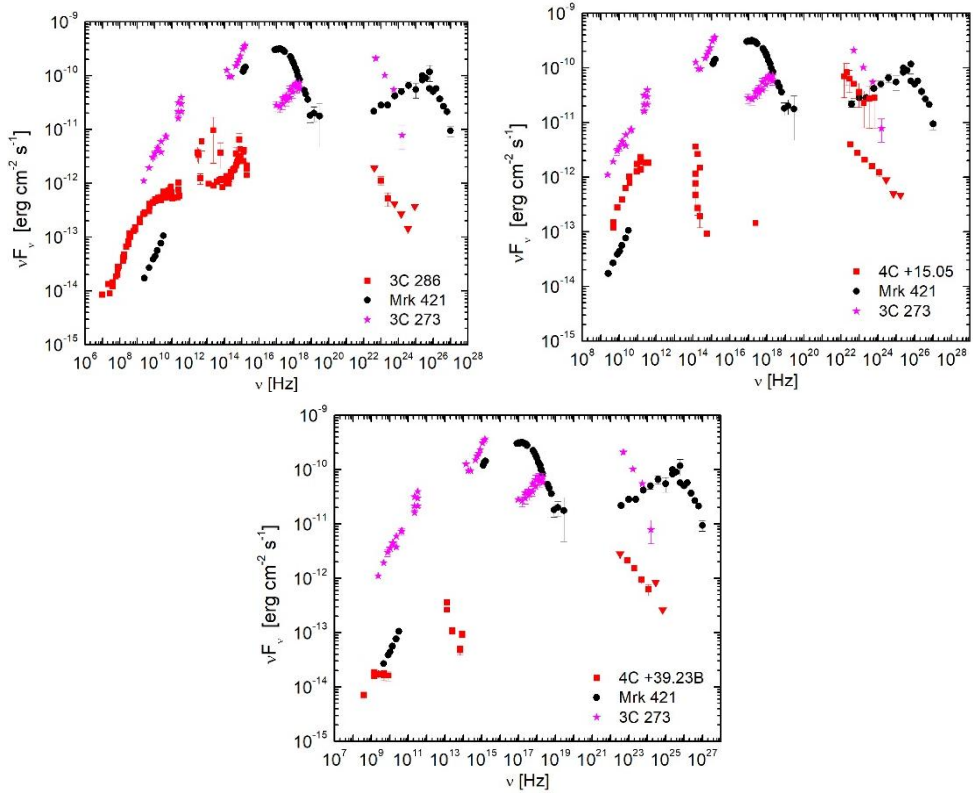
Fig1. *SEDs of the three gamma-ray emission CSSs. The gamma-ray emission data in the Fermi/LAT band for the three CSSs are taken from our work (in preparation). The other data, for 3C 286 are from An et al. (2016) and NED, for 4C+15.05 are from Bloom et al. (1994), Comastri et al. (1997), Stickel et al. (1996) and Montigny et al. (1995), for 4C 39.23B are from SSDC (https://tools.ssdc.asi.it/SED/). The data of two typical blazars, one BL Lac (Mrk 421) and one FSRQ (3C 273), are taken from Zhang et al. (2012, 2014).*

3. Comparisons of Broadband SEDs between CSSs and Blazars

We collected the data of broadband SEDs for the three CSSs from the literature, as illustrated in Figure 1. The average spectra in the gamma-ray band observed by the *Fermi*/LAT are from our work in preparation. For comparisons, the broadband SEDs of two typical blazars, one BL Lac (Mrk 421) and one FSRQ (3C 273), are also presented in Figure 1. In the radio band, 3C 286 and 4C+15.05 have the higher fluxes than Mrk 421. However, in other energy bands the radiation fluxes of the three CSSs are much lower than that of the two blazars. Especially in the X-ray band, except for 4C+15.05, which has an observational data point in the soft X-ray band, no other observation data are available for the three CSSs, indicating that their X-ray emission is very weak. This is very different from blazars since blazars normally have very strong emission in the X-ray band. The broadband SEDs of the three CSSs, similar to that of blazars, shape two bumps. The peak frequencies of the first bumps for the three CSS SEDs approximately locate at 10^{12}-10^{13} Hz, similar to the typical values of FSRQs. Comparing with the two blazars, the morphology of the broadband SEDs for the three CSSs is more analogous to FSRQs than BL Lacs. The broadband SEDs of blazars are thought to be

dominated by the pc-scale jet radiation. The radiation mechanisms of CSSs in multi-wavelengths are very unclear. The larger viewing angle of CSSs than that of the blazar jets may challenge the one-zone leptonic models to represent the observed SEDs of CSSs.

References

[1]   Abdo, A. A., Ackermann, M., Ajello, M., et al. 2009, ApJ, 699, 31

[2]   Ackermann, M., Ajello, M., Atwood, W. B., et al. 2015, ApJ, 810, 14

[3]   Akujor, C. E., & Garrington, S. T. 1995, A&AS, 112, 235

[4]   An, T., Cui, Y.-Z., Baan, W. A., Wang, W.-H., & Mohan, P. 2016, ApJ, 826, 190

[5]   An, T., Lao, B.-Q., Zhao, W., et al. 2017, MNRAS, 466, 952

[6]   Berton, M., Foschini, L., Caccianiga, A., et al. 2017, Frontiers in Astronomy and Space Sciences, 4, 8

[7]   Bloom, S. D., Marscher, A. P., Gear, W. K., et al. 1994, AJ, 108, 398

[8]   Cohen, A. M., Porcas, R. W., Browne, I. W. A., Daintree, E. J., & Walsh, D. 1977, MmRAS, 84,

[9]   Comastri, A., Fossati, G., Ghisellini, G., & Molendi, S. 1997, ApJ, 480, 534

[10] de Vries, W. H., O'Dea, C. P., Baum, S. A., et al. 1997, ApJS, 110, 191

[11] Fanti, C., Pozzi, F., Dallacasa, D., et al. 2001, A&A, 369, 380

[12] Fukazawa, Y., Finke, J., Stawarz, L., et al. 2015, ApJ, 798, 74

[13] Ghisellini, G., Maraschi, L., & Dondi, L. 1996, A&AS, 120, 503

[14] Herbig, T., & Readhead, A. C. S. 1992, ApJS, 81, 83

[15] Jones, K. M., Ghosh, T., & Salter, C. J. 2018, AJ, 155, 254

[16] Law-Green, J. D. B., Leahy, J. P., Alexander, P., et al. 1995, MNRAS, 274, 939

[17] Lilly, S. J. 1989, ApJ, 340, 77

[18] Maraschi, L., Ghisellini, G., & Celotti, A. 1992, ApJ, 397, L5

[19] Massaro, F., Thompson, D. J., & Ferrara, E. C. 2015, A&A Rev., 24, 2

[20] Migliori, G., Grandi, P., Torresi, E., et al. 2011, A&A, 533, A72

[21] Migliori, G., Siemiginowska, A., Kelly, B. C., et al. 2014, ApJ, 780, 165

[22] O'Dea, C. P. 1998, PASP, 110, 493

[23] Perlman, E. S., Padovani, P., Giommi, P., et al. 1998, AJ, 115, 1253

[24] Roche, N., Eales, S., & Rawlings, S. 1998, MNRAS, 297, 405

[25] Sikora, M., Stawarz, L., Moderski, R., Nalewajko, K., & Madejski, G. M. 2009, ApJ, 704, 38

[26] Spencer, R. E., McDowell, J. C., Charlesworth, M., et al. 1989, MNRAS, 240, 657

[27] Stickel, M., Rieke, G. H., Kuehr, H., & Rieke, M. J. 1996, ApJ, 468, 556

[28] Sun, X.-N., Zhang, J., Lin, D.-B., et al. 2015, ApJ, 798, 43

[29] Tavecchio, F., & Ghisellini, G. 2014, MNRAS, 443, 1224

[30] Urry, C. M., & Padovani, P. 1995, PASP, 107, 803

[31] von Montigny, C., Bertsch, D. L., Chiang, J., et al. 1995, ApJ, 440, 525

[32] Xue, Z.-W., Zhang, J., Cui, W., Liang, E.-W., & Zhang, S.-N. 2017, Research in Astronomy and Astrophysics, 17, 090

[33] Zhang, J., Liang, E.-W., Zhang, S.-N., & Bai, J. M. 2012, ApJ, 752, 157

[34] Zhang, J., Sun, X.-N., Liang, E.-W., et al. 2014, ApJ, 788, 104

[35] Zhang, J., Xue, Z.-W., He, J.-J., Liang, E.-W., & Zhang, S.-N. 2015, ApJ, 807, 51

Quick search for optical partners of bursts of very high energy gamma-ray radiation

I.M. Dzaparova[1,2,*], I.S. Savanov[2], V.B. Petkov[1,2], A.V. Sergeev[1,2],
D.D. Dzhappuev[1], A.N. Kurenya[1], V.B. Puzin[2], E.A. Gorbacheva[1],
O.I. Mikhailova[1], M.A. Nalivkin[2], S.A. Naroenkov[2], A.A. Shlyapnikov[3]

[1]*Institute for Nuclear Research of the Russian Academy of Sciences, 60th October Anniversary Prospect, 7a, 117312 Moscow, Russia*

[2]*Institute of Astronomy of the Russian Academy of Sciences, 48 Pyatnitskaya St., 119017, Moscow, Russia; dzaparova@yandex.ru*

[3]*Crimean Astrophysical Observatory of the Russian Academy of Sciences*

Abstract   Quick search for optical partners of bursts of gamma radiation of high and ultrahigh energy range are conducted using the facilities of the Baksan Neutrino Observatory (BNO) of the INR RAS and a complex of astronomical telescopes at peak Terskol Observatory of the Institute of Astronomy of RAS. The bursts of cosmic ray intensity and cosmic gamma radiation are detected at the complex of BNO facilities. The search and subsequent study of optical flares associated with the detected BNO events are carried out with a complex of astronomical telescopes at the peak Terskol. To search by external target designations (from BNO installations, the GCN network, etc.) of transient phenomena in the optical range a universal program for managing a complex of astronomical telescopes was developed and created. The current state and preliminary results of the experiment are discussed.

Keywords: Gamma Radiation, Bursts, Optical Flares, Multimessenger Astronomy

1. Introduction

Currently, the methods of multimessenger astronomy are widely used in the study of astrophysical objects that emit a large amount of energy in a wide range of electromagnetic radiation spectrum. Our experiment is aimed at obtaining new experimental data on astrophysical objects generating bursts of cosmic gamma radiation of high energy together with optical flashes. Such bursts of radiation can be generated by processes in the nuclei of galaxies, by the interaction of astrophysical objects, at the last stage of the evolution of stars, including supernova bursts.

The search for bursts of cosmic ray intensity and cosmic gamma radiation is carried out by the method of a search for spatiotemporal concentrations (clusters) of showers recorded by EAS array. Previously this method was widely used to search for very high energy gamma radiation from cosmic gamma-ray bursts (CGRB) and from evaporating primordial black holes (PBH) at EAS arrays and underground telescopes [1 – 5].

2. The finding of shower clusters.

The algorithm for finding cluster of the showers is as follows: for each shower **i** having absolute time t_i and coordinates in the Equatorial system $(\alpha, \delta)_i$ there was a chain of events **i, i+1, i+2,. . . , i+N -1** such that the directions of the shower arrival differ by less than the a_r value from the weighted average direction. Thus, each cluster is characterized by multiplicity **k**, duration Δt, absolute time and coordinates of its center (α, δ). Because the search is carried out within some interval ΔT (from 1 ms to 900 s), then $\Delta t \leq \Delta T$. This algorithm was used previously for searching of bursts with BNO facilities (Baksan Underground Scintillation Telescope – BUST, EAS arrays "Carpet-2" and "Andyrchy"). The problem is that the experimentally measured frequencies of cluster registration of different multiplicity are in agreement (within one standard deviation) with the frequencies expected from the background of random coincidences (i.e., background fluctuations of cosmic rays). Therefore to use as an alert to search for transient phenomena in the optical range the additional background suppression is needed. For additional selection of clusters the average angular distance of showers from the center of the cluster (a_{aver} parameter) is used. In Fig. 1 an example of a modeled cluster with **k = 6** from point source is shown. The true center of the cluster (the position of a point source) is placed at the origin of coordinates. The distances of showers (**a**) from true center are distributed in according to Rayleigh distribution. The restored center of cluster is at the distance a_c from true center and a_i is the distance from the restored center to the i-th shower. The average angle distance of showers from the cluster center is defined as:

$$a_{aver} = \frac{1}{k} \sum_{i=1}^{k} a_i \tag{1}$$
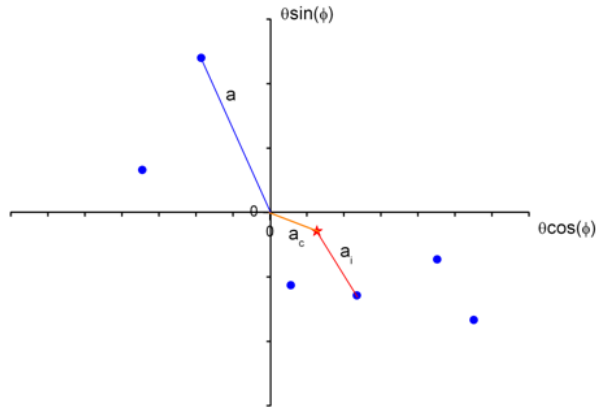
Fig1. *An example of a modeled cluster with k = 6.*

The distributions of clusters with different multiplicities from point sources by a_{aver} parameter have been obtained by simulations. These distributions are notably dependent on cluster multiplicity. Comparisons of distributions of modeled and experimentally registered clusters are shown in Figures 2 – 4.
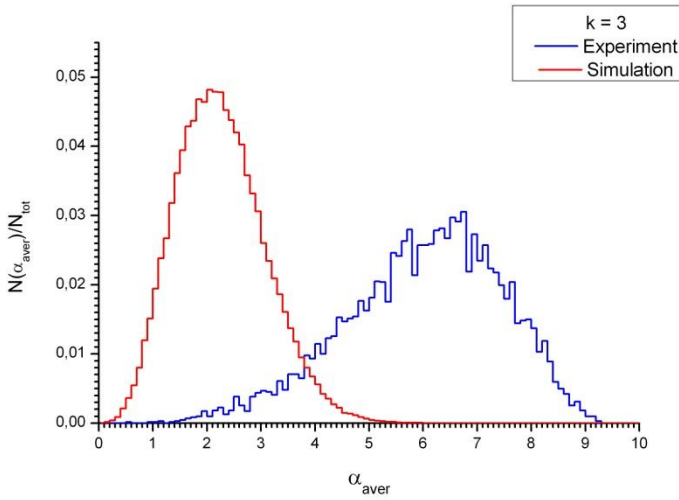
Fig2. Distributions of modeled and experimentally registered clusters with k = 3 by the a_{aver} parameter for the EAS array "Carpet-2".
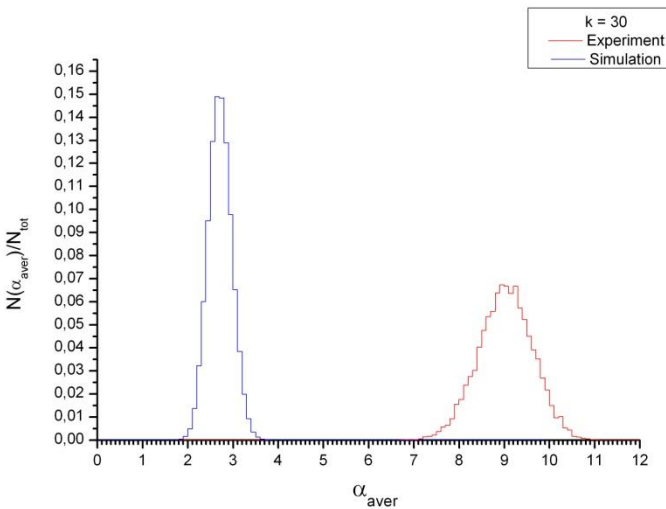
Fig3. Distributions of modeled and experimentally registered clusters with k = 30 by the a_{aver} parameter for the EAS array "Carpet-2".

It is obvious that using of $\mathbf{a_{aver}}$ parameter allows entirely separating clusters of large multiplicities from point sources and from background fluctuations of cosmic rays. It should be noted that multiplicity distribution of experimentally registered clusters depends on $\mathbf{\Delta T}$. Multiplicity distributions of clusters registered at BUST during 953.8 days of data taking are shown in Fig. 5 for a number of $\mathbf{\Delta T}$ values.
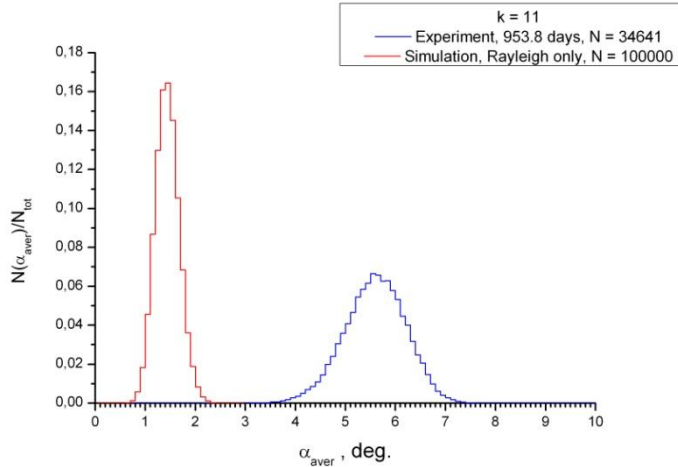
Fig4. *Distributions of modeled and experimentally registered clusters with k = 11 by the a_{aver} parameter for BUST.*
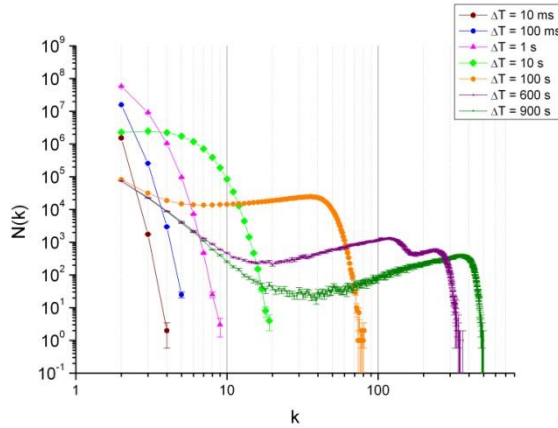
Fig5. *Multiplicity distributions of clusters experimentally registered at the BUST.*

3. Search for clusters of showers in the near-real-time mode

Primary experimental data of BNO installations are accumulated in the memory of an on-line computer of the registration system of each facility for a fixed time, which is 15 minutes (20 minutes for the "old" registration system of the "Carpet-2" installation), and then recorded to the hard disk of a file-server. After data recording the information is processed at dedicated workstations and for each of registered showers the direction of arrival in the horizontal coordinate system (zenith and azimuth angles) is obtained. After that the search for clusters of showers is conducted using the method described above. At first the selection of clusters as alerts for astronomical telescopes is carried out using the condition $\alpha_{aver} \leq \alpha_b(k)$. The $\alpha_b(k)$ values are chosen thus that within $\alpha_b(k)$ is placed 99% of events with relatively low multiplicity (k < 10), for which there is no complete separation of simulated and recorded

events. For clusters with complete separation of the simulated and experimentally recorded events (large multiplicity clusters) all clusters from the point sources are inside $\alpha_b(k)$. To use clusters of small multiplicity as alerts for searching for transient phenomena in the optical range, an additional selection is made for duration of clusters (depending on their multiplicity) so that the frequency of alerts from the "Carpet-2" and BUST installations is ~ 1 per day. Alerts information (coordinates, time, etc.) is recorded to a data collection server in BNO.

Access to these data is realized by means of two communications paths. The first one unites the local networks of the BNO and the observatory at the Terskol peak through a radio channel based on three CiscoAironet 1410 modules at a distance of about 20 km. One module operates at Cheget peak in the access point mode. Two others modules operate in bridge mode at the "Andyrchy" EAS array and at the Terskol peak. The module operated at the "Andyrchy" EAS array is connected with BNO laboratory building by an optical cable. Second one is routing through the Internet with a fixed IP address. Both communications paths allow us to connect with dedicated server via HTTP and FTP, and over the local network using the SMB protocol. The communications paths and the dedicated server are protected from the extraneous access.

4. Search for optical partners of clusters of showers

Search for transient phenomena in the optical range by target designations from BNO facilities will be carried out with a telescope complex at the Terskol peak, including the automatic telescope "Meade 14" f / 10 LX200. A universal program for controlling the complex of astronomical telescopes has been developed and created for this.

The search for optical transients on alerts from BNO facilities have been conducted in test mode using the Officina Stelare RH-200 wide-angle (with a field of view of 3.5 degrees) robotic telescope installed at the Zvenigorod Observatory of INASAN. As an example for one of alerts from EAS array "Carpet-2" 61 images were taken. The coordinates of the frame center are approximately R.A. = 08h45m и Decl. = +70º10'. The overlap of images is presented in Fig. 6. There is some shift of the frame center due to errors of telescope driving at high declinations. The detailed analysis of this frame gives 55 galaxies, 67 radio source, 7 infrared and 7 X-ray sources. No optical transients were discovered in this event.
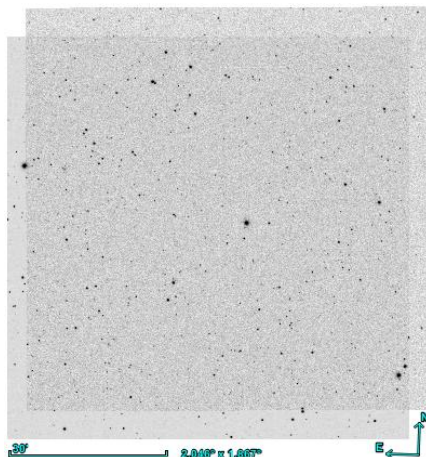
Fig6. The overlap of images obtained by the Officina Stelare RH-200 wide-angle telescope on "Carpet-2" alert.

5. Conclusion

The experiment under development is aimed at obtaining new experimental data on astrophysical objects generating bursts of ultrahigh-energy cosmic gamma radiation in conjunction with optical flashes. At the moment the search for bursts of cosmic ray intensity and cosmic gamma radiation by means of detection of clusters of showers is implemented in the near-real-time mode. Because the experimentally measured frequencies of cluster registration of different multiplicity are in agreement with the frequencies expected from the background fluctuations of cosmic rays the new method of background suppression was developed. This method of background suppression allows us using selected clusters of showers as alerts to search for transient phenomena in the optical range.

Acknowledgements

References

[1] M. Aglietta et al. Search for gamma-ray bursts at photon energies E$\geq$ 10 GeV and 80 TeV. Astrophys.J., 469, 305, 1996.

[2] D.V. Smirnov et al. Search for UHE gamma-ray short transients at Andyrchy EAS array. Proc. 29 ICRC, 4, 451, 2005.

[3] D.V. Smirnov, V.B. Petkov, S.N. Karpov. Search for TeV gamma rays from GRBs at Baksan Underground Scintillation Telescope. Proc. 29 ICRC, 4, 447, 2005.

[4] D.V. Smirnov, V.B. Petkov, and S. N. Karpov. Search for Ultrahigh-Energy Cosmic Gamma-Ray Bursts on the Baksan Underground Scintillation Telescope. Astronomy Letters, 32, 1, 2006.

[5] V.B. Petkov et al. Searching for Very-High-Energy Gamma-Ray Bursts from Evaporating Primordial Black Holes. Astronomy Letters, 34, 509, 2008.

Search for double K-capture of ^{124}Xe with the large volume copper proportional counter

Yu.M. Gavrilyuk[1], A.M. Gangapshev[1], V.V. Kazalov[1,*], V.V. Kuzminov[1], S.I. Panasenko[2], A.D. Petrenko[2], S.S. Ratkevich[2], D.A. Tekueva[1], and S.P. Yakimenko[1]

[1]Institute for Nuclear Research, RAS, Moscow, Russia; kazalov@inr.ru

[2]V.N.Karazin Kharkiv National University, Kharkiv, Ukraine

Abstract   During several years at the Baksan Neutrino Observatory INR RAS is carrying out the experiment for searching of 2K (2ν)-capture in ^{124}Xe. This isotope has several advantages: 1) it has the largest kinetic energy of transition among candidates of nuclei for which predicted the existence of *ECEC*; 2) since xenon is the noble gas, then it could be easily used as a system isotope-detecting medium in a gas detector. To search for 2K-capture in ^{124}Xe the large volume copper proportional counter (CPC) is used.

In our work, we present the results of the simulation, with the Geant4 package, of CPC background from the decays of ^{238}U and ^{232}Th nuclei in the construction materials of the CPC case, as well as in elements of the low-background shield. The influence of neutrons produced in the rock of the underground laboratory from the decay of ^{238}U and ^{232}Th, where the experimental setup is located, on the production of the isotope ^{125}I in the working gas of the detector, upon capture of thermalized neutrons by the ^{124}Xe isotope is considered. The ^{125}I isotope can have a significant influence on the background of the experiment since the total energy release in its decay belongs to the same energy region as ROI of 2K-capture in ^{124}Xe.

Keywords: Double beta-decay, 2k-Capture, Proportional Counter, Low-Background Experiments

1. Introduction

A unique state is formed in the daughter atom in the case of the capture of two electrons from the *K*-shell. This state represents a neutral atom with the inflated shell, exposing two vacancies in the *K*-shell. In order to detect such a process, we have to keep in mind that for Z > 30, where *K*-fluorescence yields are large, the dominant decay of double *K* vacancy states happens through the sequential emission of two characteristic fluorescence quanta.

The primary contribution (76.7%) to the ECEC process in ^{124}Xe is produced by the capture of two electrons from the *K*-shell [1]. The result of the ^{124}Xe $(2\nu, 2e_K)$ reaction is a neutral ^{124}Te atom with a "lifted" shell, which leaves both *K*-shell vacancies exposed. The residual excitation of the atomic shell in daughter isotope ^{124}Te** relaxes via the emission of Auger electrons (e_A, e_A), a single characteristic quantum and an Auger electron (K, e_A), or two characteristic quanta and low-energy Auger electrons (K, K, e_A). In actual experiments, the almost simultaneous emission of two characteristic fluorescence quanta produced in the filling of two vacancies offers considerable advantages in terms of detection of such events.

The detection of the relaxation response of atomic processes after the capture of atomic electrons in a gas medium offers several significant advantages over liquid and solid-state

detectors. At the same time, the impact of the background depends strongly on the energy resolution, which gives the event detection in a gas medium another advantage over detection in liquid. In addition, the interaction of radiation in gas provides an opportunity to determine the topological signature of a rare event, which was demonstrated in our earlier studies [2, 3].

In contrast, extremely small primary ionization tracks typical of interactions in liquid make it difficult to identify the specific features of the signal from low-energy primary particles.

The search technique in our experiment is based to the registration triple coincidences of "shaked" electrons and two fluorescence photons produced in the process of filling of a double *K*-shell vacancy in daughter atoms. A proportional counter filled with gas containing the studied isotope is used as a detector. Useful events have a unique feature set in such a detector. Their total signal comprises three partial pulses with known amplitudes formed as a result of absorption of two characteristic photons and a cascade of low-energy Auger electrons within the working volume. The selection of events with such features from the entire set of digitized pulses allows one to raise the effect/background ratio up to several thousand times. Thus, in our case, the main contribution of the background in the energy region of interest stems from three-point events in the detector. The main contribution to such events can result from the processes of double ionization of the *K*-shell or the emission of a low-energy gamma-quantum with simultaneous registration of the relaxation products of the daughter atomic shell.

2. Setup description

The model of the experimental setup "*2K-CAPTURE*" was created with the help of the Monte-Carlo *Geant4* package [4] for studying the detector response to decays of radionuclides from U/Th families. The same model was used for simulate neutron transport and scattering. Fig. 1 shows a cross section of the setup as implemented in the simulation. All the most relevant geometrical features are included, such as the multilayer shield with their real shapes and positions. The experimental setup consists of a copper proportional counter (CPC) with a casing made of M1-grade copper (the inner surfaces of casing and flanges were covered additionally with 1.5 and 3 mm layers of M0k copper correspondingly) and passive shield. Shield consists of 18 cm of copper, 15 cm of lead and 8 cm of borated polyethylene.
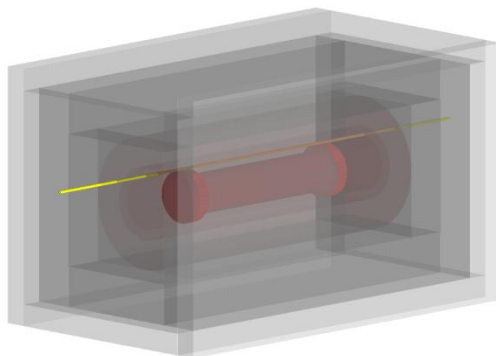
Fig1. Simulated geometry for the installing "2K-CAPTURE" with a calibration channel in Monte-Carlo Geant4 package.

Additional constructive parts located on the detector flanges, which have high voltage inputs designed to supply high voltage to the anode of the CPC, as well as the pickup of the

signal through a high-voltage separating capacitor, were not taken into account in the model. In the model, the body of the CPC is presented as a 710-mm-long copper cylinder with a working length of 595 mm and an inner diameter of 137 mm, closed on both sides with flanges, Fig.2.

Fig2. *Model of copper proportional counter. A darker color indicates the operating area of the detector.*

The following structural parts were taken into account in the internal volume of the CPC: a) the anode wire made from gold-plated tungsten with a diameter of 10μm thick is stretched along the cylinder axis; b) the anode wire passes through the copper tubes along the edges of the detector, which in turn is inserted into the Teflon insulators. The gas volume of the detector is represented by two logical volumes: the full volume and the fiducial volume of the detector, which is part of the full volume, and is located between the copper tubes in which the anode wire is included. The same volume is a sensitive area of the detector; in Fig.2 it is represented in a darker color.

The CPC is filled with xenon gas to a pressure of 4.8 atm. Xenon has a certain isotopic composition that was taken into account when creating the model. The isotopic composition of gas is presented in Table 1.

Table 1. *The isotope composition of working gas of xenon.*

Isotope	124	126	128	129	130	131	132	134	136
Content, %	20.311	27.12	33.44	18.812	0.071	0.057	0.026	0.088	0.0806

As mentioned above, the CPC is surrounded by multi-layer low-background shield. For example, copper shield also has several volumes. Therefore, to simplify the simulation: a) copper layer around the detector housing located between the counter flanges; b) copper layers on the ends of the detector; c) a layer of copper that surrounds the detector and copper portions on the ends of the detector, in this volume calibrated holes are made, and through it the Teflon calibration channel.

3. Simulation results

The following libraries were used for modeling and calculations: *G4DecayPhysics* – for modeling decays of unstable particles indicated in *PhysicsList*, as well as for all unstable particles that may occur during the simulation; *G4RadioactiveDecayPhysics* [5] - allows to simulate radioactive decays of various isotopes, based on ENSDF data [6]; the *G4EmPenelopePhysics* library was used to simulate electromagnetic processes, and *G4EmLivermorePhysics* (for test) was also considered; The

G4HadronPhysicsQGSP_BIC_HP library was used to simulate the interaction of neutrons with matter, this library was chosen based on [7]. The radioactive source (nuclear decay, alpha, beta and gamma radiation) is specified in a mac-file using the *General Particle Source* library. The models we created on the basis of two libraries allowed us to obtain a good agreement between the calculated and experimental response functions from an external calibration gamma source in most of the analyzed cases.

Fig. 3 shows a comparison of the measured and simulated spectra from an external [109]Cd-source. The source is placed above the detector in the calibration channel, which is located inside the low-background shield, Fig.4. To reduce the absorption of gamma-quanta in the shield substance, three calibration holes are made above the center of the detector and along the edges of the sensitive zone of the detector. In standard mode, calibration is carried out in the center hole. The same was done in the model.
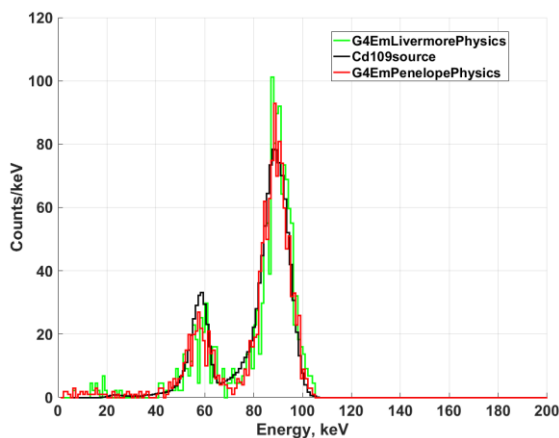
Fig3. *A comparison of experimental and simulated spectra of CPC obtained from 109Cd-source. Red and green histograms are the Geant4 simulations obtained with the Penelope and Livermore model respectively. Black histogram are experimental data from 109Cd-source.*
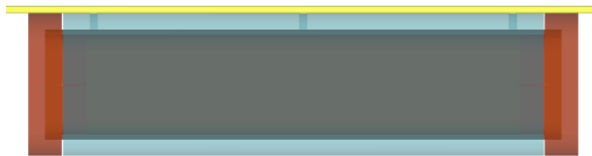
Fig 4. *Calibration channel and calibration holes.*

As noted in the introduction, the purpose of our experiment is the search for rare events from 2ν2K capture using registration a time correlation (coincidence) between the two K-fluorescence quantum that are emitted after the decay of double K-vacancy states and Auger electrons. The magnitude of the probable effect is estimated on the basis of the results of comparative analysis of background data of the proportional counter of the proportional counter filled with samples of pure xenon with different concentrations of the studied isotope. The ultimate sensitivity of the setup to the effect of interest depends primarily on the intrinsic detector background and the quality of the methods used to separate the desired signal with a specified set of characteristics. This requires an extra small gamma-background. In the same

time, a double K-shell photoionization of the atom can create the "hollow atom" by absorbing a single photon and releasing both K electrons. Relaxation of the excited electron shell of a daughter atom can mimic the useful signal.

As noted in the introduction, the purpose of our experiment is the search for rare events from 2ν2K capture using registration a time correlation (coincidence) between the two K-fluorescence quantum that are emitted after the decay of double K-vacancy states and Auger electrons. The magnitude of the probable effect is estimated on the basis of the results of comparative analysis of background data of the proportional counter of the proportional counter filled with samples of pure xenon with different concentrations of the studied isotope. The ultimate sensitivity of the setup to the effect of interest depends primarily on the intrinsic detector background and the quality of the methods used to separate the desired signal with a specified set of characteristics. This requires an extra small gamma-background. In the same time, a double K-shell photoionization of the atom can create the "hollow atom" by absorbing a single photon and releasing both K electrons. Relaxation of the excited electron shell of a daughter atom can mimic the useful signal.

3.1. Gamma-background simulation.

Gamma ray background from the structural elements of the shell of the detector as well as in the elements of the shield (copper, lead) is almost exclusively coming from the uranium and thorium decay series as well as from decay of ^{40}K. External gamma backgrounds originate from these radionuclides in the surrounding rock of deep underground laboratories. Therefore, our purpose was to estimate the response of the CPC to the gamma background from surrounding material. The activity of natural radioactive isotopes content in different source materials of the low-background shield was measured by the ultra-low background germanium gamma-spectrometer [8]. The simulation included the calculation of decays of members of uranium-radium and actinium natural radioactivity chains contained in the structural elements of the detector shell as well as in the elements of the shield. Fig. 5 shows the background spectrum accumulated for one year of measurement (curve 1) using CPC and Monte-Carlo simulation of gamma-spectrum (curve 0). As can be seen in the figure, the simulated and experimental spectrum of all events with energies above 30 keV coincide quite well. The difference between the spectra at low energies can be related to the fact that at the ends of the detector the proportional amplification changes to the ionization mode, which was not taken into account in this simulation. Also edge effects at the ends were not considered.
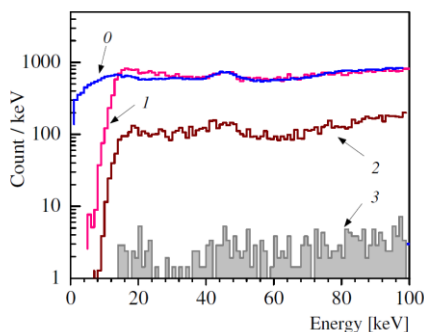
Fig 5. *Spectrum of the background of CPC filled with xenon: (1) - all events, (2) - two-point events, (3) - three-point events, (0) - Monte-Carlo simulations spectrum of low-energy gamma-quantum for interactions in the detector.*

The same figure shows the spectra of two- and three-point events, curve 2 and 3 respectively. Events that are associated with a photon-absorption are distributed among the groups of one- and two-point events in accordance with the probabilities of the Compton process, photo absorption, and the probability for the characteristic radiation yield upon the photo-absorption induced filling of the K-vacancy in the target atom. Two-point events take place if, for example, a photon undergoes the Compton scattering and it is absorbed in the counters volume, a photon undergoes photoeffect and fluorescence quantum are emitted in the process of the vacancy filling or an electron creates the bremsstrahlung. In all these cases, secondary photon is absorbed at some distance from its origin and creates second cluster of ionization. If these two clusters are located at a different distance from the anode, the detected signal will be made of two pulses, with the time difference corresponding to the moments of entering the gas amplification region by two groups of primary electrons. Three-point events can appear if all secondary radiation is absorbed inside the counter, as in, Compton scattering of a photon, followed by the photoeffect and release of the fluorescence quantum by filling the vacancy in the atomic shell, photoeffect followed by the K-shell ionization, by the photoelectron in another atom and release of two fluorescence quantum. Three-point events, which are the main goal of our study, have to be formed as a result of absorption into the fiducial volume of the counter of two characteristic photons and the Auger electrons generated by the double K-shell vacancy production in the investigated xenon samples. All more-than-three-point events are considered as multipoint events. They can appear, for example, as a result of Compton scattering of the photon by the K electron, followed by the K shell photoeffect and release of two K fluorescence quantum. Events can move around within multipoint groups because of possible overlaps of the pulses of separate components of multipoint events. A detailed description of the selection of multipoint events and their components can be found, for example, in [9].

3.2. Neutron background simulation.

The ^{125}I may be one of the most critical background sources in the energy region of interest for the search the $2\nu2K$ capture in ^{124}Xe. Since the energy and type of emission of its decay products are similar to the expected effect of $2\nu2K$ capture. In our detector, this isotope may form after the decay of ^{125}Xe. It is formed when a thermal neutron is captured by the ^{124}Xe with a sufficiently large probability (σ_{th} = 165±11 bn [10]). This can make to the impossibility to separate the desired signal from $2K$-capture with a significant flux of background thermal neutrons. The half-life of ^{125}Xe is about 17 h, after which it decays into an atom ^{125}I. Its half-life is 59.49 days and it decays by electron capture (100%) to the first excited state of the daughter ^{125}Te which then emits a 35.46 keV gamma ray photon in dropping to its ground state in $1.49{\times}10^{-9}$ seconds. Simultaneous registration of the 35.46 keV gamma-line, characteristic K fluorescence quanta, and Auger electrons in working volume of CPC can generate a three-point event with a signature that simulates an event from a $2\nu2K$ capture of ^{124}Xe.

Therefore, we decided to test the possible number of neutrons that can "penetrate" into the working volume of the detector, thermalize and interact with the ^{124}Xe. Several possible sources of neutrons were considered in the simulation calculations. The first of them is neutron production in ($\alpha - n$)-reactions during the decay of the U/Th series and their daughter nuclei (which undergo α-decay) in the detector case, as well as in the shield elements. These calculations showed that we have zero effect. The next stage included the calculation of the penetration of neutrons produced in the walls of the low-background underground laboratory and evenly distributed in the air.

In the calculations, we focused on the work in which measurements were made of neutrons of different energy ranges, in the same laboratory where the installation for searching for *2K*-capture in ^{124}Xe is located. In the first work, the measurements of the thermal neutron flux were carried out on the neutron background measurements with the [ZnS(Ag)+6LiF] scintillation detector [11]. As a result of the measurements, an estimate was obtained for the thermal neutron flux at the level $(2.6\pm0.4) \times 10^{-5}$ cm^{-2}s^{-1}. In the second work [12], measurements of neutrons with energies of ~ 700 keV were carried out. The value of the neutron flux with such energy of 5.3×10^{-7} - 1.8×10^{-7} cm^{-2}s^{-1} was obtained.

These values were incorporated into the design model of our installation. The neutron layer surrounding the shield from all sides was selected with a thickness of 100 mm. Monte-Carlo simulation of spectra of neutron passing through the material of passive shield and scattered in the CPC allowed us to obtain the following results. The thermal neutrons (in reality neutrons with energies below 0.5 eV were taken) do not penetrate through the low-background shield into the detector, and therefore do not contribute to the production of the ^{125}Xe. Neutrons with an energy of ~ 700 keV can penetrate into the detector through low-background shield. We have ~ 2.5 thermalized neutrons in the detector when normalizing the simulation results for a year of measurements. We will have 0.02 atoms of the ^{125}I in the detector in one year of measurements, taking into account the interaction cross-section and the number of ^{124}Xe atoms. This will give us no more than one atom of the ^{125}I in our detector in 4-5 years of measurements.

4. Conclusions

The reducing of the background is crucial when searching for the 2ν2K capture in ^{124}Xe because it determines the sensitivity when the total amount of ^{124}Xe is equal to fixed. To estimate the radioactive contamination of the experimental setup "*2K-CAPTURE*" has been applied the *Geant4-based* Monte-Carlo simulation of the energy spectra from background sources. The energy distributions of the detector response obtained in the *Geant4* MC simulation were compared with measurements from a calibration source, which resulted in a good description of the data. Detector response functions of thermal neutrons penetrating into the working volume of the CPC have also been calculated.

References

[1]   Doi M, Kotani T 1992 Prog. Theor. Phys. (Kyoto) **87** 1207.

[2]   Ratkevich S S et al. Phys. Rev. C **96** 6:065502.

[3]   Gavrilyuk Y M et al. 2015 Physics of Atomic Nuclei **78** 13:1563.

[4]   Geant4: a toolkit for the simulation of the passage of particles through matter. CERN 2011 https://geant4.web.cern.ch/.

[5]   Hauf Steffen et al. 2013 Nucl. Sci., IEEE Trans. **60** 4 2984.

[6]   Evaluated Nuclear Structure Data File https://www.nndc.bnl.gov/ensdf/.

[7]   Deiev O S 2013 Problems of Atomic Science and Technology **3** 236.

[8]   Gavrilyuk Yu M et al. 2011 Preprint INR RAN (Inst. Nucl. Phys. RAS) Moscow No.1301/2011.

[9]   Gavrilyuk Yu M et al. 2010 Instrum. Exp. Tech. **53** 57.

[10]   Mughabghab S F "Atlas of Neutron Resonances" 5th Ed. National Nuclear Data Center Brookhaven National Laboratory Upton, USA https://www.nndc.bnl.gov/atlas/.

[11]   Kuzminov V V et al. 2017 Nucl. Inst. Meth. Phys. Res. A **841** 156.

[12]   Abdurashitov J N et al. 2000 Physics of Atomic Nuclei, **63** 7 1276.

THESEUS and quasar microlensing

Lindita Hamolli, Mimoza Hafizi[*]

Department of Physics, University of Tirana, Albania; lindita.hamolli@fshn.edu.al

Abstract: Quasar microlensing is called the lensing effect on quasars, caused by compact objects in the mass range $[10^{-6}, 10^3]M_\odot$, inside a lens galaxy. It is shown that quasar microlensing provides a possibility to probe extragalactic planets in the lens galaxy. THESEUS will observe with a unique combination of huge FOV, angular resolution and sensitivity. We focus on the ability of THESEUS to probe, through quasar microlensing, extragalactic planets.

Keywords: Gravitational Lensing, Strong Lensing, Weak Lensing, Microlensing, Quasar Microlensing

1. Introduction

Quasars are the most luminous, powerful, and energetic objects known in the universe. They can be gravitationally lensed by a foreground galaxy, which deflects the light rays, when is close to the line of sight. In 1916, Einstein calculated the light deflection by the Sun, based on the general theory of relativity [1] and found the value $\alpha = 4GM / bc^2$, twice more than the previous value found, based on Newtonian mechanics [2]. Here G is the gravitational constant, M is the lens's mass and b is the impact parameter of the light rays. The general relativistic result was confirmed during the Solar eclipse in 1919 [3]. In 1936, Einstein published a paper describing the gravitational lensing effect caused by distant stars, considering the particular case when the source, the lens and the observer are aligned. He noticed the existence of a luminous ring, after called the Einstein ring [4], hopelessly to be observed at that epoch. In 1937, Zwicky understood that galaxies were gravitational lenses more powerful than stars and might give rise to images with a detectable angular separation [5].

Actually, there are different scales in gravitational lensing. The strong (or macro) lensing is the regime when the gravitational lens images are separated by more than a few tenths of arcsecs and can be observed as distinct images. In the case when the distortions induced by the gravitational fields are much smaller, we have the weak lensing effect. On the other side, if one considers the star-on-star lensing (as Einstein did), the resulting angular distance between the images is of the order of *mas*, generally not separable by telescopes. Gravitational lensing in this regime is called microlensing and the observable is an achromatic change in the brightness of the source star over time, due to the relative motion of the lens with respect to the line of sight towards the source [6]. Recently, a new effect, quasar microlensing, is detected inside the images obtained during the strong lensing, which is related to the uncorrelated brightness fluctuations of the macro-images due to the motion of the deflectors (the constituting objects of the lensing galaxy). By this effect, it becomes possible to constrain the fraction of free floating planets (FFPs) in other galaxies [7].

The first attempts to characterize the free floating planet population in our Galaxy were done by Sumi et al. [9], by analyzing the microlensing light curves of two-year survey of

MOA-II collaboration towards the Galactic bulge. They reported the discovery of planetary-mass objects (the mass rang $[10^{-5}, 10^{-2}]M_\odot$) either very distant from their host star ($\sim 100\,AU$) or entirely unbound. By the best-fit procedure of the observed microlensing events due to FFPs, they constrained a power-law mass function with the index $\alpha_{PL} = 1.3^{+0.3}_{-0.4}$ and defined the number of planetary mass objects per star: $N_{PL} = 5.5^{+18.1}_{-4.3}$. Current microlensing observations are performed by the ground-based telescopes OGLE [9] and MOA [10] and by the space-based telescopes Kepler [11] and Spitzer [12]. In recent years, FFPs are found in many young star forming regions by using infrared imaging surveys [13]. The origin of the FFPs is uncertain. One possibility is that they originally formed around a host star and then scattered out from orbit. A second option is that they may form on their own through gas cloud collapse, similarly to star formation.

The Transient High Energy Sky and Early Universe Surveyor (THESEUS) is a space mission concept developed by a large international collaboration, in response to the calls for M-class missions by the European Space Agency (ESA) [14]. Apart from GRBs, THESEUS will observe Quasars and AGN-s in very large distances. We discuss here about the ability of THESEUS to probe, by this way, extragalactic planets.

In the next section, we review the basics of gravitational lensing, in its regimes: strong lensing, weak lensing and microlensing. In Section 3 we discuss quasar microlensing following by description of THESEUS mission capabilities in Section 4. Our conclusions are given in Section 5.

2. Basics of Gravitational Lensing

In the general theory of relativity, light rays follow null geodesics, i.e., the minimum distance paths in a curved space-time. Therefore, when a light ray from a far source interacts with the gravitational field due to a massive body, it is bent by an angle $\alpha = 4GM / bc^2$. By looking at Figure 1, assuming the ideal case of a thin lens and noting that, $\alpha D_{LS} = (\theta - \theta_S)D_S$ one can easily derive the so-called lens equation

$$\theta - \theta_S = \theta_E^2 / \theta \qquad (1)$$

where θ_S indicates the source position and

$$\theta_E = \sqrt{\frac{4GM}{c^2}\frac{D_{LS}}{D_L D_S}} \qquad (2)$$

is the Einstein ring radius, which is the angular radius of the image when the lens and the source are perfectly aligned, $\theta_S=0$. Here, D_S, D_L and D_{LS} are the angular diameter distances between the observer, lens, and source, respectively. By solving Equation (1), one can define the positions of two images appeared in the source plane. More generally, the light deflection between the two-dimensional position of the source θ_S and that of the position of the image θ is given by the lens mapping equation [15]:

$$\theta_S = \theta - \nabla\varphi(\theta) \qquad (3)$$

where φ is the so-called lensing potential of the lens. Eqn. 3 is a transformation from the source plane to the image plane. The Jacobian of the transformation is given by:

$$J = \frac{d\theta_S}{d\theta} = A^{-1} = \begin{pmatrix} 1 - \varphi_{,11} & -\varphi_{,12} \\ -\varphi_{,12} & 1 - \varphi_{,22} \end{pmatrix} = \begin{pmatrix} 1 - \kappa - \gamma_1 & -\gamma_2 \\ -\gamma_2 & 1 - \kappa + \gamma_1 \end{pmatrix} \quad (4)$$
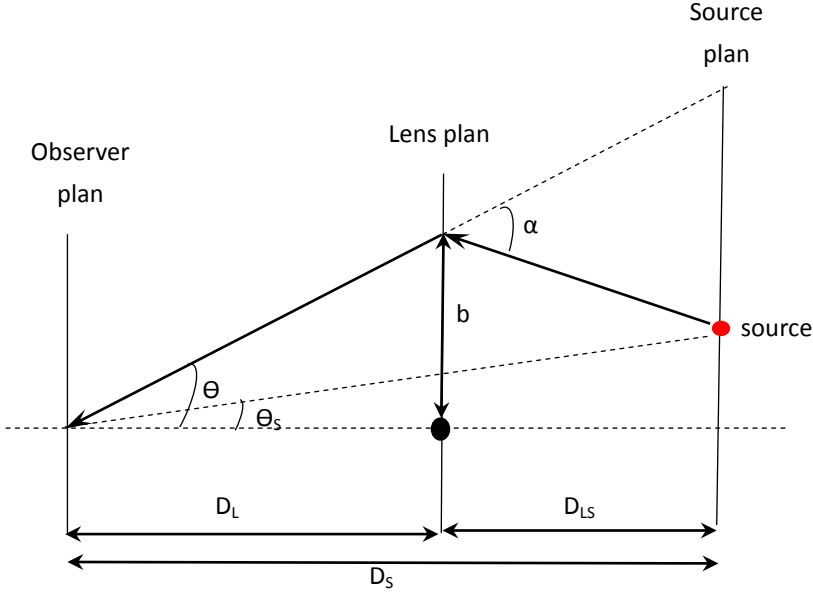
Fig1 . Schematics of the lensing phenomenon.

where the commas are the partial derivatives with respect to the two components of θ, A is named magnification matrix, k - convergence and γ - shear. The points in the source plane where A=0 form the so called caustic lines.

The optical depth τ is defined as the fraction of a given solid angle $\delta\Omega$ covered by the Einstein rings of the individual masses. To first order, it is equal to the convergence, or normalized surface mass density

$$\tau = \sum_i \frac{(\pi\theta_E^2)_i}{\delta\Omega} = \frac{\Sigma}{\Sigma_{crit}} = \kappa \quad (5)$$

where the critical density is $\Sigma_{crit} = \frac{c^2 D_S}{4\pi G D_L D_{LS}}$.

2.1. Strong lensing

The strong gravitational lensing was first observed in 1979 and was linked to a quasar (QSO 0957+561) [16]. The existence of two objects separated by about 6″ and characterized by an identical spectrum led to the conclusion that they were the doubled image of the same quasar. This double quasar was also the first object for which the time delay (about 420 days) between the two images [17], due to the different paths of the photons, has been measured. Observations can also show four images of the same quasar, as in the case of the so-called Einstein Cross, or when the lens and the source are closely aligned, one can observe the Einstein ring, as in the case of MG 1131+0456 [18]. The sources of strong lensing events are

often quasars, galaxies, galaxy clusters and supernovae, whereas the lenses are usually galaxies or galaxy clusters. The image separation is generally larger than a few tenths of an arcsec, often up to a few arcsecs. Over the years, many strong lensing events have been found in deep surveys of the sky, such as the CLASS [19], the Sloan ACS [20], the SQLS (the Sloan Digital Sky Survey for Quasar Lens Search) [21], and so on.

Strong gravitational lensing is nowadays a powerful tool for investigation in astrophysics and cosmology. It may be used as a natural telescope that magnifies dim galaxies, making them easier to be studied in detail [22].

2.2. Weak lensing

In addition to the macroscopic deformations, in the deep field surveys of the sky single distorted images with elliptical shape and weakly distorted images of galaxies have been also detected. This effect is known as weak lensing and is playing an increasingly important role in cosmology. The first weak lensing event was detected in 1990 as statistical tangential alignment of galaxies behind massive clusters [23], but only in 2000, coherent galaxy distortions were measured. The weak lensing cannot be measured by a single galaxy, but its observation relies on the statistical analysis of the shape and alignment of a large number of galaxies in a certain direction.

2.3. Microlensing

The lensing phenomenon is called microlensing when θ_E is much smaller than the typical telescope angular resolution, as in the case of stars lensing the light from background stars. In the simplest case, when the point-like approximation for both lens and source is assumed and the relative motion among the observer, lens and source are uniform and linear, individual images cannot be resolved due to their small separation, but the total brightness of the images is larger with respect to that of the unlensed source, leading to a specific time dependent amplification of the source [5], which is given by,

$$A = \frac{2+u^2}{u\sqrt{4+u^2}} \geq 1. \tag{6}$$

where $u = \theta_S / \theta_E$. The parameter u can be decomposed into components parallel and perpendicular to the direction of the relative lens-source motion and be calculated as

$$u(t) = \sqrt{\frac{(t-t_0)^2}{t_E} + u_0^2} \tag{7}$$

where t_0 and u_0 are the time and impact parameter at the closest-approach. The Einstein time scale $t_E = R_E / v_T$ is defined as the time required for the lens to traverse the Einstein radius (R_E). The light curve is determined by three parameters: t_0, t_E and u_0. However, of these parameters only t_E contains information about the lens and this gives rise to the so-called parameter degeneracy problem. To break this degeneracy, the second order effects are considered, which are: the parallax effect ([24]-[26]), the finite source effects ([27], [28]) and the binary lens effect [29]. A microlensing event can also be observed astrometrically and the elliptic trajectory of the centroid can be detected, which depends on the angular Einstein radius ([30]-[32]).

3. Quasar Microlensing

The quasars can be affected by gravitational lensing in two ways. The "Macrolensing" concerns multiply imaged quasars, with angular separations of roughly an arcsecond. These cases are produced by typical galaxy lenses with masses of the order of $10^{12}M_\odot$. About one out of 500 quasars is multiply imaged [33]. Some hundred of cases are known to date, most of them consist of double or quadruple images. The second interesting regime is "microlensing": the compact objects in the mass range $[10^{-6}, 10^3]M_\odot$ affect the apparent brightness of the quasar images. The microlenses can be ordinary stars, brown dwarfs, planets, black holes, molecular clouds, globular clusters or other compact mass concentrations. In most practical cases, the microlenses are part of a galaxy which acts as the main (macro-)lens. The brightness fluctuations on the macro-images can be used to study the size and brightness profile of quasars on one hand, and the distribution of compact (dark) matter along the line of sight on the other hand.

In strong lensing regime of the quasar, for massive galaxy with mass of $M=10^{12}M_\odot$ at a redshift $z_L = 0.5$ and a source at redshift $z_S=2.0$ (here $H_0 = 50\ km\ s^{-1}Mpc^{-1}$) the Einstein radius is

$$\theta_E \approx 1.8 \sqrt{\frac{M}{10^{12}M_\odot}}\ \text{arcsec.} \tag{8}$$

For a quasar microlensing scenario in which stars in the lensing galaxy act as a lens for a background quasar, the scale defined by the Einstein radius is

$$\theta_E \approx 10^{-6} \sqrt{\frac{M}{M_\odot}}\ \text{arcsec.} \tag{9}$$

This corresponds to a physical scale (Einstein radius in source plan)

$$r_E \approx 1.4x10^{16} \sqrt{\frac{M}{M_\odot}}\ \text{cm.} \tag{10}$$

Quasar microlensing happens to be an interesting phenomenon when the size of the optical continuum emitting region of the quasars is comparable to or smaller than the Einstein radius of stellar mass objects. In fact, the image splittings on such angular scales cannot be observed directly, but the microlensing can be observable because the observer, lens(es) and source move relative to each other and the micro-image configuration changes with time. This fluctuation in magnification can be measured and used to study the quasars and the distribution of compact (dark) matter along the line of sight. In these events, two time scales can be defined. The standard lensing time scale t_E is the time the source takes to cross the Einstein radius of the lens

$$t_E = \frac{r_E}{v_{\perp,eff}} \approx 15\sqrt{M/M_\odot}\ v_{600}^{-1}\ years \tag{11}$$

where the effective relative transverse velocity $v_{\perp,eff}$ is parametrized in units of 600 km/s: v_{600}. This time scale t_E results in large pessimistically observable values. However, in practice we can expect fluctuations on much shorter time intervals. The reason is that sharp caustic lines separate regions of low and high magnification. Hence, if the source crosses such a caustic line, we can observe a large change in magnification within the crossing time t_{cross}, which is the

time needed for the source to cross its own radius R_{source}:

$$t_{cross} = \frac{R_{source}}{v_{\perp,eff}} \approx 4R_{15}v_{600}^{-1} \; months \qquad (12)$$

Here the quasar size R_{15} is parametrized in units of 10^{15} cm.

As shown above, the fluctuations in the brightness of a quasar can have two causes: intrinsic to the quasar, or induced by microlensing. In the case when there are two or more macro-lensing images of a quasar, it is possible to distinguish between two possible causes of variability: any fluctuations caused by intrinsic variability of the quasar show up in all quasar images, with a time-lag according to the time delay. So, once a time delay is measured in a multiply-imaged quasar system, one can "shift" the light curves of the different quasar images relative to each other by the time delay, correct for the different (macro-)magnification (due to the smooth lensing galaxy mass model), and subtract them from each other. All remaining incoherent fluctuations in this "difference light curve" can be attributed to microlensing.

Recently, the Chandra observations of several gravitationally lensed quasars show evidence for flux and spectral variability of the X-ray emission that is uncorrelated between images and is thought to result from the microlensing by stars in the lensing galaxy.

Dai & Guerras [7] found that in the lens galaxy there are ~ 2000 objects per main sequence star in the mass range between Moon and Jupiter.

4. THESEUS

The Transient High Energy Sky and Early Universe Surveyor (THESEUS) is a space mission concept developed by a large international collaboration, aimed at finding answers to multiple fundamental questions of modern cosmology and astrophysics, exploiting the mission unique capability to perform an unprecedented deep monitoring of the soft X-ray transient Universe [14]. Besides high-redshift GRBs, THESEUS will serendipitously detect and localize during regular observations a large number of X-ray transients and variable sources, collecting also prompt follow-up data in the IR. The foreseen payload of THESEUS includes the following instrumentation: Soft X-ray Imager (SXI, 0.3-6 keV), a set of 4 lobster-eye telescopes units, covering a total FOV of 1 sr, with source location accuracy <1-2 arcmin; X-Gamma ray Imaging Spectrometer (XGIS, 2 keV-20 MeV), a set of coded-mask cameras using monolithic X-gamma ray detectors based on bars of Silicon diodes coupled with CsI crystal scintillator, granting a 1.5 sr FOV, a source location accuracy of 5 arcmin in 2-30 keV and an unprecedentedly broad energy band. SXI provides the capability to monitor the X-ray flux of hundreds of AGN with 10% accuracy on daily timescales, and hundreds more on longer timescales. The survey strategy will permit an unbiased look at the long-term variability of an unprecedentedly large AGN/Blazar sample at depths never reached before.

In Table 1 we show a comparison between THESEUS and Chandra capabilities (ACIS-Advanced CCD Imaging Spectrometer; HRC-High Resolution Camera), the last one being the most powerful, up to now, telescope for discovery of X-ray traces in high energy Universe and the first one to observe quasar microlensing caused by FFPs.

Table 1. *The capabilities of Theseus and Chandra telescopes.*

	Range (KeV)	FOV	Accuracy	Sensitivity erg/cm^2/s
THESEUS SXI/ Chandra ACIS	(0.3 - 6) / (0.4-10)	1sr / 17x17 arcmin	10-20 arcsec / 1 arcsec	10^{-9} / 4×10^{-15}
Theseus XGIS/ Chandra HRC	(2 KeV –20 MeV)/ (0.4-10) KeV	1.5sr / 30x30 arcmin	5 arcmin / 0.4 arcsec	10^{-10} / 10^{-16}

We remark that THESEUS is a unique combination of huge FOV, angular resolution and sensitivity and promises to further on the important discoveries in this direction.

5. Conclusions

The survey strategy of THESEUS will permit an observation of the long-term variability of an unprecedentedly large AGN sample, at depths never reached before. New quasars will be observed, with smaller Einstein Radius of lensing bodies, shorter Einstein times, smaller quasar regions to be probed and closer to the central Black Hole, so with shorter variability.

THESEUS will be characterized by higher sensitivity to study X ray lines (FeKα), which are considered as precious sources of information for different regions of the accretion disk.

Acknowledgements

References

[1] Einstein, A. "Die Grundlage der allgemeinen Relativitätstheorie", *AnP,* 1916, 354, 769E.

[2] Einstein, A. "On the Influence of Gravitation on the Propagation of Light", *Ann. Phys*, 1911, 340, 898–908.

[3] Dyson, F.W.; Eddington, A.; Davidson, C. "A determination of the deflection of light by the sun's gravitational field from observations made at the total eclipse of May 29, 1919", *Phil. Trans. Roy. Soc. A,* 1920, 220, 291–333.

[4] Einstein, A. "Lens-Like Action of a Star by the Deviation of Light in the Gravitational Field", *Science,* 1936, 84, 506–507.

[5] Zwicky, F. "On the Probability of Detecting Nebulae which Act as Gravitational lenses", *Phys. Rev,* 1937, 51, 679–679.

[6] Paczyński, B. "Gravitational microlensing by the galactic halo", *Astrophys. J.* 1986, 304, 1–5.

[7] Dai, X.; Guerras, E. "Probing Extragalactic Planets Using Quasar Microlensing", *ApJ.* 2018, 853,

27.

[8]   Sumi T. ; et al. "Unbound or Distant Planetary Mass Population Detected by Gravitational Microlensing", *Nature,* 2011, 473, 349.

[9]   Udalski, A.; Szymanski, M.; Kaluzny, J.; et al. "The Optical Gravitational Lensing Experiment", *AcA*, 1992, 42, 253-284.

[10] Muraki, Y.; Sumi, T.; Abe, F.; et al. "Search for Machos by the MOA Collaboration", *PThPS,* 1999, 133, 233-246.

[11] Hamolli, L.; De Paolis, F.; Hafizi, M.; Nucita, A.A. "Predictions on the detection of the free-floating planet population with K2 and Spitzer microlensing campaigns", *AstBu,* 2017, 72 73.

[12] Dong, Subo; Udalski, A.; Gould, A.; et al. "First Space-Based Microlens Parallax Measurement: Spitzer Observations of OGLE-2005-SMC-001", *Astrophys. J.* 2007, 664, 862.

[13] Zapatero Osorio, M.R.; et al., "Discovery of Young, Isolated Planetary Mass Objects in the σ Orionis Star Cluster", *Science,* 2000, 290, 103.

[14] Amati, L.; O'Brien, P.; Götz, D.; et al., "The THESEUS space mission concept: science case, design and expected performances", *AdSpR*, 2018, 62, 191A.

[15] Schneider, P.; Ehlers, G.; Falco, E.E. "Gravitational Lenses", *Springer Verlag: Berlin, Germany* 1992.

[16] Walsh, D.; Carswell, R.F.; Weymann, R.J. "0957 + 561 A,B: Twin quasistellar objects or gravitational lens?" *Nature*, 1979, 279, 381–384.

[17] Pelt, J.; Kayser, R.; Refsdal, S.; Schramm, T. "The light curve and the time delay of QSO 0957+561", *Astron. Astrophys,* 1996, 306, 97–106.

[18] Chen, G.H.; Kochanek, C.S.; Hewitt, J.N. "The Mass Distribution of the Lens Galaxy in MG 1131+0456", *Astrophys. J.* 1995, 447, 62–81.

[19] Browne, I.W.A.; Wilkinson, P.N.; et al. "The Cosmic Lens All-Sky Survey - II. Gravitational lens candidate selection and follow-up", *Mon. Not. R. Astron. Soc*, 2003, 341, 13–32.

[20] Bolton, A.S.; Burles, S.; Koopmans, L.V.E.; Treu, T.; Moustakas, L.A. "The Sloan Lens ACS Survey. I. A Large Spectroscopically Selected Sample of Massive Early-Type Lens Galaxies", *Astrophys. J.* 2006, 638, 703–724.

[21] Oguri, M.; Inada, N.; Pindor, B.; Strauss, M.A.; et al. "The Sloan Digital Sky Survey Quasar Lens Search. I. Candidate Selection Algorithm", *Astrophys. J*. 2006, 132, 999–1013.

[22] Kelly, P.L.; Rodney, S.A.; Treu, T.; Foley, R.J.; et al. "Multiple images of a highly magnified supernova formed by an early-type cluster galaxy lens", *Science* 2015, 347, 1123–1126.

[23] Tyson, J.A.; Wenk, R.A.; Valdes, F. "Detection of systematic gravitational lens galaxy image alignments—Mapping dark matter in galaxy clusters", *Astrophys. J.* 1990, 349, L1–L4.

[24] Alcock, C.; et al. "First Observation of Parallax in a Gravitational Microlensing Event", *ApJ.* 1995, 454, 125.

[25] Dominik, M. "Galactic microlensing with rotating binaries", *Astron. Astrophys.* 1998, 329, 361.

[26] Hamolli, L. Hafizi, M.; De Paolis, F.; Nucita, A.A. "Paralax effects on microlensing events caused by free-floating planets", *BlgAJ.* 2013, 19, 34

[27] Witt H. J.; Mao Sh. "Can lensed stars be regarded as pointlike for microlensing by MACHOs?", *ApJ.* 1994, 430, 505

[28] Hamolli, L. Hafizi, M.; De Paolis, F.; Nucita, A.A. "Estimating Finite Source Effects in Microlensing Events due to Free-Floating Planets with the Euclid Survey", *Adv. Astron.* 2015 ID 402303

[29] Beaulieu, J.-P.; Bennett, D. P.; et al. "Discovery of a cool planet of 5.5 Earth masses through gravitational microlensing", *Nature,* 2006, 439, 437B.

[30] Dominik, M.; Sahu, K. C. "Astrometric microlensing of stars", *ApJ.* 2000, 534, 213.

[31] Nucita, A.A.; et al. "Astrometric microlensing", *IJMPD.* 2017, 2641015N.

[32] Hamolli, L.; et al. "The astrometric signal of microlensing events caused by free floating planets", *Ap&SS.* 2018, 363, 153.

[33] Schmidt, R. W.; Wambsganss, J. "Quasar microlensing", *Gen Relativ Gravit*, 2010, 42, 2127–2150.

Statistical study of spin dynamics in precessing binary black holes in eccentric orbits

Pankaj Jain[1,*], Khun Sang Phukon[1], Anuradha Gupta[2,3], Sukanta Bose[4,5]

[1]*Department of Physics, Indian Institute of Technology, Kanpur, India;
pkjain@iitk.ac.in*

[2]*Department of Physics, The Pennsylvanisa State University, University Park, PA,
U.S.A.*

[3]*Institute for Gravitation & the Cosmos, The Pennsylvanisa State University, University
Park, PA, U.S.A.*

[4]*Inter-University Centre for Astronomy and Astrophysics, Pune, India*

[5]*Department of Physics & Astronomy, Washington State University, Webster, Pullman,
U.S.A.*

Abstract We study the evolution of spins of binary black holes taking eccentricity into account. We are interested in determining the probability that these binaries may get locked in spin-orbit resonance configurations. We numerically evolve a large set of binaries starting from a large separation by using post-Newtonian approximation. The initial spin distribution is taken to be isotropic as is expected in many astrophysical environments. We find that a large fraction of the binaries get locked into or oscillate about the spin-orbit resonance configuration towards the end of inspiral. This can be tested in future observations which, using our results, will allow us to deduce the initial spin distributions.

1. Introduction

The black hole (BH) spin is an important parameter in binary black holes (BBHs). It has a significant effect on the emitted gravitational waves. The spin induced effects are more dramatic when the two BH spins in a BBH are not exactly aligned or anti-aligned with the orbital angular momentum. Taking the spins into account introduces six additional parameters in the binary system. Resultantly the extraction of parameters from the observed gravitational waves becomes substantially more complicated [1].

There are three phases in the evolution of BBHs: inspiral, merger and ringdown. The inspiral phase can be handled by using the post-Newtonian (PN) approximation [2-4]. The spins and the orbital angular momentum vectors significantly evolve during this phase although the spin magnitudes remain unchanged. Due to the general relativistic spin-orbit and spin-spin coupling, the spin vectors as well as the orbital angular momentum undergo precession about the total angular momentum $\vec{J}$ which remains fixed on small time scales and changes only on the radiation reaction time scale. The important time scales in the PN limit are:

(i)   Orbital time scale t_{orb} ,
(ii)   Precession time scale t_P,

(iii) Radiation-reaction time scale t_{GW}.

These obey, $t_{orb} \ll t_P \ll t_{GW}$. The directions of spin and orbital angular momentum change on the precession time scale as well as on radiation-reaction time scale.

We are interested in determining the statistical distribution of spins of BBHs near merger assuming an initial distribution at large separation. The binary can get locked in a spin-orbit resonance depending on its initial parameters. In this configuration the spin vectors and the orbital angular momentum vector lie in the same plane and precess about $\vec{J}$ at the same resonant frequency. In this study we shall determine the probability that the binaries may get trapped in a spin-orbit resonance at late inspiral. It has been shown earlier that if the distribution of spins is initially isotropic, i.e. the spins of BHs in BBHs have equal probability to point in any direction, then the distribution remains isotropic during evolution. However it undergoes significant change if it is initially non-isotropic [4]. In general the initial spin distribution of the binary partners is expected to be partially aligned and depends on the astrophysical environment of the binary. Through our study we can deduce the initial spin distribution once we have a sufficiently large sample of gravitational waves from BBHs and hence can deduce the nature of the astrophysical environment of the binary system [5]. These predictions can be further tested by multi-messenger astronomy since the populations of BH-NS (Neutron Star) and NS-NS binaries are related to those of BBHs.

2. Evolution of Binary Spins

Let $\vec{S}_1$ and $\vec{S}_2$ denote the spin vectors of the two BHs and $\vec{L}$ be the orbital angular momentum vector. Consider a system in which the $\hat{z}'$ axis points along $\vec{L}$. Let θ_1 and θ_2 be the polar angles of the two spin vectors and $\Delta\varphi$ be their azimuthal angle separation. In a spin-orbit resonance (SOR) configuration, the three angular momenta vectors of BBH occupy a planar configuration with $\Delta\varphi = 0, \pi$ [3,6,7]. Hence we can split the binaries into the following three classes or morphologies:

1. Circulating: The three spin vectors are non-planar, freely precessing and $\Delta\varphi$ can take any value.
2. SOR-0: The spin vectors and orbital angular momentum vector librate about co-planar configuration with $\Delta\varphi = 0$ on precession time scale.
3. SOR-180: The spin vectors and orbital angular momentum vector librate about co-planar configuration with $\Delta\varphi = \pi$ on precession time scale.

We are interested in determining the relative probability of BBHs to be in these three classes at near merger. The initial distribution of spins is taken to be partially aligned. This question has earlier been addressed by assuming that the eccentricity e is zero ([6]-[8]). However this is not true in reality. The eccentricity is expected to become smaller during inspiral, however beyond a certain point it is expected to start increasing [9, 10]. Furthermore even if we set $e = 0$ initially, it is expected to become non-zero during subsequent evolution. Here we examine the general case in which eccentricity is non-zero.

The basic evolution equations for the spin vectors are given in ([6]-[8]). Here we use the radiation reaction equations at 3PN order in order to evolve the binary from $a = 1000M$ to $a = 10M$, where a is the binary separation. The PN approximation breaks down at smaller a values.

3. Results

The evolution of eccentricity for a set of BBHs is shown in Fig. 1. Depending on the values of initial eccentricities, the evolution of eccentricity during inspiral exhibits three distinct patterns: (i) monotonic decay of eccentricity, (ii) monotonic growth of eccentricity, and (iii) growth of eccentricity after decaying to a minimum. In Fig. 1, the initial eccentricities correspond to those values for which $d\,e^2/dt$ vanishes at 2PN order. The eccentricities cannot be decreased beyond these values. We evolve 4000 such maximally spinning eccentric binaries with mass ratios q = 0.40, 0.60, 0.80, and 0.95 (1000 eccentric binaries for each mass ratio), where $q = \frac{m_2}{m_1} \leq 1$. In Fig. 1, the median of eccentricity evolution for each set of 1000 binaries are plotted. Since, the growth of eccentricity is a spin induced phenomenon, there is no significant difference in eccentricity evolution for the four different mass ratio cases. The eccentricities rise to 10^{-3} towards the end of inspiral. Such eccentricities are not negligible in numerical relativity simulations.

In Fig. 2, we show the morphology obtained for the evolved spin configurations from Fig.1 at the initial (a = 1000M) and final (a = 10M) orbital separation. At a = 1000M, most of the binaries are in the circulating morphology i.e. freely precessing. The morphologies predict average behaviour of binaries in a precessional time period which preserve information about initial configurations. During inspiral, the morphologies of spin configurations evolve slowly. At the separation a = 10M, a large fraction of binaries from the circulating morphology transit to the resonant morphologies. The behaviour of morphology transition of eccentric binaries is similar to that of circular binaries despite significant rise in eccentricity. This implies that morphology classification is a useful tool to study spin dynamics in eccentric binaries too which eventually would give information about the initial distribution of spins. The morphology evolution of eccentric binaries is similar to that of circular binaries owing to the fact that eccentricity growth is not dependent on the mass ratio, whereas mass ratio is a dominant parameter of the dynamics spinning binaries.
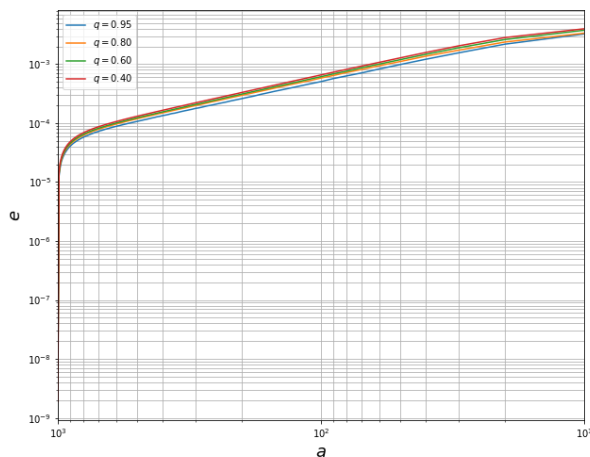
Fig1. *The evolution of eccentricities during inspiral. The binaries with four mass ratios q = (0.4, 0.6, 0.8, 0.95) are maximally spinning. We observe significant growth in eccentricity near merger of binaries.*
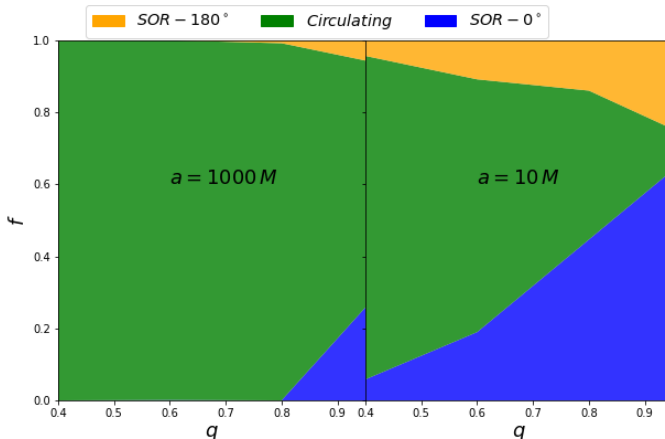
Fig2. *In this figure, we show the evolution of morphologies of binaries during inspiral. As in case of circular binaries, the freely precessing binaries in eccentric orbits also gradually transit to resonant morphologies (SOR-180 and SOR-0) where the angular momentum vectors of binaries occupy a planar configuration or oscillate about the planar configurations.*

4. Conclusion

We have shown that a significant fraction of black hole binaries get locked up in the spin-orbit resonance configurations or oscillate about them towards the end of inspiral. This result has earlier been obtained by ignoring the eccentricity of the binary orbits. We find that statistically the result remains unchanged even if we include the effect of eccentricity.

Acknowledgements

References

[1] Apostolatos, T. A., Cutler, C., Sussman, G. J. and Thorne, K. S., Phys. Rev. D 49, 6274 (1994).

[2] Racine, E., Phys. Rev. D 52, 821 (2008).

[3] Schnittman, J. D., Phys. Rev. D 70, 124020 (2004).

[4] Kesden, M, Sperhake, U. and Berti, E., Phys. Rev. D 81, 084054 (2010)

[5] Gerosa, D., Kesden, E., Berti, E, O'Shaughnessy, R and Sperhake, U. Phys. Rev. D 87, 104028 (2013).

[6] Kesden, M., Gerosa, D., O'Shaughnessy, R., Berti, E. and Sperhake, U, Phys. Rev. Lett. 114, 081103 (2013).

[7] Gerosa, D., Kesden, M., Sperhake, U., Berti, E. and O'Shaughnessy, R., Phys. Rev. D 92, 064016 (2015).

[8] Gerosa, D. and Kesden, M. Phys. Rev. D 93, 124066 (2016).

[9] Klein, A. and Jetzer, P., Phys. Rev. D 81, 124001 (2010).

[10] Loutrel, N., Liebersbach, Yunes, N. and Cornish, N. (2018), arXiv:1801:09009.

[11] Abbott, B. P. et. al. (Virgo, LIGO Scientific), Astrophys. J. 818, L22 (2016).

BSUIN – Baltic Sea Underground Innovation Network

P. Jalas[1], V. Isoherranen[1], J. Joutsenvaara[1], E.-R. Niinikoski[1],
R. Heikkilä[1], T. Makkonen[1], H. Ahola[2], P. Aro[2], T. Vuorela[2], J. Kisiel[3],
K. Karpa[3], K. Szkilniarz[3], M. Laaksoharju[4], M. Ohlsson[4], W. Pytel[5],
D. Horner[6], H. Mischo[6], R. Giese[7], K. Jaksch[7], V. Mockus[8], T. Valys[8],
K. Jędrzejczak[9], M. Kasztelan[9,*], J. Szabelski[9], V. Gostilo[10], V. Shekov[11],
A. Stepanov[12], T. Lindborg[13], V. Karu[14], A. Paat[14]

[1]*University of Oulu*

[2]*Oulu University of Applied Sciences, Oulu, Finland*

[3]*University of Silesia, Katowice, Poland*

[4]*Swedish Nuclear Fuel and Waste Management Co., Stockholm, Sweden.*

[5]*KGHM S.A., Research development center Cuprum, Wroclaw, Poland*

[6]*TU Bergakademie Freiberg, Freiberg, Germany*

[7]*German Research Centre for Geosciences, Potsdam, Germany*

[8]*Vilnius University, Vilnius, Lithuania*

[9]*National Centre for Nuclear Research, Astrophysics Division in Łódź, Poland;*

mk@zpk.u.lodz.pl

[10]*Baltic Scientific instruments, Riga, Latvia*

[11]*Karelian Research Center of Russian Academy of Sciences, Petrozavodsk, Russia*

[12]*Khlopin Institute, St Petersburg, Russia*

[13]*Sotkamo Silver AB, Stockholm, Sweden*

[14]*Tallinn University of Technology, Department of Geology, Tallinn, Estonia*

Abstract The aim of the BSUIN project is to join efforts in making the underground laboratories in the Baltic Sea Region's (BSR) more accessible for innovation, business development and science by improving the availability of information about the underground facilities, service offerings, user experience, safety and marketing.

1. Introduction

The main goal of the project is to combine activities for the better use of different Underground Locations (UL), both the locations of operating underground laboratories as well as less known potential underground sites.

The project activity duration is 36 months and it will end in September 2020.

Baltic Sea Underground Innovation Network (BSUIN) [1] project is funded by Interreg Baltic Sea funding cooperation [2]. Currently 6 underground laboratories are involved in the BSUIN project. Total budget of this project is 3.4M€.

2. BSUIN Basics

A key aspect of the BSUIN project is a transfer of technology and use of research infrastructure for business purposes. In addition to scientific applications, there are a number of potential applications that use the unique conditions at underground locations. There is a range of possibilities to develop various types of mine technologies, tunnel construction, radiation protection systems, geophysics and other research instruments. Underground locations can potentially be used to produce food under different conditions and use geothermal energy for different purposes.

The main assumptions of the BSUIN project are schematically presented in Figure 1. It is important to how cooperation can be strengthened and lead to competitive advantages.
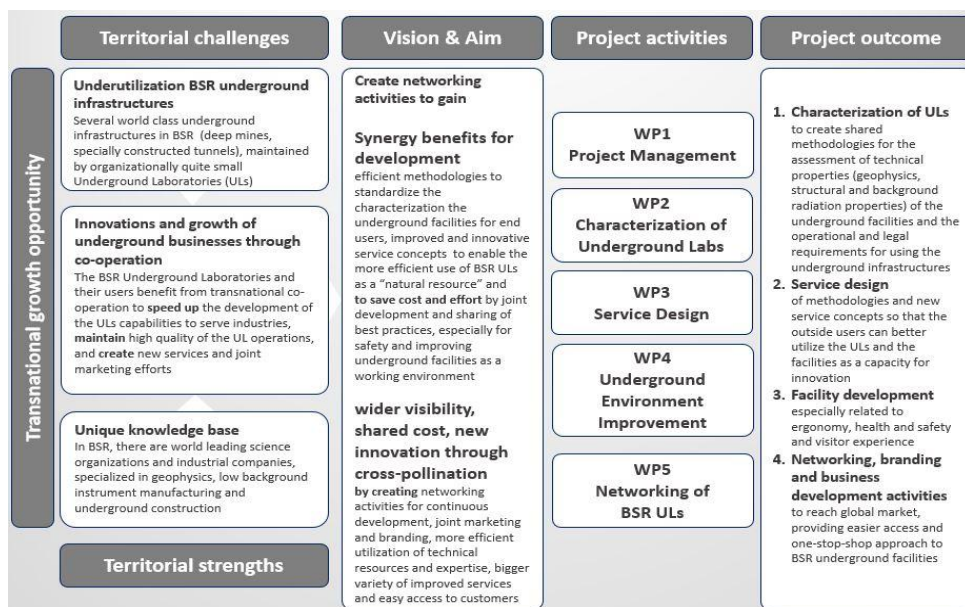
Fig1. *Main benefits from the BSUIN Project.*

3. Project activities

The project is divided into 5 smaller Work Packages (WP) focusing on different aspects:

1.   WP1 Project management and administration
2.   WP2 Characterization of underground facilities
3.   WP3 Service design, market design and branding of ULs as a capacity for innovation
4.   WP4 Underground environment improvement
5.   WP5 Networking of BSR ULs and their users

Different institutions are involved in various work packages, both from project partners and 14 associated partners. In Figure 2 the relations between different work packages and the activities are schematically shown.
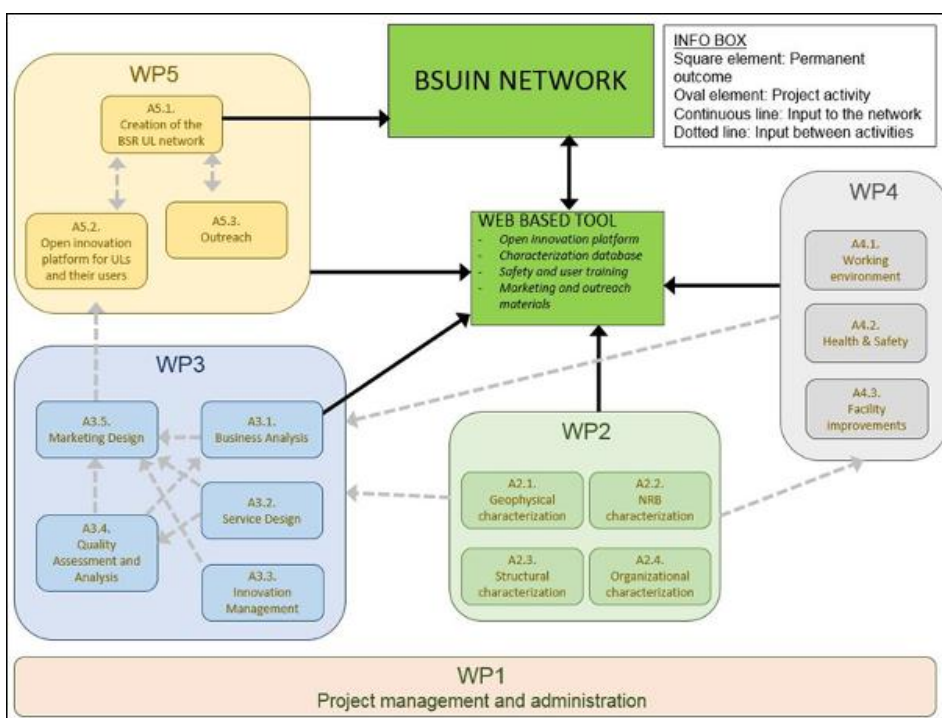
Fig 2. *The BSUIN project work packages (WP) scheme. Relations between different work packages and the activities are schematically shown. In each of the work packages, institutions from many countries of the Baltic Sea region participate.*

Due to the fact that underground locations are significantly different from the Earth's surface, it is necessary to characterize individual locations. The characteristics of underground locations presented in a friendly way can be used by potential commercial customers. This is the main objective of WP2.

The goal of WP3 is to highlight the innovative possibilities that can be developed. Many of the underground locations do not have adequate infrastructure to conduct the organized activities. In order for innovative projects to be developed there, it is necessary to

organize safety procedures. Development of standards is needed for the transfer of innovative technologies to the wide application market.

The WP4 package will define the conditions of work organization in ULs and safety rules as well as risk assessment. Dissemination of best practices and development guidelines will be shared.

The last WP5 package is organizing cooperation between underground locations. Creation is planned of a common web page platform for innovative activities and sharing of various types of information, training, security procedures, marketing materials and all kinds of other information that may be useful for other partners.

4. Results & Outcomes

The most important benefit of the BSUIN project is the cooperation of underground laboratories and potential places where such a laboratory can be organized. One of the benefits will be a database containing the characteristics of underground laboratories in the Baltic Sea region. This information will be organized in a friendly website, where those interested in underground infrastructure will be able to get acquainted with it. Cooperation of the Baltic countries in the use of underground locations can bring tangible benefits to a profit-making industry.

The main result of the project is a balanced network organization that disseminates technical, marketing, operational quality, training and other information about UL BSR generated during the project. The online tool and network organization will be designed to provide an open innovation platform for further quality and innovation development and to share best practice on service concepts, infrastructure improvements and methodological recommendations from pilot actions.

Underground locations are also very important for science that can take place in them. Multi-messenger astronomers can benefit by placing underground cosmic ray detectors, neutrino experiments, and those seeking scarce phenomena. Space weather, supernova explosions, neutrino oscillations are just some of the topics that are explored underground. Many of the places mentioned here and potential underground locations can contribute to the development of science in a very wide range.

5. Project and associated partners

The BSUIN consortium has 14 members from eight Baltic Sea countries. Six underground labs (sec. 6) are looking for new collaboration in the project.

Partner	Country
University of Oulu, Kerttu Saalasti Institute	Finland
Oulu University of Applied Sciences	Finland
University of Silesia in Katowice	Poland
Swedish Nuclear Fuel and Waste Management Co	Sweden
KGHM Cuprum Research & Development Centre Ltd.	Poland
TU Bergakademia Freiberg Technical University	Germany
German Research Centre for Geosciences	Germany
Vilnius University	Lithuania
National Center for Nuclear Research	Poland

Baltic ScientificInstruments	Latvia
Karelian Research Center of Russian Academy of Sciences	Russia
Joint stock company "Khlopin Radium Institute"	Russia
Sotkamo Silver AB	Sweden
Tallinn University of Technology	Estonia

Associated partners of the BSUIN Project:

- The Henryk Niewodniczański Institute of Nuclear Physics Polish Academy of Sciences, Poland
- Rockplan Oy, Finland
- Normet Oy, Finland
- K+S GmbH, Germany
- Kalmar regional Council, Sweden
- Pyhäjärvi Municipality, Finland
- DMT GmbH, Germany
- M-Solutions Oy, Finland
- Muon Solutions Oy, Finland
- University of Tartu, Institute of Physics, Estonia
- Kolmas Karelia LLC, Russia
- Geological Institute of Karelia, Russia
- Pyhäsalmi Mine Oy, Finland
- University of Aarhus, Denmark
- University of Oulu, Department of Architecture, Finland
- University of Jyväskylä, Department of Physics, Finland
- Amberg Group including Versuchsstollen Hagerbach (VSH), Switzerland

6. Underground laboratories

Underground laboratories involved in the BSUIN project:

- Callio Lab, Pyhäsalmi mine, Finland
- Äspö Hard Rock Laboratory, Oskarshamn, Sweden
- Reiche Zeche, TU Freiberg Research and Education mine, Germany
- Conceptual Lab development co-ordinated by KGHM Cuprum R&D centre, Poland
- Khlopin Institute Underground Laboratory, Russia
- Ruskeala, Russia

Fig 3. *Map with denoted locations of underground   locations involved in the BSUIN project.*

Acknowledgements

References

[1]   Baltic Sea Underground Innovation Network. [Online]. Available: http://bsuin.eu/   and https://projects.interreg-baltic.eu/projects/bsuin-102.html

[2]   Interreg   Baltic   Sea   Region   funding   cooperation.   [Online].   Available: https://www.interreg-baltic.eu/

Fast neutrons in the Baksan Underground Scintillation Telescope: the background for core-collapse supernova searches

Kochkarov M. M.[1,*], Alikhanov I.A.[1], Boliev M. M.[1], Dzaparova I. M.[1,2], Novoseltsev Yu. F.[1], Novoseltseva R. V.[1], Petkov V. B.[1,2], Yanin A. F.[1]

[1]*Institute for Nuclear Research of the Russian Academy of Sciences, Moscow, Russia;*

makhti.kochkarov@yandex.ru

[2]*Institute of Astronomy of the Russian Academy of Sciences, Moscow, Russia*

Abstract   We report on the measurement of the flux and spectra of the fast neutron background at BUST with a rock overburden of about 850 m w e, using a special method for the neutron flux estimation based on neutron activation analysis. The neutron-induced events are identified by a two-pulse signature of neutron inelastic scattering process.

1. Introduction

In experiments searching for rare events, signals from neutrons have the same signature as a useful signal. In particular, the registration of electron anti-neutrinos at the Baksan Underground Scintillation Telescope [1] (BUST) made mainly through the inverse beta-decay reaction of electron antineutrinos on protons $\tilde{\nu}_e + p \rightarrow e^+ + n$.

The signal from the positron appears as a single operation of one of the internal counters, at the absence of signals from other counters [2]. Since the cross-sections of reactions with neutrinos are relatively small, all possible reactions with neutrons effectively mimic signals from neutrinos. Neutrons produce background via elastic scattering on protons. At the same time, inelastic neutron-induced reactions with the carbon of the scintillator allow measuring the neutron flux with a sufficient accuracy. During the passage of neutrons through the scintillator, unstable radioactive isotopes are generated.

We have estimated the fast neutron flux (up to some 100 MeV) in the BUST experiment (Figure 1) which has been excavated at a depth of 300 m (850 m w e) under the slope of Mt. Andyrchy (North Caucasus, 43.28°N and 42.69°E).

The aim of the measurement is:

1) To assess as precisely as possible the neutron contribution to the total counting rate in the detector in view of its use for core-collapse supernova search experiments.

2) To evaluate the spurious events and background produced by cosmic ray induced neutrons in the detectors that will be installed in the underground laboratories for experiments in particle physics and astrophysics.
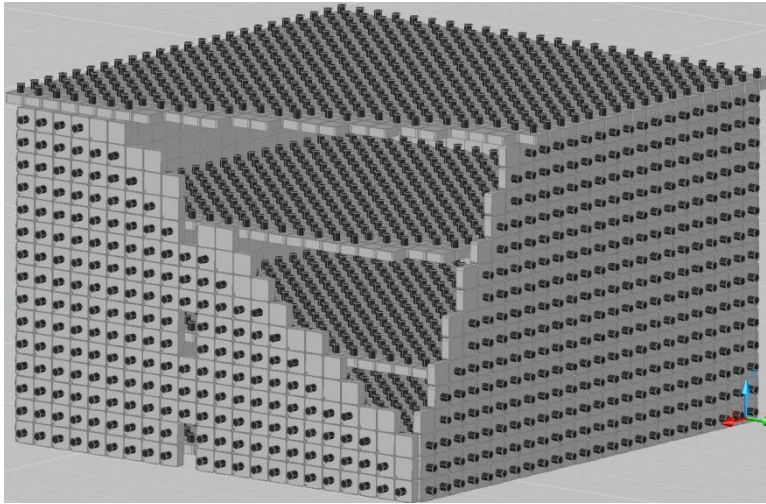
Fig1. *The layout of the Baksan Underground Scintillation Telescope of BNO INR RAS.*

2. Measurements

Neutron-induced reactions in organic scintillator are interesting due to a possibility to get information about the neutron background. Significant in this respect are the reactions leading to emission of charged particles. The ^{12}C(n, p)^{12}B reaction is among them.

The ^{12}B reaction leads to emission of protons and energetic electrons above the threshold of BUST counters. The prompt signal from the proton and the delayed signal from the electron from the unstable isotope beta decay constitute the double signature. The BUST can detect unstable radioactive isotope formation and its subsequent beta decay. The ^{12}C(n, p)^{12}B reaction has been exploited in the present analysis. Theoretically, the ^{12}N isotope is known to be not directly produced by the primary neutron, but rather the recoil proton (n + p → n + p) interacting with the ^{12}C: ^{12}C(p, n)^{12}N. The ^{12}N decay has the same signature as the ^{12}B decay reaction, so these background events can only be statistically subtracted from the data.

A large number of signal pairs allows constructing distribution of time intervals between the signals in the pair. The approximation of distribution of time intervals between signals in a pair by the decay curve makes it possible to estimate the number of radioactive isotopes produced during the observation time. The produced number of ^{12}B nuclei neutrons N_B related to the neutron flux j(E) is obtained from the following expression:

$$N_B = n \cdot f \cdot t \cdot \int_{E_{thr}}^{E_{max}} \sigma(E) \cdot j(E) dE \tag{1}$$

where n is the number of target nuclei, f is the detection efficiency, $\sigma(E)$ is the differential cross section of reaction, t is the observation time. The energy range covered by the integral spans from the counter threshold for neutrons up to highest neutron energy E_n.

The values of the cross section largely vary depending on the selected model. We use as a benchmark for the predictions of the model calculations the integral measurement of the ^{12}C(n, p)^{12}B reaction performed at the neutron time-of-flight facility at CERN. The best evidence for the ^{12}C(n, p)^{12}B cross-section comes from the n_TOF experiment [3]. The n_TOF result has been compared with evaluated cross-sections used in GEANT4. Among

models in GEANT4 good agreement is noticed only with a combined Bertini/Binary cascade model.

In this work, the neutron flux was estimated on basis of the cross-section from the Binary/Bertini model evaluation up to 100 MeV.

The neutron flux from the rock above 10 MeV is roughly inversely proportional to the neutron energy [4]. In this case, equation (1) reduces to

$$N_B = n \cdot f \cdot t \cdot k \cdot \int_{E_{thr}}^{E_{max}} \sigma(E)\,/E\,dE \qquad (2)$$

This allows one to determine the proportionality factor k. Thus, the differential neutron flux can be written as

$$j(E) = \frac{N_B}{n \cdot f \cdot t \cdot \int_{E_{thr}}^{E_{max}} \sigma(E)/E\,dE} \cdot \frac{1}{E} \qquad (3)$$

Because of the quenching of the proton light yield in scintillator, and taking into account the detector energy threshold ($E = 8$ MeV), the neutrons with the double signature have energies greater than 28.6 MeV (i.e. $E_{thr} = 28.6$ MeV).

2.1. Data analysis

To estimate the neutron flux, the BUST data collected from 2001 to 2018 were used (the live time data taking was 16.35 years). Only those events that appear as two consecutive signals from the same counter in the absence of any signal from the other counters were selected. From each counter, we get information which includes the coordinate of the triggered counter, energy deposition in the volume of the counter and the time information. To have the decay of the ^{12}B nucleus with high probability, the time interval between a pair of events was chosen to be equal to 6 half-lives of ^{12}B. We fitted the distribution of signal pairs per counter by the Poisson distribution (Figure 2) throughout the observation time. The counters which gave the number of signals pairs exceeding that predicted by Poisson distribution were excluded from the data processing.
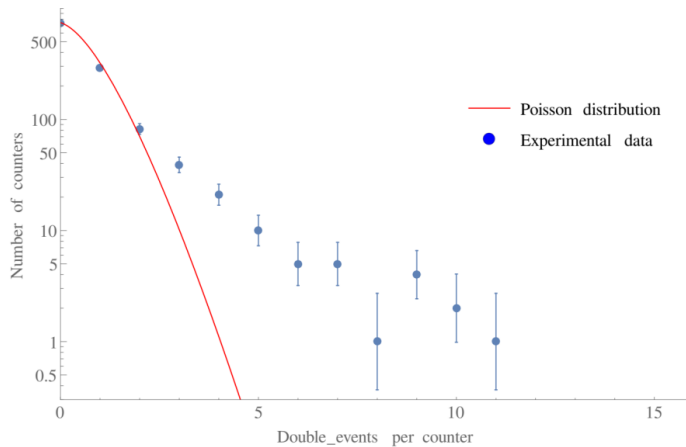
Fig2. Distribution of the signal pairs per counter (points). The solid curve represents the Poisson distribution.

The presence of the radioactive boron is indicated by fitting the distribution of the time intervals between each pair of signals (Figure 3) by the decay curve $F(t) = a \cdot exp(-\Delta t/\tau_B) + a_N \cdot exp(-\Delta t/\tau_N) + b$ (τ_B and τ_N is the mean lifetime of ^{12}B and ^{12}N respectively).
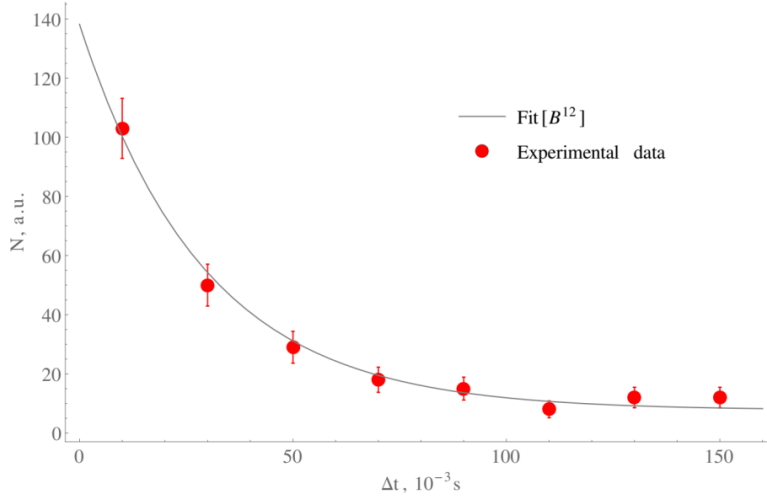
Fig3. Time delay distribution between the signals at BUST. The solid line is the fit by the decay curve.

From the parameter a we obtain the number of ^{12}B isotopes, while b and a_N give the level of background events. The chi-square distribution minimization method was applied to fitting. Subsequently, the number of the produced ^{12}B nuclei was converted into the neutron flux according to equation (3). The response function f of the individual counter to double event reactions has been evaluated using the Monte-Carlo code. All involved processes, including energy loss, multiple scattering etc., have been taken into account.
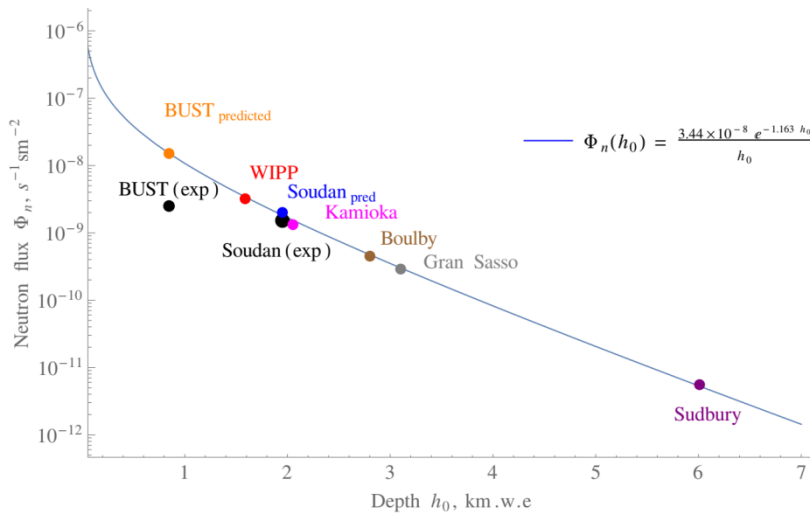
Fig 4. Comparison between experimental results and Monte-Carlo (Mei&Hime) predictions

The BUST counters are commonly divided into two groups: the inner counters (for search neutrino signals from supernova remnants) and the outer counters (used as an active muon veto). We calculated the average neutron flux for an internal group of counters using equation (3).

After taking into account the above-mentioned considerations, the total neutron flux with E_n from 10 to 100 MeV is $\Phi_n = (2.5 \pm 5) \cdot 10^{-9}$ cm^{-2}s^{-1} for the internal counters of the BUST detector. According to Monte-Carlo simulations [5] the following equations predict the muon-induced neutron flux as a function of depth:

$$\Phi_{pred}\left(h_0\right) = P_0 \cdot \left(P_1 / h_0\right) \cdot e^{h_0 / P_1} \tag{4}$$

where h_0 is the equivalent depth in km w e relative to a flat overburden, and P_0, P_1 are the fitting parameters.

The muon-induced neutron flux at the 0.85 km w e (BUST) was obtained using the scaling method $\Phi_{pred}(0.85) = 15.1 \cdot 10^{-9}$ cm^{-2}s^{-1}. The value $\Phi_{pred}(0.85)$ is in qualitative agreement with our results.
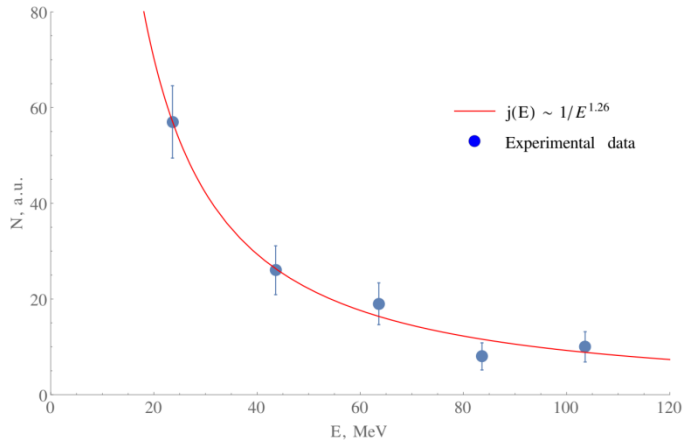
Fig 5. Neutron energy spectra measured with BUST using the delayed coincidence method.

The neutron energy distribution is derived from energy release data in selected double events. The calculation does not take into account the energy resolution of the counters. Fitting the distribution with a power function (Figure 5) gives us a spectral index of 1.26. This value is close to the results obtained in the LVD, KARMEN and Soudan experiments [6].

3. Conclusion

The experimental data collected by the BUST detector (16.35 years of live time) were used to estimate the neutron flux at the external counters of facility. The experimental method is based on the delayed coincidences between two signals from any of the BUST counters.

It is assumed that the first signal is due to inelastic interaction of a neutron with the organic scintillator, while the second signal comes from the decay of an unstable radioactive

isotope formed when the fast neutron interacts with the ^{12}C nuclei. The experimentally found muon-induced neutron flux (for neutron energies E ≥ 10 MeV) is in a qualitative agreement with predictions of the Monte-Carlo models.

Acknowledgements

References

[1]   Alekseev E. N. et al. 1998 Phys. Part. Nucl. 29 254

[2]   Novoseltseva R. V. et al. 2011 Bull. Russ. Acad. Sci., Phys. 75 419

[3]   Žugec P. et al. 2014 Phys. Rev. C 90 021601

[4]   Agafonova N. Y. et al. 2013 Phys. Rev. D 87 113013

[5]   Mei D.-M. et al. 2006 Phys. Rev. D. 73 053004

[6]   Malgin A. S. 2017 JETP 125 728

Machine learning techniques for analysis of photometric data from the Open Supernova catalog

M.V. Kornilov[1,2,*], M.V. Pruzhinskaya[1], K.L. Malanchev[1,2], E.E.O. Ishida[3], F. Mondon[3], A.A. Volnova[4], V.S. Korolev[5]

[1]*Sternberg Astronomical Institute, Lomonosov Moscow State University, Russia; matwey.kornilov@gmail.com*

[2]*National Research University Higher School of Economics; Moscow, Russia*

[3]*Université Clermont Auvergne, CNRS/IN2P3, LPC, France*

[4]*Space Research Institute of the Russian Academy of Sciences (IKI), Moscow, Russia*

[5]*Central Aerohydrodynamic Institute, Zhukovsky, Russia*

Abstract   The next generation of astronomical surveys will revolutionize our understanding of the Universe, raising unprecedented data challenges in the process. One of them is the impossibility to rely on human scanning for the identification of unusual/unpredicted astrophysical objects. Moreover, given that most of the available data will be in the form of photometric observations, such characterization cannot rely on the existence of high resolution spectroscopic observations. The goal of this project is to detect the anomalies in the Open Supernova Catalog (http://sne.space/) with use of machine learning. We will develop a pipeline where human expertise and modern machine learning techniques can complement each other. Using supernovae as a case study, our proposal is divided in two parts: the first developing a strategy and pipeline where anomalous objects are identified, and a second phase where such anomalous objects submitted to careful individual analysis. The strategy requires an initial data set for which spectroscopic is available for training purposes, but can be applied to a much larger data set for which we only have photometric observations. This project represents an effective strategy to guarantee we shall not overlook exciting new science hidden in the data we fought so hard to acquire.

Keywords: Machine Learning Techniques, Supernovae, Astronomical Surveys

1. Introduction

Supernova stars (SNe) are ones of the most brightness and interesting objects in the Universe. They are responsible for chemical enrichment of interstellar medium; density waves induced by their energetic explosions causes the star formation; SNe are origin of high energy cosmic rays; moreover, thanks to SNe we are studying the composition and distance scale of the Universe which defines its following destiny.

The generation of precise, large, and complete supernova surveys in the last years has increased the need of developing automated analysis tools to process this large amount of data. These scientific observations present both great opportunities and challenges for astronomers and machine learning (ML) researchers.

The lack of spectroscopic support makes the photometrical supernova typing is very required. The analysis of big supernova dataset with ML methods is needed to distinguish the supernova by types on base of N-parameter grid. Such study allows us to purify the considered

SN sample from non-supernova contamination as well — the problem, which is relevant for all large supernova database that collect SN candidates without careful analysis of each candidate and basing on the secondary indicators (proximity to the galaxies, transient behaviour, arise/decline rate on light curves (LCs), absolute magnitude). It is also expected that during such analysis the unknown variable objects or SNe with unusual properties can be detected. As an example of unique objects one can refer to SN 2006jc — SN with very strong but relatively narrow He I lines in early spectra (~30 similar objects are known, [25]), SN 2005bf — supernova attributed to SN Ib but with two broad maxima on LCs, SN 2010mb — unusual SN Ic with very low decline rate after the maximum brightness that is not consistent with radioactive decay of 56Ni, ASASSN-15lh — for some time it was considered as the most luminous supernova ever observed (two times brighter than super-luminous SNe), later the origin of this object was challenged and now it is considered as a tidal disruption of a main-sequence star by a black hole. Finding such objects (and then studying them more closely) is one of the main aims of the current project. As such sources are typically rare, the task of finding them can be framed as an anomaly detection problem.

Astronomers have already benefited from developments in machine learning [2], in particular for exoplanet search [22, 29, 26], but the synergy is far from that achieved by other endeavours in genetics [17], ecology [9] or medicine [30], where scientific questions drive the development of new algorithms. Moreover, given the relatively recent advent of large data sets, most of the ML efforts in astronomy are concentrated in classification [16, 15, 19] and regression [13, 6] tasks.

Astronomical anomaly detection has not been yet fully implemented in the enormous amount of data that has been gathered. As a matter of fact, barring a few exceptions, most of the previous studies can be divided into only two different trends: clustering [27] and subspace analysis [12] methods. More recently, random forest algorithms have been extensively used by themselves [3] or in hybrid statistical analysis [24]. Although all of this has been done to periodic variables there is not much done for transients and even less for supernova.

In this study we search the anomalies in photometrical data of the Open Supernova Catalog[a] [11]. We use the Isolation Forest as an outlier detection algorithm that identifies anomalies instead of normal observations [18]. This technique is based on the fact that anomalies are data points that are few and different. Similarly to Random Forest it is built on an ensemble of binary (isolation) trees.

2 Data

2.1 The Open Supernova Catalog

The data are drawn from the Open Supernova Catalog [11]. The catalog is constructed by combining many publicly available data sources (such as Asiago Supernova Catalog, Carnegie Supernova Project, Gaia Photometric Science Alerts, Nearby Supernova Factory, Panoramic Survey Telescope & Rapid Response System (Pan-STARRS), SDSS Supernova Survey, Sternberg Astronomical Institute Supernova Light Curve Catalogue, Supernova Legacy Survey (SNLS), MASTER, All-Sky Automated Survey for Supernovae (ASAS-SN), iPTF, etc.) and from individual publications. It represents an open repository for supernova metadata,

---

[a] https://sne.space/

light curves, and spectra in an easily downloadable format. This catalog also includes some contamination from non-SN objects.

Our choice is justified by the fact that the catalog incorporates the data for more than 5×10^4 SNe/SNe candidates ($\sim 1.2 \times 10^4$ of SNe have > 10 photometrical observations and $\sim 5 \times 10^3$ of SNe have spectra). For comparison, SDSS supernova catalog contains only $\sim 4 \times 10^3$ of SNe LCs and ~ 600 SNe with spectra.

The catalog contains the data in different photometrical passbands. To have a more homogeneous data sample, we chose only those SNe that have LCs in $g'r'i'$, gri or BRI filters. We assume that $g'r'i'$ filters are close enough to gri and transform BRI to gri (see Sect. 2.2). We require $>= 3$ photometrical points in each filter with a 3-day binning. After this cut, our sample contains 3197 objects (2026 objects in $g'r'i'$, 767 objects in gri, and 404 objects in BRI).

2.2 Transformation between *BRI* and *gri*

To increase the sample we convert the Bessel's BRI into gri filters using the Lupton's (2005) transformation equations[b]. These equations are derived by matching SDSS DR4 photometry to Peter Stetson's published photometry for stars:

$$
\begin{cases}
B = u - 0.8116\,(u - g) + 0.1313 \\
B = g + 0.3130\,(g - r) + 0.2271 \\
V = g - 0.2906\,(u - g) + 0.0885 \\
V = g - 0.5784\,(g - r) - 0.0038 \\
R = r - 0.1837\,(g - r) - 0.0971 \\
R = r - 0.2936\,(r - i) - 0.1439
\end{cases}
\tag{1}
$$

3 Anomaly detection

3.1. LCs fit

It is more convenient to implement the ML algorithm to the data with uniform time grid which is unfortunately not the case with supernovae. Commonly used technique to transform unevenly distributed data onto uniform grid is to fit them with Gaussian processes (GP). Usually, each light curve is fitted by GP independently. However, in this study we developed the MULTIVARIATE GAUSSIAN PROCESS [c] interpolation that allows correlating multi-color LCs and approximates the data by GP in all filters in a one global fit (for details see Kornilov et. 2019, in prep.).

When the fit by MULTIVARIATE GAUSSIAN PROCESS was done, we checked the results of approximation by eye. Those SNe with unsatisfactory fit were removed from the further consideration (mainly the objects with bad photometrical quality). We also extrapolated the fit to have a bigger temporal coverage. In the end we got a sample that consists of 1999 objects.

---

[b] http://www.sdss3.org/dr8/algorithms/sdssUBVRITransform.php
[c] https://github.com/matwey/gp-multistate-kernel

Based on the results of approximation we extracted photometry (in flux) in the range of [−20, 100] days with 1-day bin relative to the LC maximum in *r* filter and the kernel parameters.

After the approximation procedure, each object has 373 features: 121×3 fluxes in three bands, 9 fitted parameters of Gaussian Process kernel, and logarithm of likelihood of the fit. We examine two cases of outliers search: with all features and with smaller number of features obtained by dimensionality reduction.
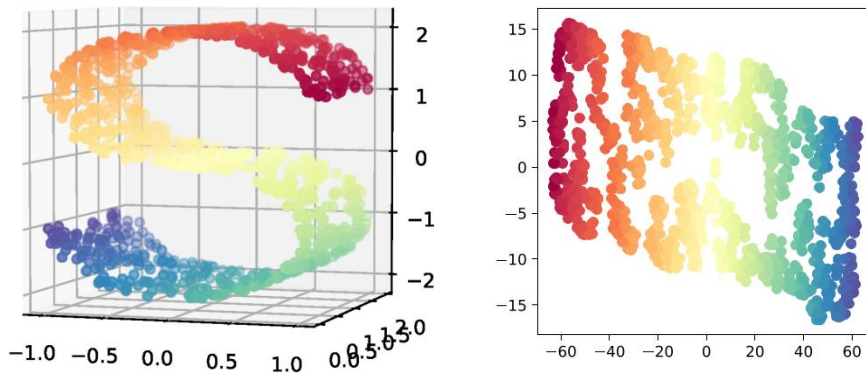
Fig1. *Left panel: sample three-dimensional set of labeled data. Right panel: the same data set reduced into two-dimensional space by t-SNE algorithm.*
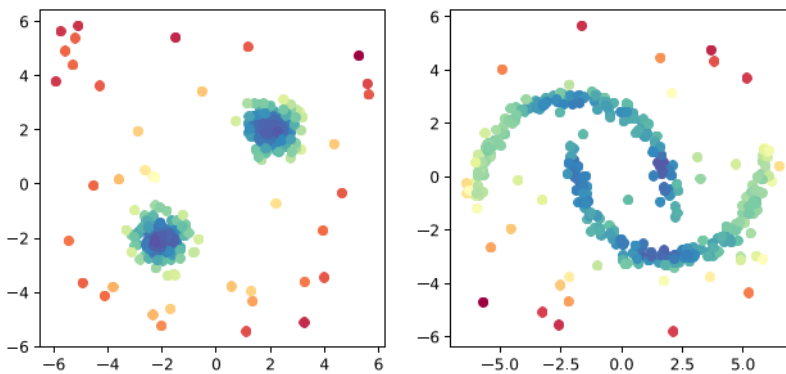
Fig2. *Isolation forest applied to the two different sample data sets (left panel and right panel respectively). Redder points are ranked as anomalies.*

3.2. Dimensionality Reduction

Each object has its own flux scale due to the different origin and different distance. So, before the dimensionality reduction procedure we normalized each vector of 363 photometrical points by its maximum value and used the maximum value as one more feature. Then, we applied t-SNE [21] for dimensionality reduction of the data with 374 features: we obtained 7 feature reduced data sets: from 2 to 8 features.

In Fig. 1 we show t-SNE applied to sample data set in three-dimensional space. One may see that t-SNE is a nonlinear dimensionality reduction technique keeping vicinity of adjacent points.

Table1. List of found anomalies.

Name	Coordinates	Object type	Ref.
SN2016bln	13 34 45.49 +13 51 14.3	Ia-91T	[7]
SN2013cv	16 22 43.16 +18 57 35.6	SN Ia-pec	[35, 5]
SN1000+0216	10 00 05.87 +02 16 23.6	SLSN	[8]
SN2006kg	01 04 16.98 +00 46 08.9	AGN	[4, 34, 28]
Gaia16aye	19 40 01.13 +30 07 53.4	Binary microlensing event	[1,33]

3.3. Isolation Forest

Isolation forest is an ensemble of random isolation trees. Each isolation tree is a space partitioning tree similar to a widely-know Kd-tree. However, in contrast to Kd-tree, space coordinate (a feature) and a split value are selected at random for every node of the isolation tree. This algorithm leads to an unbalanced tree unusable for spatial search, but the tree has the following important property. A path distance between the root and a leaf is shorter on average for points distanced in space from "normal" data. This allows us to construct enough random trees to estimate average root-leaf path distance for every data sample that we have, and then rank the data samples based on the path length.

In Fig. 2 we show isolation forest applied to the different sample data sets. Note that the major advantage of the isolation forest is that it doesn't make any assumptions on normal data distribution. At the left panel of Fig. 2 we could fit the data by two normal probability distribution function and then find outliers. This approach fails for the right panel of Fig. 2 where the isolation forest still succeeded.

We run the Isolation Forest algorithm on each data set (see Sect. 3.2) and obtained a list of anomalies.

4. Results

We visually inspected $\sim$ 100 outliers among a total 1999 objects. Using the publicly available sources we checked what kind of astrophysical objects they are. The most prominent outliers are listed in Table 1 and described below, the rest are still being studied.

4.1. Peculiar SNe Ia

Type Ia supernova phenomenon is an explosion of a carbon-oxygen white dwarf that exceed the Chandrasekhar limit either by matter accretion from a companion star or by merging with another white dwarf [32, 14, 31]. SNe Ia are used as universal distance ladder since their luminosity at maximum light is approximately the same. However, SNe Ia can be divided by subtypes and not all of them are suitable for cosmology.
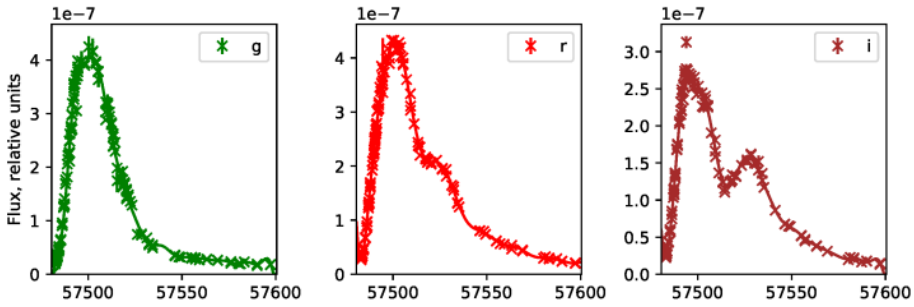
Fig3. Light curves in gri filters of SN Ia-91T 2016bln [23].

SN2016bln [7], classified by our code as anomaly, belongs to the so-called 1991T-like-supernovae subtype (see Fig. 3). SNe Ia-91T are characterized by higher peak luminosity and broader LCs than a normal SN Ia, and different early spectrum evolution.

Another novelty is SN2013cv ([35], see Fig. 4). This peculiar supernova has large peak optical and UV luminosity and show an absence of iron absorption lines in the early spectra. Cau at al. suggest that SN2013cv is an intermediate case between the normal and super-Chandrasekhar events [5].

4.2. Superluminous SNe

Superluminous SNe (SLSN) are supernovae with an absolute peak magnitude $M < -21$ mag in any band. According to [10] SLSN can be divided into three broad classes: SLSN-I without hydrogen in their spectra, hydrogen-rich SLSN-II that often show signs of interaction with circum-stellar material (CSM), and finally, SLSN-R, a rare class of hydrogen-poor events with slowly evolving LCs, powered by the radioactive decay of ^{56}Ni.

SN 1000+0216 (Fig. 5) was discovered in the framework of the Canada-France-Hawaii Telescope Legacy Survey Deep Fields and has a redshift $z = 3.9$. It may be an example of a pulsational pair-instability SN or a SLSN-II which extreme optical emission is explained by the strong interaction between the expanding ejecta and massive CSM [8].

4.3. AGN

SN2006kg was erroneously classified as Type II supernovae ([4], see Fig. 6). The following studies identified it as an active galactic nucleus (AGN [34, 28]).
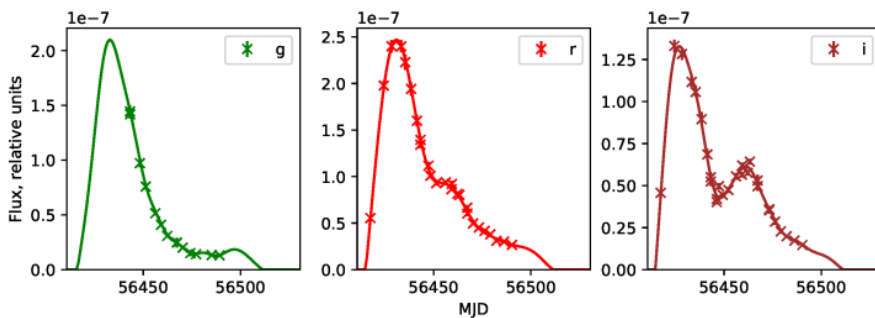
Fig4. Light curves in gri filters of peculiar SN2013cv [5, 34].
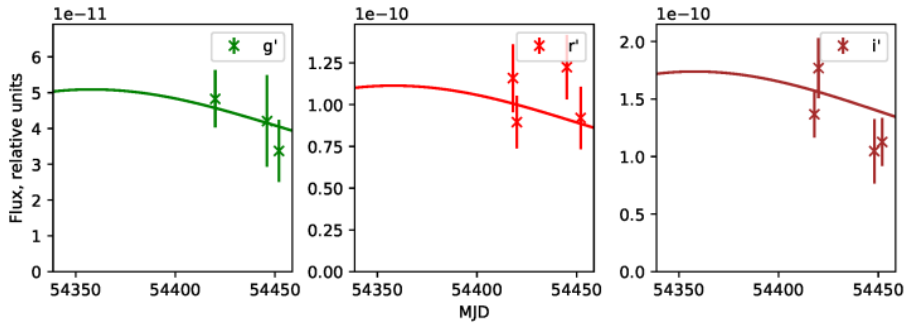
Fig5. *Light curves in gri filters of superluminous SN1000+0216 [8].*
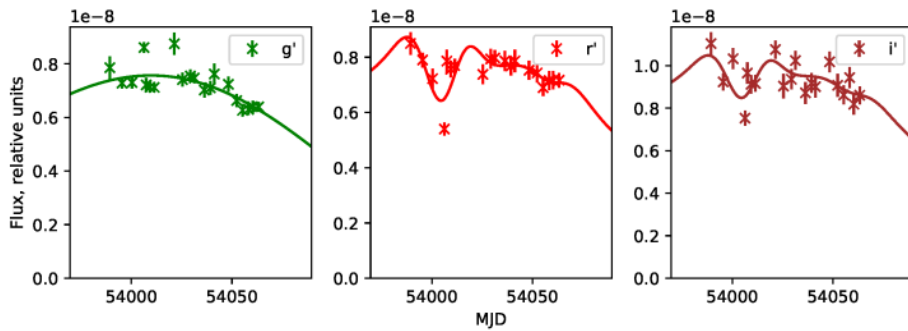
Fig6. *Light curves in gri filters of SN2006kg [28].*

4.4. Binary microlensing event

Gaia16aye [1] is an object with the most non-SN behaviour in our set of outliers (Fig. 7). In [33] it was reported that Gaia16aye is a binary microlensing event – gravitational microlensing by binary systems — the first ever discovered towards the Galactic Plane.
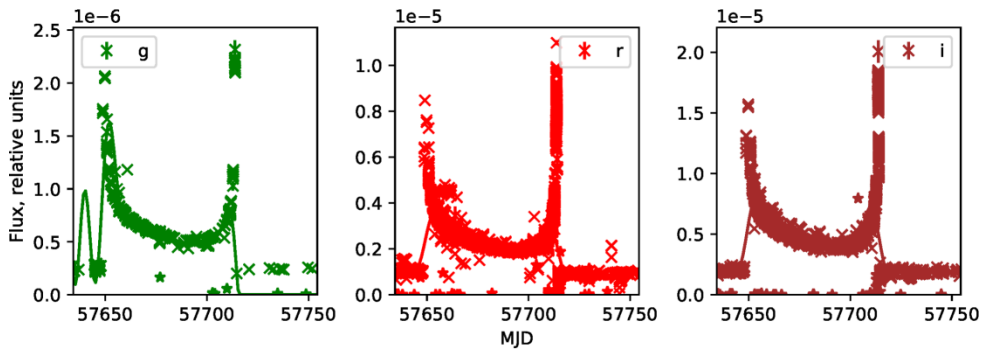
Fig7. *Light curves in gri filters of binary microlensing event Gaia16aye*
(http://gsaweb.ast.cam.ac.uk/alerts/alert/Gaia16aye/followup)

5. Conclusions

The development of large synoptic sky surveys has led to a discovery of huge number of supernovae and supernova candidates. Among the SN discovered every year, only 10% have spectroscopic confirmation. The amount of astronomical data increases dramatically with time and already beyond human capabilities. While now community has dozens of thousands SN candidates, during ten-year survey Large Synoptic Sky Telescope (LSST, [20]) will discover over ten million supernovae (and only a small fraction of them will receive a spectroscopic confirmation). The LSST cadence will allow receiving the light curves for ~ 105 SNe, but before these SNe will be used in any physical analysis, they must be classified by types. In order to process this information and to extract all possible knowledge, machine learning techniques become necessary. Such approach will allow not only to classify supernova candidates by known types, but to reveal other variable objects (novae, counterparts of GW alerts, kilonovae, GRB afterglows) that were mistakenly classified as SN and what is even more important to detect astronomical objects with strange physical properties – anomalies. Finding such objects (and then studying them more closely) is of high priority and one of the main aims of the current study.

We used the Isolation Forest algorithm to search the anomalies in the Open Supernova Catalog. During the data pre-processing we fitted the supernova LCs in three (*gri*) filters by Gaussian processes. The GP-MULTISTATE-KERNEL[d] (Kornilov et al. 2019, in prep.) was specially developed to introduce the correlation between the filters. As a result, we found ~ 100 anomalies, among which peculiar Type Ia SNe, SLSN, AGN, binary microlensing event.

Acknowledgements

References

[1] V. Bakis, U. Burgaz, T. Butterley, J. M. Carrasco, V. S. Dhillon, M. Dominik, A. Floers, L. K. Hardy, G. Leto, S. P. Littlefair, J. R. Maund, P. Ochner, A. Pastorello, A. Piascik, L. Rhodes, R. Z. Sanchez, K. V. Sokolovsky, I. Steele, S. Taubenberger, G. Terreran, L. Tomasella, R. W. Wilson, L. Wyrzykowski, and A. M. Zubareva. Gaia16aye: a flaring object of uncertain nature in Cygnus. *The Astronomer's Telegram*, 9376, Aug. 2016.

---

[d] https://github.com/matwey/gp-multistate-kernel

[2]   N. M. Ball and R. J. Brunner. Data Mining and Machine Learning in Astronomy. International Journal of Modern Physics D, **19**, 1049–1106,2010.

[3]   D. Baron and D. Poznanski. The weirdest SDSS galaxies: results from an outlier detection algorithm. MNRAS, **465,** 4530–4555, Mar. 2017.

[4]   B. Bassett, A. Becker, H. Brewington, C. Choi, D. Cinabro, F. Dejongh, J. Dembicky, D. L. Depoy, B. Dilday, M. Doi, J. Frieman, P. Garnavich, M. Harvanek, C. Hogan, J. Holtzman, S. Im, S. Jha, K. Konishi, J. Krzesinski, H. Lampeitl, R. Kessler, B. Ketzeback, D. Long, O. Malanushenko, J. Marriner, D. McGinnis, R. McMillan, G. Miknaitis, T. Morokuma, R. Nichol, K. Pan, J. L. Prieto, M. Richmond, A. Riess, R. Romani, M. Sako, G. Saurage, D. Schneider, M. Smith, S. Snedden, N. Takanashi, K. Tokita, K. van der Heyden, S. Watters, C. Wheeler, N. Yasuda, C. Zheng, A. Aragon-Salamanca, M. Bremer, M. Turatto, A. Goobar, J. Sollerman, P. Ruiz-Lapuente, F. Castander, A. Romer, C. Collins, J. Lucey, A. Edge, M. Stritzinger, U. Hopp, W. Kollatschny, J. Eastman, L. Watson, R. Assef, K. Schlesinger, and A. Crotts. Supernovae 2006kg-2006lc. Central Bureau Electronic Telegrams, 688, Oct. 2006.

[5]   [5] Y. Cao, J. Johansson, P. E. Nugent, A. Goobar, J. Nordin, S. R. Kulkarni, S. B. Cenko, O. D. Fox, M. M. Kasliwal, C. Fremling, R. Amanullah, E. Y. Hsiao, D. A. Perley, B. D. Bue, F. J. Masci, W. H. Lee, and N. Chotard. Absence of fast-moving iron in an intermediate type ia supernova between normal and super-chandrasekhar. The Astrophysical Journal, **823(2)**, 147, 2016.

[6]   S. Cavuoti, M. Brescia, C. Tortora, G. Longo, N. R. Napolitano, M. Radovich, F. La Barbera, M. Capaccioli, J. T. A. de Jong, F. Getman, A. Grado, and M. Paolillo. Machine-learning-based photometric redshifts for galaxies of the ESO Kilo-Degree Survey data release 2. MNRAS, **452**, 3100–3105, Sept. 2015.

[7]   S. B. Cenko, Y. Cao, M. Kasliwal, A. A. Miller, C. Fremling, M. West, M. Gregg, and S. R. Kulkarni. DCT and Gemini Spectroscopic Classification of AT 2016bln (=iPTF 16abc). The Astronomer's Telegram, 8909, Apr. 2016.

[8]   J. Cooke, M. Sullivan, A. Gal-Yam, E. J. Barton, R. G. Carlberg, E. V. Ryan-Weber, C. Horst, Y. Omori, and C. G. D´ıaz. Superluminous supernovae at redshifts of 2.05 and 3.90. Nature, **491,** 228–231, Nov. 2012.

[9]   C. Criscia, B. Ghattasb, and G. Pererac. A review of supervised machine learning algorithms and their applications to ecological data. Ecological Modelling, **240,** 113–122, 2012.

[10]   A. Gal-Yam. Luminous Supernovae. Science, **337**, 927, Aug. 2012.

[11]   J. Guillochon, J. Parrent, L. Z. Kelley, and R. Margutti. An Open Catalog for Supernova Data. ApJ, **835**, 64, Jan. 2017.

[12]   M. Henrion, D. J. Hand, A. Gandy, and D. J. Mortlock. Casos: a subspace method for anomaly detection in high dimensional astronomical databases. Statistical Analysis and Data Mining: The ASA Data Science Journal, **6(1)**, 53–72.

[13]   H. Hildebrandt, S. Arnouts, P. Capak, L. A. Moustakas, C. Wolf, F. B. Abdalla, R. J. Assef, M. Banerji, N. Benítez, G. B. Brammer, T. Budavári, S. Carliles, D. Coe, T. Dahlen, R. Feldmann, D. Gerdes, B. Gillis, O. Ilbert, R. Kotulla, O. Lahav, I. H. Li, J.-M. Miralles, N. Purger, S. Schmidt, and J. Singal. PHAT: PHoto-z Accuracy Testing. A&A, **523**, A31, Nov. 2010.

[14]   I. Iben, Jr. and A. V. Tutukov. Supernovae of type I as end products of the evolution of binaries with components of moderate initial mass (M not greater than about 9 solar masses). ApJS, **54**, 335–372, Feb. 1984.

[15]   E. E. O. Ishida and R. S. de Souza. Kernel PCA for Type Ia supernovae photometric classification.

MNRAS, **430**, 509–532, Mar. 2013.

[16] R. Kessler, B. Bassett, P. Belov, V. Bhatnagar, H. Campbell, A. Conley, J. A. Frieman, A. Glazov, S. Gonz´alez-Gait´an, R. Hlozek, S. Jha, S. Kuhlmann, M. Kunz, H. Lampeitl, A. Mahabal, J. Newling, R. C. Nichol, D. Parkinson, N. Sajeeth Philip, D. Poznanski, J. W. Richards, S. A. Rodney, M. Sako, D. P. Schneider, M. Smith, M. Stritzinger, and M. Varughese. Results from the Supernova Photometric Classification Challenge. PASP, **122**, 1415, Dec. 2010.

[17] M. W. Libbrecht and W. S. Noble. Machine learning applications in genetics and genomics. Nature Reviews Genetics, **16**, 321–332, 2015.

[18] F. T. Liu, K. M. Ting, and Z.-H. Zhou. Isolation-based anomaly detection. ACM Trans. Knowl. Discov. Data, **6(1)**, 3:1–3:39, Mar. 2012.

[19] M. Lochner, J. D. McEwen, H. V. Peiris, O. Lahav, and M. K. Winter. Photometric Supernova Classification with Machine Learning. ApJS, **225**, 31, Aug. 2016.

[20] LSST Science Collaboration, P. A. Abell, J. Allison, S. F. Anderson, J. R. Andrew, J. R. P. Angel, L. Armus, D. Arnett, S. J. Asztalos, T. S. Axelrod, and et al. LSST Science Book, Version 2.0. ArXiv e-prints, Dec. 2009.

[21] L. v. d. Maaten and G. Hinton. Visualizing data using t-sne. Journal of machine learning research, **9(Nov)**, 2579–2605, 2008.

[22] S. D. McCauliff, J. M. Jenkins, J. Catanzarite, C. J. Burke, J. L. Coughlin, J. D. Twicken, P. Tenenbaum, S. Seader, J. Li, and M. Cote. Automatic Classification of Kepler Planetary Transit Candidates. ApJ, **806**, 6, June 2015.

[23] A. A. Miller, Y. Cao, A. L. Piro, N. Blagorodnova, B. D. Bue, S. B. Cenko, S. Dhawan, R. Ferretti, O. D. Fox, C. Fremling, A. Goobar, D. A. Howell, G. Hosseinzadeh, M. M. Kasliwal, R. R. Laher, R. Lunnan, F. J. Masci, C. McCully, P. E. Nugent, J. Sollerman, F. Taddia, and S. R. Kulkarni. Early Observations of the Type Ia Supernova iPTF 16abc: A Case of Interaction with Nearby, Unbound Material and/or Strong Ejecta Mixing. ApJ, **852**, 100, Jan. 2018.

[24] I. Nun, K. Pichara, P. Protopapas, and D.-W. Kim. Supervised Detection of Anomalous Light Curves in Massive Astronomical Catalogs. ApJ, **793**, 23, Sept. 2014.

[25] A. Pastorello, X.-F. Wang, F. Ciabattari, D. Bersier, P. A. Mazzali, X. Gao, Z. Xu, J.-J. Zhang, S. Tokuoka, S. Benetti, E. Cappellaro, N. Elias-Rosa, A. Harutyunyan, F. Huang, M. Miluzio, J. Mo, P. Ochner, L. Tartaglia, G. Terreran, L. Tomasella, and M. Turatto. Massive stars exploding in a He-rich circumstellar medium - IX. SN 2014av, and characterization of Type Ibn SNe. MNRAS, **456**, 853–869, Feb. 2016.

[26] K. A. Pearson, L. Palafox, and C. A. Griffith. Searching for exoplanets using artificial intelligence. MNRAS, **474**, 478–491, Feb. 2018.

[27] U. Rebbapragada, P. Protopapas, C. E. Brodley, and C. Alcock. Finding anomalous periodic time series. Machine Learning, **74(3)**, 281–313, Mar 2009.

[28] M. Sako, B. Bassett, A. C. Becker, P. J. Brown, H. Campbell, R. Wolf, D. Cinabro, C. B. D'Andrea, K. S. Dawson, F. DeJongh, D. L. Depoy, B. Dilday, M. Doi, A. V. Filippenko, J. A. Fischer, R. J. Foley, J. A. Frieman, L. Galbany, P. M. Garnavich, A. Goobar, R. R. Gupta, G. J. Hill, B. T. Hayden, R. Hlozek, J. A. Holtzman, U. Hopp, S. W. Jha, R. Kessler, W. Kollatschny, G. Leloudas, J. Marriner, J. L. Marshall, R. Miquel, T. Morokuma, J. Mosher, R. C. Nichol, J. Nordin, M. D. Olmstead, L. Östman, J. L. Prieto, M. Richmond, R. W. Romani, J. Sollerman, M. Stritzinger, D. P. Schneider, M. Smith, J. C. Wheeler, N. Yasuda, and C. Zheng. The Data Release of the Sloan Digital Sky Survey-II Supernova Survey. PASP, **130(6)**, 064002, June 2018.

[29] S. E. Thompson, F. Mullally, J. Coughlin, J. L. Christiansen, C. E. Henze, M. R. Haas, and C. J. Burke. A Machine Learning Technique to Identify Transit Shaped Signals. ApJ, **812**, 46, Oct. 2015.

[30] M. Vidyasagar. Identifying predictive features in drug response using machine learning: Opportunities and challenges. Annual Review of Pharmacology and Toxicology, **55(1)**, 15–34, 2015. PMID: 25423479.

[31] R. F. Webbink. Double white dwarfs as progenitors of R Coronae Borealis stars and Type I supernovae. ApJ, **277**, 355–360, Feb. 1984.

[32] J. Whelan and I. Iben, Jr. Binaries and Supernovae of Type I. ApJ, **186**, 1007–1014, Dec. 1973.

[33] L. Wyrzykowski, G. Leto, G. Altavilla, V. Bakis, N. Britavskiy, U. Burgaz, T. Butterley, J. M. Carrasco, V. S. Dhillon, M. Dominik, A. Gomboc, L. K. Hardy, S. P. Littlefair, J. R. Maund, A. Piascik, L. Rhodes, R. Z. Sanchez, K. V. Sokolovsky, I. Steele, R. W. Wilson, A. Hamanowicz, P. Mroz, M. Pawlak, K. Rybicki, M. Sitek, P. Mikolajczyk, Z. Kolaczkowski, R. Street, P. Bendjoya, V. Bozza, J. Dziedzic, K. Niczyj, R. Nowicki, and M. Porebski. Gaia16aye is a binary microlensing event and is crossing the caustic again. The Astronomer's Telegram, **9507**, Sept. 2016.

[34] O. Yaron and A. Gal-Yam. WISeREP — An Interactive Supernova Data Repository. PASP, **124**, 668, July 2012.

[35] L. Zhou, X. Wang, K. Zhang, J. Chen, J. Liang, T. Zhang, X. Zhou, F. Huang, X. sZhao, X. Wang, T. Zhang, D. D. Balam, M. L. Graham, and E. Y. Hsiao. Supernova 2013cv = Psn J16224316+1857356. Central Bureau Electronic Telegrams, **3543**, June 2013.

DAQ system for the complex of BUST – Andyrchy – Carpet-2 facilities

A.N. Kurenya[1,*], I.M. Dzaparova[1,2], D.D. Dzhappuev[1], E.A. Gorbacheva[1], O.I. Mikhailova[1], V.B. Petkov[1,2], V.S. Romanenko[1], A.F. Yanin[1]

[1]*Institute for Nuclear Research, Russian Academy of Sciences, Moscow, 117312 Russia;*

Kurenya.Alex@yandex.ru

[2]*Institute of Astronomy, Russian Academy of Sciences, Moscow, 119017 Russia*

Abstract   The work in the field of multi-messenger astronomy imposes increased requirements to the experimental facilities and their data acquisition systems. Therefore the fundamental modernization of data acquisition systems of experimental facilities of the Baksan Neutrino Observatory (BNO) is now performed. In this paper the upgrading of data acquisition systems and processing data of the Baksan Underground Scintillation Telescope (BUST), "Carpet-2" and "Andyrchy" EAS arrays is discussed.

Keywords: EAS, VME, DAQ, Gamma-Ray Burst, Cosmology

1. Introduction

The study of astrophysical objects by methods of multi-messenger astronomy demands increased requirements to the data acquisition (DAQ) systems. Especially it concerns the fast response astronomy, i.e. the quick searchers of other messenger partners after an alert. The development of modern experimental facilities and fast data acquisition systems (DAQ) gives a possibility to analyze experimental data in the real-time mode. The fundamental modernization of data acquisition systems of experimental facilities of the Baksan Neutrino Observatory is being performed now. This modernization will make it possible to produce the low-latency alerts from experimental facilities of BNO to a great number of various telescopes. New data acquisition systems of the Baksan Underground Scintillation Telescope, "Carpet-2" and "Andyrchy" EAS arrays are based on the VME interface and provide full compatibility with existing front-end electronics.

2. BUST

The BUST consists of four horizontal and four vertical planes. Its size is 16.7 x 16.7 x 11.1 m^3. All planes are completely covered with standard scintillation counters. Eight planes of the telescope consist of 3180 scintillation counters. The existing DAQ system, the architecture of which was developed in the 70s of the last century, does not allow the full use of the capabilities of scintillation counters. The dead time of the new DAQ system is an order of magnitude less than that of the previous one. The new system is based on a VME interface and is totally compatible with existing front-end electronics of the BUST. A

hodoscope of pulse channels (HPC) is developed anew and is iimplemented using FPGA and LVDS chips.

Figure 1 shows the functional diagram of the DAQ system. HPC consist of 3180 channels, according to the number of scintillation counters of BUST. Constructively the entire HPC is located in four CAMAC crates. All crates have controllers that serve all receiving blocks of their crates and provide data transmission and control signals via the V1495 module. Each plane of the BUST is divided into groups - structures. The time measurements of eight planes and 29 plane structures are made by the TDC V1190 module. In this case, the signals coming from the shaper with front compensation (SFC) should be converted from the NIM standard to the LVDS standard.

To measure the energy release, the analog signals from the scintillation counters are summed by 100 and fed to the trigger block. In the trigger unit the analog signals are matched to the wave impedance of flat cable of twisted pairs for transmitting them to QDC V792 module. The trigger unit delays analog signals by 30 nanoseconds. Such a delay is necessary for formation of the QDC GATE input signal before arrival of the measured analog signals. The duration of the GATE signal must be greater than the measured signal.

The Hodoscope of amplitude channels (HAC), in contrast to QDC, measures not the charge of the planes, but the individual charge of each counter. HAC was developed and launched in 2002. All signals from logarithmic converters of eight BUST planes are connected to seven CAMAC blocks. In addition to the HAC blocks, a dead time DAQ block and two four-channel blocks with 12-bit analog-digital converters (ADC) are installed in the crates.
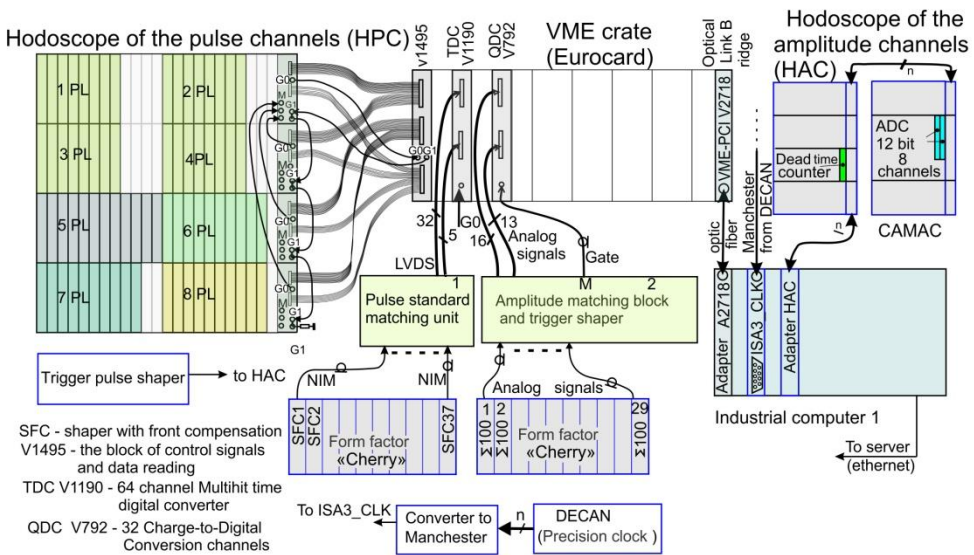
Fig1. *Block diagram of the BUST.*

To study the energy spectrum it is necessary to know not only the energy release, but also the waveform of the signals. The waveform of signals allows us to separate a useful signal from the noise and to analyze parameters of particles, to study the decay processes inside the

scintillation counters. The total energy release signals from the eight planes are fed to the inputs of the NI PCI 5124 fast ADC boards located in the industrial computer. The ADC boards make it possible to measure the energy release of events with high accuracy, which allows studying the energy spectrum of neutrinos emitted by collapsing stars.
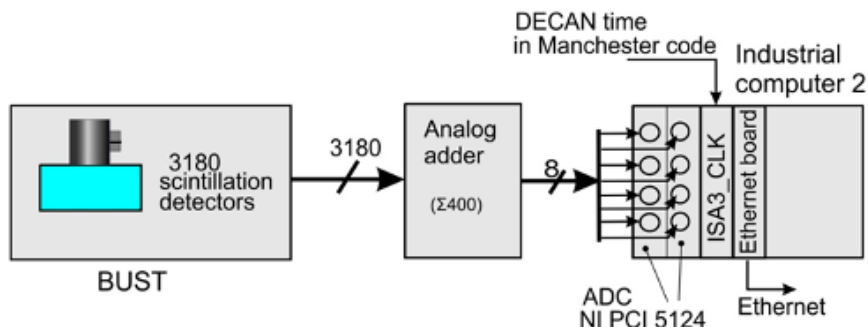
Fig2. Functional diagram of signal form measurement from each plane by fast ADC.

3. "Carpet-2"

The diagram of the DAQ system of the «Carpet -2» EAS array is presented in Fig.3. This array consists of the ground part of the «Carpet» (400 liquid scintillation counters, continuous covering square of 200 m^2), six remote vans (in each van there are 18 similar liquid scintillation counters), and an underground Muon Detector (MD) with an area of 175 m^2 (175 plastic scintillation counters). Signals from six remote vans are used to determine the direction of arrival of showers. EAS muon component with energy above 1 GeV is registered by MD.

Analog signals from «Carpet» and vans modules are branched into two groups. One part passes into trigger block 2, in which the GATE control signal for QDC is generated, the cable delay of all analog signals is produced and then signals are fed to the measuring inputs QDC V792 module. The second parts of signals via SFC are fed to trigger block 1. There the signals are converted from NIM to the LVDS standard and are fed to the measuring inputs TDC V1190B module.

The signals from MD come in different kinds: analog, signals from SFC, signals from logarithmic converter, and signals from RC converters. In MD, the analog signals from scintillation counters are summed by 35 (5 signals) and fed to the inputs of QDC module implemented in the CAMAC standard. Also, these signals are summed and fed to the 6th input QDC. Signals from RC converters (175 signals) are fed to the hodoscope inputs of amplitude channels implemented in the CAMAC standard

The MD is being upgraded. It is planned to connect 205 already manufactured detectors. The MD DAQ system based on CAMAC standard will be replaced by the system in the VME standard.
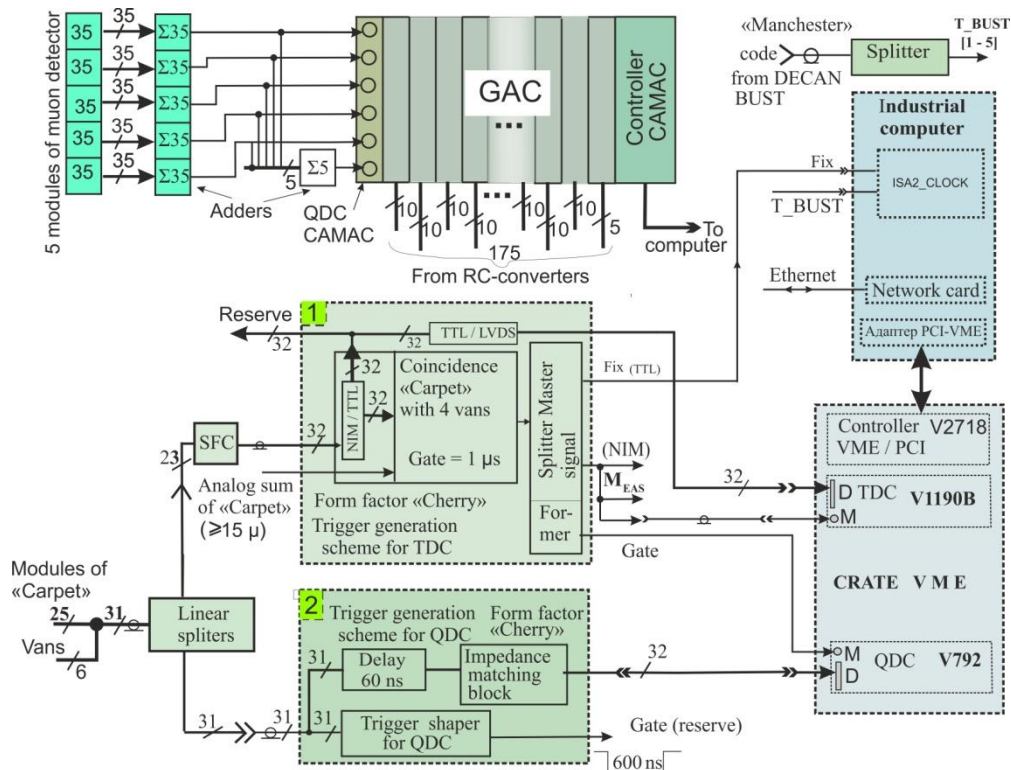
Fig3. *Block diagram of the "Carpet-2" EAS array.*

4. "Andyrchy"

The DAQ system of the "Andyrchy" EAS array (Fig. 4) is similar to the "Carpet-2" DAQ system discussed above. Energy release of the 36 scintillation counters is measured by the QDC V792 and V965A modules. The analog signals in this case pass through the QDC trigger block 2 and fed to the inputs of QDC V792 and V965A modules, as in the previous scheme, the analog signals are also delayed. The signals from the RC converters are fed to the TDC trigger block 1, from which, after conversion to the LVDS standard, are fed to inputs of the TDC V1190B module and, through the TBI-24/DC-3 galvanic isolation board, to the modules UNIO-96-5 to measure count rates of all scintillation counters of the array.
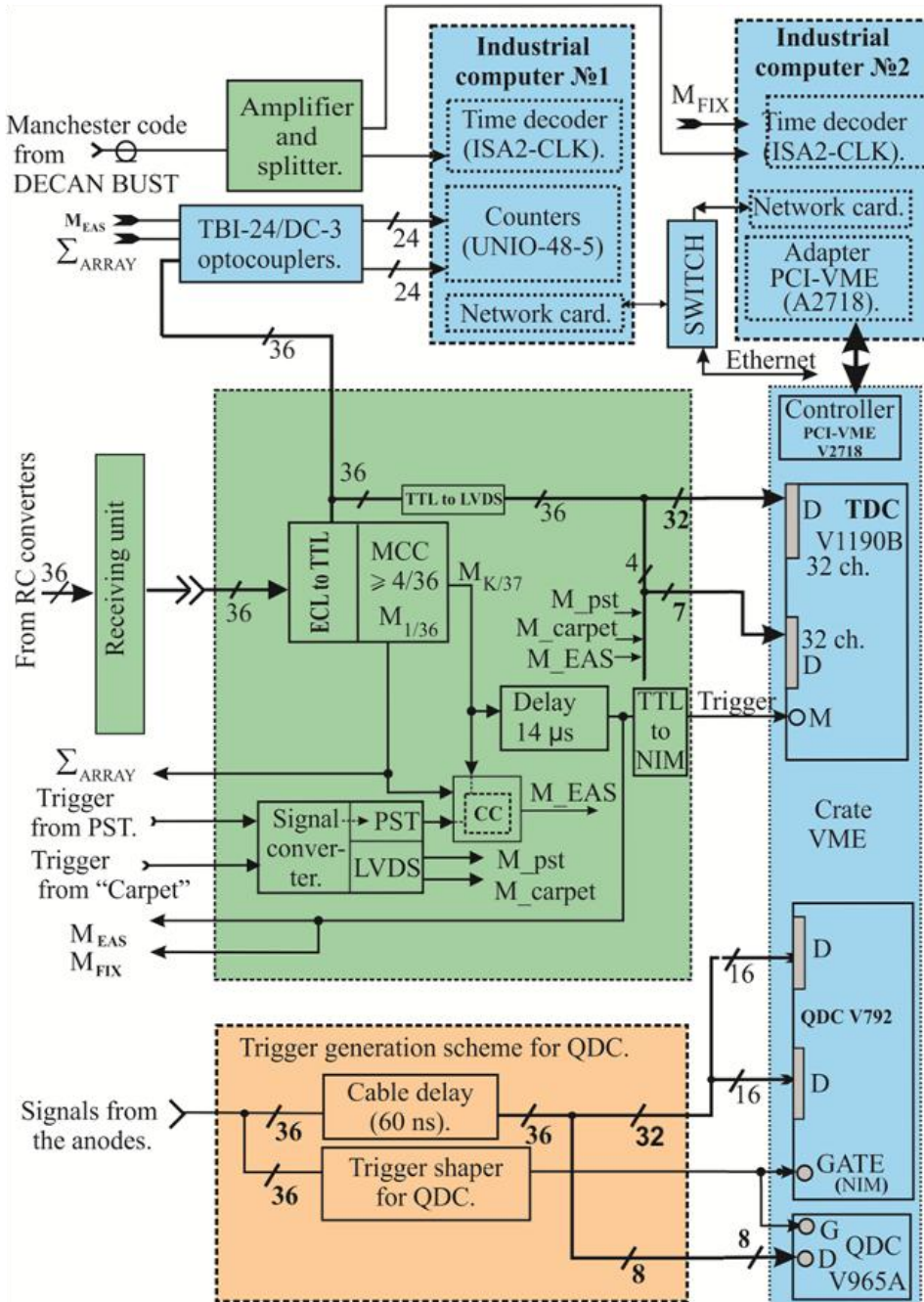
Fig4*. Block diagram of the "Andyrchy" EAS array.*

5. Software, data storage and transmission

The structure of on-line programs of BUST, "Carpet-2" and "Andyrchy" EAS array have the following architecture: at the beginning the equipment is initialized, then several data reading streams from devices and several information processing flows are formed. DAQ systems transfer the collected information to the file-server. Two dedicated workstations process the received information (Fig.5). First, the EAS direction is calculated in the local coordinate system, then in the astronomical one. Then the search for spatiotemporal concentrations (clusters) of showers recorded by the Underground Telescope or EAS array is performed. Search results are written to files on a dedicated server. A dedicated server sends information to the mailing list and provides access via HHTP and FTP. Currently, three event search algorithms are performed during the processing of information: the search for neutrino events in the BUST, the search for event clusters on the BUST, and the search for clusters of showers at the "Carpet-2" EAS array.

The main problem in searching of clusters from astrophysical object is their separation from background ones. For the problem of finding clusters, a method of the separating of events [7] was developed. The method has high reliability of separating events from the background according on the multiplicity of cluster events and time interval of cluster.
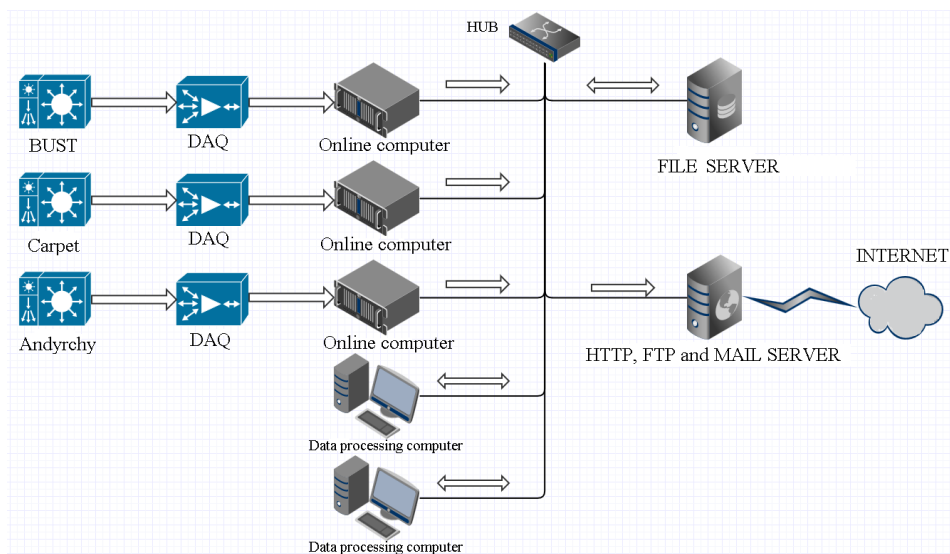
Fig5. Network diagram.

6. Conclusion

At present the fundamental modernization of data acquisition systems of experimental facilities of Baksan Neutrino Observatory is performed. This modernization will make it possible to produce the low-latency alerts from experimental facilities of BNO to the great number of various experimental facilities, including global nets of optical robotic telescopes.

References

[1] E. N. Alekseyev, et al. (BUST Collab.), "Baksan underground scintillation telescope" in Proceedings of the 16th International Cosmic Ray Conference, Kyoto, 1979, Vol. 10, p. 276.

[2]   E. N. Alekseyev, et al. (BUST Collab.), "The Baksan underground scintillation telescope," Phys. Part. Nucl.29, 254 (1998).

[3] V. B. Petkov, et al. "Andyrchy facility for detection of cosmic rays," Instrum. Exp. Tech. 49,785 (2006).

[4] D. D. Dzhappuev, et al. "Modernization of the Carpet-2 array of the Baksan NeutrinoObservatory," Bull. Russ. Acad. Sci.: Phys. 71, 525(2007).

[5] D. D. Dzhappuev, et al. "The Carpet-3 experiment to search for diffuse gamma rays with energies of more than 100 TeV," Bull. Russ. Acad. Sci.:Phys. 81, 424 (2017).

[6] CAEN. http://www.caen.it.

[7] I. M. Dzaparova, et al. "Quick search for optical partners of bursts of very high energy gamma-ray radiation". These Proceedings.

Gamma-ray Burst Optical Afterglow

Long Li[1], Lang Xie[1], Jie-Wan Yang[1], Jing Li[1], Xiang-Gao Wang[1,*], En-Wei Liang[1], WeiKang Zheng[2]

[1]Guangxi Key Laboratory for Relativistic Astrophysics, Department of Physics,

Guangxi University, Nanning 530004, China; wangxg@gxu.edu.cn

[2]Department of Astronomy, University of California, Berkeley, CA 94720-3411, USA

Abstract Regardless of the progenitor and central engine, the gamma-ray burst (GRB) afterglows are produced by the synchrotron emission external forward shock. *Swift* and the ground-based telescopes provide a rich early afterglow data which revealed many unexpected and interesting features. Based on the statistics of a large GRB sample, this paper gives a brief introduction of the GRB optical afterglow, including observations, emission components and the afterglow puzzle "achromatic or chromatic?". The afterglows provide a very important window between the afterglows and prompt emission to reveal the veil of the progenitor, central engine, ejecta composition and radiation mechanism. GRB 140323A is a good case interpreted with circumburst medium transition from a stellar wind to a homogenous density medium in the external shock model. GRB 140419A and 150910A are good cases for a magnetar spin down to a stable neutron star and the collapse in black hole, respectively.

Keywords: Gamma-Rays Bursts: General, Methods: Statistical, Radiation Mechanisms: Non-Thermal

1. Introduction

Gamma-ray bursts (GRBs) are the most luminous phenomena observed in the Universe, with an isotropic γ-ray energy up to $E_{\gamma, iso} \sim 10^{55}$erg [1], and they are still mysteries after 46 years since they were first discovered by Vela Satellites [2]. Based on the observations, e.g., long GRBs associated with supernovae and the short GRB can be detected associated with the gravitational waves (GW170817/GRB 170817A), they have been proposed to originate from a super-massive black hole or a rapidly spinning magnetized neutron star during core collapses of massive stars or mergers of binary compact objects. (e.g., [3-10]).

Regardless of the progenitor and central engine, a relativistic jet is launched, which is decelerated by a circumburst medium by a pair of external (forward and reverse) shocks. The reverse shock is likely short-lived. The forward shock continues to plow into the medium as the jet is decelerated. The synchrotron radiation of electrons accelerated from the external forward shock powers the broadband electromagnetic radiation, during the interaction between the fireball ejecta and the circumburst medium, and produce the broadband afterglow of GRBs [11-16]. Since *Swift* satellite launched [17], abundant and complicated properties can be discovered by scientist. The afterglows provide a very important window between the afterglow and prompt emission to reveal the veil of the progenitor, central engine, ejecta composition and radiation mechanism.

This paper gives a brief introduction of the GRB optical afterglow, including the

observations, emission components in Section 2; the talk about the afterglow puzzle "achromatic or chromatic?" is in Section 3; a recent result of our observation will be shown in Section 4; and then we give a summary in Section 5.

2. Observations

Broadband GRB afterglows were predicted before their discoveries [4], [11], [18]. Shortly after the paper of predictions for the broad-band afterglow based on the external shock model can be seen in the publication by Mészáros and Rees on Feb. 10, 1997 [11], 18 days later, (Feb. 28, 1997), the first X-ray and optical afterglows were discovered for GRB 970228 [19], [20]. 69 days later, the first radio afterglow was discovered for GRB 970508 [21]. Afterglow observations are routinely carried out nowadays.

The GRB optical afterglow observations are relied on the ground-based telescopes. In the pre-*Swift* era [22], observations usually started several hours after the burst trigger. Thanks to rapid *Swift*'s trigger and the rapid ground notification to alert large follow-up telescope network (GCN), we obtain a lot of optical data. Figure 1 shows the GRB optical afterglow apparent magnitude distributions [23]. We can observe the optical just after several seconds later, e.g. GRB 08319B, 080413A and 130427A.For some GRBs the optical prompt emission also can be discovered, e.g. GRB 990123, 041219, 050401, 050820A, 061121, 080913B. This opened a new window to the study of GRBs. The launch of the high-energy mission *Fermi* and other programs, e.g., MAGIC [24], Konus-Wind [25], Insight-HXMT [26], Suzaku [27], has led to discovery of an extended GeV afterglow emission for many bright GRBs, e.g. 090902B, 130427A and 190114C.
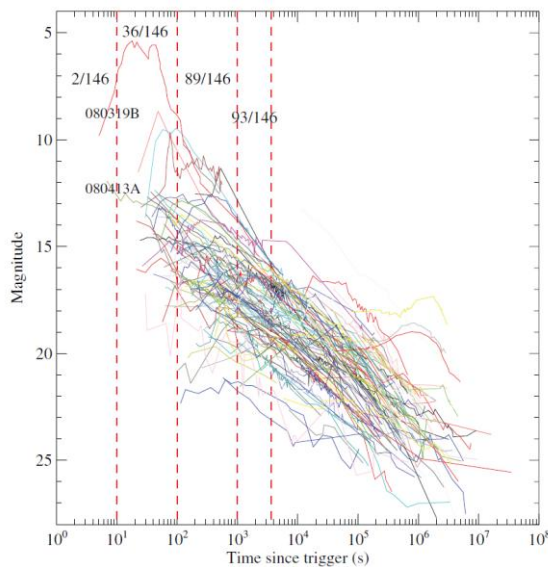
Fig1. *GRB optical afterglow apparent magnitude distributions [wang 2013]*

One can see that the individual X-ray/optical light curves differ significantly. Reference [28] after synthesizing the *Swift*/XRT light curves, summarizes the observational properties of the X-ray afterglow emission as five-component canonical X-ray light curve [28] (as shown in

the left panel of Figure 2）:

- I. Steep decay phase, which is the tail of prompt emission;
- II. Shallow decay phase (or plateau), which is incorporated within the external shock, and need continuous energy injection into the blast wave [28-30];
- III. Normal decay phase, which is the typical decay expected in the standard forward shock afterglow model;
- IV. Late steepening phase, which is the jet break expected in the standard forward shock afterglow model;
- V. X-ray fares, which are related to late central engine activities.

Similarly, the synthetic optical light curve includes eight components, which have distinct physical origins.

The joint light curve of optical and X-ray afterglows also can be delineated as a canonical light curve, which generally includes 8 emission components [31]. These components are as follows.

- Ia. Prompt & late optical flares, which is related the prompt emission;
- Ib. Reversed shock emission, which is an early optical flare from the reverse shock in the standard forward shock afterglow model, observing only in few cases;
- II. Shallow decay:, which need energy injection from center engine;
- III. Standard afterglow component with an onset hump followed by a normal decay segment, which is the typical decay expected in the standard forward shock afterglow model;
- IV. Post-jet-break phase, which is the jet break expected in the standard forward shock afterglow model;
- V: Optical flares, which is related the prompt emission;
- VI: Rebrightening humps, which is similar to the early afterglow onset hump but occurs much later;
- VII. Late supernova (SN) bumps.

Components II–V in the optical light curves can find their counterparts in X-ray. It should be notified that not all GRBs show all these components.
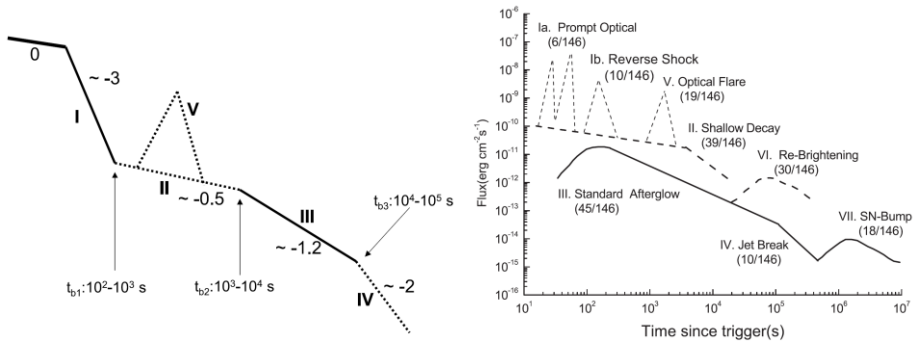
Fig2. Left: Synthetic Cartoon X-ray Light Curve Based on the Observational Data from the Swift XRT; Right: Synthetic Cartoon Optical Light Curve Based on the Observational Data from the Ground Based Telescopes.

3. Achromatic or Chromatic?

According to such an interpretation that the afterglow comes from the external shock, there are two types of temporal breaks. The first one is related to a characteristic frequency in the observational band [13], e.g. spectral breaks occur at different epochs in different energy bands (called chromatic). The second one is related to the hydrodynamic or geometric properties of the system, temporal breaks in different energy bands (e.g., X-ray and optical bands) should occur around the same observational time (called achromatic). The observations show that there are no spectral changes across the break time [32-33], and the theoretical simulations also show spectral beaks are very smooth and barely observable [34]. However, some authors based on the statistical data shows that most GRB afterglows are chromatic. Is the multiband afterglow achromatic or chromatic? Actually, the answer is related to the open question: how bad or how good are the external forward shock models in interpreting the GRB afterglow data?

Trying to answer this question, reference [35] systematically investigated all *Swift* GRBs that have X-ray and optical afterglow data, including 900 X-ray light curves from the *Swift* XRT data archive and 260 optical light curves from published papers or GCN Circulars. Based on the rich afterglow data, and using the closure relation predicted by the external shock model, at least ~53% of GRBs can be interpreted within the external shock models. Up to ~96% of GRBs may be accounted for external shock models, which need a more advanced modeling invoked, e.g., long-lasting reverse shock, structured jets, arbitrary circumburst medium density profile. Only less than 4% GRBs with direct evidence of chromatic behaviors, can be classified as truly violate external shock models.

4. Recently interesting observations

As is known, the afterglow not only can present the properties of the external shock, but also provide a very important window to constrain the physics of progenitor, central engine, ejecta composition and radiation mechanism. Ground-based optical telescopes continue to observe the GRB afterglow, e.g., KAIT [36], GWAC-F60, TNT [37], SAO-RAS [38], ISON-NM [39], NOT [40], GROND [41], BOOTES [42], MONDY [43], MASTER [44]. Here we list the GRB 140423A, 140419A and 150910A as an example.

The optical observation shows that GRB 140423A have an onset bumps in the early epoch [45], then show steeper $(\alpha_1 \sim -1.6)$ to flatter decay $(\alpha_2 \sim -1.1)$ with a break at ~5000 s. It can be well interpreted with the standard external shock model by considering the circumburst medium which transited from a stellar wind having a density distribution $\rho(r) \propto r^{-2}$ to a homogenous density medium.

The GRBs central engines could be a black hole with accretion disk systems or a millisecond magnetar. When a millisecond magnetar as central engine for a long GRB, they can produce an internal plateau as it spins down in the afterglow light curves. If the post plateau the temporal decay index is steeper than -3, it may indicate that the magnetar collapses into a black hole. If the mass of the magnetar is not so massive, it may spin down to a stable neutron star, and post plateau decay index between -2 and -3. GRB 140419A [46] and 150910A [47] are good cases for a magnetar spin down to stable neutron star and collapse in black hole, respectively. For GRB 140419A, we obtain the magnetar parameters with magnetic field of the magnetar B_p, the spin period of the magnetar P_0, and the radiative efficiency of prompt emission η is $\sim 10^{15}$ G, ~ 0.96 ms, and $\sim 2.2\%$, respectively. However, the radiative

efficiency of internal plateau η_X is larger than 18.1%. For GRB 150910A, the deriving of physical parameters of the putative magnetar is $P_0 \sim (0.96 \sim 1.52)$ ms and Bp $\sim (0.41 \sim 1.03) \times 10^{15}$ G, respectively.

5. Summarizes

The scientist have learn a lot of the GRB in the past a half century. However, there are still a lot things we need to understand more, e.g. progenitor, central engine, ejecta composition and radiation mechanism, and will push the observation forwards. The GRBs occur randomly in space at unknown time. We not only need the larger space mission to detect the high energy emission in the future, e.g., SVOM [48], ATHENA [49], HESEUS [50], eXTP [51], ET [52], TAP [53] and ISS-TAO. We also need large survey ground-based optical telescopes with deeper detection ability, to discover or follow the GRB-like transients. We believe the next decade will be an exciting era of GRB study.

Acknowledgements

References

[1] Kumar, P. , & Zhang, B. . (2015). The physics of gamma-ray bursts & relativistic jets. Physics Reports, 561, 1-109.

[2] Klebesadel, R. W., Strong, I. B., & Olson, R. A. (2004). Observations of gamma-ray bursts of cosmic origin. Astrophysical Journal, 182(182), L85.

[3] S.E. Woosley, Gamma-ray bursts from stellar mass accretion disks around black holes, ApJ 405 (1993) 273–277.

[4] B. Paczýnski, J.E. Rhoads, Radio transients from gamma-ray bursters, ApJ 418 (1993) L5.

[5] S.E. Woosley, J.S. Bloom, The supernova gamma-ray burst connection, Ann. Rev. Astron. Astrophys. 44 (2006) 507–556.

[6] N. Gehrels, C.L. Sarazin, P.T. O'Brien, B. Zhang, L. Barbier, S.D. Barthelmy, A. Blustin, D.N. Burrows, J. Cannizzo,A.A. Wells, N.E. White, R.A.M.J. Wijers, A short γ -ray burst apparently associated with an elliptical galaxy at redshift z = 0.225, Nature 437 (2005) 851–854.

[7] Berger, & Edo. (2014). Short-duration gamma-ray bursts. Annual Review of Astronomy and Astrophysics, 52(1), 43-105.

[8] Zhang, B. , Fan, Y. , Dyks, J. , Kobayashi, S. , Meszaros, P. , & Burrows, D. , et al. (2006). Physical processes shaping gamma-ray burst x-ray afterglow light curves: theoretical implications from the swift x-ray telescope observations. Astrophysical Journal, 642(1), 354-370.

[9] B. Zhang, Gamma-Ray bursts in the swift era, Chin. J. Astron. Astrophys. 7 (2007) 1–50.

[10] B. Zhang, B. Zhang, F.J. Virgili, E. Liang, D.A. Kann, X. Wu, D. Proga, H. Lv, K. Toma, P. Mészáros, D.N. Burrows, P.W.A. Roming, N. Gehrels, Discerning the Physical Origins of

Cosmological Gamma-ray Bursts Based on Multiple Observational Criteria: The Cases of z = 6.7 GRB 080913, z = 8.2 GRB 090423, and Some Short/Hard GRBs, ApJ 703 (2009) 1696–1724.

[11] P. Mészáros, M.J. Rees, Optical and Long-Wavelength Afterglow from Gamma-Ray Bursts, ApJ 476 (1997) 232

[12] P. Mészáros, M.J. Rees, R.A.M.J. Wijers, Viewing Angle and Environment Effects in Gamma-Ray Bursts: Sources of Afterglow Diversity, ApJ 499 (1998).

[13] R. Sari, T. Piran, R. Narayan, Spectra and light curves of gamma-ray burst afterglows, ApJ 497 (1998) L17.

[14] Sari, R., & Piran, T. (1999). Predictions for the very early afterglow and the optical flash. Astrophysical Journal, 520(2), 641-649.

[15] J.E. Rhoads, The Dynamics and Light Curves of Beamed Gamma-Ray Burst Afterglows, ApJ 525 (1999) 737﹣749.

[16] R.A. Chevalier, Z.-Y. Li, Wind interaction models for gamma-ray burst afterglows: The case for two types of progenitors, ApJ 536 (2000) 195–212.

[17] Gehrels, N. (2004). The swift gamma-ray burst mission. Astrophysical Journal, 611(2), 1309.

[18] Katz, J. I. . (1994). Two populations and models of gamma ray bursts. The Astrophysical Journal, 422(1).

[19] Costa, E., Frontera, F., Heise, J., Feroci, M., Zand, J. I. '., & Fiore, F., et al. (1997). Discovery of an x-ray afterglow associated with the |[gamma]|-ray burst of 28 february 1997. Nature, 387(6635), 783.

[20] J. van Paradijs, P.J. Groot, T. Galama, C. Kouveliotou, R.G. Strom, J. Telting, R.G.M. Rutten, G.J. Fishman, C.A. Meegan, M. Pettini, N. Tanvir, J. Bloom, H. Pedersen, H.U. Nørdgaard-Nielsen, M. Linden-Vørnle, J. Melnick, G. van der Steene, M. Bremer, R. Naber, J. Heise, J. in'tZand, E. Costa, M. Feroci, L.Piro, F. Frontera, G. Zavattini, L. Nicastro, E. Palazzi, K. Bennet, L. Hanlon, A. Parmar, Transient optical emission from the error box of the γ -ray burst of 28 February 1997, Nature 386 (1997) 686–689.

[21] D.A. Frail, S.R. Kulkarni, L. Nicastro, M. Feroci, G.B. Taylor, The radio afterglow from the γ -ray burst of 8 May 1997, Nature 389 (1997) 261–263.

[22] Gehrels, N. (2004). The swift gamma-ray burst mission. Astrophysical Journal, 611(2), 1309.

[23] Wang, X. G., Liang, E. W., Li, L., Lu, R. J., Wei, J. Y., & Zhang, B. (2013). A comprehensive study of gamma-ray burst optical emission: iii. brightness distributions and luminosity functions of optical afterglows. Astrophysical Journal, 774(2), 1201-1205.

[24] Galante, N., Bastieri, D., Gaug, M., Garczarczyk, M., Longo, F., & Scapin, V., et al. (2008). MAGIC Observation of the Prompt and Afterglow Emission from GRBs.

[25] Aptekar, R. L., Frederiks, D. D., Golenetskii, S. V., Ilynskii, V. N., Mazets, E. P., & Panov, V. N., et al. (1995). Konus-w gamma-ray burst experiment for the ggs wind spacecraft. Space Science Reviews, 71(1-4), 265-272.

[26] Li, T. P., & Li, T. P. (2007). Hxmt: a chinese high-energy astrophysics mission. Nuclear Physics B, 166, 131-139.

[27] Koyama, K., Tsunemi, H., Dotani, T., Bautz, M. W., Hayashida, K., & Tsuru, T. G., et al. (2007). X-ray imaging spectrometer (xis) on board suzaku. Publications of the Astronomical Society of

Japan, 59(sp1), 23-33.

[28] Zhang, B. , Fan, Y. , Dyks, J. , Kobayashi, S. , Meszaros, P. , & Burrows, D. , et al. (2006). Physical processes shaping gamma-ray burst x-ray afterglow light curves: theoretical implications from the swift x-ray telescope observations. Astrophysical Journal, 642(1), 354-370.

[29] J.A. Nousek, C. Kouveliotou, D. Grupe, K.L. Page, J. Granot, E. Ramirez-Ruiz, S.K. Patel, D.N. Burrows, V. Mangano, S. Barthelmy, A.P. Beardmore, S.Campana, M. Capalbi, G. Chincarini, G. Cusumano, A.D. Falcone, N. Gehrels, P. Giommi, M.R. Goad, O. Godet, C.P. Hurkett, J.A. Kennea, A. Moretti, P.T. O'Brien, J.P. Osborne, P. Romano, G. Tagliaferri, A.A. Wells, Evidence for a Canonical Gamma-Ray Burst Afterglow Light Curve in the Swift XRT Data,ApJ 642 (2006) 389–400.

[30] Panaitescu, A. (2006). Phases of swift x-ray afterglows. IL Nuovo Cimento B, 483(2), L87-L90.

[31] Liang, L., Liang, E. W., He, G., & Bing, Z. (2012). Optical afterglows as probes for the central engine and fireball of gamma-ray bursts†. Proceedings of the International Astronomical Union, 8(S290), 263-264.

[32] E.-W. Liang, B.-B. Zhang, B. Zhang, A Comprehensive Analysis of Swift XRT Data. II. Diverse Physical Origins of the Shallow Decay Segment, ApJ 670(2007) 565–583.

[33] E.-W. Liang, J.L. Racusin, B. Zhang, B.-B. Zhang, D.N. Burrows, A Comprehensive Analysis of Swift XRT Data. III. Jet Break Candidates in X-Ray and Optical Afterglow Light Curves, ApJ 675 (2008) 528–552.

[34] Z.L. Uhm, B. Zhang, Fast-cooling synchrotron radiation in a decaying magnetic field and γ -ray burst emission mechanism, Nat. Phys. 10 (2014) 351–356.

[35] Wang, X-G, Zhang, B., Liang, E, -W., et al. (2015). How Bad/Good Are the External Forward Shock Afterglow Models of Gamma-Ray Bursts?. The Astrophysical Journal Supplement Series, 774(2), 1201-1205..

[36] Filippenko, A. V. , Li, W. D. , Treffers, R. R. , & Modjaz, M. . (2016). The lick observatory supernova search with the katzman automatic imaging telescope.

[37] Zheng, W. , Deng, J. , Zhai, M. , Xin, L. , Qiu, Y. , & Lu, X. , et al. (2008). A grb follow-up system at the xinglong observatory and detection of the high-redshift grb 060927 ⋆. 中国天文和天体物理学报（英文版）, 8(6), 693-699.

[38] Afanasiev, V. L., Dodonov, S. N., & Moiseev, A. V. (2001). Kinematics of Circumnuclear Regions of Galaxies: 2D Spectroscopy on SAO RAS 6m Telescope. Stellar Dynamics: from Classic to Modern.

[39] Elenin, L. , Savanevych, V. , & Bryukhovetskiy, A. . (2012). Minor planet observations [h15 ison-nm observatory, mayhill]. Minor Planet Circulars, 75285.

[40] Djupvik, A. A., & Andersen, J. (2009). The Nordic Optical Telescope. Highlights of Spanish Astrophysics V.

[41] Sudilovsky, V. , Kann, D. A. , & Greiner, J. . (2013). Grb 130925a: grond afterglow candidate. Grb Coordinates Network, 15247.

[42] Castrotirado, A. J., Soldán, J., Bernas, M., Páta, P., Rezek, T., & Hudec, R., et al. (1999). The burst observer and optical transient exploring system (bootes). Astronomy & Astrophysics Supplement, 138(3).

[43] Klunko, E., Volnova, A., & Pozanenko, A. (2009). Grb 090618: mondy optical observations. Grb

Coordinates Network, 9613.

[44] Lipunov, V. M. , Gorbovskoy, E. , Kornilov, V. G. , Tyurina, N. , Balanutsa, P. , & Kuznetsov, A. , et al. (2017). Master optical detection of the first ligo/virgo neutron stars merging gw170817. Astrophysical Journal Letters, 850(1).

[45] WeiKang Zheng et al., 2014, GRB Coordinates Network, Circular Service, No. 16156, #1 (2014), 16156

[46] WeiKang Zheng et al., 2014, GRB Coordinates Network, Circular Service, No. 16119, #1 (2014), 16119

[47] WeiKang Zheng et al., 2014, GRB Coordinates Network, Circular Service, No. 18265, #1 (2014), 18265

[48] Wei, J., Cordier, B., Antier, S., Antilogus, P., Atteia, J. -L., & Bajat, A., et al. (2016). The deep and transient universe in the svom era: new challenges and opportunities - scientific prospects of the svom mission.

[49] Nandra, K., Barret, D., Barcons, X., Fabian, A., Herder, J. W. D., & Piro, L., et al. (2013). The hot and energetic universe: a white paper presenting the science theme motivating the athena+ mission. Eprint Arxiv, 1306.

[50] Amati, L., O'Brien, P., Götz, D., Bozzo, E., Tenzer, C., & Frontera, F., et al. (2018). The theseus space mission concept: science case, design and expected performances. Advances in Space Research, 62(1), 99051L.

[51] Zhang, B. (2016). Mergers of charged black holes: gravitational wave events, short gamma-ray bursts, and fast radio bursts. Astrophysical Journal, 827(2).

[52] Hild, S., Chelkowski, S., & Freise, A. (2008). Pushing towards the ET sensitivity using 'conventional' technology. arXiv:0810.0604

[53] Camp, J.(2018), Transient Astrophysics Probe, American Astronomical Society, HEAD meeting #16, id.103.22

Problems with the dark matter and dark energy hypotheses, and alternative ideas[e]

Martín López-Corredoira[1,2]

[1]*Instituto de Astrofísica de Canarias, C/.Vía Láctea, s/n, E-38205 La Laguna (Tenerife), Spain; martinlc@iac.es*
[2]*Department of Astrophysics, University of La Laguna, E-38206 La Laguna (Tenerife), Spain*

Abstract   Two exotic elements have been introduced into the standard cosmological model: non-baryonic dark matter and dark energy. The success in converting a hypothesis into a solid theory depends strongly on whether we are able to solve the problems in explaining observations with these dark elements and whether the solutions of these problems are unique within the standard paradigm without recourse to alternative scenarios. We have not achieved that success yet because of numerous inconsistencies, mainly on galactic scales, the non-detection so far of candidate particles for dark matter, and the existence of many alternative hypotheses that might substitute the standard picture to explain the cosmological observations. A review of some ideas and facts is given here.

Keywords: Dark Matter, Dark Energy

1. History of the idea of Dark Matter

The existence of dark or invisible matter detectable through its gravitational influence has been known by astronomers for a long time now [14]. Bessel [15] in 1844 argued that the observed proper motions of the stars Sirius and Procyon could be explained only in terms of the presence of faint companion stars. In 1846, Le Verrier and Adams independently predicted the existence of Neptune based on calculations of the anomalous motions of Uranus. Le Verrier later proposed the existence of the planet Vulcan to explain anomalies in the orbit of Mercury, but he failed this time because the solution was not invisible matter but a change of gravitational laws, as was solved years later by Einstein with General Relativity. The dynamical analysis of dark matter in form of faint stars in the Milky Way using the motion of stars was carried out by Lord Kelvin in 1904, Poincaré in 1906, Öpik in 1915, Kapteyn in 1922, Jeans in 1922, Lindblad in 1926, and Oort in 1932 with different results [14].

With regard to extragalactic astronomy, Zwicky's [100] 1933 paper on dark matter in rich clusters applied the virial theorem to these data and found a mass-to-light ratio of ~60 in solar units (rescaled to the present-day value of the Hubble constant). In 1959 Kahn & Woltjer [39] determined the mass of the Local Group and obtained a mass-to-light ratio of 43 in solar units. In the 1950s, Page [71, 72] also found that pairs of elliptical galaxies had a mass-to-light ratio

of 66 in solar units. This showed that such binaries must have massive envelopes or be embedded in a massive common envelope. Similar results were obtained in the 1950s from 26 binary galaxies by Holmberg [36]. In 1939 Babcock [5] first showed the need for dark matter for an individual galaxy by measuring the rotation curve of the outer regions of M31 out to 100 arcminutes ($\approx$ 20 kpc) from its center. However, the majority of astronomers did not become convinced of the need for dark matter halos in galaxies until the publication of theoretical papers in the 1970s, such as the one on the stability of galactic disks by Ostriker & Peebles [69]. Later, rotation curves in the radio by Albert Bosma [18] and in the visible by Vera Rubin, Kent Ford, and Nortbert Thonnard [79] easily convinced the community. This shows the typical mentality of astrophysicists: accepting facts only when there is a theory to support them with an explanation, a not-so-empirical approach that dominates the development of cosmology.

Cosmology has indeed played a very important role in the idea of dark matter on galactic scales. The first predictions based on Cosmic Microwave Backgro und Radiation (CMBR) anisotropies were wrong. It was predicted in the 1960s that $\Delta T/T$ should be one part in a hundred or a thousand [80]; however, fluctuations with this amplitude could not be found from observations in the 1970s. In order to solve this problem, non-baryonic dark matter was introduced *ad hoc* and was thought to be composed of certain mysterious particles different from known matter. In a short time, the connection between particle physics and the missing mass problem in galaxies arose. Many astrophysicists considered dark matter halos surrounding galaxies and galaxy clusters possibly to consist of a gas of non-baryonic particles rather than faint stars or other astrophysical objects. This was a happy idea without any proof; there is no proof that directly connects the problem of the amplitude of CMBR anisotropies with the rotation curves of galaxies or the missing mass in clusters, but the idea was pushed by leading cosmologists, who made the idea fashionable among the rest of the astrophysical community.

Part of the success of these non-baryonic dark matter scenarios in the halos of the galaxies was due to the good agreement of simulations of large scale structure with the observed distributions of galaxies. At first, in the 1980s, with the attempt to fit the data using hot dark matter composed of neutrinos, the simulations showed that very large structures should be formed first and only later go on to form galaxy-sized halos through fragmentation, which did not match the observations [99], whereas cold dark matter (CDM) models were more successful, at least on large scales (> 1 Mpc).

This tendency towards selling a prediction of failure as a success for a model via the *ad hoc* introduction of some convenient form of unknown dark matter still prevails. An instance of this predilection is the introduction in 2018 of some peculiar form of dark matter [8] in order to cool the gas at z $\approx$ 18 and solving the discrepancies in the measurements of 21 cm line amplitude with respect to the *a priori* predictions [19].

2. Dark matter and inconsistencies of the theory at galactic scales

That there is some dark matter, either baryonic or non-baryonic, is clear, but how much, and what is its nature? The success of the standard model in converting a hypothesis into a solid theory depends strongly on the answer to these open questions. Stellar and cold gas in galaxies sum to baryonic matter content that is 8^{+4}_{-5}% of the total amount of the predicted Big Bang baryonic matter [10]. Where is the rest of the baryonic material? What is the nature of the putative non-baryonic dark matter required to achieve the current value of $\Omega_m \approx 0.3$?

Current CDM models predict the existence of dark matter haloes for each galaxy whose density profile falls approximately as r^{-2}, although the original idea [98] concerning hierarchical structures with CDM, which gave birth to the present models, was that the dark matter was distributed without internal substructure, more like a halo with galaxies than galaxies with a halo [9], something similar to the scenario in [51, 52].

Some authors have been led to question the very existence of this dark matter on galactic scales since its evidence is weak [9, 59, 29, 90] and the predictions do not fit the observations: CDM has a "small scale crisis" since there are some features of the galaxies that are very different from the predictions of the cosmological model. Nonetheless, many researchers are eagerly trying to find solutions that make data and model compatible, assuming a priori that the model "must be" correct. Some of the problems are the following.

There is a problem with an observed lower density of the halo in the inner galaxy than predicted. ΛCDM (CDM including a Λ term for the cosmological constant; see §5) predicts halo mass profiles with cuspy cores and low outer density, while lensing and dynamical observations indicate a central core of constant density and a flattish high dark mass density outer profile [74]. The possible solutions of core-cusp problem without abandoning the standard model are: bar-halo friction, which reduces the density of the halo in the inner galaxy [85]; haloes around galaxies may have undergone a compression by the stellar disc [33] or/and suffered from the effects of baryonic physics [23].

Another problem is that the predicted angular momentum is much less than the observed one. Binney et al. [16] claim that the problem of an excess of predicted dark matter within the optical bodies and the fact that the observed discs are much larger than expected can be solved if a considerable mass of low angular momentum baryons is ejected (massive galactic outflows) and the discs are formed later from the high angular momentum baryons which fell in the galaxy. The conspiracy problem is also solved if the ejection begins only once $M_{baryons}(r)$ ~ $M_{dark\ matter}(r)$. Another solution within the standard cosmological model for the angular momentum problem is the tidal interaction of objects populating the primordial voids together with the Coriolis force due to void rotation [21].

Another fact that could cast doubt upon the existence of very massive halos of dark matter is that strong bars rotating in dense halos should generally slow down as they lose angular momentum to the halo through dynamical friction [22], whereas the observed pattern speed of galactic bars indicates that almost all of them rotate quite fast [1]. There should be a net transference of angular momentum from bars to halos, although friction can be avoided under some special conditions [86].

The enclosed dynamical mass-to-light ratio increases with decreasing galaxy luminosity and surface brightness, which is not predicted by dark matter scenarios [60].

Galaxies dominate the halo with little substructure whereas the model predicts that galaxies should be scaled versions of galaxy clusters with abundant substructure [25, 43]. Moreover, ΛCDM simulations predict that the majority of the most massive subhalos of the Milky Way are too dense to host any of its bright satellites ($L_V > 105\ L_\odot$) [20]. Also, the distribution of satellites is in a plane, incompatible with ΛCDM [43, 42, 73]. Kroupa [44] says that these are arguments against the standard model in which one cannot make the typical rebuff of incompleteness of knowledge of baryonic physics. Furthermore, there is a correlation between bulge mass and the number of luminous satellites in tidal streams [43, 55] that is not predicted by the standard model, and it is predicted by models of modified gravity without dark matter. The disc of satellites and bulge-satellite correlation suggest that dissipative events forming bulges are related to the processes forming phase-space correlated satellite populations. These events are well known to occur, since in galaxy encounters energy and angular momentum are

expelled in the form of tidal tails, which can fragment to form populations of tidal-dwarf galaxies and associated star clusters. If Local Group satellite galaxies are to be interpreted as Tidal Dwarf galaxies then the substructure predictions of the standard cosmological model are internally in conflict [43].

Perhaps, that most severe caveat to retain the hypothesis of dark matter is that, after a long time looking for it, it has not yet been found, although non-discovery does not mean that it does not exist. Microlensing surveys [45, 92] constrain the mass of the halo in our Galaxy in the form of dim stars and brown dwarfs to be much less than that necessary for dark matter halos. In any case, as already mentioned, the primordial nucleosynthesis model constrains baryonic matter to be around 10% of the total mass [10], so these objects could not be compatible with the preferred cosmological model. Some observations are inconsistent with the dominant dark matter component being dissipationless [67]. Neither massive black hole halos [66] nor intermediate-mass primordial black holes [61] provide a consistent scenario. The nature of dark matter has been investigated and there are no suitable candidates among astrophysical objects.

3. Dark matter particles

The other possibility is that dark matter is not concentrated in any kind of astrophysical object but in a gas of exotic non-baryonic particles. There are three possible types of candidates [14]: 1) particles predicted by the supersymmetry hypothesis, which are electrically neutral and not strongly interacting, including superpartners of neutrinos, photons, Z bosons, Higgs bosons, gravitons, and others (neutralinos have been the most recently studied candidates in the last decades); 2) axions, typically with masses between 10^{-6} and 10^{-4} eV, predicted to resolve certain problems in quantum chromodynamics; and 3) Weakly Interacting Massive Particles (WIMPs), which are those particles that interact through the weak force.

The latest attempts to search for exotic particles have also finished without success. Technologies used to directly detect a dark matter particle have failed to obtain any positive result [57, 49]. Attempts have also been made to detect neutralinos with the MAGIC and HESS Cerenkov telescope systems for very high energy gamma rays through their Cherenkov radiation, but so far without success and only emission associated with the Galaxy has been found [3]. Dwarf galaxies are expected to have high ratios of dark matter and low gamma ray emission due to other astrophysical processes so the search is focused on these galaxies, but without positive results. As usual, the scientists involved in these projects attribute their failure of detection to the inability of the detectors to reach the necessary lower cross section of the interaction, or to the possibility that they may be 3–4 orders of magnitude below the possible flux of gamma rays emitted by dark matter [83], and ask for more funding to continue to feed their illusions: a never-ending story. As pointed out by David Merritt [63], this will never constitute a falsification of the CDM model because although success of detection will confirm the standard paradigm, non-detection is not used to discard it.

4. Scenarios without non-baryonic cold dark matter

Note also that some other dynamical problems in which dark matter has been claimed as necessary can indeed be solved without dark matter: galactic stability [93] or warp creation [52], for instance. Rotation curves in spiral galaxies can be explained without non-baryonic dark matter with magnetic fields [9], or modified gravity [81], or baryonic dark matter in the

outer disc [31] or non-circular orbits in the outer disc [13]. Velocities in galaxy pairs and satellites might also measure the mass of the intergalactic medium filling the space between the members of the pairs [51, 52] rather than the mass of dark haloes associated with the galaxies.

The most popular alternative to dark matter is the modification of gravity laws proposed in MOND (Modified Newtonian Dynamics; [82]), which modifies the Newtonian law for accelerations lower than 1×10^{-10} m/s^2. This was in principle a phenomenological approach. It was attempted to incorporate elements that make it compatible with more general gravitation theories. The AQUAdratic Lagrangian theory (AUQAL) [11] expanded MOND to preserve the conservation of momentum, angular momentum, and energy, and follow the weak equivalence principle. Later, a relativistic gravitation theory of MOND would be developed under the name Tensor-Vector-Scalar (TeVeS) [12], which also tried to provide consistency with certain cosmological observations, including gravitational lensing. However, the successes of MOND and its relativistic version are mostly limited to galactic scales and cannot compete with ΛCDM to explain the large-scale structure and other cosmological predictions. Moreover, a search was made for evidence of the MOND statement in a terrestrial laboratory: a sensitive torsion balance was employed to measure small accelerations due to gravity, and no deviations from the predictions of Newton's law were found down to 1×10^{-12} m/s^2 [48]. Therefore, unless these experiments are wrong, or we interpret the transition regime acceleration of 1×10^{-10} m/s^2 in terms of total absolute acceleration (including the acceleration of the Earth, Sun, etc.) rather than the relative one, MOND/TeVes is falsified by this experiment.

There are also proposals that the dark matter necessary to solve many problems may be baryonic: positively charged, baryonic (protons and helium nuclei) particles [26], which are massive and weakly interacting, but only when moving at relativistic velocities; simple composite systems that include nucleons but are still bound together by comparable electric and magnetic forces [58], making up a three-body system "tresinos" or four-body system "quatrinos"; antiparticles which have negative gravitational charge [35], etc.

In my opinion, the problem of 'dark matter' is not only one problem but many different problems within astrophysics that might have different solutions. The idea that the same non-baryonic dark matter necessary to explain the low anisotropies in the CMBR is going to solve the large-scale structure distribution, the lack of visible matter in clusters, the dispersion of velocities of their galaxies, the measurements of gravitational lensing, the rotation curves, etc., is a happy fantasy that has dominated astrophysics for the last 40 years. It would be wonderful if we also get a happy ending with the discovery of the particles of dark matter that constitute the dark halos of galaxies, but, in absence of that outcome, maybe it would be prudent to bet on a combination of different elements to explain the entire set of unexplained phenomena: possibly some baryonic dark matter in some cases, possibly a modification of gravity is part of the explanation for a wide set of events, and maybe cold dark matter dominates some phenomena and hot dark matter other phenomena. Certainly, a unified picture of a unique non-baryonic type of cold dark matter to explain everything would be a simpler and more elegant hypothesis; the question, however, is not one of simplicity but one of ascertaining how reality is, whether simple or complex.

5. Dark energy and the cosmological constant or quintessence

The question of the cosmological constant to maintain a static universe [70] was considered

Einstein's biggest blunder, and it was introduced by Lemaître [46] in his equations for the evolution of the expanding universe. Indeed, it is equivalent to positing an attractive gravitational acceleration $a(r) = -GM/r^2 + Br$, already proposed by Newton for B < 0, but with B > 0 instead [41]. It is not usual physics but an exotic suggestion, since the usual thermodynamics for fluids with positive heat capacity and positive compressibility is not applicable to dark energy with negative pressure [7].

Twenty-five years ago, most cosmologists did not favour the scenarios dominated by the cosmological constant [32]. In the eighties, the cosmological constant was many times disregarded as an unnecessary encumbrance, or its value was set at zero [50], and all the observations gave a null or almost null value. However, since other problems in cosmology have risen, many cosmologists at the beginning of the '90s realized that an Ω_Λ ranging from 0.70 to 0.80 could solve many problems in CDM cosmology [28]. Years later, evidence for such a value of the cosmological constant began to arrive. A brilliant prediction or a prejudice which conditions the actual measurements?

All present claims about the existence of dark energy have measured Ω_Λ through its dependence on the luminosity distance vs. redshift dependence [27]. In the mid-1990s the position of the first peak in the power spectrum of the CMBR was determined to be at $\ell \approx 200$. White et al. in 1996 [97] realized that the preferred standard model at that time (an open universe with $\Omega = \Omega_m \approx 0.2$ and without dark energy) did not fit the observations, so that they needed a larger Ω. Between 1997 and 2000 a change of mentality in standard cosmology occurred. This was one of the elements, together with Type Ia Supernovae (SN Ia) observations and the age problem of the universe, that would encourage cosmologists to include a new ad hoc element: dark energy.

One measurement of the cosmological constant comes nowadays from supernovae, whose fainter-than-expected luminosity in distant galaxies can be explained with the introduction of the cosmological constant. It was criticized as being due possibly to intergalactic dust [2, 34, 64]. The presence of grey dust is not necessarily inconsistent with the measure of a supernova at $z = 1.7$ (SN 1997ff) [34]. Dimming by dust along the line of sight, predominantly in the host galaxy of the SN explosion, is one of the main sources of systematic uncertainties [40]. Also, there was an underestimate of the effects of host galaxy extinction: a factor which may contribute to apparent faintness of high-z supernovae is the evolution of the host galaxy extinction with z [78]; therefore, with a consistent treatment of host galaxy extinction and the elimination of supernovae not observed before maximum, the evidence for a positive Λ is not very significant. Fitting the corrected luminosity distances (corrected for internal extinctions) with cosmological models Balazs et al. [6] concluded that the SNIa data alone did not exclude the possibility of the $\Lambda = 0$ solution.

SNe Ia also possibly have a metallicity dependence and this would imply that the evidence for a non-zero cosmological constant from the SNIa Hubble Diagram may be subject to corrections for metallicity that are as big as the effects of cosmology [87]. The old supernovae might be intrinsically fainter than the local ones, and the cosmological constant would not be needed [24]. As a matter of fact, some cases, such as SNLS-03D3bb, have an exceptionally high luminosity [37]. Claims have been made about the possible existence of two classes of Normal-Bright SNe Ia [76]. If there is a systematic evolution in the metallicity of SN Ia progenitors, this could affect the determination of cosmological parameters. This metallicity effect could be substantially larger than has been estimated previously and could quantitatively evaluate the importance of metallicity evolution for determining cosmological parameters [75]. In principle, a moderate and plausible amount of metallicity evolution could mimic a Λ-dominated, a flat universe in an open, Λ-free universe. However, the effect of metallicity

evolution appears not to be large enough to explain the high-z SNIa data in a flat universe, for which there is strong independent evidence, without a cosmological constant.

Furthermore, our limited knowledge of the SN properties in the U-band has been identified as another main source of uncertainty in the determination of cosmological parameters [40]. And the standard technique with SNe Ia consists in using spectroscopic templates, built by averaging spectra of well observed (mostly nearby) SNe Ia. Thus, the uncertainty in K-corrections depends primarily on the spectroscopic diversity of SNe Ia.

Even if we accept the present-day SN Ia analyses as correct and without any bias or selection effect, other cosmologies may explain the apparent cosmic acceleration of SNe Ia without introducing a cosmological constant into the standard Einstein field equation, thus negating the necessity for the existence of dark energy [88]. There are four distinguishing features of these models: 1) the speed of light and the gravitational "constant" are not constant, but vary with the evolution of the universe, 2) time has no beginning and no end, 3) the spatial section of the universe is a 3-sphere, and 4) the universe experiences phases of both acceleration and deceleration. An inhomogeneous isotropic universe described by a Lemaître–Tolman–Bondi solution of Einstein's fields equations can also provide a positive acceleration of the expansion without dark energy [77]. Quasi-Steady-State theory predicts a decelerating universe at the present era, it explains successfully the recent SNe Ia observations [95]. Carmeli's cosmology fits data for an accelerating and decelerating universe without dark matter or dark energy [68]. Thompson [91] used available measurement for the constraints on the variation the proton to mass electron with redshift, and with $\Delta\alpha/\alpha = 7 \times 10^{-6}$ he finds that almost all of the dark energy models using the commonly expected values or parameters are excluded. A static universe can also fit the supernovae data without dark energy [89, 47, 54, 30, 56].

There are other sources of Λ measurement such as the anisotropies of the CMBR, but they are not free of inaccuracies owing to contamination and anomalies found in it [53, 84]. In the last two decades, many proofs have been presented to the community to convince us that the definitive cosmology has $\Omega_\Lambda \approx 0.7$, which is surprising taking into account that in the rest of the history of the observational cosmology proofs have been presented for $\Omega_\Lambda \approx 0$. Furthermore, recent tests indicate that other values are available in the literature. For instance, from the test angular size vs. redshift for ultracompact radio sources, it is obtained that Λ is negative [38]. Using the brightest galaxies in clusters, the fit in the Hubble diagram is compatible with a non-accelerated universe instead of $\Omega_\Lambda = 0.7$ [94, 4]. Concordance models produce far more high redshift massive clusters than observed in all existing X-ray surveys [17].

The actual values of Ω_Λ have some consistency problem in the standard scenario of the inflationary Big Bang. The cosmological constant predicted by quantum field theory has a value much larger than those derived from observational cosmology. This is because the vacuum energy in quantum field theory takes the form of the cosmological constant in Einstein's equations. If inflation took place at the Grand Unified Theory epoch, the present value would be too low by a factor $\sim 10^{-108}$, and if the inflation took place at the quantum gravity epoch, the above factor would be lower still at $\sim 10^{-120}$ [96]. The intrinsic absence of pressure in the "Big Bang Model" also rules out the concept of "Dark Energy", according to some opinions [65].

Furthermore, the standard model has some surprising coincidences. There is the coincidence that now the deceleration of the Hubble flow is compensated by the acceleration of the dark energy; the average acceleration throughout the history of the universe is almost null [62]. Again, everything is far from being properly understood.

Acknowledgements

References

[1] Aguerri, J.A.L., Méndez-Abreu, J., Falcón-Barroso, J., et al.: Bar pattern speeds in CALIFA galaxies. I. Fast bars across the Hubble sequence. Hierarchic models for laminated composites. Astron. Astrophys. **576** (2015), A102, 17 pp.

[2] Aguirre, A., and Haiman, Z.: Cosmological Constant or Intergalactic Dust? Constraints from the Cosmic Far-Infrared Background. Astrophys. J. **532** (2000), 28–36.

[3] Aharonian, F., Akhperjanian, A.G., Bazer-Bachi, A.R., et al.: The H.E.S.S. Survey of the Inner Galaxy in Very High Energy Gamma Rays. Astrophys. J. **636** (2006), 777–797.

[4] Andrews, T.B.: Falsification of the Expanding Universe Model. In: E. J. Lerner, and J. B. Almeida, J.B. (Eds.), *1st Crisis in Cosmology Conference* (AIP Conf. Ser. 822(1)), pp. 3–22. AIP, Melville, 2006.

[5] Babcock, H.W.: The rotation of the Andromeda Nebula. Lick Obs. Bull. 19 (**498**) (1939), 41–51. 9

[6] Balázs, L.G., Hetesi, Zs., Regály, Zs., Csizmadia, Sz., Bagoly, Zs., Horváth, I., and Mészáros, A.: A possible interrelation between the estimated luminosity distances and internal extinctions of type Ia supernovae. Astron. Nachrichten **327** (2006), 917–924.

[7] Barboza, E.M. Jr., Nunes, R. da C., Abrey, E.M.C., and Neto J.A.: Is this the end of dark energy? arXiv.org, 1501.03491 (2015).

[8] Barkana, R.: Possible interaction between baryons and dark-matter particles revealed by the first stars. Nature **555** (2018), 71–74.

[9] Battaner, E., and Florido, E.: The Rotation Curve of Spiral Galaxies and its Cosmological Implications. Fund. Cosmic Phys. **21** (2000), 1–154.

[10] Bell, F.B., McIntosh, D.H., Katz, N., and Weinberg, M.D.: A First Estimate of the Baryonic Mass Function of Galaxies. Astrophys. J. Lett. **585** (2003), L117–L120.

[11] Bekenstein, J., and Milgrom, M.: Does the missing mass problem signal the breakdown of Newtonian gravity? Astrophys. J. **286** (1984), 7–14.

[12] Bekenstein, J.D.: Relativistic gravitation theory for the modified Newtonian dynamics paradigm. Phys. Rev. D **70** (2004), id. 083509.

[13] Benhaiem, D., Joyce, M., and Sylos Labini, F.: Transient Spiral Arms from Far Out-of-equilibrium Gravitational Evolution. Astrophys. J. **851** (2017), id. 19, 10pp.

[14] Bertone, G., and Hooper, D.: A History of Dark Matter. arXiv.org, 1605.04909 (2016).

[15] Bessel, F. W. On the variations of the proper motions of Procyon and Sirius. Mon. Not. R. Astron. Soc. **6** (1844), 136–141.

[16] Binney, J., Gerhard, O., and Silk, J.: The dark matter problem in disc galaxies. Mon. Not. R. Astron. Soc. **321** (2001), 471–474.

[17] Blanchard, A.: Evidence for an accelerating universe or lack of? In: J.-C. Pecker, and J. V. Narlikar (Eds.), *Current issues in Cosmology*, pp. 76–84, Cambridge University Press, Cambridge (U.K.), 2006.

[18] Bosma, A.: *The distribution of kinematics of neutral hydrogen in spiral galaxies of various morphological types*. Ph.D. thesis, University of Groningen, 1978.

[19] Bowman, J.D., Rogers, A.E.E., Monsalve, R.A., Mozdzen, T.J., and Mahesh, N.: An absorption profile centred at 78 megahertz in the sky-averaged spectrum. Nature **555** (2018), 67–70. 10

[20] Boylan-Kolchin, M., Bullock, J.S., and Kaplinghat, M.: Too big to fail? The puzzling darkness of massive Milky Way subhaloes. Mon. Not. R. Astron. Soc. **415** (2011), L40–L44.

[21] Casuso E., and Beckman J.E.: On the Origin of the Angular Momentum of Galaxies: Cosmological Tidal Torques and Coriolis Force. Mon. Not. R. Astron. Soc. **449** (2015), 2910–2918.

[22] Debattista, V.P., and Sellwood, J.A.: Constraints from Dynamical Friction on the Dark Matter Content of Barred Galaxies. Astrophys. J. **543** (2000), 704–721.

[23] Di Cintio, A., Brook, C.B., Macci`o, A.V., Stinson, G.S., Knebe, A., Dutton, A.A., and Wadsley, J.: The dependence of dark matter profiles on the stellar-tohalo mass ratio: a prediction for cusps versus cores. Mon. Not. R. Astron. Soc. **437** (2014), 415–423.

[24] Domínguez I., Höflich P., Straniero O., and Wheeler C.: Evolution of type Ia supernovae on cosmological time scales. Mem. Soc. Astron. Ital. **71** (2000), 449–460.

[25] D'Onguia, E., Lake, G.: Cold Dark Matter's Small-Scale Crisis Grows Up. Astrophys. J. **612** (2004), 628–632.

[26] Drexler, J.: Identifying Dark Matter Through the Constraints Imposed by Fourteen Astronomically Based 'Cosmic Constituents'. arXiv.org, astro-ph/0504512 (2005).

[27] Durrer, R. What do we really know about Dark Energy? J. Cosmol. **15** (2011), 6065–6078.

[28] Efstathiou, G., Sutherland, W.J., and Maddox, S.J.: The cosmological constant and cold dark matter. Nature **348** (1990), 705–707.

[29] Evans, N.W.: No Need for Dark Matter in Galaxies? In: N.J.C. Spooner, and V. Kudryavtsev (Eds.), *Proceedings of the 3rd International Workshop on the Identification of Dark Matter*, pp. 85–92. World Scientific, Singapore, 2001.

[30] Farley, F.J.M.: Does gravity operate between galaxies? Observational evidence re-examined. Proc. R. Soc. A **466** (2010), 3089–3096.

[31] Feng, J.Q., and Gallo, C.F.: Deficient Reasoning for Dark Matter in Galaxies. Phys. Int. **6** (2015), 11–22.

[32] Fukugita, M., and Lahav, O.: Ly-alpha clouds at low redshift and the cosmological constant. Mon. Not. R. Astron. Soc. **253** (1991), 17P–20P. 11

[33] Gnedin, O.Y., Kravtsov, A.V., Klypin, A.A., and Nagai, D.: Response of Dark Matter Halos to Condensation of Baryons: Cosmological Simulations and Improved Adiabatic Contraction Model. Astrophys. J. **616** (2004), 16–26.

[34] Goobar, A., Bergström, L., and Mörtsell, E.: Measuring the properties of extragalactic dust and implications for the Hubble diagram. Astron. Astrophys. **384** (2002), 1–10.

[35] Hajdukovic, D.S.: Virtual gravitational dipoles: The key for the understanding of the Universe?

Physics of the Dark Universe **3** (2014), 34–40.

[36] Holmberg, E.: On the masses of double galaxies. Meddelanden fran Lunds Astronomiska Observatorium Series I **186** (1954), 1–20.

[37] Howell, D.A., Sullivan, M., Nugent, P.E., et al.: The type Ia supernova SNLS-03D3bb from a super-Chandrasekhar-mass white dwarf star. Nature 443 (2006), 308–311.

[38] Jackson, J.C., and Dodgson, M.: Deceleration without dark matter. Mon. Not. R. Astron. Soc. **285** (1997), 806–810.

[39] Kahn F.D., and Woltjer L.: Intergalactic Matter and the Galaxy. Astrophys. J. **130** (1959), 705–717.

[40] Knop, R.A., Aldering, G., Amanullah, R., et al.: New Constraints on Ω_M, Ω_Λ, and w from an Independent Set of 11 High-Redshift Supernovae Observed with the Hubble Space Telescope. Astrophys. J. **598** (2003), 102–137.

[41] Komatsu, E., 2011, What Every Dynamicist should know about... Cosmology. In: *American Astronomical Society, DDA meeting #42* (Bull. Am. Astron. Soc. 43), id.4.01, 2011.

[42] Kroupa, P., Theis, C., and Boily, C.M.: The great disk of Milky-Way satellites and cosmological sub-structures. Astron. Astrophys. **431** (2005), 517–521.

[43] Kroupa, P., Famaey, B., de Boer, K.S., et al.: Local-Group tests of dark-matter concordance cosmology . Towards a new paradigm for structure formation. Astron. Astrophys. **523** (2010), id. A32, 22 pp.

[44] Kroupa, P.: The Dark Matter Crisis: Falsification of the Current Standard Model of Cosmology. Publ. Astron. Soc. Australia **29** (2012), 395–433.

[45] Lasserre, T., Afonso, C., Albert, J.N., et al.: Not enough stellar mass Machos in the Galactic halo. Astron. Astrophys. **355** (2000), L39–L42.

[46] Lemaître, G.: Evolution of the Expanding Universe. Proc. Nat. Acad. Sci. USA **20** (1934), pp. 12-17 12

[47] Lerner, E. J.: Tolman Test from $z = 0.1$ to $z = 5.5$: preliminary results challenge the expanding universe model. In: F. Potter (Ed.), *Second Crisis in Cosmology Conference* (ASP Conf. Ser. 413), pp. 12–23. ASP, S. Francisco, 2009.

[48] Little, S., and Little, M.: Laboratory test of Newton's law of gravity for small accelerations. Class. Quantum Grav. **31** (2014), id. 195008.

[49] Liu, J., Chen, X., Ji, X.: Current status of direct dark matter detection experiments. Nature Physics **13** (2017), 212–216.

[50] Longair, M.S.: Observational Cosmology 1986. In: A. Hewitt, G. Burbidge, and L.Z. Fang (Eds.) *Observational Cosmology* (IAU Symp. 124), pp. 823–840. Reidel, Dordrecht, 1987.

[51] López-Corredoira, M., Beckman, J.E., and Casuso E.: High-velocity clouds as dark matter in the Local Group. Astron. Astrophys. **351** (1999), 920–924.

[52] López-Corredoira, M., Betancort-Rijo, J., and Beckman, J.E.: Generation of galactic disc warps due to intergalactic accretion flows onto the disc. Astron. Astrophys. **386** (2002), 169–186.

[53] López-Corredoira, M.: Some doubts on the validity of the foreground Galactic contribution subtraction from microwave anisotropies. J. Astrophys. Astron. **28** (2007), 101–116.

[54] López-Corredoira, M.: Angular-size test on the expansion of the Universe. Int. J. Mod. Phys. D **19**

(2010), 245–291.

[55] López-Corredoira, M., and Kroupa, P.: The Number of Tidal Dwarf Satellite Galaxies in Dependence of Bulge Index. Astrophys. J. **817** (2016), id. 75, 7 pp.

[56] Marosi, L.A.: Hubble Diagram Test of Expanding and Static Cosmological Models: The Case for a Slowly Expanding Flat Universe. Advances in Astronomy **2013**, id. 917104.

[57] Marrodán Undagoitia, T., and Rauch, L.: Dark matter direct-detection experiments. Journal of Physics G: Nuclear and Particle Physics **43** (2016), id. 013001.

[58] Mayer, F.J., and Reitz, J.R.: Electromagnetic Composites at the Compton Scale. Int. J. Theor. Phys. **51** (2012), 322–330.

[59] McGaugh, S.S.: Boomerang Data Suggest a Purely Baryonic Universe. Astrophys. J. Lett. **541** (2000), L33–L36.

[60] McGaugh, S.: The Third Law of Galactic Rotation. Galaxies **2** (2014), 601–622. 13

[61] Mediavilla, E., Jiménez-Vicente, J., Muñoz, J.A., Vives-Arias, H., and Calder´on-Infante, J.: Limits on the Mass and Abundance of Primordial Black Holes from Quasar Gravitational Microlensing. Astrophys. J. Lett. **836** (2017), id. L18, 5 pp.

[62] Melia, F., and Shevchuk, A.S.: The $R_h = ct$ universe. Mon. Not. R. Astron. Soc. **419** (2012), 2579–2586.

[63] Merritt, D.: Cosmology and convention. Studies in History and Philosophy of Modern Physics **57** (2017), 41–52.

[64] Milne, P.A., Foley, R.J., Brown, P.J., and Narayan, G.: The Changing Fractions of Type Ia Supernova NUV–Optical Subclasses with Redshift. Astrophys. J. **803** (2015), id. 20, 15 pp.

[65] Mitra, A.: Why Friedmann cosmology cannot describe the observed universe having pressure and radiation. J. Mod. Phys. **2** (2011), 1436–1442.

[66] Moore, B.: An upper limit to the mass of black holes in the halo of the galaxy. Astrophys. J. Lett. **413** (1993), L93–L96.

[67] Moore, B.: Evidence against dissipation-less dark matter from observations of galaxy haloes. Nature **370** (1994), 629–631.

[68] Oliveira, F.J., and Hartnett, J.G.: Carmeli's Cosmology Fits Data for an Accelerating and Decelerating Universe Without Dark Matter or Dark Energy. Foundations of Physics Letters **19** (2006), 519–535.

[69] Ostriker, J.P., and Peebles, J.P.E.: A Numerical Study of the Stability of Flattened Galaxies: or, can Cold Galaxies Survive? Astrophys. J. **186** (1973), 467–480.

[70] Padmanabhan, T.: Cosmological constant-the weight of the vacuum. Phys. Reports **380** (2003), 235–320.

[71] Page, T.: Radial Velocities and Masses of Double Galaxies. Astrophys. J. **116** (1952), 63–84.

[72] Page, T.: Average Masses and Mass-Luminosity Ratios of the Double Galaxies. Astrophys. J. **132** (1960), 910–912.

[73] Pawlowski, M.S., and Kroupa, P.: The rotationally stabilized VPOS and predicted proper motions of the Milky Way satellite galaxies. Mon. Not. R. Astron. Soc. **435** (2013), 2116–2131.

[74] Perivolaropoulos, L.: Six Puzzles for LCDM Cosmology. arXiv.org, 0811.4684 (2008). 14

[75] Podsiadlowski, P., Mazzali, P.A., Lesaffre, P., Wolf, C., and Forster, F.: Cosmological Implications of the Second Parameter of Type Ia Supernovae. arXiv.org, astro-ph/0608324 (2006).

[76] Quimby, R., H¨oflich, P., and Craig Wheeler, J.: SN 2005hj: Evidence for Two Classes of Normal-Bright SNe Ia and Implications for Cosmology. Astrophys. J. **666** (2007), 1083–1092.

[77] Romano, A.E.: Lemaitre-Tolman-Bondi universes as alternatives to dark energy: Does positive averaged acceleration imply positive cosmic acceleration? Phys. Rev. D **75** (2007), id. 043509.

[78] Rowan-Robinson, M.: Do Type Ia supernovae prove $\Lambda > 0$? Mon. Not. R. Astron. Soc. **332**(2002), 352–360.

[79] Rubin, V., and Ford, W.K. Jr., Thonnard, N.: Rotational Properties of 21 Sc Galaxies with a Large Range of Luminosities and Radii from NGC 4605 (R=4 kpc) to UGC 2885 (R=122 kpc). Astrophys. J. **238** (1980), 471–487.

[80] Sachs, R.K., and Wolfe, A.M.: Perturbations of a Cosmological Model and Angular Variations of the Microwave Background. Astrophys. J. **147** (1967), 73–90.

[81] Sanders, R.H., and McGaugh, S.S.: Modified Newtonian Dynamics as an Alternative to Dark Matter. Ann. Rev. Astron. Astrophys. **40** (2002), 263–317.

[82] Sanders, R.H.: A historical perspective on modified Newtonian dynamics. Canadian J. Phys. **93** (2015), 126–138.

[83] Sánchez-Conde, M.A.: Gamma-ray dark matter searches in the Milky Way. Oral presentation in: *Distribution of Mass in the Milky Way*, Leiden, Netherlands, 13-17 July 2009.

[84] Schwarz, D.J, Copi, C.J., Huterer, D., and Starkman G.D.: CMB anomalies after Planck. Classical and Quantum Gravity 33 (2016), id. 184001.

[85] Sellwood, J.A.: Bar-Halo Friction in Galaxies. III. Halo Density Changes. Astrophys. J. **679** (2008), 379–396.

[86] Sellwood, J.A., and Debattista, V.P.: Bar-Halo Friction in Galaxies. II.Metastability. Astrophys. J. **639** (2006), 868–878.

[87] Shanks, T., Allen, P.D., Hoyle, F., and Tanvir, N.R.: Cepheid, Tully-Fisher and SNIa Distances. arXiv.org, astro-ph/0102450 (2001).

[88] Shu, W.-Y.: The Geometry of the Universe. arXiv.org, 1007.1750 (2010). 15

[89] Sorrell,W.H.: Misconceptions about the Hubble recession law. Astrophys. Space Sci. 323 (2009), 205–211. Erratum: Astrophys. Space Sci. **323** (2009), 213.

[90] Tasitsiomi, A.: The State of the Cold Dark Matter Models on Galactic and Subgalactic Scales. Int. J. Mod. Phys. D **12** (2003), 1157–1196.

[91] Thompson, R.I.: Constraints on quintessence and new physics from fundamental constants. Mon. Not. R. Astron. Soc. **422** (2012), L67–L71.

[92] Tisserand, P., Le Guilou, L., Afonso, C., et al.: Limits on the Macho content of the Galactic Halo from the EROS-2 Survey of the Magellanic Clouds. Astron. Astrophys **469** (2007), 387–404.

[93] Toomre, A.: What amplifies the spirals. In: S.M., Fall, and D. Lynden-Bell(Eds.), *The Structure and Evolution of Normal Galaxies*, pp. 111-136. Cambridge University Press, Cambridge (U.K.), 1981.

[94] Vauclair, S.C., Blanchard, A., Sadat, R., et al.: The XMM-Omega project. II. Cosmological implications from the high redshift L - T relation of X-ray clusters. Astron. Astrophys. **412** (2003), L37–L41.

[95] Vishwakarma, R.G., and Narlikar, J.V.: Modeling Repulsive Gravity with Creation. J. Astrophys. Astr. **28** (2007), 17–27.

[96] Weinberg, S.: The cosmological constant problem. Rev. Mod. Phys. **61** (1989), 1–23.

[97] White, M., Viana, P.T.P., Liddle, A.R., and Scott, D.: Primeval Adiabatic Perturbation in an Expanding Universe. Mon. Not. R. Astron. Soc. **283** (1996), 107–118.

[98] White, S.D.M., Rees, M.J.: Core condensation in heavy halos - A two-stage theory for galaxy formation and clustering. Mon. Not. R. Astron. Soc. **183** (1978), 341–358.

[99] White, S.D.M., Frenk, C.S., and Davis, M.: Clustering in a neutrino-dominated universe. Astrophys. J. **274** (1983), L1–L5.

[100] Zwicky, F.: Die Rotverschiebung von extragalaktischen Nebeln Helvetica Phys. Acta **6** (1933), 110–127.

Spatial distribution of gamma-ray bursts (both in redshift and in the angular sky position)

Attila Mészáros

Astronomical Institute, Faculty of Mathematics and Physics, Charles University, V

Holešovičkáach 2, CZ18000 Prague 8, Czech Republic; meszaros@cesnet.cz

Abstract Gamma-ray bursts (GRBs) are at cosmological distances. Because there is no gap at the Galactic plane, they can well serve to test the fulfillment of the cosmological principle requiring a spatially homogeneous and isotropic distribution. In this contribution the author's and his collaborators' efforts are surveyed concerning the spatial distribution - both in redshift and in the angular distribution. Bold anisotropies are found in the dataset gained by the BATSE instrument of the Compton Gamma Ray Observatory.

Keywords: Gamma-Ray Burst, Spatial Distribution, Redshift

1. Introduction

The observable part of the universe is finite and has the size of $\sim (10 - 20)$ Gpc depending on the omega parameters. On the other hand, the redshifts of observed objects can be arbitrarily large. The relevant exact formulas for this behavior can be found, e.g., in Weinberg (1972) and Carroll et al. (1992). In this observable part the cosmological principle should be fulfilled, i.e. the Universe should be spatially homogeneous and isotropic on scales larger than the size of any structure, because in accordance with the cosmological principle "...in the large scale average the visible parts of our universe are isotropic and homogeneous" (Peebles 1993, page 15). But, on the other hand, the averaging should happen far below the $\sim(10 - 20)$ Gpc scales.

Trivially, any observational results from the high redshifts regions of the Universe are highly useful from the cosmological point of view. For smaller redshifts, say till z ~ 1, the Universe is hardly homogeneous and isotropic (see, e.g., Yadav et al. (2010) and Clowes et al. (2013)) - for larger redshifts there are also some hints about the possible departure from the isotropy (cf. Birch (1982)).

The gamma-ray bursts (GRBs) are partly at higher redshifts (for the survey of the topic see, e.g., Vedrenne & Atteia (2009)). In addition, they are not vanishing at the Galactic plane. Hence, they are ideal objects to test observationally the fulfillment of the cosmological principle.

In this contribution the statistical studies of the spatial distribution of gamma-ray bursts (GRBs) - done mainly by the author and his collegues - are briefly summarized.

2 Redshifts

Probably the first article about the redshifts of GRBs was presented by Usov & Chibisov

(1975). The article claims that, if GRBs are at cosmological distances, there should be a deviation from the log $N(> F) \propto (-3/2) \log F$ relation expected for the Euclidean space (F is the so called peak-flux, and $N(> F)$ denotes the number of bursts having bigger peak-fluxes than F). In addition, from the character of this deviation the redshifts of objects can be deduced. In 1986, i.e. at the year when even the cosmological origin was in doubt, Paczyński (1986) has shown that GRBs should be at $z \simeq (1 - 2)$ (z denotes the redshift).

In 1995-98 the author and his colleagues confirmed the Paczyński's conclusion and have shown that GRBs can be till $z \simeq 20$ (Mészáros & Mészáros 1995, Mészáros & Mészáros 1996, Horváth et al. 1996). Note here that also in 1995-96 only indirect evidences existed for the cosmological origin, because the first direct measurement of a redshift appeared at 1997 by the BeppoSAX satellite (Costa et al. 1997).

In 2006 it was shown that mainly the long GRBs should follow the star-formation-rate (Mészáros et al. 2006).

A highly remarkable result was published in 2011 claiming that in average the fainter bursts can be at smaller distances (Mészáros et al. 2011).

3. Angular sky distribution

The angular sky distribution of the Galactic objects should show a concentration toward the Galactic plane in the angular sky distribution. On the other hand, the extragalactic objects should have no concentration toward the Galactic plane. From this expectation the first indirect observational proof for the cosmological origin of GRBs was given by Meegan et al. (1992). No concentration on the sky positions of GRBs toward the Galactic plane was observed. This indirect support of the cosmological origin was then provided by Tegmark et al. (1996). This study also did not find any concentration toward the Galactic plane and, in addition, did not find any deviations from the isotropic celestial distribution. It is essential to precise here there are two things here: No concentration toward the Galactic plane proves simply the extragalactic origin, but no deviation from the isotropic distribution in generals expected from the fulfillment of the cosmological principle. Both these expectations were declared in 1996 by Tegmark et al. (1996).

In 1998 Balázs et al. (1998) accepted the extragalactic origin of GRBs, and hence did not search for any concentration toward the Galactic plane. But in this study by statistical tests the isotropy of the sky distribution were provided in general. Today it is clear that this paper claimed first that the sky distribution of short BATSE's GRBs was not isotropic. This highly remarkable result was then verified by several other articles of the author and his collaborators (Balázs et al. 1999, Mészáros et al. 2000a, Vavrek et al. 2008). In addition, both the BATSE's intermediate and long subclasses were found to be distributed also anisotropically (see Mészáros et al. (2000b), Mészáros & Štoček (2003) and Vavrek et al. (2008) for more details and references).

In Figures 1-3 the angular distributions of the BATSE's three subgroups are shown.

After Vavrek et al. (2008) these statistical tests allowed to claim in 2009 the existence of the Gpc structures and thus the huge problems of the cosmological principle (Mészáros et al. 2009a, 2009b).
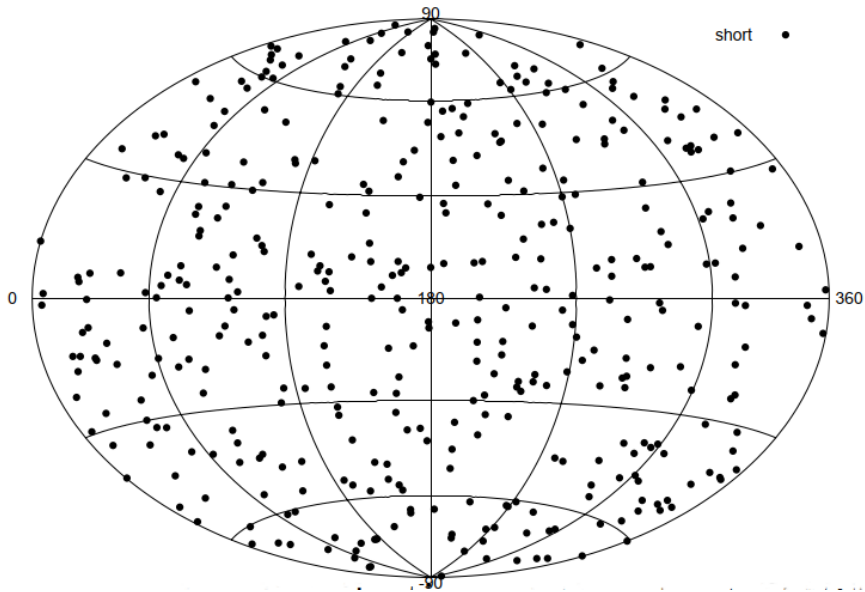
Fig1. *The angular sky distribution of the short BATSE's bursts in equatorial coordinates. Balázs et al. (1998) claim that the distribution is anisotropic.*
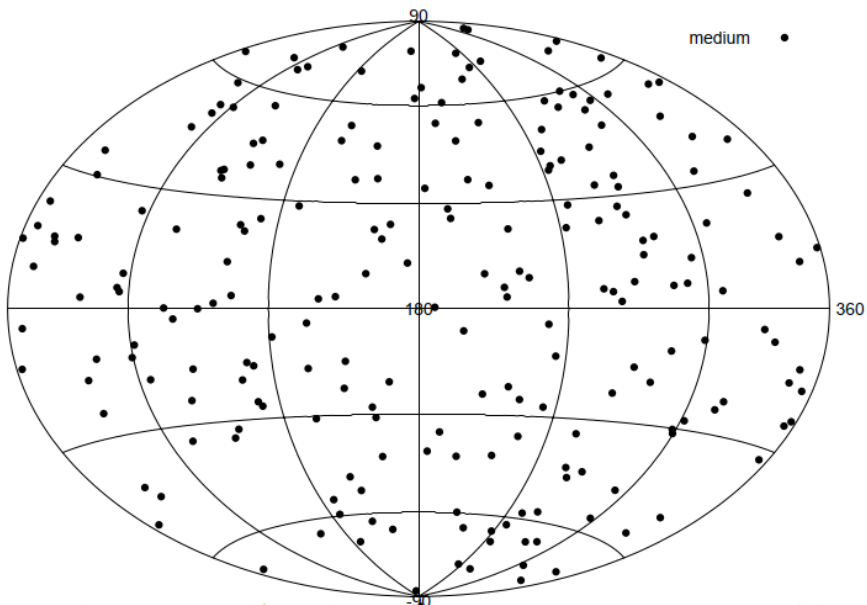
Fig2. *The angular sky distribution of the intermediate BATSE's bursts in equatorial coordinates. Mészáros A. et al. (2000) claim that the distribution is anisotropic.*
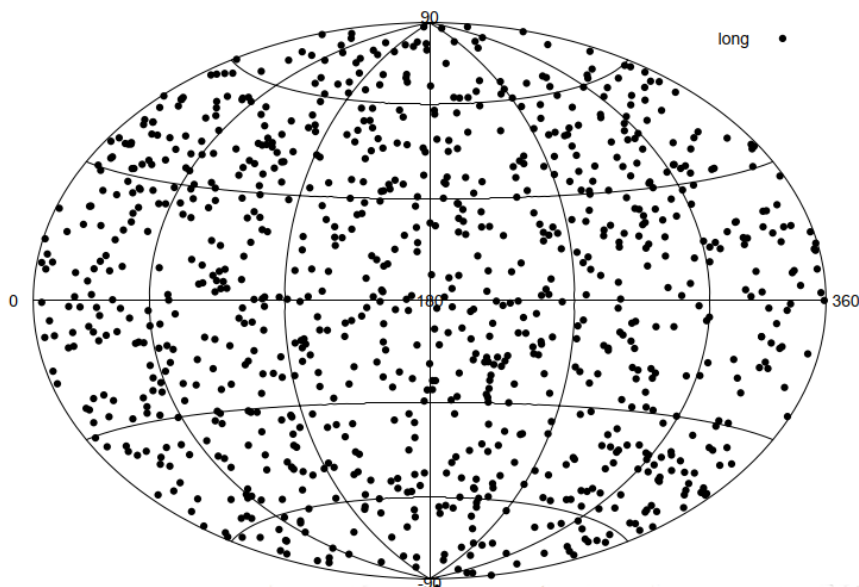
Fig3. *The angular sky distribution of the long BATSE's bursts in equatorial coordinates. Mészáros A. & Štoček (2003) claim that the distribution is anisotropic.*

4. Further studies

The studies, mentioned at the previous section were 2D studies and were based on the BATSE data. Direct 3D study of the BATSE data is not possible, because in the BATSE dataset only few GRBs have measured redshifts (Bagoly et al. 2003, Mészáros et al. 2011).

Recently two other groups obtained remarkable results from the 2D study of the dataset of the Fermi satellite.

At the whole Fermi dataset Tarnopolski (2017) found anisotropy for the short subclass of GRBs; for the long subclass the assumption of isotropy was not rejected by his tests. Řípa & Shafieloo (2017) - using the whole Fermi dataset - tested the isotropy of the observed properties of GRBs. This means that it was studied the possibility that at different directions GRBs had different properties such as their durations, fluences, and peak fluxes at various energy bands and different timescales. In other words, not the isotropy of the angular sky positions itself, but the isotropies of the observed properties themselves, were tested. Some noticeable anisotropic features were found, but a later study on a larger Fermi sample (Řípa & Shafieloo 2018) did not confirm any deviation from the isotropy of the observed properties. The same result was obtained for the BATSE and Swift datasets, respectively, too (Řípa & Shafieloo 2018).

For a small sample of GRBs, which have directly measured redshifts from the afterglows, the study of 3D structures became directly possible. But, only a small fraction of GRBs has directly measured redshifts (Perley 2017), and hence selection effects can play here an important role. Under these conditions huge spatial structures on the Gpc scales were found (Horváth et al. 2014, Horváth et al. 2015, Balázs et al. 2015, Sokolov et al. 2015, Verkhodanov et al. 2015, Bagoly et al. 2016a, Bagoly et al. 2016b), but Balázs et al. (2018) notes that "the large-scale spatial pattern of the GRB activity does not necessarily reflects the large-scale

distribution of the cosmic matter".

5. Conclusion

The results of the author's, his collaborators' and others' efforts can be summarized as follows.

1. Existence of huge redshifts were claimed already in years 1995-96, when even the direct proof of the cosmological origin did not exist yet.

2. Both the 2D and 3D studies show that in the distribution of GRBs structures on the huge Gpc scales can well exist. All this challenges the cosmological principle.

References

[1] Bagoly, Z. et al. 2003, A&A, **398**, 919

[2] Bagoly, Z. et al. 2016a, Galaxies at High Redshift and Their Evolution Over Cosmic Time, IAU Symp. **319**, 2

[3] Bagoly, Z. et al. 2016b, Galaxies at High Redshift and Their Evolution Over Cosmic Time, IAU Symp. 319, 3

[4] Balázs, L.G., Mészáros, A., & Horváth, I. 1998, A&A, **339**, 1

[5] Balázs, L.G. et al. 1999, A&AS, **138**, 417

[6] Balázs, L.G. et al. 2015, MNRAS, **452**, 2236

[7] Balázs, L.G. et al. 2018, MNRAS, **473**, 3169

[8] Birch, P. 1982, Nature, **298**, 451

[9] Carroll, S.M., Press, W.H. & Turner, E.L. 1992, ARAA, **30**, 499

[10] Clowes, R.G. et al. 2013, MNRAS, **429**, 2910

[11] Costa, E. et al. 1997, Nature, **387**, 783

[12] Horváth, I., Mészáros, P. & Mészáros, A. 1996, ApJ, **470**, 56

[13] Horváth, I., Hakkila, J. & Bagoly, Z. 2014, A&A, **561**, L12

[14] Horváth, I. et al. 2015, A&A, **584**, A48

[15] Meegan, C.A. et al. 1992, Nature, **355**, 143

[16] Mészáros, A. & Mészáros, P. 1996, ApJ, **466**, 29

[17] Mészáros, P. & Mészáros, A. 1995, ApJ, **449**, 9

[18] Mészáros, A., Bagoly, Z. & Vavrek, R. 2000a, A&A, **354**, 1

[19] Mészáros, A. et al. 2000b, ApJ, **539**, 98

[20] Mészáros, A. & Štoček, J. 2003, A&A, **403**, 443

[21] Mészáros, A. et al. 2006, A&A, **455**, 785

[22] Mészáros A. et al. 2009a, Baltic Astronomy, **18**, 293

[23] Mészáros A. et al. 2009b, Sixth Huntsville GRB Symposium, AIP Conf. Proc., **1133**, 483

[24] Mészáros, A. et al. 2011, A&A, **529**, A55

[25] Paczyński, B. 1986, ApJL, **308**, L43

[26] Peebles, P.J.E. 1993, Principles of Physical Cosmology (Princeton University Press)

[27] Perley, D. 2018, http://www.astro.caltech.edu/grbox/grbox.php

[28] Řípa, J. & Shafieloo, A. 2017, ApJ, **851**, article id. 15,

[29] Řípa, J. & Shafieloo, A. 2018, arXiv:1809.03973

[30] Sokolov, I.V. et al. 2015, Quark Phase Transition in Compact Objects, SAO, Russia, 111

[31] Tarnopolski, M. 2017 MNRAS, **472**, 4819

[32] Tegmark, M. et al. (1996), ApJ, **468**, 214

[33] Usov, N.V. & Chibisov, G.V. 1975, Soviet Astronomy, **19**, 115

[34] Vavrek, R. et al. 2008, MNRAS, **391**, 1741

[35] Vedrenne, G. & Atteia, J.-L. 2009, Gamma-Ray Bursts: The brightest explosions in the Universe (Springer)

[36] Verkhodanov, O.V., Sokolov, V.V. & Khabibullina, M.L. 2015, Quark Phase Transition in Compact Objects, SAO RAS, Russia, 142

[37] Weinberg, S. 1972, Gravitation and Cosmology (J.Wiley, New York - London - Sydney - Toronto)

[38] Yadav, J.K., Bagla, J.S. & Khandai, N. 2010, MNRAS, **405**, 2009

The diversity of GRBs statistically (is there a third group? physical meaning? relation to XRFs?)

Attila Mészáros

Astronomical Institute, Faculty of Mathematics and Physics, Charles University, V

Holešovičkáach 2, CZ18000 Prague 8, Czech Republic; meszaros@cesnet.cz

Abstract   The separation of gamma-ray bursts (GRBs) into short/hard and long/soft subclasses, respectively, is today well supported. Since 1998 there are several statistical tests suggesting the existence of more than two subgroups. The author with other collaborators provided several statistical studies in this topic. The references concerning this GRB diversity are briefly surveyed in this contribution.

Keywords: Gamma-Ray Burst, Statistics

1. Separation into two subgroups

After the discovery of gamma-ray bursts (GRBs) (Klebesadel et al. 1973) Mazets et al. (1981) have shown that there are two types of GRBs. This separation of GRBs into short/hard and long/soft subgroups was then confirmed by several other studies (for a survey see, e.g., Mészáros (2006)). The limiting duration is around $\simeq 2$ sec.

2. The third subgroup?

In 1998 two articles declared simultaneously the existence of a third subgroup (Mukherjee et al. 1998, Horváth 1998). This claim came from the statistical studies of the dataset of BATSE instrument being on the Compton Gamma Ray Burst Observatory[f]. Since that time several other papers confirmed the same result for the BATSE dataset (Horváth 2002, Hakkila et al. 2003, Hakkila et al. 2004, Horváth et al. 2006). This third subgroup should have an intermediate duration (between $\simeq 2$ and 10 seconds). This means that in essence the earlier long subgroup should further be separated.

The subgroup was found also in the Swift dataset[g] (Veres et al. 2010). For the RHESSI[h] satellite the existence of the third subgroup was also found (Řípa et al. 2012). On the other hand, no intermediate subgroup was found in the Fermi's[i] observations (Tarnopolski 2015).

[f] https://heasarc.gsfc.nasa.gov/docs/cgro/index.html
[g] https://swift.gsfc.nasa.gov
[h] https://hesperia.gsfc.nasa.gov/rhessi3
[i] https://fermi.gsfc.nasa.gov

Similarly, no third subgroup is declared to exist in the Konus/WIND[j] catalog (Tsvetkova et al. 2017).

It must be added that even in the case, when the three subgroups are found by statistical tests, it is not sure that there are really three astrophysically different phenomena, because different biases, selection effects, etc. can play a role (Hakkila et al. 2003, Tarnopolski 2016). For example, in the Swift database the third group is found by tests, but a more detailed study shows that the third group is given by the so-called X-Ray Flashes (XRFs) - which are in essence long GRBs (Veres et al. 2010). But, on the other hand, in some cases it is claimed that the third subgroup cannot entirely be given by the long GRBs. For example, for the BATSE and mainly for the RHESSI database, the identification of the intermediate GRBs with XRFs cannot be done (Řípa & Mészáros 2016).

3. Further subgroups?

There are studies claiming the existence of other subgroups - being not identical - to the intermediate one.

In the BATSE database there were hints for the separation of the long GRBs themselves into the harder and softer parts (Pendleton et al. 1997).

The longest GRBs can also form an extra - ultra-long - subgroup (Tikhomirova & Stern 2005, Virgili et al. 2013, Levan et al. 2014). Because there are only few GRBs in this ultra-long subgroup, from the statistical point of view this subgroup hardly can be declared as an astrophysically different phenomenon - for example, they can simply be outliers.

Recently, in the Fermi database five subgroups were found (Acuner & Ryde 2018). Theoretically, it is meant that even seven different subgroups should exist (Ruffini et al. 2018). This paper means that the long subgroup should further be separated.

It is already possible to study the diversity of GRBs also from other intrinsic quantities for the limited sample, when the redshifts are known. This follows from the fact that the intrinsic luminosity (L_{iso}) and the intrinsic total emitted energy (E_{iso}) can be calculated for a given GRB, if its redshift is known. Such a probe is provided by (Levan et al. 2014) on the duration vs. L_{iso} (E_{iso}, respectively) plane. In Fig.2 of Levan et al. (2014) such effort is done. Several possible subgroups are seen beyond the long and short GRBs (soft gamma repeaters, low luminosity long GRBs, ultra-long GRBs, tidal disruption events, etc.). On the other hand, there is no intermediate subgroup.

4. Conclusion

There are known several statistical tests, theories, ideas, modeling, etc... about the further subgroups beyond the well confirmed short/hard and long/soft subclasses. A brief - never complete - survey was provided here. Summing these works it can be said that mainly the long/soft subgroup does not seem to be a unique one single subclass. But, on the other hand, any astrophysically different phenomenon - beyond the two (short/hard and long/soft) types - is further in doubt, because both the intermediate subgroup and the possible subgroup of the low-luminosity long GRBs are not proven yet unambiguously. In addition, any eventual further subgroups are also in doubt, because they are low populated.

[j] http://www.ioffe.ru/LEA/kw/

References

[1]   Acuner, Z. & Ryde, F. 2018, MNRAS, **475**, 1708

[2]   Hakkila, J., et al. 2003, ApJ, **582**, 320

[3]   Hakkila, J., et al. 2004, Baltic Astronomy, **13**, 2011

[4]   Horváth, I. 1998, ApJ, **508**, 757

[5]   Horváth, I. 2002, A&A, **392**, 791

[6]   Horváth, I., et al. 2006, A&A, **447**, 23

[7]   Klebesadel, R.W., Strong, I.B., & Olson, R.A. 1974, ApJ (Letters), **182**, L85

[8]   Levan, A.J. et al. 2014, ApJ, **781**, id.13

[9]   Mazets, E.P., et al. 1981, ApSS, **80**, 3

[10] Mészáros, P. 2006, Reports on Progress in Physics, **69**, 2259

[11] Mukherjee, S., et al. 1998, ApJ, **508**, 314

[12] Pendleton, G.N., et al. 1997, ApJ, **489**, 175

[13] Řípa, J., et al. 2012, ApJ, **756**, id.44

[14] Řípa, J. & Mészáros, A. 2016, ApSS, **361**, id.370

[15] Ruffini, R., et al. 2018, ApJ, **859**, id.30

[16] Tarnopolski, M. 2015 A&A, **581**, id.A29

[17] Tarnopolski, M. 2016, MNRAS, **458**, 2024

[18] Tikhomirova, Ya.Yu. & Stern, B.E. 2005 Astronomy Letters, **31**, 291

[19] Tsvetkova, A., et al. 2017, ApJ, **850**, id.161

[20] Veres, P., et al. 2010, ApJ, **725**, 1955

[21] Virgili, F.J., et al. 2015, ApJ, **778**, id.54

Robotic telescope of Zvenigorod observatory

Naroenkov Sergey[1*], Nalivkin Mikhail[2]

[1]*Department of Solar system research, INASAN, Moscow, Russia;
  snaroenkov@inasan.ru*

[2]*Department of the experimental astronomy, INASAN, Moscow, Russia;*

Abstract The Institute of Astronomy is working on the develompent of robotic monitoring systems to solve a wide range of astrophysical problems. As a result of the work, a robotic optical system with the 20-cm wide-angle telescope was created. The special software has been developed. This software allows us making observations in the automatic mode without operator's participation. The robotic telescope IRT-20 is located in the Zvenigorod Observatory of INASAN. Photometric observations of variable stars and searching of optical transients are carried out with the telescope in a constant mode.

Keywords: Robotic Telescope, Photometry, Optical Transients

1. Introduction

Recently, robotized telescope systems have been mainly used to solve problems of monitoring the near-earth space and observing space objects. Recall that the term "robotized" means the ability of a software and hardware complex to perform its tasks and interact with the external environment without human involvement. The widespread access to the Internet and the rapid development of the hardware market have led to the fact that robotic telescopes are becoming more common. In turn, the traditional work of the observer in outdated observatories gradually gives way to automatics. Reducing the role of the human factor is a general trend that improves the quality of scientific observations.

According to a predetermined observation plan, robotized telescopes perform the necessary actions during the entire observation session such as directing telescope to a specific area of the sky, making frames in different filters and with the specified exposures. Such robotic systems allow to perform routine operations without the intervention of an observer and to achieve the highest possible speed of sight. With the help of a telescope robot, we can quickly respond to special events, such as a gamma-ray burst, which is given priority. An equally important part of the work of the robotic review is the stream processing of information using special software.

2. Robotic telescope IRT-20

In Zvenigorod Observatory of INASAN, a robotic telescope IRT-20 (INASAN ROBOTIC TELESCOPE) was created. The robotic telescope IRT-20 consists of Officina Stellare RH-200 wide-angle telescope, ASA DDM 85 mount, FLI Proline 16803 CCD camera with a UBVRI filter wheel and a focuser, ScopeDome 3M dome, special power supply and lightning protection equipment, a weather station for monitoring the weather parameters, control

computer and data storage. Parameters of the Officina Stellare RH-200 telescope are: focal length - 600 mm, field of view – 5 sq. deg, aperture 200 mm, focal ratio - 3. Parameters of the CCD camera FLI Proline 16803: chip size - 36x36 mm, pixel size - 9 μm, chip capacity - 4Kx4K.

The IRT-20 robot telescope is the first telescope in the series of robotic telecsopes of the observational optical network created in INASAN. Since 2016, telescopic observations are constant. The IRT-20 robotic telescope is fully automated, which makes it possible to carry out observations without operator intervention, and an Internet connection allows us to monitor the operation of the telescope from anywhere in the world. A general view of the telescope robot of the Zvenigorod Observatory of INASAN is presented in Figure 1.

Fig 1. General view of the robotic telescope IRT-20.

Each of the devices used in the observations has software and hardware interfaces for connecting to a computer. The software part of the robotic telescope includes:
- scheduler and observing session program;
- program-driver of the control of the slewing device AutoSlew;
- driver software for controlling a CCD camera, filter wheel, focuser;
- program-driver dome control ScopeDome 3M;
- software module for determining weather conditions.
- Apex II Special Streaming Software [1]

Most manufacturers of astronomical equipment complete their products with drivers that support the standard ASCOM (AStronomy Common Object Model), which allows us to simplify the development of a program to control such devices. The advantage of ASCOM is that a single set of control commands is used to control different types of mounts or CCD cameras, regardless of the manufacturer of the equipment. The ASCOM driver completely hides from the developer of the control program the lower level of interaction with the equipment.

3. The observation session management program

The observation session management program combines the control functions of all astronomical devices involved in an observation session. Figure 2 shows a diagram of the informational interaction of software modules and robot telescope drivers. The observation session control program operates according to the observation plan prepared by the operator. In observation plan, the coordinates of the objects to be observed, the tracking modes of the object, the required number of frames, the exposure time, the required photometric filter or the sequence of filter changes are specified. The observational session management program is able to respond to trigger events in the observation process, for example, urgent applications received from the Baksan Neutrino Observatory (BNO) or other events generated by the application server. Each image obtained with a telescope is stored on a data storage server, and key data about the file and the observed object are stored in a special database. At the end of the observation session, a report on the tasks implementation is generated, including the results of the tasks and the errors that have occurred are indicated. The end of the observation session (closure of the dome, and telescope parking) is performed either with the end of the observation plan, or due to weather deteriorating.
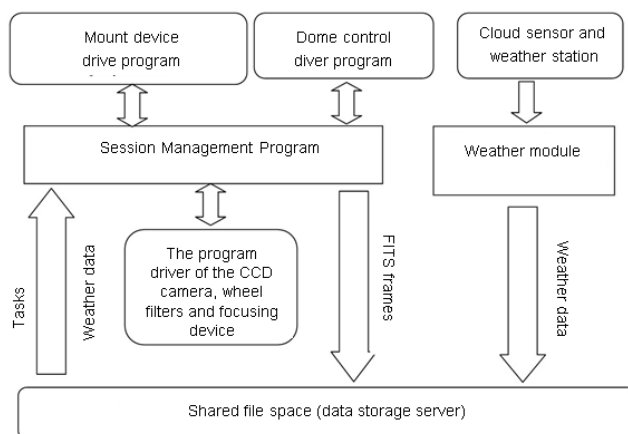
Fig2. *Diagram of information interaction of software modules and driver programs of a robotic telescope.*

Stream processing of data for the asteroids and transients detection is carried out using the Apex II software package and a special streaming processing software module that allows the forming of observation packages from a set of received fits frames. For example, with sky surveys for detecting unknown asteroids, a streaming processing software module forms a

packet of several (minimum four) frames of a single sky site, and starts processing this packet with Apex II. After detecting an unknown object, the streaming processing module generates a protocol for detecting a new object and creates a task for additional monitoring on the request server.

4. Meteo station and software for determining weather conditions

During the session, the observation session program receives weather data from the weather station. The weather station collects data on various environmental parameters from the AAG CloudWatcher cloud sensor, the Davis Vantage Pro 2 weather station and the Starlight Xpress Oculus-180 wide-angle camera. The meteo station and the program module for determining weather conditions operate independently of the robotic telescope during the whole day and night, thus collecting and storing information about the weather and climate at the telescope's installation site. The special database stores data on the ambient temperature, humidity, precipitation, cloud conditions, wind speed and direction. Continuous observations of weather conditions at the Zvenigorod Observatory in 2017-2018 showed that the percentage of cloudy, partly cloudy and clear nights in 2017 was 41, 28 and 31 percent, respectively. In 2017, the total number of clear hours was 928. In 2018, the total number of clear hours at night already reached 1200 hours.

5. Obtained scientific results

The IRT-20 robot telescope is mainly used for carrying out photometric studies of fast-variable stars, such as FC Com, LO Peg, BZ Cam, ET Dra, etc., as well as triggers from the BNO. The robot telescope allows us to observe objects up to 15m with 180 seconds exposure. The "seeing" image quality parameter for the Zvenigorod Observatory is about 3 ... 5 ". The accuracy of photometric measurements at good nights for bright objects is ± 0.01m. For example, Figure 3 shows two curves of the brightness variation of the FK Com star, obtained in March-May 2018. In general, over 2017–2018, more than 16,000 images of variable stars in various filters were obtained. The results of the observations were published in [2].
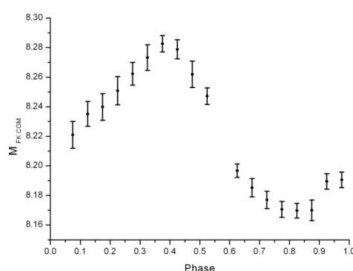
Fig3. V light curve of FK Com, obtained during March -May 2018 period
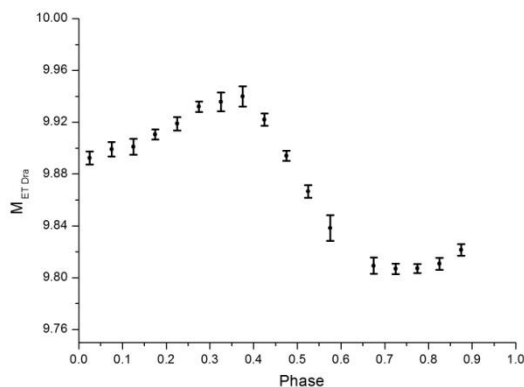
Fig 4. *V light curve of ET DRA, obtained during August -September 2018 period*

Note that the capabilities of the IRT-20 telescope for photometric and prospecting observations are significantly limited by a small image scale of 3.1 "/ pixel and large central screening. In addition, poor astroclimate and sky background illumination is limiting magnitude of robotic telescope IRT-20.

6. Robotic telescope MEADE LX-200

In 2019 a new 35-cm robotic telescope at Terskol branch of INASAN will be created. The main objective of the new robotic telescope will be to perform an operational search and subsequent study of astrophysical objects generating bursts of cosmic radiation of high and ultrahigh energy together with optical flares. The robotic telescope MEADE LX-200 consist of the Meade 14" telescope, EQ8 Pro mount, QHY 163M CMOS camera with a UBVRI filter wheel and a focuser. The automation of the 5-meter dome of the Meade LX200 telescope dome at the Terskol peak was completed in 2018.

References

[1]   Devyatkin A. V., Gorshanov D. L., Kouprianov V. V., Verestchagina, I. A. Apex I and Apex II software packages for the reduction of astronomical CCD observations. 2010, Solar System Research, Volume 44, Issue 1, pp.68-80.

[2]   Savanov, I.S., Naroenkov, S.A., Nalivkin, M.A., Puzin, V.B., Dmitrienko, E.S. Photometric Observations of LO Peg in 2017. 2018, Astrophysical Bulletin, Volume 73, Issue 3, pp. 344-350.

A search for neutrino bursts in the Galaxy with the Baksan Underground Scintillation Telescope; 38 years of exposure

R.V. Novoseltseva[1,*], M.M. Boliev[1], I.M. Dzaparova[1,2], M.M Kochkarov[1], Kochkarov[1], A.N. Kurenya[1], Yu. F. Novoseltsev[1], V.B. Petkov[1,2], P.S.Striganov[1], A.F. Yanin[1]

[1]Institute for Nuclear Research of the Russian Academy of Sciences, 60th October Anniversary Prospect, 7a, 117312 Moscow, Russia, novoseltsev@inr.ru

[2]Institute of Astronomy of the Russian Academy of Sciences, 48 Pyatnitskaya St., 119017, Moscow, Russia

Abstract   The experiment on recording neutrino bursts has been carried out since the mid-1980. As the target, we use two parts of the facility with the total mass of 242 tons. Over the period from June 30, 1980 to December 31, 2018, the actual observational time is 33.02 years. No candidate for the stellar core collapse has been detected during the observation period. An upper bound of the mean frequency of core collapse supernovae in our Galaxy is 0.070 year^{-1} (90% CL).

Keywords: Neutrino, Supernova

1. Introduction

Core-collapse supernovae are among the most powerful sources of neutrinos in the Universe. Recording the supernova SN 1987A has made a considerable impact on both theoretical investigation of SN phenomenon and experimental facilities development. The detection of neutrinos from the supernova SN1987A experimentally proved the crucial role of neutrinos in the explosion of massive stars, as was suggested more than 50 years ago [1, 2, 3].

Due to their high penetration power, neutrinos deliver information on physical conditions in the core of the star during the gravitational collapse. SN1987A has become the nearest supernova in the past several hundred years, which allowed the SN formation process to be observed in unprecedented detail beginning with the earliest time of radiation. It was the first time that a possibility arose for comparing the main parameters of the existing theory - total radiated energy, neutrino temperature, and neutrino burst duration - with the experimentally measured values [4, 5].

The SN1987A event has demonstrated significant deviations from spherical symmetry. It means the SN phenomenon is substantially multidimensional process. In recent years great progress has been achieved in two-dimensional (2D) and three-dimensional (3D) computer simulations of an SN explosion. 3D simulations of the evolution of massive stars at the final stage of their life (SN progenitors) have revealed very important role of non-radial effects. However, further analysis would be mandatory when high-resolution 3D-simulations will become available.

Since light (and electromagnetic radiation in general) can be partially or completely

absorbed by dust in the galactic plane, the most appropriate tool for finding supernovae with core collapse are large neutrino detectors. In the past decades (since 1980), the search for neutrino bursts was carried out with such detectors as the Baksan Scintillation Telescope[6, 7], Super-Kamiokande [8], MACRO [8], LVD [10], AMANDA [11] and SNO [12]. Over the years, our understanding of how massive stars explode and how the neutrino interacts with hot and dense matter has increased by a tremendous degree. At present the scale and sensitivity of the detectors capable of identifying neutrinos from a Galactic supernova have grown considerably so that current generation detectors [13, 14, 15] are capable of detecting of order ten thousand neutrinos for a supernova at the Galactic Center.

The Baksan Underground Scintillation Telescope (BUST) [16] is the multipurpose detector intended for wide range of investigations in cosmic rays and particle physics. One of the current tasks is the search for neutrino bursts. The facility operates under this program almost continuously since the mid-1980s. The total galaxy observation time amounts to 90% of the calendar time.

The paper is built as follows. Section 2 is a brief description of the facility. Section 3 is dedicated to the method of neutrino burst detection. Conclusion is presented in Section 4.

2. The facility

The Baksan Underground Scintillation Telescope is located in the Northern Caucasus (Russia) in the underground laboratory at the effective depth of 8.5×10^4 g·sm^{-2} (850 m of w.e.) [16]. The facility has dimensions $17 \times 17 \times 11$ m^3 and consists of four horizontal scintillation planes and four vertical ones (Fig. 1).
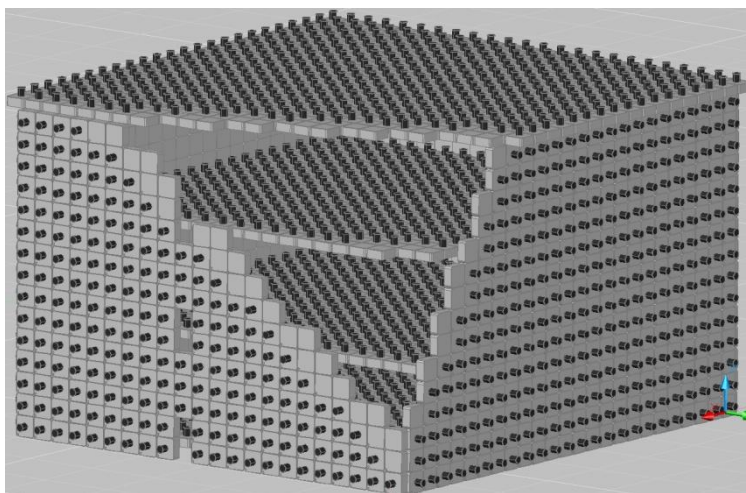
Fig1. The Baksan underground scintillation telescope

The upper horizontal plane has an area of 290 m^2 and consists of 576 (24×24) liquid scintillator counters of the standard type, three lower planes have 400 (20×20) counters each. The vertical planes have 15×24 and 15×22 counters. The horizontal scintillation planes are located on the floors that consist of an 8-mm-thick iron bottom plate, steel beams (the total iron thickness is 2.5 cm or 20 g·cm$^{-2)}$, and a 78-cm-thick fill of low-background rock (dunite) (a

concrete cap is at the top). The total thickness of one telescope layer (the scintillator layer plus the floor) is 165 g·cm^{-2}. The vertical walls of the BUST building are also composed of dunite with iron reinforcement. The charge and atomic weight of the nuclei of BUST material atoms averaged over the volume of one facility layer are $\bar{Z} = 12.8$ and ove $\bar{A} = 26.5$, respectively. The radiation unit of length for the telescope material is $t_0 = 23.5$ g·cm^{-2}.

The distance between neighboring horizontal scintillation layers is 3.6 m. The angular resolution of the facility is 2.5^o (if the trajectory length exceeds 8 m), time resolution is 5 ns.

The standard autonomous counter is an aluminum tank $0.7 \times 0.7 \times 0.3$ m^3 in size, filled with an organic C_nH_{2n+2} (n ≈ 9) scintillator. The scintillator volume is viewed by one FEU-49 photomultiplier (PM) with a photocathode diameter of 15 cm through a 10-cm-thick organic glass window (the thick window serves to reduce the light collection nonuniformity).

Four signals are taken from each counter. The signal from the PM anode is used to measure the plane trigger time and the energy deposition up to 2.5 GeV (the most probable energy deposition of a muon in a counter is 50 MeV ≡ 1relativistic particle). The anode signals from the counters of each plane are successively summed in three steps: $\sum25$, $\sum100$, and $\sum400$. In addition to the signals from the entire plane, this also allows the signals from its parts to be used. The current output (the signal from the PM anode through an integrating circuit) is used to adjust and control the PM gain. The signal from the 12th dynode is fed to the input of a discriminator (the so-called pulse channel) with a trigger threshold of 8 and 10 MeV for the horizontal and vertical planes, respectively. The signal from the fifth PM dynode is fed to the input of a logarithmic converter, where it is converted into a pulse whose length is proportional to the logarithm of the signal amplitude [17]. The logarithmic channel (LC) allows the energy deposition in an individual counter to be measured in the range 0.5-600 GeV.

The signal from each plane $\sum400$ is fed to linear coders which have the measurement range of $(6 - 80)$ MeV and the energy resolution 60 KeV. These coders allow us to measure with high accuracy an energy deposition amplitude of single events (see below) which will appear in case of a neutrino burst.

The trigger is an operation of any counter pulse channel of the BUST.

3. The method of neutrino burst detection

The BUST consists of 3184 standard autonomous counters arranged in four horizontal and four vertical planes. The total scintillator mass is 330 t, and the mass enclosed in three lower horizontal layers (1200 standard counters) is 130 tons. The majority of the events recorded with the Baksan telescope from a supernova explosion will be produced in inverse beta decay (IBD) reactions:

$$\bar{v}_e + p \rightarrow n + e^+ \tag{1}$$

If the mean antineutrino energy is $E_{v_e} = 12$ - 15 MeV [18, 19] the path of e$^+$ (produced in reaction (1) will be confined, as a rule, in the volume of one counter. In such a case the signal from a supernova explosion will appear as a series of events from singly triggered counters (one and only one counter from 3184 operates; below we call such an event "the single event") during the neutrino burst. The search for a neutrino burst consists in recording of single events cluster within time interval of $\tau = 20$ s (according to the modern collapse models the burst duration does not exceed 20 s).

The expected number of neutrino interactions detected during an interval of duration Δt from the beginning of the collapse can be expressed as:

$$N_{ev}^{H} = N^{H} \int_0^{\Delta t} dt \int_0^{\infty} dE \times F(E,t) \times \sigma(E) \times \eta(E) \tag{2}$$

here N_H is the number of free protons, $F(E,t)$ is the flux of electron antineutrinos, $\sigma(E)$ - the IBD cross section, and $\eta(E)$ is the detection efficiency. The symbol "H" in left side indicates that the hydrogen of scintillator is the target. In calculating (2), we used the Fermi-Dirac spectrum for the $\bar{\nu}_e$ energy spectrum integrated over time (with the antineutrino temperature $k_B T = 3.5$ MeV) and the IBD cross section, $\sigma(E)$, from [20].

For an SN at a "standard" distance of 10 kiloparsecs, a total energy radiated into neutrinos of $\varepsilon_{tot} = 3 \times 10^{53}$ erg, and a target mass of 130 t (the three lower horizontal planes, see Fig. 1), we obtain (we assume the $\bar{\nu}_e$ flux is equal to $1/6 \times \varepsilon_{tot}$)

$$N_{ev}^{H} \cong 38 \quad \textit{(no oscillations)} \tag{3}$$

Flavor oscillations are unavoidable of course. However, it was recognized in recent years that the expected neutrino signal depends strongly on the oscillation scenario (see e.g. [21, 22, 23, 24]).

The oscillation effects depend on many unknown or poorly known factors. These are the self-induced flavor conversions, the matter suppression of self-induced effects, specific flavor conversions at the shock-fronts, stochastic matter flows fluctuations. In the absence of a quantitatively reliable prediction of the flavor-dependent fluxes and spectra it is difficult to estimate the oscillation impact on ν_e and $\bar{\nu}_e$ fluxes arriving to the Earth. Therefore, it is an open question how the estimation (3) is changed under the influence of flavor conversions effects.

Background events are 1) radioactivity (mainly from cosmogeneous isotopes) and 2) cosmic ray muons if only one counter from 3184 hit. The total count rate from background events (averaged over the period of 2001 - 2018 years) is f1 = 0.0207 s^{-1} in internal planes (three lower horizontal layers) and ≈ 1.5 s^{-1} in external ones. Therefore three lower horizontal layers are used as a target; below, we will refer to this counter array as the D1 detector (the estimation (3) has been made for the D1 detector).

Background events can imitate the expected signal (k single events within sliding time interval τ with a count rate

$$p(k) = f_1 \times \exp(-f_1 \times \tau) \times \frac{(f_1 \times \tau)^{k-1}}{(k-1)!} \tag{4}$$

Processing of experimental data (single events over a period 2001 - 2018 y; $T_{actual} = 15.5$ years) is shown by squares and triangles in Fig. 1 in comparison with the expected distribution according to the expression (4) calculated at $f_1 = 0.0207$ s^{-1}. Note that there is no normalization in Fig. 2.

It should be explained that the sliding time interval moves in discrete steps from one single event to the next, so that at least one event is always present in the cluster (at the beginning of the interval). This gives rise to the coefficient f_1 in the expression (4). If a new single event falls into the τ-sec window when the beginning of the interval passes to the next event, then the number of clusters with a given multiplicity increases by one. If, however, no new event is added and the newly formed cluster has a multiplicity smaller by one than the preceding one, then this cluster is considered to be a "fragment" of the preceding one and is disregarded in the distribution.
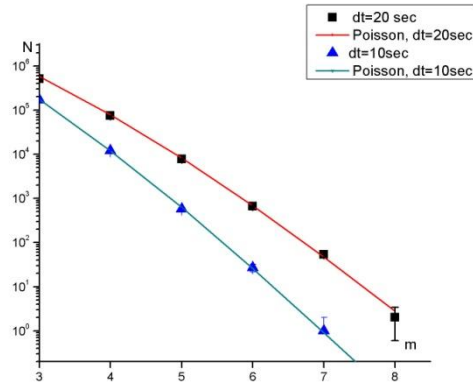
Fig2. *The number of clusters with k single events within time interval dt= 20 s and dt= 10 s. Squares and triangles are experimental data, the curves are the expected number according to the expression (4).*

This variant of processing guarantees against the loss of a cluster with a greater multiplicity (because some of the events fall into the neighboring cluster), but, at the same time, some clusters overlap in time, which leads to some deviation from the Poisson distribution.

According to the expression (4), background events create clusters with k = 8 with the rate 0.178 y^{-1}. The expected number of such clusters during the time interval T = 15.5 y is 2.75 that we observe (2 events). The formation rate of clusters with k = 9 background events is 9.2 $\approx$ 10^{-3} y^{-1}, therefore the cluster with multiplicity k$\geq$ k_{th} = 9 should be considered as a neutrino burst detection.

3.1. Two independent detectors

To increase the number of detected neutrino events and to increase the "sensitivity radius" of the BUST, we use those parts of external scintillator layers that have relatively low count rate of background events. The total number of counters in these parts is 1030, the scintillator mass is 112 tons. We call this array the D2 detector, it has the count rate of single events f_2 = 0.12 s^{-1}. The joint use of the D1 and the D2 detectors allows us to increase the number of detected neutrino events and the detection reliability of a neutrino burst.

We use the following algorithm: in case of cluster detection with k1 $\geq$ 6 in the D1, we check the number of single events k2 in the 10-second time frame in the D2 detector. The start of the frame coincides with the start of the cluster in D1. Mass ratio of D2 and D1 detectors 1030/1200 = 0.858 implies that for the mean value of neutrino events k1 = 6 in D1, the mean number of neutrino events in D2 will be $\overline{k2}$ times 0.858 *0.8 = 4.12 (factor 0.8 takes into account that the frame duration in the D2 is 10 seconds instead of 20 seconds in the D1). Since the background adds f_2 $\times$10 s = 1.2 events, we obtain finally $\overline{k2}(\overline{k1}=6) = 4.12+1.2 = 5.32$.

According to the exp. (2), the expected average number of detected neutrino events in the D2 detector is $N_{ev}^H \cong 29$ (under the same conditions and assumptions as in (3). So the expected total number of detected neutrino events (in IBD reactions (1)) is

$$N_{ev}^H = N_{ev}^H(D1) + N_{ev}^H(D2) \approx 67 \ \ (no\ oscillations) \tag{5}$$

The D1 and the D2 detectors are independent therefore the imitation probability of clusters

with multiplicities k1 in the D1 and k2 in the D2 by background events is the product of appropriate probabilities

$$P(k1,k2) = P1(k1) \times P2(k2) \qquad (6)$$

and we obtain $P(6,5) = 0.23$ y^{-1}, $P(6,6) = 0.045$ y^{-1} (note that P1 is determined according to the expression (4) and P2 is the Poisson distribution).

Therefore the events with $k1 \geq 6$, $k2 \geq 6$ should be considered as candidates for a neutrino burst detection (since mean values of k1 and k2 are significantly exceeded in two independent detectors simultaneously and the imitation probability of such events by background is very small).

Notice that in case of a real neutrino burst, the remainder of counters (which do not belong to the D1 and the D2) can be used as the third independent detector – the D3 with the mass of 100 ton.

3. Conclusion

The Baksan Underground Scintillation Telescope operates under the program of search for neutrino bursts since June 30, 1980. As the target, we use two parts of the BUST (the D1 and D2 detectors) with the total mass of 242 tons. The estimation (5) allows us to expect ≈ 10 neutrino interactions from a most distant SN (≈ 25 kpc) of our Galaxy.

Background events are 1) decays of cosmogeneous isotopes (which are produced in inelastic interaction of muons with the scintillator carbon and nuclei of surrounding matter) and 2) cosmic ray muons if only one counter from 3184 hit.

Over the period of June 30, 1980 to December 31, 2018, the actual observation time was 33.02 years. This is the longest observation time of our Galaxy with neutrino at the same facility. No candidate for the core collapse has been detected during the observation period. This leads to an upper bound of the mean frequency of gravitational collapses in the Galaxy

$$f_{col} < 0.070 \ y^{-1}$$

at 90% CL. Recent estimations of the Galactic core-collapse SN rate give roughly the value ≈ 2-5 events per century (see e.g. [25].

Acknowledgements

References

[1]   Gamow G. and Shoenberg M., The Possible Role of Neutrinos in Stellar Evolution, Phys. Rev., 58, 1117 (1940)

[2]   Zeldovich Ya.B. and Guseinov O.Kh., Neutronization of matter during collapse and the neutrino spectrum, Dokl. Akad. Nauk SSSR, 162, 791,(1965)

[3] Colgate S.A. and White R.H., The hydrodynamic behavior of supernovae explosions, Astrophys. J., 143, 626 (1966)

[4] Loredo T.J., Lamb D.Q., Bayesian Analysis of Neutrinos from Supernova SN1987A, Phys.Rev.D, 65, 063002 (2002)

[5] Pagliaroli G., Vissani F., Costantini M.L., Ianni A., Improved analysis of SN1987A antineutrino events, Astropart. Phys., 31, 163 (2009)

[6] E.N. Alekseev, L.N. Alekseeva, V.I. Volchenko et al., Upper bound on the collapse rate of massive stars in the Milky Way given by neutrino observations with the Baksan underground telescope, Zh. Eksp.Teor.Fiz.,104, 2897 (1993)

[7] Novoseltseva R.V., Boliev M.M., Dzaparova I.M. et al., The Search for Neutrino Bursts from Core Collapse Supernovae at the Baksan Underground Scintillation Telescope, Phys. Part. Nucl. {\bf 47}, 968 (2016)

[8] M. Ikeda, A. Takeda, Y. Fukuda et al., (Super-Kamiokande Collaboration) "Search for Supernova neutrino bursts at Super-Kamiokande", Astrophys.J., 669, 519 (2007)

[9] Ambrosio M. et al. (MACRO Collaboration) Search for stellar gravitational collapses with the MACRO detector, Eur.Phys.J.C, 37, 265 (2004)

[10] Aglietta M. et al. (LVD Collaboration), The most powerful scintillator supernovae detector: LVD, Nuovo Cimento A, 105, 1793 (1992)

[11] Ahrens J. et al. (AMANDA Collaboration), Search for supernova neutrino bursts with the AMANDA detector, Astropart.Phys., 16, 345 (2002)

[12] B. Aharmim, S.N. Ahmed, A.E. Anthony et al., Low Multiplicity Burst Search at the Sudbury Neutrino Observatory, Astrophys. J., 728, 83 (2011)

[13] T. Lund, A. Marek, C. Lunardini et al., Fast time variations of supernova neutrino fluxes and their detectability, Phys. Rev. D 82, 063007 (2010)

[14] Bellini G. et al.(Borexino Collaboration), First real time detection of 7Be solar neutrinos by Borexino, Phys. Lett. B 658 (4), 101 (2007)

[15] Bellini G., Novel results on low energy neutrino physics, Talk at TAUP 2011 conference, Munich, 5-9 Sept. 2011,

[16] Eguchi K. et al. (KamLAND Collaboration), First Results from KamLAND: Evidence for Reactor Antineutrino Disappearance, Phys. Rev. Lett. 90, 021802 (2003)

[17] E.N.Alexeyev, V.V.Alexeyenko, Yu.M.Andreyev et al., Baksan underground scintillation telescope, in proceedings of 16 ICRC, Kyoto, 10,276 (1979)

[18] Achkasov V.M., Bakatanov V.N., Novoseltsev Yu.F.et al., An investigation of the energy spectrum and inelastic muon interaction at the Baksan Underground scintillation telescope, Bull. Russ. Acad. Sci. Phys.,50, 2224 (1986)

[19] Imshennik V.S., Nadezhin D.K. Final stages of star evolution and supernova explosions, Itogi Nauki i Tehniki, ser. Astronomy 21, 63 (1982)

[20] Hillebrandt W., Hoish P., The supernova 1987A in the Large Magellanic Cloud, Rep. Prog. Phys. 52, 1421 (1989)

[21] Strumia A. and Vissani F., Precise quasielastic neutrino/nucleon cross section, Phys. Lett.

B 564, 42, (2003); [astro-ph/0302055]

[22] Pantaleone J., Neutrino oscillations at high densities, Phys. Lett. B 287,128 (1992)

[23] Sawyer R.F., Speed-up of neutrino transformations in a supernova environment, Phys. Rev. D 72, 045003 (2005)

[24] Duan H., Fuller G.M., Carlson J. et al., Simulation of Coherent Non Linear Neutrino Flavor Transformation in the Supernova Environment I: Correlated Neutrino Trajectories, Phys. Rev. D 74, 105014 (2006)

[25] I. Tamborra, G. Raffelt, F. Hanke et al., Neutrino emission characteristics and detection opportunities based on three-dimensional supernova simulations, Phys. Rev. D 90, 045032 (2014)

[26] Adams S.M., Kochanek C.S., Beacom J.F. et al., Observing the Next Galactic Supernova, Astrophys.J., 778, 164(2013)

Search and study of optical transients with Mini-MegaTORTORA

N.V. Orekhova[4,*], G.M. Beskin[1, 2], A.V. Birykov[2, 5], S.F. Bondar[4], E.A. Ivanov[4], S.V. Karpov[1,2,6], E.V. Katkova[4], A.V. Perkov[4], V.L. Plokhotnichenko[1], V.V. Sasyk [2 ,3]

[1]*Special Astrophysical Observatory of RAS, Nizhny Arkhyz, Russia*

[2]*Kazan Federal University, Kazan, Russia*

[3]*JS "Parallax" Enterprise, Kazan, Russia*

[4]*Optical observation station "Arkhyz", RPC PSI, Nizhny Arkhyz, Russia;*

elvilforeva@gmail.com

[5]*Sternberg Astronomical Institute, Moscow State University, Moscow, Russia*

[6] *CEICO Institute of Physics, Czech Academy of Sciences, Prague, Czech Republic*

Abstract We present the four-year observation results of the Mini-MegaTORTORA (MMT-9) nine-channel wide-field optical sky monitoring system with subsecond temporal resolution. This instrument scans the sky on every clear night with a FoV as large as 900 deg^2. It is used for real-time detection and classification of optical transients, three-filter photometry close to Johnson's BVR system, and polarimetry of detected objects. The limiting magnitude of the system is V = 11m for 0.1 s (one frame duration) temporal resolution, and reaches V = 13-14 m for an exposure of several minutes. The system is equipped with a powerful computing facility and a dedicated software pipeline to perform automatic detection, real-time classification, and investigation of transient events of different natures moving in the near-Earth space located in the Galaxy and at cosmological distances. Properties of meteors and satellite samples, variable stars, and GRBs detected using MMT-9 are discussed.

Keywords: Gamma-Ray Bursts, Meteors, Satellites, Astronomical Databases, High Temporal Resolution

1. Introduction

In order to address the problems of detection and study of near-Earth (space debris, artificial satellites, meteors, minor bodies of the solar system) and deep space (flaring variable stars, novae and supernovae, gamma-ray bursts, etc.) transient events, a new field in astronomy has emerged – "Time Domain astronomy" (Table 1). The IAU website provides data on 62 instruments under "Time domain astronomy" [1]. They have various technical characteristics and are intended for investigating sources spanning a wide range of magnitudes, radiation duration, and angular velocities.

To detect optical emission from transient sources occurring at arbitrary moments in time and coming from random directions (gamma-ray bursts), the use of instruments with wide fields of

view and subsecond temporal resolution was suggested in [2], [3].

Table1. *Transient events zoo*

Time scale	Near-Earth, the Solar system	Inside our Galaxy	Nearby galaxies	Cosmological Distances
< 0.1 s	meteors, LEO satellites and debris	novae, flaring stars, star occultations	nearby supernovae	GRBs, FRBs, gravitational wave events
1 s	HEO and GEO satellites and debris			
10 s				
100 s	asteroids, comets		intra-day variable AGNs	
> 1000 s		variable stars, MACHOs		supernovae

This approach was implemented with development of the FAVOR (2003-2009 in Nizhniy Arkhyz) and TORTORA (starting from 2006 in Chile, La Silla observatory, European Southern Observatory) facilities [3], [4], [5]. These are small-lens (120-150 mm) telescopes with an optical efficiency of 1/1.2. A combined system was used as the detector consisting of an electron-optical converter and a fast low-noise Sony IXL285 array. Such a combination gave a 340-760 square-degree field of view and a limiting magnitude of up to 10.5 in the B-band for a frame rate of 7.5 Hz (128 ms exposure).

With the TORTORA camera, the optical flare accompanying the Naked-Eye Burst of GRB 080319b was detected in 2008. A visual light curve was obtained with a resolution of less than one second, which allowed us to study the temporal structure of this event and match the optical flare with the structure of gamma-ray emission [6].

A large number of near-Earth objects were detected with the FAVOR camera: artificial Earth satellites and debris, including low-orbit space objects with angular velocities up to 1 degree/second. Many meteor events were also detected, including those with magnitudes of up to 8-9, previously undetectable in optical observations using other methods [7].

A natural modernization of this approach led to development of multichannel (multi-lens) systems with wide fields of view and subsecond temporal resolution. Such instruments allow one to monitor and study in detail the discovered transient event. In the latter case, individual channels register simultaneously in various color- and polarization filters the image of the region containing the new source. Thus, spectral and polarization studies are now possible for rapid events and processes.

The principles outlined above were implemented in the Mini-MegaTORTORA system.

2. Mini-MegaTORTORA (MMT-9)

Mini-MegaTORTORA is an automated multi-channel monitoring telescope. The system consists of 9 channels-objectives, installed on 5 mounts located under a common sliding cylindrical cover (Fig.1).

A movable coelostat mirror is mounted in an individual channel of MMT-9 in front of the objective allowing one to quickly change its field of view. It is also equipped with a set of BVR-filters and a polaroid, which can be introduced into the optical beam during observations should the need arise [8], [9].

Fig1. *Mini-MegaTORTORA*

Andor Neo sCMOS cameras are used as the detector. They have low readout noise (1-2,5 electrons per detector element) and a high quantum efficiency (up to 60% at 600 nm).

The field of view of a single channel amounts to ~100 square degrees; the total field of view is determined by the task at hand and depends on the selected sky area configuration (see observing modes below) and reaches 900 square degrees in the wide-field monitoring mode.

The entire system is controlled by the central server. The software installed on the server is responsible for planning and conducting observations. The server gathers data on the weather conditions obtained using the meteostation (Boltwood Cloud Sensor II + allsky camera + Sky Quality Meter), and signals the start of observations in the event of clear, favorable weather: the automated cover opens, the channels are calibrated, and observations begin. At the end of the night, or if the weather conditions become unfavorable, the server orders the stop of operations.

Each channel has an individual computer dedicated to equipment control and data collection functions. Data obtained in the process of observations is transferred to the channel computer in the form of a flow of frames and is reduced in real time. This allows one to detect transient events independently during the night.

Observations are conducted in several modes: wide-field monitoring, deep survey, research mode, work with internal and external alerts. The main mode is the wide-field monitoring. The system targets the selected region in the sky, positions the channels in a 3×3 configuration (one area equals 900 square degrees), and obtains a frame flow with 0.1 second exposures (10 Hz frame rate); the limiting magnitude in this mode reaches 11 st.mag. The areas targeted for monitoring are computed using the observation planning software in a way that would allow the maximum area of the celestial sphere to be covered in a single night, with the positions of the Sun and Moon also taken into account. If the fields of view of the FERMI and Swift gamma-ray space telescopes come into the MMT-9 visibility range, the region where these two fields of view overlap is selected for wide-field monitoring. Each sky area is monitored for 1000 seconds, then the next area is selected.

For independent transient detection in real time, this mode uses specialized software, allowing one to detect light variations in the frame flow and determine the type of the possible source. If the registered object is stationary and newly emerged, it is classified as a flare. Moving new sources are defined as satellites and meteors depending on the angular velocities and durations [5]. Discovered transients are saved in the corresponding databases. When registering events are classified as flares, the system goes into internal follow-up observing mode. All channels position their fields of view based on the coordinates of the detected burst (10×10 degree total field of view). Each channel is set with its own filter configuration and

exposure time. As a result, the transient event is observed simultaneously in three color bands as it passes through three polaroids with different orientations, which allows one to determine its spectral and polarization (3 Stokes parameters) properties.

When the MMT-9 system receives telegrams from the FERMI and SWIFT telescopes in the event of gamma-ray burst registration, and, if the coordinates of the discovered alert are in the visibility zone, the system goes into external follow-up mode. The total field of view dimensions, exposure times for each channel, and the filter sets are determined depending on information in the received telegram. After carrying out alert-based observations, the system returns to the basic mode.

Before the start of wide-field monitoring of each area with a high temporal resolution and immediately after such, a deep survey of that sky region is carried out. Frames are obtained with 60 second exposure and 900 square degree field of view, the limiting apparent magnitude reaches 14-15 mag. Images obtained in this mode are stored in the database since August 2014. Based on this array of frames, one can conduct studies of transient objects with long times of light variations (variable stars, minor bodies of the Solar System).

A possibility is provided to observe selected sources or events in different modes, the data on which are entered into the planning software. The software incorporates this task into the observation list and executes it when the source is in the visibility zone.

3. Four-year work results

MMT-9 carries out regular monitoring of the celestial sphere continuously since June 2014.

3.1. Rapid Flashes and Gamma-ray bursts

Observations of regions where Swift and Fermi gamma-ray space telescopes registered transients are conducted since 2015; this mode was implemented 71 times: 15 follow-ups to Swift and 56 to Fermi. The diagram in Fig.2 shows the time distribution of realignment based on telegrams.
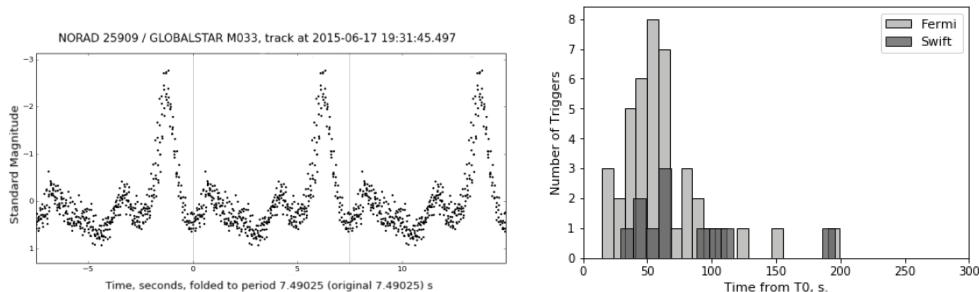
Fig2. *Right: time between observations in the follow-up mode after Fermi and Swift telegrams received and T0. Left: photometry of satellites with MMT-9 example*

Time of switching to observations of areas noted in the telegrams varies in the range from 14 seconds to several minutes from the moment of transient detection from space (T0). Long delays in the start of optical observations (exceeding 5 minutes) are usually related to either a delay in the emergence of this sky region above the horizon, or waiting for better weather conditions.

In particular, in 2016, 2 minutes after the Fermi telescope detected the GRB160625B gamma-ray burst, the follow-up mode allowed us to detect an optical flare accompanying the hard emission from this source [10].

3.2. Artificial Satellites and debris

MMT-9 allows us to register several hundred near-Earth space objects every clear night (artificial satellites, space debris). The program for detecting all sources classified as satellites determines the coordinates and derives magnitude estimates for each frame. The sequence of the object's positions in all frames where it was detected will henceforth be referred to as one follow-through.

Based on the data of the obtained follow-throughs, the sources are identified with satellites and space debris listed in available orbital data catalogs, and are stored in the photometry database of MMT-9 [11], [12].

As of January 1, 2019, the artificial satellite database of MMT-9 contains photometric data on 6048 space objects on near-Earth orbits, measured in 201157 follow-throughs.

For each object we compute the average reduced (to a distance of 1000 kilometers and a 90° phase angle) magnitude based on all obtained measurements. When working in the BVR-filter mode, the reduced magnitude in the specified filter (figure) is computed. An example is shown in Fig.2.
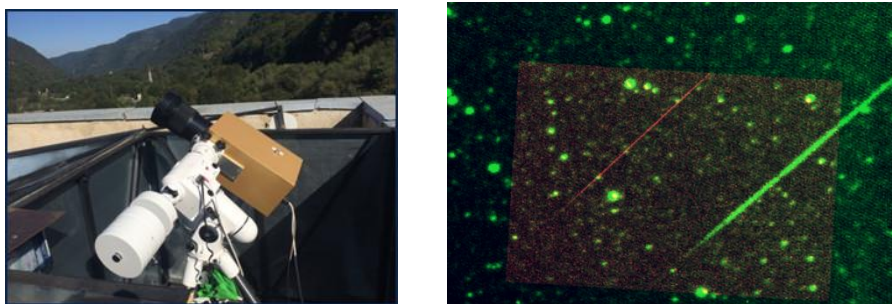
Fig3. *Right: the FAVOR camera was mounted with a base of 3.5 km from MMT-9; Left: image with combined frames of one meteor, parallax is seen*

Information stored in the artificial satellite database is used to analyze light variations of the space objects. For objects with obvious light periodicity, we determine the period of magnitude variations (in seconds).

In addition to the measured and reduced magnitudes of the objects, data on distance and phase angle during the observations are stored in the database.

3.3. Meteors

Several hundred meteor events are registered with Mini-MegaTORTORA during every observing night.

The detection program classifies objects as meteors in real time and analyzes them. For each meteor event we determine the coordinates, visual magnitude, angular velocities, durations, etc. This information is stored in the Database [13].

As of the end of December 2018, the meteor database contains over 220 thousand events detected with MMT-9 since 2014 and 10117 events detected with FAVOR in 2006-2009 [14].

To improve the capabilities of MMT-9 in studying meteor events, base observations (in the test mode) are being conducted since the end of 2018 with FAVOR, which was modernized and equipped with a time service. As a pair, they form a base of 3.5 km (Fig.3). Primary meteor observations allow one to estimate heights and velocities of the meteor particles burned up in the atmosphere, which, in turn, allows one to switch to the heliocentric coordinate system and study the orbital parameters of both individual meteoroids and meteor showers. Base test observations in the fall of 2018 have shown that the accuracy of height determination amounts to about 1.5-3%. Over one hundred primary meteors have been detected. We show examples of computing the absolute magnitude variations of several observed meteors with loss of height and motion along the trajectory (Fig. 4).
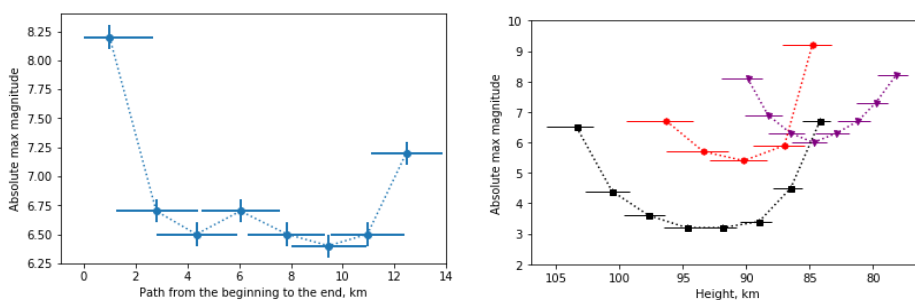
Fig4. Dependence of absolute magnitude on height and path

The number of meteor events observed during a night allows one to study their apparent sky distribution. Meteor tracks, extrapolated backwards by 50 degrees, are plotted on the map of the sky, and the more of these tracks cross in one area, the higher their density there [13]. The so-called "statistical" radiants are detected in zones with the highest density. The same map is used to plot radiants of meteor showers listed in [15]. Based on many confirmed showers, there is a correspondence with the areas of maximum density of meteor tracks and radiants, which is especially noticeable for major meteor showers (PER, GEM, LYR, SOA, DRA, NOA, ORI, LEO, etc.). These statistical radiants may be used to determine meteor shower candidates, which must then be studied in base observations.

Observing meteors with BVR-filters enabled us to estimate the color change of the meteors along the track [13]. Evidently, a meteor track does not exhibit black body radiation, but a combination of the continuum and various emission lines. The conducting of future joint multicolor observations with MMT-9 and FAVOR will allow us to investigate the possible connection between belonging to meteor showers, meteor velocities, and their color indices.

Acknowledgements

References

[1]   (2017) IAU Working Group on Time Domain Astronomy website. [Online]. Available: http://timedomainastronomy.net

[2]   Karpov S., Beskin G., Biryukov A., Bondar S., Hurley K., Ivanov E., Katkova E., Pozanenko A., Zolotukhin I. Optical Camera with high temporal resolution to search for transients in the wide field. Il Nuovo Cimento C 2005;   vol. 28, Issue 4, p.747.

[3]   Zolotukhin I., Beskin G., Biryukov A., Bondar S., Hurley K., Ivanov E., Karpov S., Katkova E., Pozanenko A. Optical camera with high temporal resolution to search for transients in the wide field. Astronomische Nachrichten 2004; Vol.325, Issue 6, p.675-675.

[4]   Beskin G., Bondar S., Ivanov E., Karpov S., Katkova E., Pozanenko A., Guarnieri A., Bartolini C., Piccioni A., Greco G., Molinari E., Covino S. Monitoring with high temporal resolution to search for optical transients in the wide field. High Time Resilution Astrophysics: The Universe at Sub-Second Timescales. AIP Conference Proceedings, Vol. 984, pp. 73-80 (2008).

[5]   Karpov S., Beskin G., Bondar S., Guarnieri A., Bartolini C., Greco G., Piccioni A. Wide and Fast: Monitoring the Sky in Subsecond Domain with the FAVOR and TORTORA Cameras. Advances in Astronomy, 2010, article id. 784141.

[6]   Beskin G., Karpov S., Bondar S., Greco G., Guarnieri A., Bartolini C., Piccioni A., Molinari E., Chinkarini G. TORTORA discovery of Naked-Eye Burst fast optical variability. 2008 NANJING GAMMA-RAY BURST CONFERENCE. AIP Conference Proceedings, Vol. 1065, pp. 251-254 (2008).

[7]   Bagrov A.V., Beskin G.M., Biryukov A.V., Bondar S.F., Zolotukhin I.Y., Karpov S.V., Ivanov E.I., Pozanenko A.S. Wide field fast optical camera to search for flashing and moving objects./ Near-Earth Astronomy − 2003. Proceedings. vol.2. Terskol, 8-13 september. 2003 // Institute of Astronomy RAS. – Saint-Petersburg.: VVM, 2003.- pp.101-106.

[8]   Beskin G., Bondar S., Karpov S., Plokhotnichenko V., Guarnieri A., Bartolini C., Greco G. Multi-objective transforming telescope for wide-field optical monitoring of the sky with high-temporal resolution. Ground-based and Airborne Telescopes III. Proceedings of the SPIE, Vol. 7733, article id. 77330V, 17 pp. (2010).

[9]   Beskin G., Karpov S., Biryukov A., Bondar S., Ivanov E., Katkova E., Orekhova N., Perkov A., Sasyuk V. Wide-field optical monitoring with Mini-MegaTORTORA (MMT-9) multichannel high temporal resolution telescope. Astrophysical Bulletin, Volume 72, Issue 1, pp.81-92.

[10] Zhang B.B., Zhang B., Castro-Tirado A.J., Dai Z.G., Tam P.H.T., Wang X.Y., Hu Y.D., Karpov S., Pozanenko A., Zhang F.W., Mazaeva E., Minaev P., Volnova A., Oates, S., Gao H., Wu X.F., Shao L., Tang Q.W., Beskin G., Biryukov A., Bondar S., Ivanov E., Katkova E., Orekhova N., Perkov A., Sasyuk V., Mankiewicz L., Zarnecki A.F., Cwiek A., Opiela R., Zadrozny A., Aptekar R., Frederiks D., Svinkin D., Kusakin A., Inasaridze R., Burhonov O., Rumyantsev V., Klunko E., Moskvitin A., Fatkhullin T., Sokolov V.V., Valeev A.F., Jeong S., Park I.H., Caballero-Garcia M.D., Cunniffe R., Tello J.C., Ferrero P., Pandey S.B., Jelinek M., Sanchez-Ramirez R., Castellon A. Transition from fireball to Poynting-flux-dominated outflow in the three-episode GRB 160625B //Nature Astronomy. – 2018. – Т. 2. – №. 1. – С. 69.

[11] Katkova E., Beskin G., Biryukov A., Bondar s., Davidov D., Ivanov E., Karpov S., Orekhova N., Perkov A., Sasyuk V. Mass photometry of low orbital artificial satellites on MMT-9 //Near-Earth Astronomy-2015. - 2016. - pp. 261-267.

[12] (2018) MMT-9 satellites database [Online]. http://mmt9.ru/satellites.

[13] Orekhova N., Beskin G., Biryukov A., Bondar S., Ivanov E., Karpov S., Katkova E., Perkov A., Sasyuk V., Usanin V. Meteors observation with Mini-MegaTORTORA (MMT-9) system //Near-Earth Astronomy-2015. - 2016. - pp. 76-82.

[14] (2018) MMT-9 meteors database [Online]. http://mmt9.ru/meteors.

[15] (2018) IAU Meteor Data Center [Online]. http://pallas.astro.amu.edu.pl/~jopek/MDC2007.

The multi-messenger astronomy: experiments in the Baksan Neutrino Observatory

V. B. Petkov[1,2]

[1]Institute for Nuclear Research of the Russian Academy of Sciences, 60th October Anniversary Prospect, 7a, 117312 Moscow, Russia; vpetkov@inr.ru

[2]Institute of Astronomy of the Russian Academy of Sciences, 48 Pyatnitskaya St., 119017, Moscow, Russia

Abstract An overview of current and future experiments in the field of multi-messenger astronomy at experimental facilities of the Baksan Neutrino Observatory is presented. Different types of these experiments are discussed.

1. Introduction

Because the high-energy sky has revealed a large number of powerful astrophysical objects capable to emit radiation across the entire electromagnetic spectrum the multi-messenger approach is widely applied now for the study of astrophysical objects and transient phenomena. It is obvious that the joint study of different "cosmic messengers" (cosmic rays, neutrinos, photons, and gravitational waves) is necessary for the complete understanding of the most energetic phenomena in the Universe.

Multi-messenger observations can be conditionally divided into 3 types. To the first type we attribute independent measurements of different messengers which physically are closely connected. (e.g. gamma-rays and neutrino). The synchronous observations of astrophysical objects by means of different messengers relate to the second type. The third type corresponds to the fast response astronomy observations, namely, the quick search of other messenger partners after the alert. All three types are practically accessible to experimental facilities of the Baksan Neutrino Observatory.

The Baksan Neutrino Observatory of the Institute for Nuclear Research of the Russian Academy of Sciences (BNO INR RAS) is one of the centers, in which the research in this direction is being conducted. The observatory is located in the North Caucasus in the Baksan River valley (the geographic coordinates are 43.28° N and 42.69° E, the effective rigidity of geomagnetic cutoff is 5.7 GV). BNO has a unique set of surface and underground experimental facilities, which have been used for the research in the area of the fundamental physics for more than forty years [1]. The research program of the observatory was constantly expanding as new ground and underground setups were put into operation.

2. Complex of experimental facilities

The complex of experimental facilities used in the multi-messenger astronomy studies

consists of the Baksan Underground Scintillation Telescope (BUST) and the "Andyrchy" and EAS "Carpet-2" ("Carpet-3") arrays.

The BUST is located in an underground laboratory under the slope of the Andyrchy Mountain at an effective depth of 850 m.w.e.; its height above sea level is 1700 m [2, 3]. Its size is $17 \times 17 \times 11$ m^3 and it consists of four horizontal and four vertical scintillation planes. The planes of the telescope are covered with scintillation counters, the total number of which is 3184. A standard scintillation counter of BUST is an aluminum container of a size of $0.7 \times 0.7 \times 0.3$ m^3 filled with liquid whitespirit-based organic scintillator. The scintillator volume is viewed by a FEU-49B photomultiplier with a photocathode diameter of 15 cm. The most probable energy release in the counter from muons is 50 MeV. The DAQ system is triggered by a pulse from the channel of any BUST counter. The counting rate of such a trigger is 17 s^{-1}.

The "Andyrchy" EAS array is located on the slope of the Andyrchy Mountain above the BUST and consists of 37 scintillation counters based on plastic scintillators [4]. A plastic scintillator with an area of 1 m^2 is viewed by a FEU-49B photomultiplier. Scintillation counters are designed for both temporal measurements (to determine the direction of an EAS arrival) and for measuring the energy release (to determine the position of the axis and the total number of particles in the EAS). The EAS trigger operates at a simultaneous triggering of four or more counters of the setup, the frequency of the trigger is ~9 s^{-1}. The distance between counters in the horizontal plane is 40 m. The central counter of an array is located directly above the BUST, the vertical distance is ≈350 m. Total area of the "Andyrchy" EAS array is 5×10^4 m^2 and the solid angle visible from the telescope is 0.35 steradian. The center of the setup is at an altitude of 2057 m above sea level, the height difference between the upper and lower rows of scintillation counters is 150 m.

The "Carpet-2" EAS array [6] is located at the foot of Andyrchy Mountain at a distance of 900 m from BUST, at an altitude of 1700 m above sea level (which corresponds to a depth in the atmosphere of 840 g /cm^2). The central part of the setup (the "Carpet" itself [5]) is located in a building under a roof of 29 g/cm^2 thickness and consists of 400 liquid scintillation counters (of the same type as the BUST), arranged in a square with a side of 14 m and covering an overall area of 196 m^2. Around the "Carpet-2" there are six remote points (RP) with a thin roof (~1.2 g/cm^2), in each of them there are 18 identical counters. Signals from a RP are used to determine direction of the EAS arrival.

The building of the muon detector (MD) consists of three tunnels with an area of 205 m^2 each. The thickness of the absorber is 500 g/cm^2, which corresponds to the threshold energy of muons of 1 GeV for the vertical direction. The distance between the centers of "Carpet" and MD is 47 m. Since 1999, the first MD stage of 175 m^2 area has been put into operation, consisting of 175 scintillation counters located in the central tunnel, of the type identical to that of the "Andyrchy" EAS array.

At present the "Carpet-3" EAS array is designed on base of the "Carpet-2" array [7]. Within the framework of creation of new apparatus, two tunnels were completely filled with scintillation counters and the total area of MD was brought up to 410 m^2. Realization of the EAS array suggests that continuous area of MD should be then increased up to 615m^2. At the same time, to increase the detection area of the EAS axes, 20 additional modules with liquid scintillation counters in each module will be installed. The results of calculations of selection efficiency of air showers from primary gamma rays demonstrated that the new array will have the world-best sensitivity to the flux of cosmic gamma rays with energies in the range 100 TeV – 1 PeV.

3. Multi-messenger astronomy at BNO: independent measurements of different messengers

An impressive example of the first type of multi-messenger observations is the measurement of fluxes of astrophysical gamma-rays and neutrinos. There is a connection between these fluxes because energetic photons accompany energetic neutrinos. The general model for production of energetic astrophysical neutrinos implies their creation in decays of charged pi-mesons (pions), produced in turn in high-energy hadronic or photohadronic interactions. These charged pions are necessary accompanied by neutral pions which decay to photons. Since the neutrinos propagate freely through the Universe while the photons may be absorbed, a comparison of the two fluxes may give important information about the distribution of sources.

The diffuse flux of astrophysical neutrinos has been measured in the IceCube experiment [8]. If such neutrinos are a result of decays of charge pions in the Galaxy halo the corresponding diffuse flux of primary gamma rays with energies higher than 100 TeV is close to experimental limits in this energy range [9]. Future searches for the diffuse gamma-ray background in this energy range just below current upper limits will give a crucial diagnostic tool for distinguishing between the Galactic and extragalactic models of origin of the IceCube events. The "Carpet-3" EAS array which is under development now will have the world-best sensitivity to the flux of cosmic gamma rays with energies in the range 100 TeV – 1 PeV [7]. So the measurement of diffuse flux of cosmic gamma rays in the "Carpet-3" experiment gives a principal possibility to resolve the problem of origin of astrophysical neutrinos detected in the IceCube experiment.

The search for primary photons with energies > 1 PeV, directionally associated with the IceCube high-energy neutrino events, has been performed using data obtained in 3080 days of Carpet-2 live time [10]. The first ever limits on PeV photons coming from the arrival directions of IceCube high-energy neutrino events were obtained. These limits may be used to constrain potential models of the neutrino origin in Galactic point sources. Besides, if the extragalactic origin of neutrinos is independently assumed, these results could constrain new-physics models affecting gamma-ray propagation.

4. Multi-messenger astronomy at BNO: synchronous observations.

For synchronous observations of astrophysical objects by means of different messengers it is necessary that these objects were simultaneously located in the field of view of different experimental facilities. Because the experimental facilities of the BNO must be operating all time the first requirement – simultaneity – is always automatically realized.

As the BUST cannot identify the arrival direction of low energy electron neutrinos/antineutrinos, the whole sky is accessible for us in the searching of these particles. First of all, it is necessary to note the search for neutrino bursts from supernovae at the BUST [11]. In this experiment the best limit on the mean frequency of collapses in the Galaxy has been obtained.

For the reason of the background suppression, for the search of electron neutrino/antineutrino in the energy range from 21 MeV to 100 MeV the reactions of their interaction with carbon in a scintillator are used [12, 13]. This technique was used at the BUST for the search of neutrino signal in time coincidence with cosmic gamma-ray bursts (GRBs) and gravitational wave events. So, no neutrino signals associated with 97 gamma-ray bursts

recorded during 2012 by SWIFT in the time window ±1000 s were found [12]. Also no neutrino signals in the interval of ±500 s from the gravitational wave events GW150914, GW151226, GW170104, GW170608, GW170814, and GW170817 have been detected. Only limits on the fluxes of low-energy electron neutrinos and antineutrinos from astrophysical sources of gravitational bursts have been obtained [13]. Figures 1 and 2 show the upper limits (at 90% C.L.) obtained at the BUST on the fluxes of electron neutrinos and antineutrinos from gravitational wave events as functions of their energy (for a monoenergetic spectrum) in comparison with the Borexino, KamLAND, and Super-Kamiokande results.
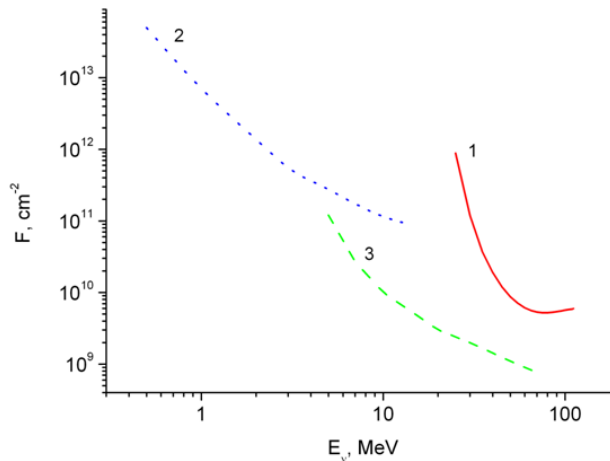
Fig1. Upper limits on the flux of electron neutrinos versus their energy (for a monoenergetic spectrum) according to (1) reaction with carbon at the BUST, (2) elastic scattering at the Borexino detector, and (3) elastic scattering at the Super-Kamiokande detector.
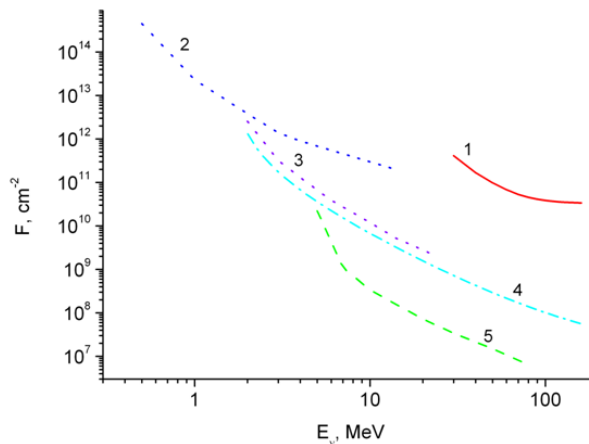
Fig2. Upper limits on the flux of electron antineutrinos versus their energy (for a monoenergetic spectrum) according to (1) reaction with carbon at the BUST, (2) elastic scattering at the Borexino detector, (3) inverse beta decay at the Borexino detector, (4) inverse beta decay at the KamLAND detector, and (5) inverse beta decay at the Super-Kamiokande detector.

The BUST construction allows us to identify tracks of muons crossing the telescope. Muons from the lower hemisphere can be only from muon neutrinos whose traveling through the rock may interact with nucleons to create energetic muons. Separation of arrival directions between the upper and lower hemispheres is carried out using the time-of-flight method. Hence we can perform the search of muon neutrinos from astrophysical objects only for objects located in the lower hemisphere at the moment. Selection criteria of neutrino events in the BUST cut off particles with energies below 1 GeV.

The search for muon neutrinos with energy ≥1 GeV correlated with GRBs has been carried out at the BUST [14]. Between December 1978 and December 2013 more than 1500 localized GRBs, which occurred in the field of view of the BUST, coincided with the BUST operation periods. No neutrino signal from GRBs was detected. Figure 3 shows the model-independent GRB neutrino upper limits on GRB neutrino fluence per GRB obtained at the BUST in comparison with results of other experiments.
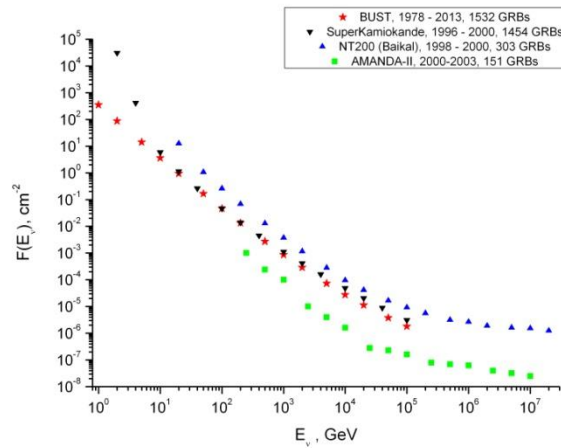
Fig3. The 90% CL upper limits versus their energy (for a monoenergetic spectrum) on GRB neutrino fluence per GRB obtained at the BUST, Super-Kamiokande, AMANDA and Baikal.

5. Multi-messenger astronomy at BNO: fast response astronomy

The search for optical partners of bursts of cosmic gamma-ray radiation and cosmic ray intensity of high and very high energy range is conducted using the experimental facilities of the BNO and a complex of astronomical telescopes at Peak Terskol Observatory of the Institute of Astronomy of RAS. The bursts of cosmic ray intensity and cosmic gamma radiation are detected at the BNO experimental facilities. The search and subsequent study of optical flares associated with the detected BNO events are carried out on a complex of astronomical telescopes at the peak Terskol. This experiment is aimed at obtaining new experimental data on astrophysical objects generating bursts of cosmic gamma radiation of high energy together with optical flashes. Such bursts of radiation can be generated by processes in the nuclei of galaxies, by interaction of astrophysical objects, at the last stage of evolution of stars including supernova bursts. Now the search for bursts of cosmic ray intensity and cosmic gamma radiation is carried out by means of method of a search for

spatiotemporal concentrations (clusters) of showers recorded by the EAS array. Previously this method was used to search at experimental facilities of BNO for high energy gamma-radiation from cosmic gamma-ray bursts (CGRB) and from evaporating primordial black holes (PBH) [15 – 18]. At present the search for bursts of cosmic ray intensity and cosmic gamma radiation by means of detection of clusters of showers is realized in the near-real-time mode. Because the experimentally measured frequencies of cluster registration of different multiplicity are in agreement with the frequencies expected from the background fluctuations of cosmic rays the new method of background suppression was developed [19]. This method of background suppression allows us using selected clusters of showers as alerts to search for transient phenomena in the optical range.

The search for optical counterparts of the high energy ($E_\nu \geq 1$ GeV) muon neutrinos is carried out now in the near-real-time mode using the neutrino alerts from BUST. The follow up optical observations is conducted at the robotic telescopes of the Global MASTER Robotic Net [20].

6. Conclusion

The multi-messenger astronomy is now in the stage of rapid growth. This growth is provided both by a large number and variety of telescopes conducting the joint search in a wide range of electromagnetic radiation (from radio to gamma) and by participating in joint projects of installations recording gravitational waves and ultrahigh-energy neutrinos. The development of modern experimental facilities and fast data acquisition systems (DAQ) gives a possibility to analyze experimental data in real-time mode. Such methodical approach gives, in turn, a possibility to study of the dynamics of explosive processes in the detected transient objects. At present the fundamental modernization of data acquisition systems of experimental facilities of BNO is performed [21]. This modernization will make it possible to produce the low-latency alerts from experimental facilities of BNO for various nets of robotic telescopes.

Acknowledgements

References

[1] V.V. Kuzminov. The Baksan Neutrino Observatory. Eur. Phys. J. Plus 127, 113, 2012.

[2] E.N. Alekseyev et al. Baksan underground scintillation telescope. Proc. 16 ICRC, 10, 276, 1979.

[3] E.N. Alekseyev et al. The Baksan underground scintillation telescope. Phys. Part. Nucl. 29, 254, 1998.

[4] V.B. Petkov et al. Andyrchy facility for detection of cosmic rays. Istrum. Exp. Tech., 49, 785, 2006.

[5] E.N. Alekseyev et al. Installation for study of the central part of EAS by a scintillation detector with an area of 200 m^2. Izv. Akad. Nauk SSSR, Ser. Fiz. 40, 994, 1976.

[6]   D.D. Dzhappuev et al. Modernization of the Carpet-2 array of the Baksan Neutrino Observatory. Bull. Russ. Acad. Sci.: Phys. 71, 525, 2007.

[7]   V.S. Romanenko et al. Limits on the isotropic diffuse gamma-ray flux between 100 TeV and 1 PeV: experiments Carpet-2 and Carpet-3. These proceedings.

[8]   M. G. Aartsen et al. [IceCube Collaboration]. Observation of High-Energy Astrophysical Neutrinos in Three Years of IceCube Data. Phys. Rev. Lett. 113 (2014) 101101; arXiv:1405.5303.

[9]   O.E. Kalashev, S.V. Troitsky. IceCube astrophysical neutrinos without a spectral cutoff and $(10^{15}–10^{17})$ eV cosmic gamma radiation. JETP Lett. 100, 761, 2015; arXiv: 1410.2600.

[10] D.D. Dzhappuev et al. Carpet–2 search for PeV gamma rays associated with IceCube high-energy neutrino events. . JETP Lett. 2019 (in print); arXiv: 1812.02662.

[11] Yu.F. Novoseltsev et al. Searching for neutrino bursts in the galaxy; 36 years of exposure. J. Exp. Theor. Phys. 125, 73, 2017.

[12] M.M. Kochkarov et al. Search for Low-Energy Neutrinos from Gamma-Ray Bursts at the Baksan Underground Scintillation Telescope. Physics of Particles and Nuclei, 46, 197, 2015.

[13] V.B. Petkov et al. Search for Electron Neutrinos from Gravitational Wave Events at the Baksan Underground Scintillation Telescope. Jetp Lett. 107, 398, 2018.

[14] V.B. Petkov et al. The Search for High Energy Muon Neutrinos from Southern Hemisphere Gamma-Ray Bursts with BUST. Physics of Particles and Nuclei, 46, 201, 2015.

[15] D.V. Smirnov et al. Search for UHE gamma-ray short transients at Andyrchy EAS array. Proc. 29 ICRC, 4, 451, 2005.

[16] D.V. Smirnov, V.B. Petkov, S.N. Karpov. Search for TeV gamma rays from GRBs at Baksan Underground Scintillation Telescope.   Proc. 29 ICRC, 4, 447, 2005.

[17] D.V. Smirnov, V.B. Petkov, and S.N. Karpov. Search for Ultrahigh-Energy Cosmic Gamma-Ray Bursts on the Baksan Underground Scintillation Telescope. Astronomy Letters, 32, 1, 2006.

[18] V.B. Petkov et al. Searching for Very-High-Energy Gamma-Ray Bursts from Evaporating Primordial Black Holes. Astronomy Letters, 34, 509, 2008.

[19] I.M. Dzaparova et al. Quick search for optical partners of bursts of very high energy gamma-ray radiation. These proceedings.

[20] V. Lipunov et al. Baksan Neutrino 181021: Global MASTER-net Optical Follow-up Observations. GCN CIRCULAR 23361. https://gcn.gsfc.nasa.gov/gcn3/23361.gcn3

[21] A.N. Kurenya et al. DAQ system for the complex of the BUST – Andyrchy – Carpet-2 facilities. These Proceedings.

Classification of short GRBs. Merging and postmerging.

Raikov A.A.[1,2], Shirokov S.I.[1,3], Sokolov V.V.[1] and Vlasyuk V.V.[1]

[1]*Special Astrophysical Observatory of RAS, Nizhnij Arkhyz, Russia; raikov@mail.ru*
[2]*Main Astronomical Observatory, Saint-Petersburg, Russia*
[3]*Saint-Petersburg State University, Saint-Petersburg, Russia*

Abstract   We represent a review of the short GRBs classification problem. We took four largest GRBs catalogs: BATSE, BeppoSAX, Swift and Fermi and, as a first approximation, constructed duration distributions for short GRBs, that is GRBs shorter than 2 seconds. It turned out that on 0.1, 0.2 and 1 seconds we have statistical peaks which we associate with different types of binary mergers. The multimessenger astronomy allows us to come closer to a binary mergers analysis by gravitational-wave observations. Also we offer a new test for existence of event horizon through it.

Key words: Gamma-Ray Bursts, Binary Merges, Gravitational Waves.

1. Introduction

According to modern ideas, GRBs are classified in two types: long-soft and short-hard ones. Long-duration bursts last from 2 seconds up to a few hundreds of seconds (several minutes), with an average duration of about 30 seconds. They are associated with the collapse of massive stars in supernovas. Short-duration bursts last less than 2 seconds lasting from a few milliseconds up to 2 seconds with an average duration of about 0.3 seconds (or 300 milliseconds). These bursts are associated with binary mergers. The example of duration distribution is shown in Figure 1.
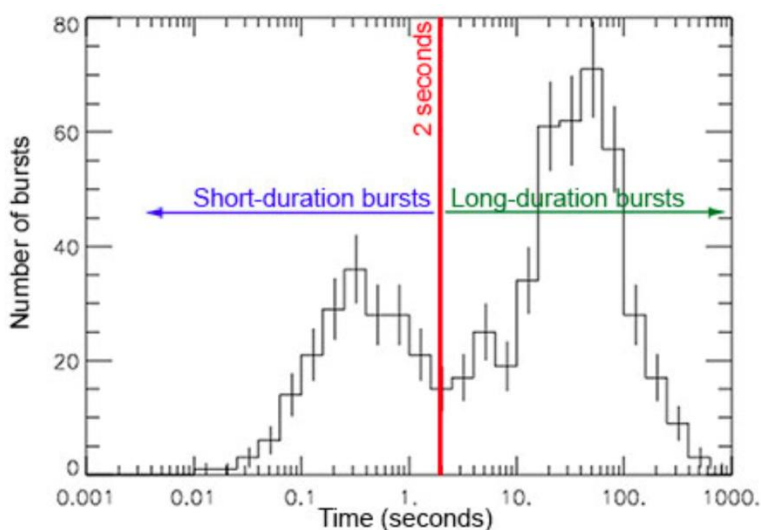
Fig1. *Graph of the time versus number of bursts for the gamma-ray bursts observed by the BATSE instrument on the Compton Gamma-ray Telescope [26].*

However, the classification can be more detailed. So, in a paper by Ruffini R. (2018) [21] seven types of the short GRBs are proposed. The separation is based on binary merges of different components. Another team of Rueda J.A. (2018) [20] introduces four subclasses of short GRBs. For example, so-called gamma-ray flashes (GRFs), that is, merges of neutron star (NS) and white dwarf (WD) have durations up to 100 seconds. In fact, this is a long GRB, but it is associated with short GRBs. Also authors note that gravitational-wave emission (GWE) must be observed in a range from 10^{-2} to 10^{-1} Hz for merges of WDs and WD with NS. The observing of GWE in the range will confirm existence of the GRFs sources and will explain its physics.

At the present time the gravitational instruments do not register GWE in the range less than 10 Hz. Figure 2 shows spectral sensitivity of modern (aLIGO) and planned (eLISA) instruments.
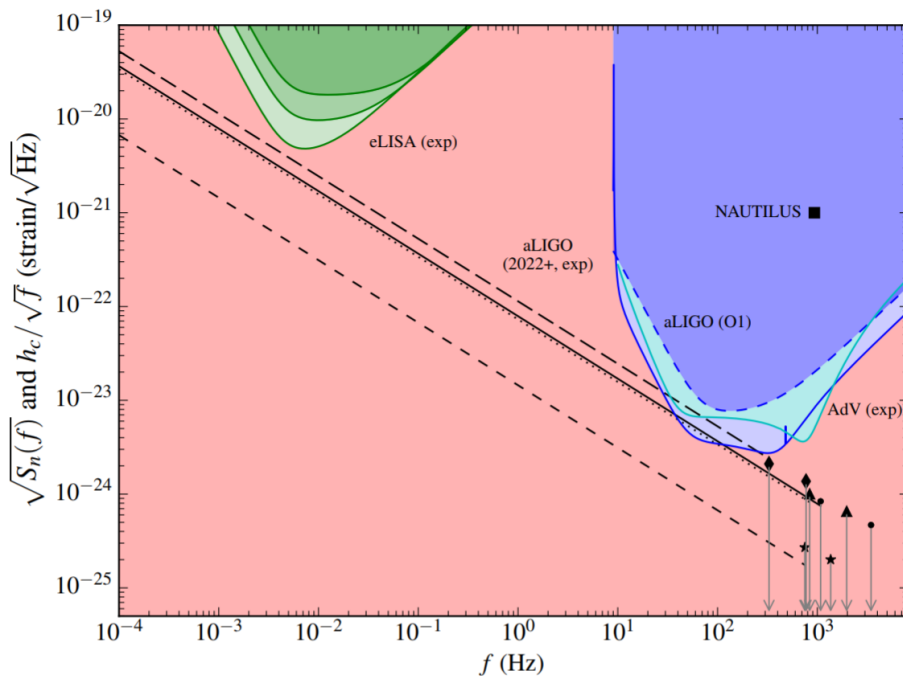
Fig2. Spectral sensitivity of aLIGO and eLISA gravitational instruments from [22].

2. Data

We considered four samples without any selections:
- 1234 BATSE GRBs [19];
- 1143 Swift GRBs [12];
- 1028 BeppoSAX GRBs [10];
- 2378 Fermi GRBs [18].

3. Duration analysis

The BATSE GRBs duration distribution in higher resolution is represent in Figure 2a. When the hard gamma-range is included in the histogram of the GRB duration T_{90}, we start seeing features at durations of 0.1-0.5 and 1 second. In our opinion, these features are related to the physics of a GRB source, that is, to different morphology of binary systems. From Figure 2b it is seen that the operating range of the Swift satellite smoothes out the distribution of short GRB durations, however there is still an indication of presence of features at 0.3 and 1 second regions. At the same times the BeppoSAX sample in Figure 2c shows a monotone rate with the strongly marked peak at 1 second. The most interesting result is shown in Figure 2d for the Fermi extended catalog. The distribution allows distinguishing between three peaks at 0.2, 0.5 and 1 seconds.
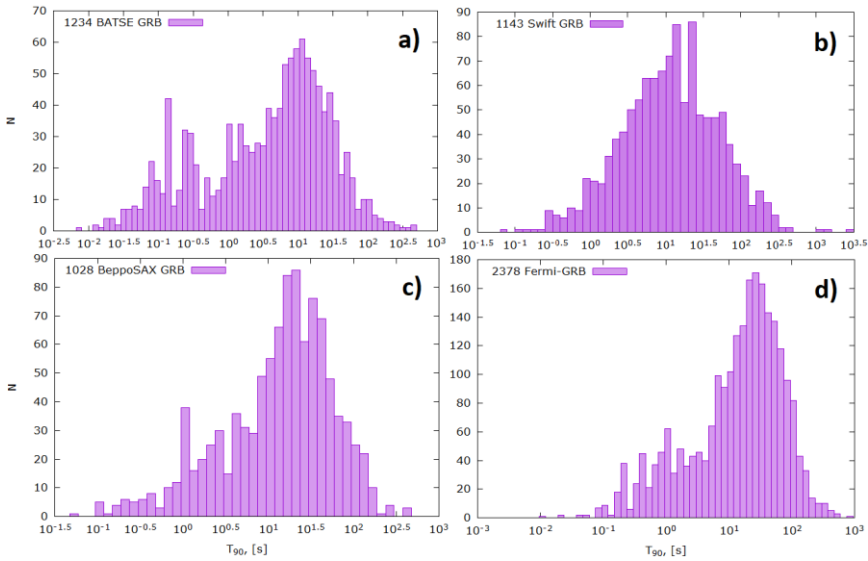
Fig3. The GRBs duration distributions.

For more strait result we summed the duration diagrams up to 2 second except of Swift. For this an equal duration steps were taken and all distributions were normalized on the Fermi GRBs number. The result is shown in Figure 4. According to integral result the peaks have duration T_{90} about 0.1, 0.2 and 1 seconds.
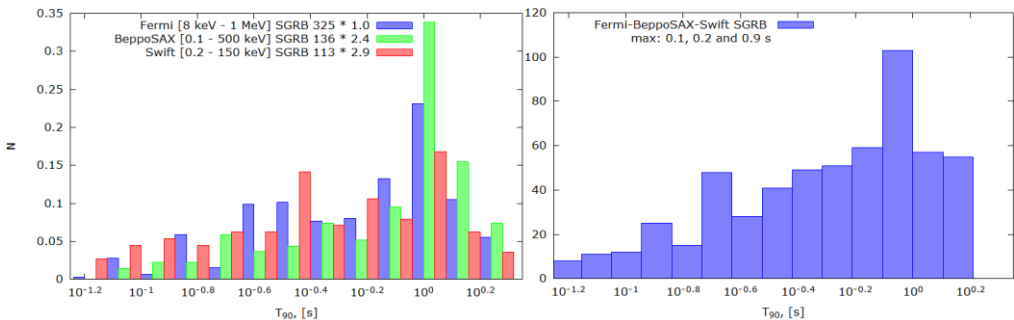
Fig4. The short-GRB duration distributions for the catalogs (the normed on the Fermi on the left and the summed on the right).

4. Multimessenger astronomy

In the era of mono-messenger astronomy we were getting all information about the Universe from observations of electromagnetic waves. New era of multi-messenger astronomy discovers for us such information sources as space particles, neutrino, and especially gravitational waves (GWs).

4.1 Solar neutrino

Solar neutrino of three leptonic flavors was discovered:
- Electron ν_e by Clyde Cowan & Frederick Reines in 1956 [9]
- Muon ν_μ by Leon Lederman, Melvin Schwartz & Jack Steinberger in 1962 [5]
- Tau ν_τ by DONUT at Fermilab collaboration in 2000 [1].

4.2 Supernovae neutrino

SN1987a, detected both by optical telescopes and by neutrino observatories, is probably the first example of a multi-messenger astronomical event. It was the first opportunity for modern astronomers to study the development of a supernova in great detail, and its observations have provided much insight into core-collapse supernovae [7]. There is evidences of correlation between gravitational and neutrino detectors [11].

4.3 Indirect evidence of GWs

The Hulse–Taylor binary pulsar PSR 1913+16 was discovered by Hulse Russell Alan and Taylor Joseph Hooton Jr., of the University of Massachusetts Amherst in 1974 [24]. The orbit has decayed since the binary system was initially discovered, in precise agreement with the loss of energy due to gravitational waves described by General Relativity. The ratio of observed to predicted rate of orbital decay is calculated to be 0.997±0.002 [25].

4.4 Observations of GWs

The first direct observation of gravitational waves was made on 14 September 2015 and was announced by the LIGO and VIRGO collaborations on 11 February 2016 [4]. The first observation of the coalescence of two compact objects through gravitational-wave instrument and gamma-ray telescopes is registered on 17 August 2017. The merger event has provided a signal in gravitational waves (GW170817) detected by Advanced LIGO and Advanced VIRGO, that has allowed us to localize the binary constraining a sky region of 31 deg^2 and a distance of a 40±8 Mpc. Moreover, Fermi Gamma-ray Burst Monitor has detected a short Gamma-Ray Burst event (GRB170817A) delayed by 1.7 second with respect to the merger time. Later, 15.3 hours after the trigger, the source was detected in the ultraviolet by the Swift Gamma-Ray Burst Mission [2].

5. Gravitational-wave afterglow

The recent research of GWs was made in [3]. In Figure 5 we see the waveforms of 10 gravitational events. Upper panels demonstrate relativistic modeled searches of waveform and bottom panels show unmodeled waveform searches. The frequency distribution is on the left. All unmodeled waveforms give a postmerging signal different from prediction of General

Relativity (GR) [15].
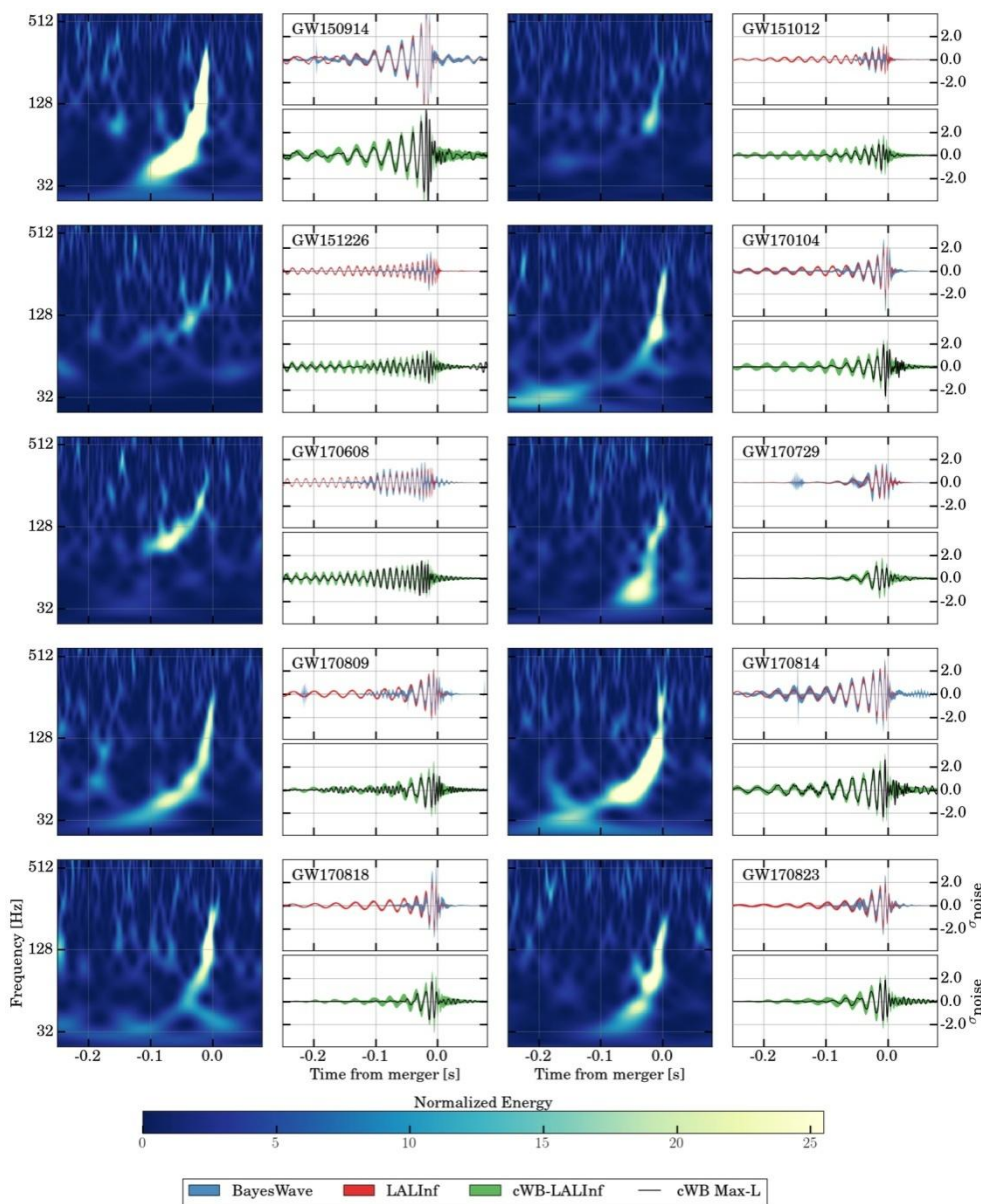
Fig5. *The waveforms of 10 gravitational events from paper [3].Upper panels demonstrate relativistic modeled searches of waveform and bottom panels show unmodeled waveform searches. On the left is a frequency distribution.*

The RCO postmerging represents a rare opportunity to test nature of merging objects. The

event waveform consists of three stages: insprial motion of an RCO, merging and postmerging. In the simplest case two gravitationally related bodies with masses m_1 and m_2, moving non-relativistically in circular orbits around their common center of mass at a distance r from each other, emit gravitational waves of the next power averaged over the period:

$$-\frac{d\mathcal{E}}{dt} = \frac{32\,G^4 m_1^2 m_2^2\,(m_1 + m_2)}{5\,c^5 r^5}. \tag{1}$$

As a result, the system loses energy, what leads to the convergence of bodies. The rate of orbital decay can be approximated by

$$\frac{dr}{dt} = -\frac{64}{5}\,\frac{G^3}{c^5}\,\frac{(m_1 m_2)(m_1 + m_2)}{r^3}, \tag{2}$$

where r is the separation between the bodies, t is the time, G is the gravitational constant, c is the speed of light, and m_1 and m_2 are the masses of the bodies. This leads to an expected time to merger of

$$t = \frac{5}{256}\,\frac{c^5}{G^3}\,\frac{r^4}{(m_1 m_2)(m_1 + m_2)}. \tag{3}$$

The merging stage is a relativistic collapse (see e.g. [17]). In the postmerging stage the GWs (gravitational-wave afterglow) emitted by an RCO rotating with period P and having ellipticity ε have the luminosity

$$L_{\mathrm{GW}} = \frac{2048\pi^6 G}{5c^5}\,\frac{I^2 \varepsilon^2}{P^6}. \tag{4}$$

It is impossible to make an accurate estimate by formula (4), because $L_{GW} \sim \varepsilon^2$ which, generally speaking, is unknown. For the Crab Pulsar, e.g., $\varepsilon \sim 10^{-2}$, $L_{GW} \sim 10^{38}$ erg/s.

6. Discussion

In all missions (except Swift) there are peaks at short duration of T_{90}, which must indicate objects with different energies and masses, for example NS+NS. It should be noted that T_{90} may drift with a rate of redshift as an instrumental effect (e.g. Kasevski [14]). Therefore, the duration profile must be considered in different redshift ranges. This and other aspects of GRBs research requires rich redshifts and durations sample, which may appear due to the THESEUS mission. Also the GRBs duration significantly depends on instrument spectral sensitivity [8, 28]. For example, GRB 150101B has a duration of 0.018 second in the Fermi and of 0.080 second in the Swift (see Table 1 in Appendix).

Very interest results for us were obtained in the Konus-*Wind* experiment [22]. In Figure 6 the GRBs hardness-duration distribution is shown. One can see that the short-hard GRBs and long-soft GRBs distributions are localized and, cconsequently, these are two different subsamples which should be separated in the cosmological tests performed by GRBs.

According to GR there is no gravitational-wave afterglow [15]. The simulations show that GWs from the merging of objects having an event horizon are fade out quickly [27],   that is, all information goes beyond measuring instruments. However, it may be a consequence of low

sensitivity of gravitational-wave instruments, but not the absence of this effect. At present, there is no direct proof of existence of objects with the event horizon. It may be a collision of relativistic compact objects (RCO) with a gravitational-wave afterglow. If such an afterglow is actually observed, then the problem of existence of objects of another nature (e.g. strange quark stars) is raising and the development of appropriate physics is required. In the alternative case of gravitational-wave afterglow we can obtain important information about nature of the objects including the equation of state.
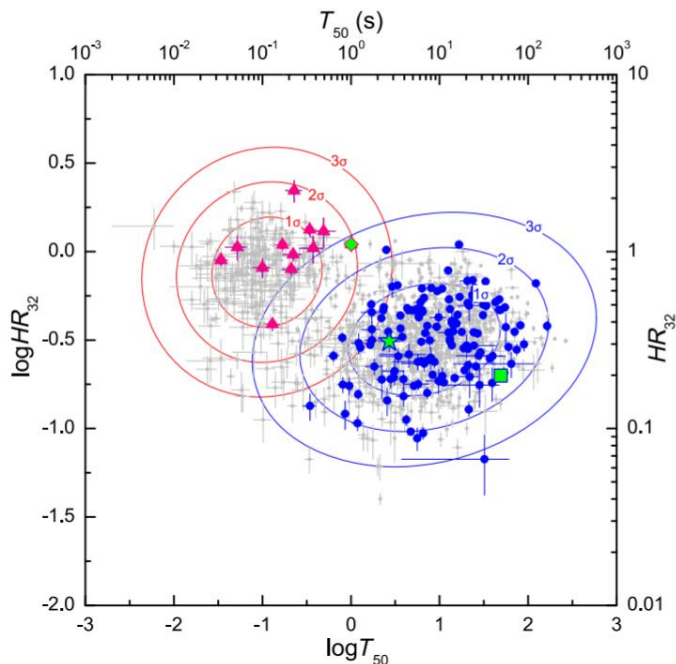
Fig6. *The hardness-duration distribution of GRBs with known redshifts detected by the Konus-Wind experiment from paper [23].*

Field gravity theories are an alternative of GR. In such field theories there is no event horizon (see e.g. [13]). Also we do not know the equation of state for a RCO with masses greater than 1-3 solar masses [29].

7. Conclusion

Based on last results of the GWs observations we can conclude with a high probability that any geometric gravitational theory in the postmerging stage does not work. We have very little information about this, but it is enough to make this assumption.

Our summary:

- Short GRBs are divided into subclasses by the type of merging components in binary systems. The SGRBs duration of T_{90} can reach several minutes.
- The prospects of the understanding of the RCO nature by neutron stars is a very actual problem for the modern physics.
- Progress of sensitivity in the future (or a closer burst) will allow us to see a fine

structure of the gravitational-wave afterglow signal. This method is an alternative of the Event Horizon Telescope and its cost is cheaper.

Recently, the extended emission (EE) in gravitational radiation during GRB170817A was discovered in [16]. This is possibly the first evidence of the gravitational-wave afterglow signal.

Appendix

Table1. A short GRBs catalog of the Swift and Fermi missions.

#	name	T90 [s]	f[erg/sm2]	p[erg/sm2]	z	mission	s[erg/s/sm2]	R[Mpc]	E[erg]	L[erg/s]	Ep[erg]
1	90426	1.200	1.80E-07	2.40E-07	2.609	Swift	1.50E-07	5956.4	9.98E+51	8.32E+51	1.33E+52
2	50813	0.450	4.40E-08	9.40E-08	1.800	Swift	9.78E-08	4881.1	9.86E+50	2.19E+51	2.11E+51
3	150423A	0.220	6.30E-08	9.00E-08	1.394	Swift	2.86E-07	4166.0	7.52E+50	3.42E+51	1.07E+51
4	GRB090927	0.512	3.03E-07	0.00E+00	1.370	Fermi	5.92E-07	4118.8	3.46E+51	6.77E+51	0
5	100724A	1.400	1.60E-07	1.90E-07	1.288	Swift	1.14E-07	3953.0	1.57E+51	1.12E+51	1.86E+51
6	140622A	0.130	2.70E-08	6.00E-08	0.959	Swift	2.08E-07	3205.4	1.28E+50	9.83E+50	2.84E+50
7	GRB100117A	0.256	4.23E-07	0.00E+00	0.920	Fermi	1.65E-06	3107.1	1.81E+51	7.06E+51	0
8	070429B	0.470	6.30E-08	1.76E-07	0.904	Swift	1.34E-07	3066.1	2.58E+50	5.48E+50	7.20E+50
9	GRB090510A	0.960	3.37E-06	0.00E+00	0.903	Fermi	3.51E-06	3063.5	1.37E+52	1.43E+52	0
10	90510	0.300	3.40E-07	9.70E-07	0.903	Swift	1.13E-06	3063.5	1.39E+51	4.62E+51	3.96E+51
11	61217	0.210	4.20E-08	1.49E-07	0.827	Swift	2.00E-07	2863.2	1.38E+50	6.57E+50	4.89E+50
12	101219A	0.600	4.60E-08	4.10E-07	0.718	Swift	7.67E-07	2559.7	1.07E+51	1.78E+51	9.51E+50
13	GRB131004A	1.152	5.10E-07	0.00E+00	0.717	Fermi	4.43E-07	2556.9	1.18E+51	1.02E+51	0
14	131004A	1.540	2.80E-07	3.40E-07	0.717	Swift	1.82E-07	2556.9	6.48E+50	4.20E+50	7.86E+50
15	141212A	0.300	7.20E-08	1.20E-07	0.596	Swift	2.40E-07	2195.8	1.06E+50	3.54E+50	1.77E+50
16	051221A	1.400	1.15E-06	1.20E-06	0.547	Swift	8.21E-07	2041.9	1.38E+51	9.83E+50	1.44E+51
17	GRB160624A	0.448	1.21E-07	0.00E+00	0.483	Fermi	2.70E-07	1834.2	1.07E+50	2.40E+50	0
18	160624A	0.200	4.00E-08	5.00E-08	0.483	Swift	2.00E-07	1834.2	3.55E+49	1.78E+50	4.44E+49
19	GRB150120A	1.728	4.17E-07	0.00E+00	0.460	Fermi	2.41E-07	1757.6	3.29E+50	1.91E+50	0
20	150120A	1.200	1.40E-07	1.80E-07	0.460	Swift	1.17E-07	1757.6	1.11E+50	9.22E+49	1.42E+50
21	070724A	0.400	3.00E-08	1.00E-07	0.457	Swift	7.50E-08	1747.5	2.33E+49	5.83E+49	7.78E+49
22	GRB100206A	0.128	8.69E-07	0.00E+00	0.407	Fermi	6.79E-06	1577.0	5.13E+50	4.01E+51	0
23	71227	1.800	2.20E-07	1.60E-07	0.383	Swift	1.22E-07	1493.4	1.13E+50	6.26E+49	8.19E+49
24	130603B	0.180	6.30E-07	6.40E-07	0.356	Swift	3.50E-06	1398.0	2.72E+50	1.51E+51	2.76E+50
25	140903A	0.300	1.40E-07	2.50E-07	0.351	Swift	4.67E-07	1380.2	5.84E+49	1.95E+50	1.04E+50
26	060502B	0.131	4.00E-08	6.20E-08	0.287	Swift	3.05E-07	1147.4	1.05E+49	7.99E+49	1.62E+49
27	050509B	0.073	9.00E-09	2.80E-08	0.225	Swift	1.23E-07	913.8	1.35E+48	1.85E+49	4.21E+48
28	080905A	1.000	1.40E-07	1.30E-07	0.122	Swift	1.40E-07	508.2	5.46E+48	5.46E+48	5.07E+48
29	61201	0.760	3.34E-07	3.86E-07	0.111	Swift	4.39E-07	463.6	1.06E+49	1.40E+49	1.23E+49
30	GRB150101B	0.080	2.38E-07	0.00E+00	0.093	Fermi	2.98E-06	390.1	5.19E+48	6.49E+49	0
31	150101B	0.018	2.30E-08	0.00E+00	0.093	Swift	1.28E-06	390.1	5.02E+47	2.79E+49	0

References

[1] Fermilab: Physicists find first direct evidence for Tau neutrino at Fermilab. // In 1989, experimenters at CERN found proof that the tau neutrino is the third and last light neutrino of the Standard Model, but a direct observation was not yet feasible. (2000)

[2] LIGO Scientific Collaboration, Virgo Collaboration, Fermi Gamma-Ray Burst Monitor, INTEGRAL: Gravitational Waves and Gamma-Rays from a Binary Neutron Star Merger: GW170817 and GRB 170817A // Astrophys. J., 848, L13 (2017)

[3] The LIGO Scientific Collaboration and The Virgo Collaboration. GWTC-1: A Gravitational-Wave Transient Catalog of Compact Binary Mergers Observed by LIGO and Virgo during the First and Second Observing Runs // E-print arXiv:1811.12907 (2018)

[4] Abbott, B.P.; et al. (LIGO Scientific Collaboration and Virgo Collaboration): Observation of Gravitational Waves from a Binary Black Hole Merger // Phys. Rev. Lett. 116 (6): 061102. arXiv:1602.03837 (2016)

[5] Anicin, I. V. (2005). "The neutrino – its past, present, and future". *SFIN (Institute of Physics,*

Belgrade) Year XV. A: Conferences. 2: 3–59. arXiv:physics/0503172 (2002)

[6]   Amati L. et al.: // Adv. Space Res. Vol.62. Iss.1. P.191 (2018)

[7]   Arnett, W. D.; Bahcall, J. N.; Kirshner, R. P.; Woosley, S. E.: Supernova 1987A // Annual Review of Astronomy and Astrophysics. 27: 629–700 (1989)

[8]   Castro-Tirado A.J., Sokolov V.V., Guziy S.S.: Gamma-ray bursts: Historical afterglows and early-time observations // in Proceedings of The International Conference "SN 1987A, Quark Phase Transition in Compact Objects and Multimessenger Astronomy", Russia, Terskol (BNO INR RAS), Nizhnij Arkhyz (SAO RAS). p.41 (2018),{https://www.sao.ru/hq/grb/conf_2017/proceedings.html}

[9]   Cowan Jr. C. L., et al.: Detection of the Free Neutrino: a Confirmation. // *Science*. 124 (3212): 103–104 (1956)

[10]   Frontera F. et al.: The Gamma-Ray Burst Catalog Obtained with the Gamma-Ray Burst Monitor Aboard BeppoSAX // Astroph.J.Suppl.S. V.180. N.1 (2009)

[11]   Galeotti P. and Pizzella G.: New analysis for the correlation between gravitational waves and neutrino detectors during SN1987A // Eur.Phys.J.C 76-426 (2016)

[12]   Gehrels N. et al.: The Swift Gamma-Ray Burst Mission // Astroph.J. V.621, P.558 (2005)

[13]   Logunov A.A.: Relativistic Theory of Gravitation // Moscow: Nauka, in russian, 253 (2012)

[14]   Kocevski D. & Petrosian V.: On the Lack of Time Dilation Signatures in Gamma-ray Burst Light Curves // Astroph.J., 765:116 (7pp) (2013)

[15]   Maggiore M.: Gravitational waves. Volume 1: theory and experiments // Oxford University Press, 576p. (2007)

[16]   Maurice H.P.M. van Putten and Massimo Della Valle: Observational evidence for Extended Emission to GW170817 // *MNRAS: Letters*, V.482, I.1, Pages L46–L49 (2019)

[17]   Montero P.J., Janka H.-T., and Müller E. Relativistic Collapse And Explosion Of Rotating Supermassive Stars With Thermonuclear Effects // Astroph.J., V.749, N.1 (2012)

[18]   Narayana Bhat P. et al.: The Third Fermi GBM Gamma-Ray Burst Catalog: The First Six Years // Astroph.J.Suppl.S. V.223. N.2. (2016)

[19]   Paciesas W.S. et al.: The Fourth BATSE Gamma-Ray Burst Catalog (Revised) // Astroph.J.Suppl.S. Vol.122. Iss.2. P.465 (1999)

[20]   Rueda J.A. et al.: GRB 170817A-GW170817-AT 2017gfo and the observations of NS-NS, NS-WD and WD-WD mergers // JCAP, e-Print arXiv:1802.10027 (2018)

[21]   Ruffini R. et al. On the Rate and on the Gravitational Wave Emission of Short and Long GRBs // Astroph. J., Vol 859, N 1 (2018)

[22]   Svinkin D.S. et al.: The Second Konus-Wind Catalog Of Short Gamma-Ray Bursts // The Astrophysical Journal Supplement Series, 224:10 (15pp) (2016)

[23]   Tsvetkova A. et al.: The Konus-Wind Catalog of Gamma-Ray Bursts with Known Redshifts. I. Bursts Detected in the Triggered Mode // The Astrophysical Journal, 850:161 (27pp) (2017)

[24]   Weisberg, J.M.; Taylor, J. H.; Fowler, L. A.: Gravitational waves from an orbiting pulsar // *Scientific American*. 245 (4): 74–82 (1981)

[25] Weisberg, J. M.; Nice, D. J.; Taylor, J. H.: Timing Measurements of the Relativistic Binary Pulsar PSR B1913+16 // Astrophysical Journal. 722 (2): 1030–1034 (2010)

[26] https://imagine.gsfc.nasa.gov/science/objects/bursts1.html

[27] https://www.youtube.com/watch?v=gmmD72cFOU4

[28] Sokolov V.V., Castro-Tirado A.J., Sokolova T.N.: The core-collapse supernovae, gamma-ray bursts and SN 1987A // in Proceedings of The International Conference "SN 1987A, Quark Phase Transition in Compact Objects and Multimessenger Astronomy", Russia, Terskol (BNO INR RAS), Nizhnij Arkhyz (SAO RAS). – P.190 (2018, https://www.sao.ru/hq/grb/conf_2017/proceedings.html

[29] Sokolov V.V.: On the Observed Mass Distribution of Compact Stellar Remnants in Close Binary Star Systems and Possible Explanations Proposed for the Time Being // in "Proceedings of the International Workshop on Quark Phase Transition in Compact Objects and Multimessenger Astronomy: Neutrino Signals, Supernovae and Gamma-Ray Bursts", Russia, Nizhnij Arkhyz (SAO RAS), Terskol (BNO INR RAS), October, 7 - 14, 2015, p. 121 { https://www.sao.ru/hq/grb/conf_2015/proceedings.html }, publishing house "Sneg", Pyatigorsk, 2016. And references therein (see also the book Sokolov V.V. "Gravidynamics and quarks", Moscow, URSS, 2018; http://urss.ru/cgi-bin/db.pl?lang=Ru&blang=ru&page=Book&id=238152).

Limits on the isotropic diffuse gamma-ray flux between 100 TeV and 1 PeV: experiments Carpet-2 and Carpet-3

V.S. Romanenko[1*], V.B. Petkov[1,2], D.D. Dzhappuev[1], A.S. Lidvansky[1], E.A. Gorbacheva[1], I.M. Dzaparova[1,2], A.U. Kudzhaev[1], N.F. Klimenko[1], A.N. Kurenya[1], O.I. Mikhailova[1], K.V. Ptitsyna[1], M.M. Khadzhiev[1], A.F. Yanin[1].

[1]*Institute for Nuclear Research of RAS, Moscow, Russia; vsrom94@gmail.com*

[2]*Institute of Astronomy of RAS, Moscow, Russia*

Abstract   An experiment for measuring the flux of gamma rays of cosmic origin with energy above 100 TeV is currently being prepared at the Baksan Neutrino Observatory (the Carpet-3 experiment). The experiment implies the extension of the existing Carpet air shower array by increasing areas of both muon detector and surface scintillation detectors. In this paper we present estimates of sensitivity of the experiment to showers from primary gamma-rays for different configurations of the accomplished array. Using experimental data of the previous version of the array (Carpet-2) accumulated for 9.2 years, preliminary estimates of the flux upper limit is deduced for cosmic gamma-rays with energies above 700 TeV.

Keywords: Cosmic Rays, Extensive Air Showers, Primary Diffuse Gamma Rays, Muon-poor Showers

1. Introduction

Search for gamma-rays with energies higher than 100 TeV is applied in the Extensive Air Shower (EAS) method, which has been used since 1960 [1].   EAS is generated by the primary cosmic rays that strike the atmosphere and produce many secondary particles. Opposed to primary protons and other charged cosmic rays, which deflect in interstellar magnetic fields, the primary gamma rays can give information about the spatial distribution and characteristics of places of acceleration of cosmic rays, as well as about density of cosmic rays in the interstellar space.

Investigation of diffuse gamma rays at such energies by the EAS method is based on separation of the showers from primary gamma-rays and other charged particle (protons and nuclei). Because the number of muons in gamma showers is lower than that in proton showers, and if one selects muon-poor EAS, theoretically, it is possible to separate the showers initiated by primary gamma rays with reliable efficiency.

Many experiments have been carried out to search for gamma showers in a wide energy range, a review of which is given in [2, 3, 4, 5]. The experiments at Mt Chacaltaya, Tien Shan and Yakutsk are worked on this principle and announced the registration of gamma showers in the range $10^{14} - 5 \times 10^{17}$ eV. But they had insufficient statistical significance and were not confirmed later. More careful subsequent experiments (collaborations EAS-TOP, and KASCADE in the energy range $3 \times 10^{14} - 5 \times 10^{16}$ eV, and Haverah Park, Yakutsk at energies higher than 10^{18} eV) yielded only upper limits on the fluxes of cosmic gamma rays. Those limits appeared to be much lower than the fluxes of diffuse cosmic gamma rays supposedly measured in earlier works. In the MSU experiment the search for showers from primary

gamma rays in an energy range of $5 \times 10^{15} - 2 \times 10^{17}$ eV, conducted by the method of selection of muonless showers, also yielded only upper limits with an exception of the region $5 \times 10^{16} - 10^{17}$ eV. In this region some muonless showers were detected, whose number considerably exceeded an expectation for background events, which allowed one to derive a value of the flux of diffuse gamma rays with such energies. It should be noticed, however, that in the KASCADE-Grande experiment [6] in the same energy region of primary energies only flux limits for diffuse gamma rays have been obtained, and they contradict to the results of MSU. However, the full-scale reanalysis of the MSU data with modern simulations of the installation does not confirm previous indications of the excess of gamma-ray candidate events. So, the final results of the MSU experiment are also only upper limits on the flux of diffuse gamma rays in the energy range of $\sim (10^{16} - 10^{17.5})$ eV [7, 8].

2. The Carpet-2 experiment

The Carpet-2 air shower array [9, 10] of the Baksan Neutrino Observatory is located in the North Caucasus region near Mount Elbrus at an altitude of 1700 m above sea level (atmospheric depth 840 g/cm^2) (Fig. 1).
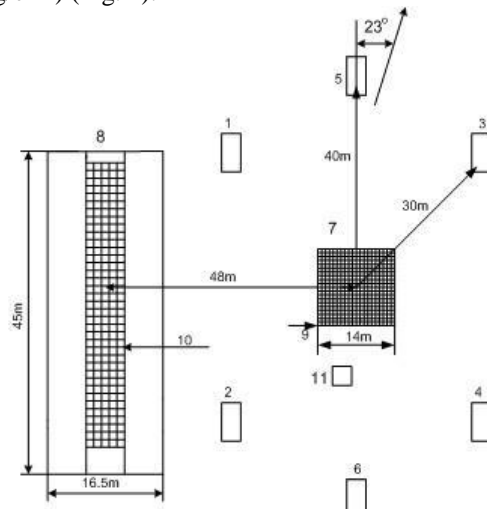
Fig1. *The layout of the Carpet-2 multipurpose air shower array: 1-6 are outdoor huts with scintillators, 7 is the Carpet, 8 is the muon detector, and 9 is a neutron monitor.*

The array consists of a ground level detector called the Carpet (200 m^2), six outdoor huts with 9 m^2 of scintillation detectors in each, an underground muon detector and a neutron monitor. The Carpet consists of 400 liquid scintillation detectors; each has an area of 0.5 m^2. The range of energy release measured by a single detector is $10 - 5000$ relativistic particles (r.p.). One r.p. is the most probable energy release produced by a cosmic ray particle crossing the detector, and it equals 50 MeV. Six outdoor huts have 18 scintillator detectors of the same type. Four of them are placed in the shape of a square at a distance of 30 m from the array center. The signals from these detectors are used as stopping pulses for the time measurement system to measure delays and reconstruct the arrival direction. The Carpet can measure the shower parameters with a good accuracy: dX = dY = 0.35 m, $dN_e/N_e = 0.1$ in the EAS size interval $N_e = 10^5 - 5 \times 10^6$.

The muon detector (MD) is located in an underground tunnel at a depth of 500 g/cm, which corresponds to the energy threshold of 1 GeV. The distance between its center and the center of the Carpet is equal to 48 m. The MD is an array of size 5×35 m, and it consists of 175 plastic scintillation counters of 1 m^2 area each that are attached to the ceiling of the underground tunnel. Two triggers of the Carpet array and the proper MD trigger formed by the coincidence scheme upon the actuation of any three out of five MD modules are used to record information. The Carpet and MD are operating independent of each other and have different dead times of recording electronics. But time markers of events in the MD and Carpet are produced by one and the same clock, so that coincident events are reliably identified within the time interval dt = 1ms. The total number of relativistic particles within the Carpet ($N_{r.p.}$) and the number n_μ of muons recorded by the MD are experimentally measured quantities used to determine the energy of EAS and the total number of muons in it, respectively. The events satisfying the following conditions are included into processing:

- shower axes are inside the Carpet (effective area ~160 m^2);
- zenith angles of showers $\theta < 40°$;
- the total energy release in the Carpet $\geq 10^4$ r.p.;
- the number of fired counters in the Carpet ≥ 300.

After such a selection, the number of showers recorded in a period from 1999 to 2011 is equal to 1.3×10^5. The net exposure time for this period is 3390 days ($\approx$ 9.2 years). The CORSIKA code v. 6720 (the QGSJET01C model for high energies FLUKA 2006 for low energies) [11] was used for modeling the showers.

3. Upper limit on diffuse flux of cosmic gamma rays.

In order to distinguish the showers from primary gamma rays on the background of ordinary EAS, we have analyzed correlation dependences in the plane $n_\mu - N_{ch}$ for detected and simulated events (Fig. 2). In this paper, we consider the energy region $N_{ch} \geq 3.5\times10^5$ where by using methods of experimental data processing, one can separate simulated gamma-ray showers from ordinary EAS events.

To evaluate the efficiency of selection of gamma-ray showers we isolated on the plane $n_\mu - N_{ch}$ the area where only simulated gamma-ray showers are present, and in reality, there are no of detected showers. A red line in Fig. 2 shows the boundary of this region.

We can use the following formula for the estimation of the flux upper limit for primary gamma rays:

$$I_\gamma = \frac{N_{90}}{S\cdot T\cdot \Omega\cdot \varepsilon_1\cdot \varepsilon_2}. \tag{1}$$

Because no experimental events below the red line N_{90} is equal to 2.3, it may be evaluated from Poisson statistics at a 90% confidence level. S is the efficient area of the Carpet without counters placed at the perimeter (~160 m^2), T is the net exposure (data acquisition) time, ε_1 is the trigger and reconstruction efficiency of events, and ε_2 is the selection efficiency for gamma showers which is given by $\varepsilon_2 = N_{select}(\geq E)/N_{total}(\geq E)$.
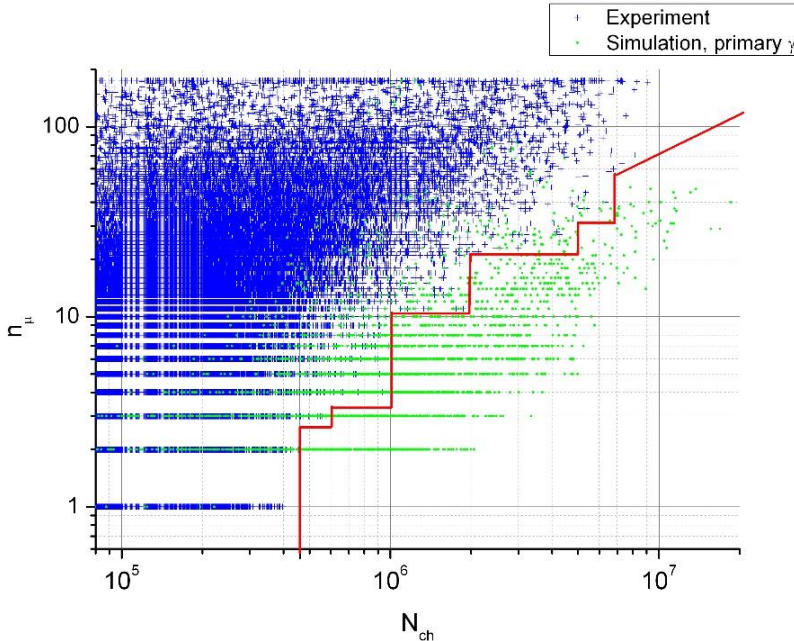
Fig. 2. *The n_μ versus N_{ch} dependence. The blue dots correspond to experimental events, the green dots are simulated gamma-rays showers and the red line is the boundary of selected region.*

Fig. 3 presents the limits on the integral flux of cosmic diffuse gamma rays as a function of energy of primary photons together with the results of other experiments. It should be noted that our results presented in this paper are preliminary, and the upper limits presented in Fig. 3 can be refined after more careful analysis of experimental data.

4. The Carpet-3 experiment

Preparation of the experiment suggests a systematic increase of the MD's continuous area: at first up to 410 m² and then up to 615 m². The area of EAS axes detection will be also increased. For this purpose, 20 additional modules will be installed with 9 scintillation counters of area 1 m² each (see Fig. 4).

At the moment 410 plastic scintillation counters with a total area of 410 m² are installed in the MD underground tunnels. They are fully equipped with necessary electronic circuits. Work on adjustment of these counters and on creation of the special data acquisition system for a new configuration of the MD is in progress. At the same time, calculations have been carried out to estimate the efficiency of selection of gamma rays and the sensitivity of different configurations of the new array to air showers initiated by primary gamma rays. Figure 3 also demonstrates the expected limits on the flux of diffuse cosmic gamma rays for two configurations of the Carpet-3 array and for two periods of data accumulation. One can see that even at the MD area equal to 410 m² the new array will have the world-best sensitivity to the flux of cosmic gamma rays with energies in the range 100 TeV – 1 PeV.
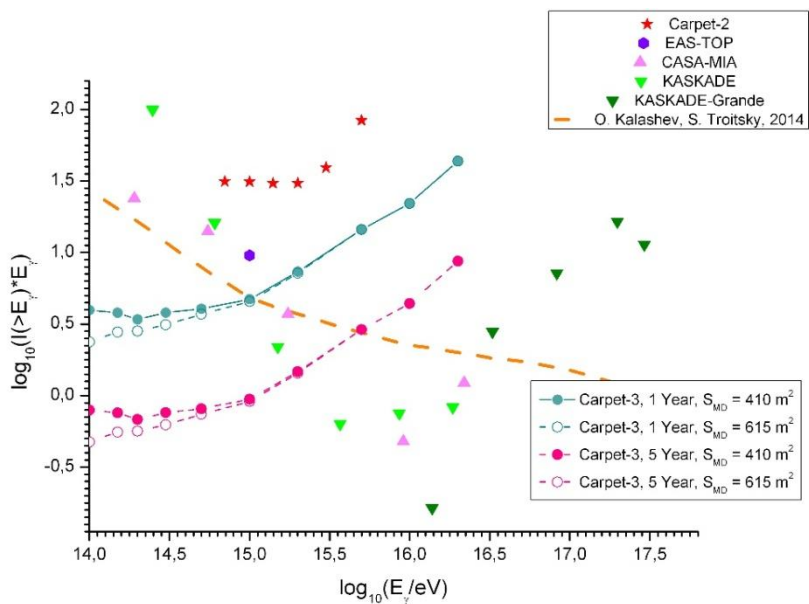
Fig3. *Limits on the integral flux of gamma rays versus their energy and sensitivity of the Carpet-3 air shower array.*
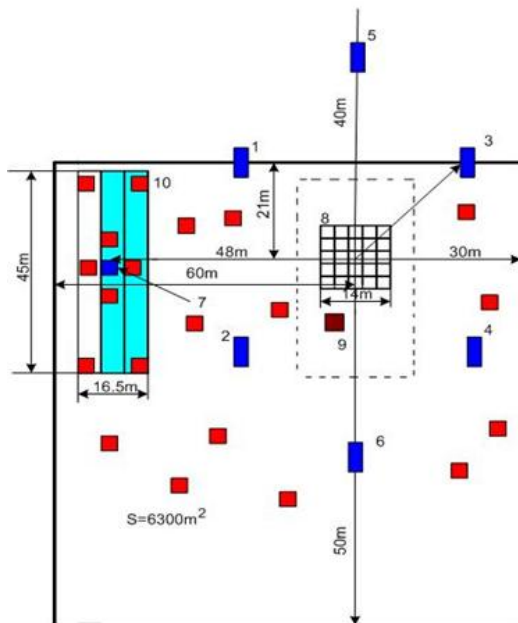
Fig4. *The layout of the Carpet-3 air shower array. The big blue rectangle shows the MD area filled with plastic scintillation counters. The dark blue and red patches present outdoor huts (modules) with scintillation detectors.*

5. Conclusions

1. From the results of the Carpet-2 air shower array the upper limits on the flux of diffuse cosmic gamma rays with energy above 900 TeV were derived.

2. In order to provide for efficient detection of air showers initiated by gamma rays with energies higher than 100 TeV, it is necessary to perform the array modernization with a considerable increase of the Muon Detector area (The Carpet-3 experiment).

3. In this case, several years of data accumulation will make it possible to improve significantly the results currently available on measuring the 100 TeV flux of cosmic diffuse gamma rays.

4. The Carpet-3 air shower array is under construction at the Baksan Neutrino Observatory by step-by-step upgrade and extension After final accomplishment of this array it can be competitive in its class and will have a chance to get the world-best limit on the flux of gamma rays of cosmic origin.

Acknowledgements

References

[1] Maze R., Zawadzki A. On an attempt of detection of primary cosmic photons of very high energy //Il Nuovo Cimento (1955-1965). – 1960. – Т. 17. – №. 5. – С. 625-633.

[2] Fomin Y. A., Kalmykov N. N., Kulikov G. V., Sulakov V. P., Troitsky S. V. Estimate of the fraction of primary photons in the cosmic-ray flux at energies ~1017 eV from the EAS-MSU experiment data //Journal of Experimental and Theoretical Physics. – 2013. – Т. 117. – №. 6. – С. 1011-1023.

[3] Fomin Y. A., Kalmykov N. N., Kulikov G. V., Sulakov V. P., Troitsky S. V. Estimates of the cosmic gamma-ray flux at PeV to EeV energies from the EAS-MSU experiment data //JETP letters. – 2015. – Т. 100. – №. 11. – С. 699-702.

[4] Fomin Y. A., Kalmykov N. N., Karpikov I. S., Kulikov G. V., Kuznetsov M. Y., Rubtsov G. I., Sulakov V. P., Troitsky S. V. No muon excess in extensive air showers at 100–500 PeV primary energy: EAS–MSU results //Astroparticle Physics. – 2017. – Т. 92. – С. 1-6.

[5] Fomin Y. A., Kalmykov N. N., Karpikov I. S., Kulikov G. V., Kuznetsov M. Y., Rubtsov G. I., Sulakov V. P., Troitsky S. V. Constraints on the flux of (1016− 1017.5) eV cosmic photons from the EAS–MSU muon data //Physical Review D. – 2017. – Т. 95. – №. 12. – С. 123011.

[6] Kang D. et al. A limit on the diffuse gamma-rays measured with KASCADE-Grande //Journal of Physics: Conference Series. – IOP Publishing, 2015. – Т. 632. – №. 1. – С. 012013.

[7] Fomin Y. A., Kalmykov N.N., Karpikov I. S., Kulikov G. V., Kuznetsov M. Y., Rubtsov G. I., Sulakov V. P., Troitsky S. V. No muon excess in extensive air showers at 100–500 PeV primary energy: EAS–MSU results //Astroparticle Physics. – 2017. – Т. 92. – С. 1-6.

[8]   Fomin Y. A., Kalmykov N.N., Karpikov I. S., Kulikov G. V., Kuznetsov M. Y., Rubtsov G. I., Sulakov V. P., Troitsky S. V. Constraints on the flux of $\sim (10^{16} - 10^{17.5})$ eV cosmic photons from the EAS–MSU muon data //Physical Review D. – 2017. – T. 95. – №. 12. – C. 123011.

[9]   Dzhappuev D. D., Alekseenko V. V., Volchenko V. I., Volchenko G. V., Guliev Z. S., Gulieva E. V., Kudzhaev A. U., Konovalov Yu. N., Lidvansky A. S., Mikhailova O. I., Petkov V. B., Smirnov D. V., Stepanov V. I., Sten'kin Yu. V., Khaerdinov N.S. Modernization of the Carpet-2 array of the Baksan Neutrino Observatory //Bulletin of the Russian Academy of Sciences: Physics. – 2007. – T. 71. – №. 4. – C. 525-527.

[10]   Dzhappuev D. D., Alekseenko V. V., Lidvansky A. S., Stenkin Yu. V., Petkov V. B., Mikhailova O. I., Kudzhaev A. U., Chernyaev A. B. and Tsyabuk A. L. Study of EAS hadronic component with hadron energy > 50 GeV. //30th International Cosmic Ray Conference (3-11 Jul 2007. Merida, Yucatan, Mexico). – 2007, – T. 4. – C. 19-22.

[11]   Heck D. et al. A Monte-Carlo code to simulate extensive air showers-report FZKA 6019 //Forschungszentrum Karlsruhe. – 1998.

Calculation of neutrino-nucleus cross section on the base of nuclear reactions data

S.V. Semenov

National Research Centre "Kurchatov Institute", Moscow, Russia;
Semenov_SV@nrcki.ru

Abstract   Calculation of neutrino–nuclei cross section is a question of considerable interest for neutrino detection, including solar, astrophysical and calibration neutrino experiments. Also it is an essential item for investigation of primary nucleosynthesis and searches for new physics in oscillations examination. Computations of cross sections for a number of nuclei, which are involved in setups for neutrino signal registration are presented.

Keywords: Neutrino Absorption Cross Section, Charge Exchange Reactions, Neutrino-Gallium Interaction

1. Introduction

Measurements of nuclear reaction characteristics, such as log ft values for electron capture or beta-decay processes, charge-exchange spectra, nuclear fluorescence intensities can give valuable information on nuclear structure necessary for model-independent neutrino-nuclei cross section computation. It can be shown that these qualities provide a possibility to obtain corresponding theoretical results, coinciding with the existing experimental data [1-7]. Here neutrino cross sections for a number of nuclei of interest are calculated.

2. Neutrino-Nuclei Interaction Cross Section

2.1.   Neutrino interaction with ^{12}C

There are two experiments on direct measurement of neutrino-^{12}C interaction cross sections performed by KARMEN [1, 2, 5, 6] and LSND [3, 7] Collaborations. The neutrino sources are the positive muon decay at rest (DAR), monoenergetic muon neutrino beam, arising from stopped positive pion decay and muon neutrino flux, produced by positive pion decay in flight (DIF). As was shown in [8], the nuclear reactions data give a possibility to obtain the according nuclear matrix elements and calculate cross section for a number of neutrino-nuclei processes, induced by charged and neutral current. The corresponding results coincide with experimental values. Particularly the neutrino absorption cross section

$$\nu_e + {}^{12}C \rightarrow {}^{12}N_{g.s.} + e^-,$$
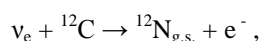
averaged over electron neutrino DAR spectrum, was obtained. Its value is $9.1 \cdot 10^{-42}$ cm^2, which agrees with the measured one.

Also transition to excited states of nitrogen $^{12}N^*$, $^{12}C(\nu_e,e^-)^{12}N^*$, with μ^+ DAR ν_e beam was experimentally investigated [3,7]. The flux averaged cross section is

$\langle\sigma\rangle = (5.7 \pm 0.6_{star} \pm 0.6_{syst})\cdot10^{-42}$ cm^2 [3], $\langle\sigma\rangle = (4.3 \pm 0.4_{star} \pm 0.6_{syst})\cdot10^{-42}$ cm^2 [7]. As DAR neutrino spectrum is characterized by the mean energy $E_\nu\sim32$ MeV, predominantly low multipoles give contribution to the cross section. Thus it can be assumed, that allowed Gamov-Teller transitions to excited 1^+ states of ^{12}N dominate. The low lying 1^+-state of ^{12}N, as it was found by the means of charge-exchange reactions, is $E_x=3.57$ MeV [9]. The expression for cross section has the following form:

$$\sigma_{GT}(E_V) = \frac{G_\beta^2 m_e^2}{\pi} g_A^2 B(GT)\pi_e \varepsilon_e F(Z_f, \varepsilon_e) \tag{1}$$

Here $B(GT)$ is the square of Gamov-Teller nuclear matrix element for transition to a certain state of the final nucleus, divided by $(2J_i+1)$, g_A is the axial-vector interaction constant, $g_A = 1.2761$, ε_e and π_e are the energy and momentum of outgoing electron in units of m_e, $\varepsilon_e = (E_\nu-\Delta)/m_e$, Δ is the mass difference of the ^{12}N* and ^{12}C nuclei and Fermi function $F(Z_f, \varepsilon_e)$ is the Coulomb correction function.

$$F(Z,\varepsilon,r) = 4(2pr)^{2(\gamma_0-1)} e^{\pi y} \frac{\left|\Gamma(\gamma_0 + iy)\right|^2}{\left[\Gamma(2\gamma_0 + 1)\right]^2}$$

Here $\gamma_0 = [1 - (\alpha Z)^2]^{1/2}$, $y=\alpha Z\varepsilon/p$, r is the distance between electron and nucleus center. Averaging of $F(Z,\varepsilon,r)$ over nucleus volume should be performed. The method of $F(Z_f, \varepsilon_e)$ calculation is presented in [10]. If transition to $E_x=3.57$ MeV 1^+-state of ^{12}N constitutes a major part of the ^{12}C$(\nu_e,e^-)^{12}$N* cross section, then $B(GT)$ can be estimated according to (1). For $\langle\sigma\rangle = 5.7\cdot10^{-42}$ cm^2 $B(GT)=0.80$. This result can be compared with $B(GT)_{g.s.}$, which corresponds to transition to the ground state of ^{12}N in ^{12}C$(\nu_e,e^-)^{12}$N$_{g.s}$ reaction, $B(GT)_{g.s.} = 0.88$. The value $B(GT)=0.80$ can be used, under the assumption made, for estimation of ^{12}C$(\nu_e,e^-)^{12}$N* cross section for meadow neutrino energies. Particularly, for $E_{\nu_e} = 40$ Mev $\sigma(E_{\nu_e}) = 9.5\cdot10^{-42}$ cm^2.

2.2. Neutrino interaction with ^{71}Ga

Calculation of cross section of electron neutrino capture by ^{71}Ga nucleus,

$$\nu_e + {}^{71}\text{Ga} \rightarrow e^- + {}^{71}\text{Ge}$$
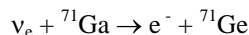
is necessary for analysis of neutrino gallium-germanium experiments. The proposed project BEST [11] at Baksan Neutrino Observatory is aimed to searches for sterile neutrinos [12] on the base of calibration procedure with artificial neutrino sources. Thus estimation of ν_e-^{71}Ga cross sections for neutrino, produced by ^{51}Cr and ^{37}Ar is a question of interest.

The ground state of ^{71}Ga has quantum numbers $3/2^-$ and ^{71}Ge g.s. has $1/2^-$. Also for ^{51}Cr and ^{37}Ar artificial sources transitions to two low-lying excited states of ^{71}Ge are possible: $E_x = 0.175$ MeV, $5/2^-$ and $E_x = 0.500$ MeV, $3/2^-$. The recent precise measurements [13] lead to the following neutrino threshold energy for ^{71}Ga transition to the ground state of ^{71}Ge:

$$B(GT)_{g.s.} = 0.5\frac{D}{g_A^2 f t_{1/2}} \tag{2}$$

$$D = \frac{2\pi^3 \ln 2}{G_F^2 \cos^2 \vartheta_C m_e^5}$$

The fundamental constants values result in $D = 6288.6$ c. Here g_A is the axial-vector coupling constant, $g_A = -1.2755$ [16]. So, as follows from (2),

$$B(GT)_{g.s.} = 0.0864 \pm 0.0003 \tag{3}$$

Cross section calculations in terms of measurement [17], $Q = 233.5 \pm 1`.2$ keV, were performed in [18]. The following values of log $ft_{1/2}$ and $B(GT)_{g.s}$ were obtained: log $ft_{1/2} = 4.353 \pm 0.005$, $B(GT)_{g.s} = 0.086 \pm 0.001$.

Artificial sources ^{51}Cr and ^{37}Ar emit neutrinos with the following energies:
^{51}Cr – 0.427 MeV, 8.95 %; 0.432 MeV, 0.93%; 0.747 MeV, 81.63 %; 0.752 MeV, 8.49%;
^{37}Ar – 0.811 MeV, 90.2%; 0.813 MeV, 9.8%.

According to (1), (3) the neutrino capture cross sections for transition to the ground state of ^{71}Ge can be calculated for ^{51}Cr and ^{37}Ar.

$$^{51}\text{Cr: } \sigma_{g.s} = (55.83 \pm 0.19) \cdot 10^{-46} \text{ cm}^2,$$

$$^{37}\text{Ar: } \sigma_{g.s} = (66.74 \pm 0.23 \cdot 10^{-46} \text{ cm}^2$$

Contributions of excited states of ^{71}Ge, $E_x = 0.175$ MeV and $E_x = 0.500$ MeV, to the cross sections can be estimated from (^{3}He,t) charge exchange reaction [19]. The derived Gamov-Teller strengths are: $E_x = 0.175$ MeV, $B(GT) = 0.0034(26)$; $E_x = 0.500$ MeV, $B(GT) = 0.0176(14)$. It should be taken into account that these results are adjusted to $B(GT)_{gs} = 0.0852$, obtained from ft measurement [20]. Total cross sections of neutrino capture are as follows:

$$^{51}\text{Cr: } \sigma_{tot} = (59.88 \pm 1.55) \cdot 10^{-46} \text{ cm}^2,$$

$$^{37}\text{Ar: } \sigma_{tot} = (72.09 \pm 1.88) \cdot 10^{-46} \text{ cm}^2$$

These values are about one percent greater, than the results of [18], for lower energy threshold, $Q = 232.443 \pm 0.093$ keV, is used. It will be observed, that certain problems, concerning $B(GT)$ extraction from the experiment should be considered. Just there are discrepancies between $B(GT)_{gs}$ magnitude, obtained from ft and (^{3}He,t) reaction for ^{100}Mo [21] and (p,n) reaction for ^{116}Cd [22]. Further increase of precision of charge-exchange reactions method is essential to matrix elements determination [23].

3. Conclusion

Determination of nuclear matrix elements by the model-independent method from experimental data gives a possibility to estimate cross sections of neutrino-nucleus processes. The calculated cross section values agree with the results of KARMEN and LSND experiments. Increase of precision of experiments on charge-exchange reactions should give exact results, necessary for interpretation of calibration experiments with neutrino. The model-independent method can be used for consideration of neutrino-nuclei interaction in different aspects of neutrino investigation.

References

[1] Bodman B., Booth N.E., Burtak F., et al. Cross section of the charged current reaction $^{12}C(\nu_e,e^-)^{12}N_{g.s.}$. Phys. Lett. B, 1992, **280**, 198-203

[2] Bodman B, Booth N.E., Drexlin G., et al. Neutrino interactions with carbon: recent measurements and a new test of ν_e, ν_μ universality. Phys. Lett. B, 1994, **332**, 252-7.

[3] Imlay R. New results on electron-neutrino carbon scattering and muon-neutrino scattering at LSND, Nucl. Phys. A, 1998, **629**, 531c-7c.

[4] B. Zenitz, KARMEN: Neutrino physics at ISIS. Prog. Part. Nucl. Phys., 1994; **32**: 351-3

[5] B. Bodman, N.E. Booth, F. Burtak et al, First observation of the neutral current nuclear excitation $^{12}C(\nu,\nu')^{12}C^*(1^+,1)$. Phys. Lett. B 1991, **267**:321-4.

[6] B. Armbruster, I. Blair, B.A. Bodman et al, Measurement of the weak neutral current excitation $12C(\nu_\mu, \nu'_\mu)^{12}C^* (1^+,1; 15.1 \text{ MeV})$ at $E_{\nu_\mu} = 29.8$ MeV. Phys. Lett. B, 1998, **423**:15-20.

[7] [Auerbach L.B., Burman R.L., Caldwell D.O. et al, Measurement of charged current ractions of ve on 12C, Phys. Rev. C, **64**, 065501 (2001)

[8] S.V. Semenov, Neutrino interaction with nuclei, Proceedings of the International Conference "SN 1987A, Quark Phase Transitions in Compact Objects and Multimessenger Astronomy", Terskol, (BNO), Nizhniy Arhyz (SAO), 2-8 July 2017, 174-190, INR RAS, Moscow, 2018.

[9] F. Ajzenberg-Selove. Energy levels of light nuclei A=11-12. Nucl. Phys. A, 1990, **506**:1-158.

[10] Kelley J.H., Purcell J.E., Sheu C.G., Energy levels of light nuclei A=12, Nucl. Phys. A, **968**, 71-253 (2017)

[11] S.V. Semenov, F. Šimkovic V.V. Khruschev, P. Domin, Contribution of the lowest 1+-intermediate state to the 2ν2β-decay amplitude, Phys. At. Nucl., **63**, 1196-8 (2000).

[12] Gorbachev V.V., Gavrin V.N., Ibragimova T.N. , Sensitivity of experiments to oscillation parameters, Physics of Particles and Nuclei, **49**, 685 (2018).

[13] Giunty C., Neutrino oscillations and sterile neutrino, Physics of Particles and Nuclei, **46**, 123-130 (2015).

[14] Khruschov V.V., Fomichev S.V., Titov O.A., Oscillation properties of active and sterile neutrinos and neutrino anomalies at short distances, Physics of Atomic Nuclei, **79**, 708 (2015)

[15] M. Alanssary, D. Frekers, T. Eronen et al, Precision ^{71}Ga-^{71}Ge mass-difference measurement, Intern J. of Mass   Spectrometry, **406**, 1-3 (2016).

[16] National nuclear data center, http://www.nndc.bnl.gov./logft (2016).

[17] J.N. Bahcall, Solar neutrino experiments, Rev. Mod. Phys., **50**, 881-903 (1978).

[18] A. Czarnecki, W.J. Marciano, and A. Sirlin, Neutron Lifetime and Axial Coupling Connection, Phys. Rev. Lett., **120**, 202002 (2018).

[19] Frekers D., Simon M.C., Andreoiu C. et al, Penning-trap Q-value determination of the Ga-71(ν_e,e^-)Ge-71 reaction using threshold charge breeding of on-line produced isotopes, Phys. Lett. B **722**, 233-7 (2013).

[20] V. Barinov, B. Cleveland, V. Gavrin et al, Revised neutrino-gallium cross section and prospects of BEST in resolving the gallium anomaly, Phys. Rev. D, **97**, 073001 (2018).

[21] D. Frekers, T. Adachi, H. Akimune et al, Precision evaluation of the ^{71}Ga(ν_e,e^-) solar neutrino capture rate from the ($^3He, t$) charge-exchange reaction, Phys. Rev. C, **91**, 034608 (2015).

[22] D. Frekers, H. Ejiri, H. Akimune, The ^{71}Ga($^3He, t$) reaction and the low-energy neutrino response, Phys. Lett. B, **706**, 134-8 (2011).

[23] J.H. Thies, T. Adachi, M. Dozono, High resolution ^{100}Mo($^3He,t$)^{100}Tc charge-exchange experiment and the impact on double-β decays and neutrino charged-current reactions, Phys. Rev. C, **86**, 044309 (2012).

[24] M. Sasano, H. Sakai, K. Yako, Determination of the Gamov-Teller transition strength to ^{116}In(g.s) by the ^{116}Cd(p,n) reaction at 300 MeV for the study of the nuclear matrix element of the two-neutrino double-beta decay, Nucl. Phys. A, **788**, 76c-81c (2007).

[25] Frekers D., Alansari M., Charge-exchange reactions and the quest for resolution, European Physical Journal A, **54**, 177 (2018).

Gamma-ray bursts as an instrument for testing cosmological models

Shirokov S.I.[1,*], Raikov A.A.[2,3], Baryshev Y.V.[1], Sokolov V.V.[2] and Vlasyuk V.V.[2]

[1]Saint-Petersburg State University, Saint-Petersburg, Russia; lakronous@mail.ru

[2]Special Astrophysical Observatory of RAS, Nizhnij Arkhyz, Russia

[3]Main Astronomical Observatory, Saint-Petersburg, Russia

Abstract   We present a review of possible cosmological applications of Gamma-Ray-Bursts multi-wavelength observations. A statistical analysis of the main pulse parameters of BeppoSAX, BATSE, Fermi and Swift GRB observational data is conducted. The spatial distribution of GRB sources with known redshifts is analyzed. Selection effects that distort the true source distribution are taken into account by comparing the observed distribution with fractal and uniform model catalogs. We review GRBs as standard candles and test of Universe isotropy by GRBs. We approximated trend of cosmological time dilation by long GRBs and discuss in detail possible effects that influence their statistics.

Key words: Gamma-Ray Bursts, Cosmological Models, Hubble's Diagram, Time Dilation, Large Scale Structure, Fractal Dimensionality

1. Introduction

Cosmology as a part of physics is based on the experiments/observations, which are used for testing the validity of existing theoretical models of the Universe. Edwin Hubble (1937) in his book *The Observational Approach to Cosmology* [13] defined it as the science which study the fair sample of the Universe, i.e. the observable region of space that can be explored with existing instruments. Sandage (1995) [27] gave the name **"Practical Cosmology"** to such strategy for the large Universe exploration and formulated 23 basic unsolved yet astronomical problems (on the analogy with "23 Gilbert problems" for mathematics). His list includes also the nature of the cosmological redshift (the 15th Sandage's astronomical problem). This observational approach to cosmology was further developed by Baryshev & Teerikorpi (2012) [4] (on the problem of cosmological redshift see [3]).

Modern state of the practical cosmology includes the multimessenger astronomy which unites observations of electromagnetic radiation (from radio up to gamma bands), cosmic rays, neutrino and gravitational waves. These new observational situation opens new possibilities for testing the basis of the cosmological models by using the observational approach of the practical cosmology. Last review of the luminosity correlations of GRBs, and implications for constraining the cosmological parameters and dark energy was given by Wang F.Y. et al. (2015) [34]. Further research of the GRBs afterglows, generally having broken power-law spectra, will give possibility to extract intergalactic medium (IGM) absorption features.

Here we give a review of cosmological tests which use observations of gamma-ray bursts (GRB) especially in view of the forthcoming mission Transient High Energy Sky and Early Universe Surveyor (THESEUS) (Amati et al. (2018) [1]; Strata G. et al. (2018) [33]). Preceding review of the GRB cosmology was given by Petrosian et al. (2009) [22].

In Sec.2 we discuss a classification of cosmological tests and formulate those observational relations which will be used in our review. Sec.3 is devoted to data analysis of the main GRB missions. In Sec.4 we discuss main results from the analysis of spatial distribution of GRB sources, test of Universe isotropy by GRBs, the Hubble diagram for GRBs and consider the cosmological time dilation effect. Sec.5 presents general discussion of T_{90} trends. Conclusion is given in Sec.6.

2. Classification of cosmological tests

In the framework of practical cosmology it is important to distinguish between *theoretically inferred cosmological laws* and *empirically measured cosmological relations,* which are used for testing theoretical models (Baryshev & Teerikorpi [4]). There are several possible classifications of observational cosmological tests, which include *parametric* tests (such as derivation of main parameters of the standard cosmological model) and *crucial* tests (such as establishing the nature of the large-scale structure of the Universe and the nature of the cosmological redshift). According to Orlov & Raikov [19] there is also general division of cosmological tests on two classes – *cosmographic* and *physical* tests.

Modern practical cosmology includes the following observational tests of world models:

- testing the validity of general relativity at largest scales;
- testing the nature of cosmological redshift and reality of space expansion;
- correlation properties of the matter distribution on largest scales;
- measuring the temperature of the background radiation at different redshifts;
- determining the ages and chemical composition of the high redshift objects in the observable Universe.

The main obstacle in extracting true physical information from the directly observed empirical relations is the different kinds of selection and distortion observational technical and physical effects, e.g. K-correction, absorption, evolution, Malmquist bias and others [4]. The most difficult part of cosmological tests is related to careful taking into account such hidden distortion effects.

Modern cosmology is developing also *neo-classical* tests which include very high redshift observations of new type objects and phenomena, such as gamma-ray bursts, very high energy cosmic rays, neutrino and gravitational radiation. For our review we choose following cosmological tests:

- The spatial distribution of GRB sources
- Hubble diagram for GRB sources
- Testing isotropy and inhomogeneity of the Universe by GRBs
- Cosmological time delay in GRB light curves

These tests relate to the fundamental aspects of cosmological models.

3. GRB missions

3.1. The BATSE

The Burst and Transient Source Experiment (BATSE) by NASA's Marshall Space Flight Center searched the sky for gamma-ray bursts (in range from 20 to >600 keV) and conducted full sky surveys for long-lived sources. The BATSE is an instrument on the Compton Gamma Ray Observatory (CGRO) in the Earth orbit which detects photons with energies from 20 keV

to 30 GeV. The observatory was launched from Space Shuttle Atlantis on April 5, 1991, and operated until its deorbit on June 4, 2000. Successors to CGRO include the ESA INTEGRAL spacecraft (launched 2002), NASA's Swift Gamma-Ray Burst Mission (launched 2004) and NASA's Fermi Gamma-ray Space Telescope (launched 2008). Description of the Fourth BATSE Gamma Ray Burst Catalog was done by Paciesas et al. in [20].

3.2. The BeppoSAX

The Gamma-Ray Burst Monitor aboard the BeppoSAX satellite was an Italian–Dutch satellite for X-ray astronomy which played a crucial role in resolving the origin of gamma-ray bursts (GRBs). It was launched on 30 April 1996 into a low inclination (<4 degree) low-Earth orbit. The expected operating life of two years was extended to April 30, 2002 due to high scientific interest in the mission and the continued good technical status. BeppoSAX was named in honor of the Italian physicist Giuseppe "Beppo" Occhialini. SAX stands for "Satellite per Astronomia a raggi X" or "Satellite for X-ray Astronomy". It was the first X-ray mission capable of simultaneously observing targets over more than 3 decades of energy, from 0.1 to 300 (keV) with relatively large area, good (for the time) energy resolution and imaging capabilities (with a spatial resolution of 1 arc minute between 0.1 and 10 keV). The BeppoSAX catalog is represent by Frontera et al. in [8].

3.3. The Swift

The Neil Gehrels Swift Observatory [10], previously called the Swift Gamma-Ray Burst Mission, is a NASA space telescope designed to detect gamma-ray bursts (GRBs). It was launched on November 20, 2004. The observatory has the following instruments: Burst Alert Telescope, X-ray Telescope and Ultraviolet/Optical Telescope. Burst Alert Telescope (BAT) detects GRB events and computes their coordinates in the sky. It locates the position of each event with an accuracy of 1 to 4 arc-minutes within 15 seconds. Energy range: 15–150 keV. X-ray Telescope (XRT) can take images and perform spectral analysis of the GRB afterglow. This provides more precise location of the GRB, with a typical error of approximately 2 arcseconds radius. Energy range: 0.2–10 keV. Ultraviolet/Optical Telescope (UVOT). After Swift has slewed towards a GRB, the UVOT is used to detect an optical afterglow. The UVOT provides a sub-arcsecond position and provides optical and ultra-violet photometry through lenticular filters and low resolution spectra (170–650 nm) through the use of its optical and UV prisms.

3.4. The Fermi

The Fermi Gamma-ray Space Telescope (FGST), formerly called the Gamma-ray Large Area Space Telescope (GLAST), is a space observatory being used to perform gamma-ray astronomy observations from low Earth orbit. Fermi was launched on 11 June 2008. Its main instrument is the Large Area Telescope (LAT), with which astronomers mostly intend to perform an all-sky survey studying astrophysical and cosmological phenomena such as active galactic nuclei, pulsars, other high-energy sources and dark matter. Energy ranges from 20 MeV to 300 GeV. Another instrument aboard Fermi, the Gamma-ray Burst Monitor (GBM) (formerly GLAST Burst Monitor) detects sudden flares of gamma-rays produced by GRB and solar flares. Its scintillators are on the sides of the spacecraft to view all of the sky which is not blocked by the Earth. The design is optimized for good resolution in time and photon energy. Ranges: from 8 keV to 1 MeV and from 150 keV to 30 MeV. Review of The Fermi GBM Burst

Catalog by Narayana Bhat P. et al. is available in [17].

4. Cosmological tests

4.1. Spatial distribution of GRB sources

One of the fundamental requirements in the ΛCDM model is homogeneity of the matter distribution on a large scale. However recent works in this area [12,15] reveal more and more inhomogeneity up to ~600 Mpc. The new evidences of existence of superstructures with sizes about 1000 Mpc in beam surveys are given in [28, 2]. These facts require elaboration of the cosmological model parameters by investigating visible matter spatial distribution, for example, fractal analysis [4]. Since GRBs are indicators of galaxy clusters [31, 32] it should be expected a correlation between statistical properties of galaxy spatial distribution and GRBs. So a statistical analysis of minimal distances between GRBs indicates a galaxy cluster, e.g. five GRBs with coordinates $23^h50^m<\alpha<0^h50^m$, $5<\beta<25$ and the redshift of $0.81<z<0.97$ [9,29,30].

As is emphasized in [4, Ch.10, 11] the Peebles's correlation function [21] $\xi(r)$ is strongly distorted by the borders of real samples and to get robust statistical characteristics of the spatial distribution of galaxies one should use the conditional density function $\Gamma(r)$. In particular for a fractal spatial distribution the slope of power-law $\Gamma(r)$ gives the robust estimation of the fractal dimension D (for homogeneous galaxy distribution D = 3).

In papers [9,23] the fractal dimension of GRBs spatial distribution was estimated in the interval D = 2.2 to D = 2.7. New method of fractal analysis proposed in Raikov & Orlov [24] and developed by Shirokov et al. [29,30] allows to estimate fractal dimension on all sample scales where statistics of pairwise distances is defined. In Figure 1 we present the normalized distributions of the pairwise distances for real GRBs sample and for fractal model catalogs with D = 2.0 and D = 2.5. The horizontal line corresponds to uniform Poison's law of spatial points distribution.
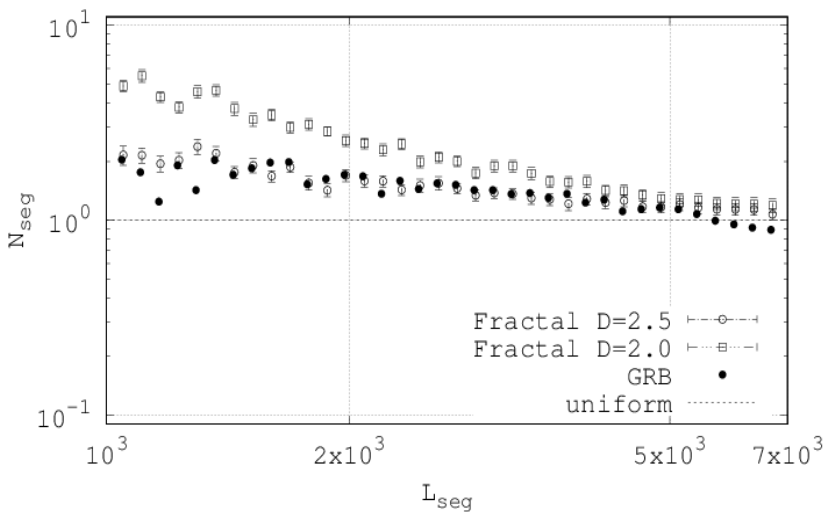
Fig2. *The distribution of pairwise distances (Mpc) for the Swift GRBs sample and model fractal catalogs.*

4.2. Isotropy and inhomogeneity of the GRB Universe

Isotropy of the GRBs distribution over the celestial sphere by the Fermi, BATSE and Swift data was analyzed in paper [25]. Authors considered the observed properties of GRBs and made the conclusion: "*...the results are consistent with isotropy confirming*".

It must be emphasized that homogeneity and isotropy of spatial distribution are different properties of the large-scale structure. For example the fractal matter distribution can have statistical isotropy and simultaneously be strongly inhomogeneous. Our above results in Sec.4.1 about discovery of fractal dimension D close to 2 on very large scales demonstrate that such situation may be realized in the GRB spatial distribution.

In the framework of the fractal cosmological model suggested in Baryshev [3] the Universe is isotropic and inhomogeneous having fractal dimension D = 2.0. Such value of the fractal dimension guaranties the linear redshift-distance law, if the cosmological redshift is interpreted as the global gravitational redshift within fractal structure on scales where such structure exists.

4.3. Hubble diagram for GRB sources

Measurements of the Hubble diagram of Type Ia supernovae (SNIa) provided the first direct evidence for cosmic acceleration [18]. However we can construct the Hubble diagram using SNIa up to z < 1.5 only. GRBs provide opportunity to continue the magnitude - distance dependence by a sample of GRBs with z > 1.5 (presented in Figure 2). It should be noted that the error bars of SNIa are about 1-2 orders smaller than the luminosity determined errors of GRBs. The behavior of the best fitted curve (red) is close to the standard ΛCDM model (grey) with matter density parameters $\Omega_m = 0.24$ and $\Omega_m = 0.33$ respectively. An agreement with the ΛCDM model also has been obtained in [35]. Future THESEUS observations will give essential extension and accuracy of the observed Hubble law.
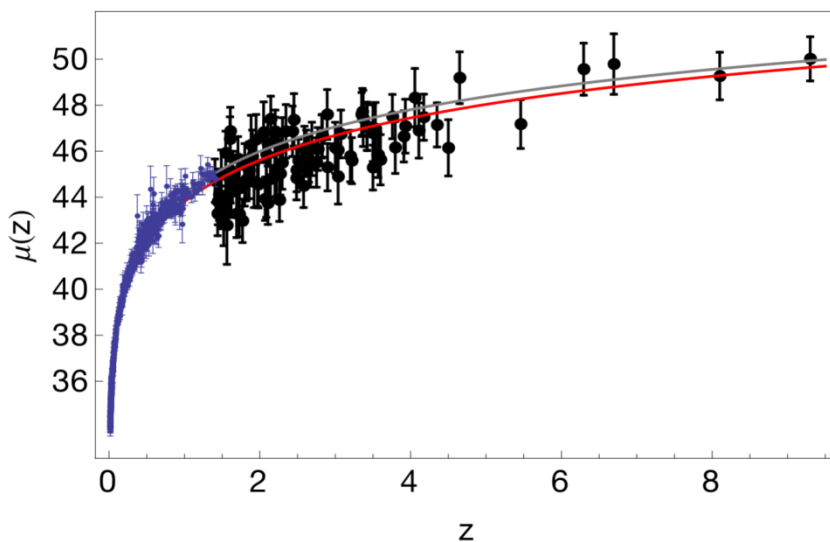
Fig2. The Hubble diagram for SNIa (blue points) and GRBs (black points) with ΛCDM prediction (grey curve) and approximation (red curve) from Demianski M. (2017) [7].

4.4. GRB time dilation and the nature of cosmological redshift

One of the simplest crucial cosmological tests on the nature of cosmological redshift is the measurement of duration of known physical processes in high redshift objects (cosmological time dilations). Studies of the SNIa light curves made by Goldhaber et. al.(2001)[11] and Blondin et al.(2008)[5] leads to conclusion about the $(1 + z)$-law.

It is important to test the time dilation effect also for GRB phenomenon. We divide the Swift GRBs in long ($T_{90} > 2s$) and short ($T_{90} < 2s$) ones that are less than 10% in the sample and approximate the trend by least squares for middle points, separately for long and short GRBs in Figure 3. There is no trend up to $z = 3$. At $3 < z < 4$ there is a significant congestion of GRBs in the region of 100 seconds, although this is not observed at $z > 5$.
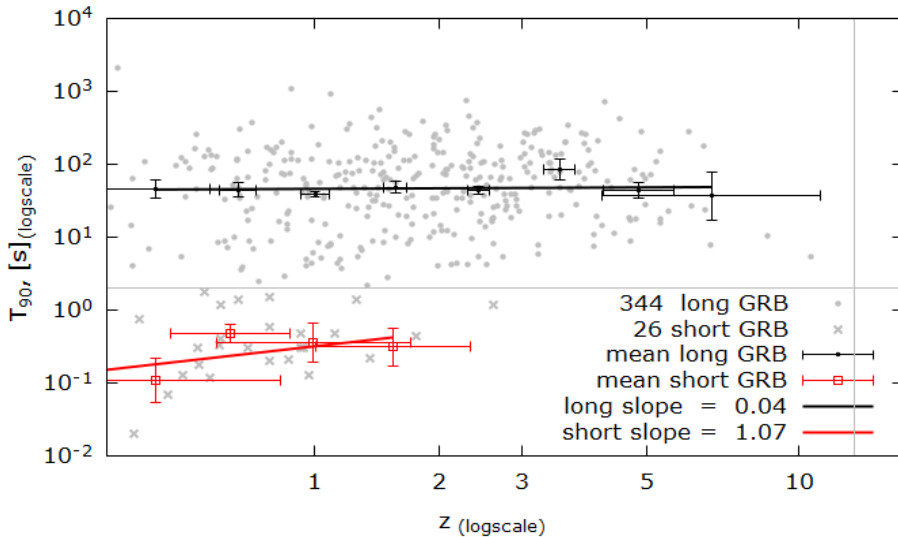
Fig3. Distribution of T_{90} verse redshift in log-scale separated by 2-second line.

5. Discussion

5.1 About T_{90} trends

The ΛCDM model prediction is $T_{90} \sim (1+z)$ for all time events at high redshifts in the Universe. The observational data analysis (without taking into account hidden selection effects) shows no trend for the separated sample with durations larger than 2 seconds. Therefore, either no time dilation effect or separating short GRBs (at the 2 second level) is incorrect. To verify the first statement it is necessary to discuss observational selection effects, e.g. D. Kocevski & V. Petrosian (2013) [14]. We will analyze these effects later. In this work we suggest to pay attention to principal difference between short GRBs and long GRBs. That is, we are talking about a new effect of observational selection, namely an incompleteness effect of GRBs sample.

The long GRBs are explosions of supernovas, but the short GRBs are merges of binary

systems. These events have a different nature and different light curves Sokolov et al. [32]. It may be that our instruments do not observe short GRBs at high redshifts, thus it is necessary to separate these two subsamples of GRBs. Since short GRBs are less than 10% in the sample, it is possible to use the rough constraint of 2 seconds. Even if a part of long GRBs is shorter than 2 seconds, this effect is insignificant due to a little amount of points, which is shown in Figure 4d for approximation from 1 up to 4 of redshift.

We also considered alternative approximations and compared them with other papers. The averaging Swift data in Figures 4a and 4b give a trend $(1+z)$ for approximation up to $z = 8$, but with a large margin of error (± 0.5), a similar results were obtained in [36]. A T_{90} trend at average points of all Swift GRBs is $(1+z)^{1.5 \pm 0.2}$ at $z < 4$ and this result is most reliable and Figure 4c shows it. A similar result $T \sim (1+z)^{1.4 \pm 0.3}$ has been obtained for the radio loud GRBs sample in paper [16].
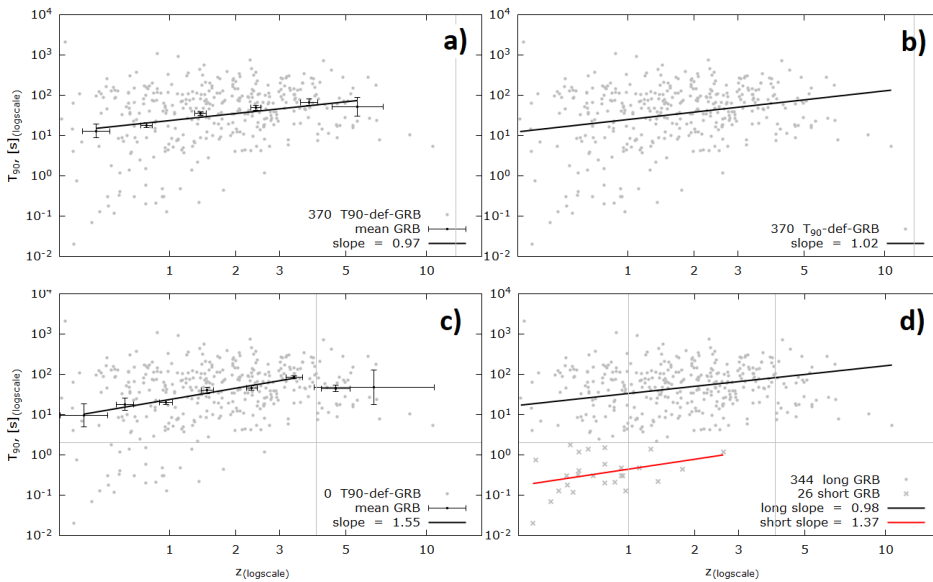
Fig4. *The different approximations of* T_{90}.

Duration of GRBs strongly depends on spectral sensitivity and other instrument features [6,14]. For example, GRB 150101B in the Fermi/GBM catalog has $T_{90} = 0.018$ sec., and at the same time its $T_{90} = 0.080$ sec in the Swift catalog. Also it is necessary to verify a light curve expansion (the GRB time dilation essence) with redshift rate by analogy with supernovae [5,11]. However these findings could be not secure in view of Orlov & Raikov [19]. Recently it was shown that some otherwise "short" GRBs have T_{90} durations up to several minutes: these events are only short in the literal sense, e.g. Rueda et al [26]. This and similar facts also demonstrate that the definition of long and short GRBs should be reconsidered.

6. Conclusion

Future THESEUS space observations of GRBs [1, 33] and corresponding multimessenger ground-based studies including large optical telescopes [6, 31, 32] will bring crucial

information for testing theoretical cosmological models.

Our summary:

- The fractal dimension estimation of the Swift GRB spatial distribution gives D = 2.55 ± 0.06 on scales of 1.5 – 5.5 Gpc. This is an indirect indication that the Universe is inhomogeneous on these scales.
- The Universe is isotropic based on the BATSE, Swift and Fermi data.
- The high redshift GRBs (z > 2) can be used as a tool to determine the basic cosmological parameters, e.g. the Hubble law, in the future when the redshift defined sample volume will increase to a several   thousands.
- For the long Swift GRBs T_{90} observed (without taking into account selection effects) durations distribution there is no the time dilation effect. The main selection effect is the uncertainty of spectral shape of the GRB at different redshifts and strong influence of the level of noise to determination of the T_{90} . Also incompleteness of GRBs sample which related to different nature of origin source (core collapse and binary merges) and can have different space, probabilistic and durations distributions.

Obviously we still have insufficient data in order to do final conclusions. The THESEUS project opens new perspectives in research of the Universe due to increase of redshift defined GRBs sample, which is shown in Figure 5.
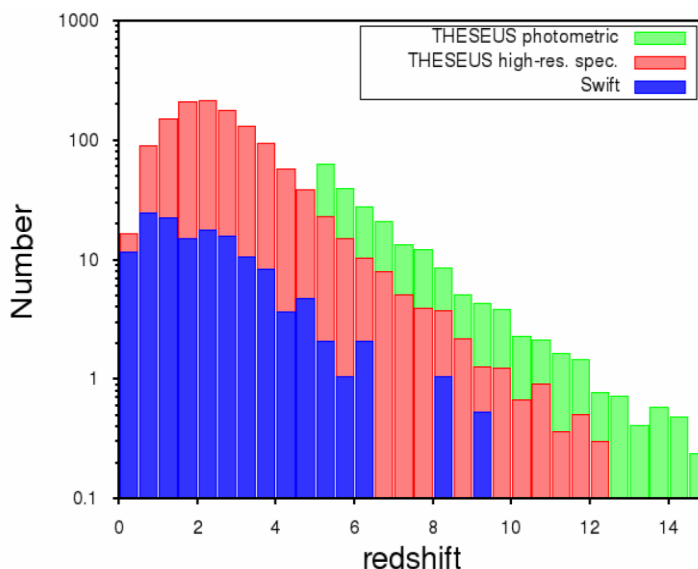
Fig5. The estimated histograms of GRB number for 5 years due to THESEUS contribute from Amati L., et al. (2018) [1].

References

[1]   Amati L. et al.: // Adv. Space Res. Vol.62. Iss.1. P.191 (2018)

[2]   Balázs L. G. et al.: A giant ring-like structure at 0.78 < z < 0.86 displayed by GRBs // Mon. Not. Roy. Astron. Soc. 452, 2236 (2015)

[3]   Baryshev, Y. V.: Hierarchical Structure of Metagalaxy – Problem Review // Astrof.Issl. (Izvestiya

SAO), Vol. 14, P. 24, (1981); Baryshev, Yu. V.: Field fractal cosmological model as an example of practical cosmology approach// in Proceedings of the International Conference "Practical Cosmology", St.-Petersburg, Russian Geographical Society, , Vol.2, P.60 (2008) (arXiv:0810.0162); Paturel, G.; Teerikorpi P. and Baryshev Y.: Hubble Law: Measure and Interpretation// Foundations of Physics, Volume 47, Issue 9, P.1208 (2017) (arXiv:1801.00128)

[4] Baryshev Yu. & Teerikorpi P.: *Fundamental Questions of Practical Cosmology: Exploring the Realm of Galaxies*, Astrophysics and Space Science Library, Volume 383. ISBN 978-94-007-2378-8. Springer Science+Business Media B.V., pp.328 (2012)

[5] Blondin S. et al.: Time Dilation In Type Ia Supernova Spectra At High Redshift // Astroph.J., V.682, P.724 (2008)

[6] Castro-Tirado A.J. et al.: Gamma-ray bursts: Historical afterglows and early-time observarions // in Proceedings of The International Conference "SN 1987A, Quark Phase Transition in Compact Objects and Multimessenger Astronomy", Russia, Terskol (BNO INR RAS), Nizhnij Arkhyz (SAO RAS). – P.41 (2018)

[7] Demianski M. et al.: Cosmology with gamma-ray bursts. I. The Hubble diagram through the calibrated Ep,I-Eiso correlation // A&A 598, A112 (2017)

[8] Frontera F. et al.: The Gamma-Ray Burst Catalog Obtained with the Gamma-Ray Burst Monitor Aboard BeppoSAX // Astroph.J.Suppl.S. V.180. N.1 (2009)

[9] Gerasim R. V., Orlov V. V. and Raikov A. A.: Study of the Large-Scale Distribution of Gamma-Ray Burst Sources by the Method of Pairwise Distances // Astrophysics, 58, 204 (2015)

[10] Gehrels N. et al.: The Swift Gamma-Ray Burst Mission // Astroph.J. V.621, P.558 (2005)

[11] Goldhaber G. et. al.: Timescale Stretch Parameterization Of Type Ia Supernova B-Band Light Curves // Astroph.J., V.558, P.359 (2001)

[12] Gott III J.R. et al.: A Map of the Universe // Astrophys.J. V.624. P.463. (2005)

[13] Hubble E.: The Observational Approach to Cosmology. // Clarendon, Oxford (1937)

[14] Kocevski D. & Petrosian V.: On the Lack of Time Dilation Signatures in Gamma-ray Burst Light Curves // Astroph.J., 765:116 (7pp) (2013)

[15] Lietzen H., et al.: Discovery of a massive supercluster system at z ~ 0.47 // Astron.Astrophys. V.588. L4. (2016)

[16] Lloyd-Ronning N.M. et al.: Cosmological Evolution of the Intrinsic Prompt Duration for Radio Bright Gamma-Ray Bursts // e-Print arXiv:1809.04190 (2018)

[17] Narayana Bhat P. et al.: The Third Fermi GBM Gamma-Ray Burst Catalog: The First Six Years // Astroph.J.Suppl.S. V.223. N.2. (2016)

[18] Neta A. Bahcall.: Hubble's Law and the expanding universe // PNAS 112 (11) 3173-3175 (2015)

[19] Orlov V. & Raikov A: Cosmological tests and evolution of extragalactic objects // Astron.Zhurn., 93, 453 (2016)

[20] Paciesas W.S. et al.: The Fourth BATSE Gamma-Ray Burst Catalog (Revised) // Astroph.J.Suppl.S. Vol.122. Iss.2. P.465 (1999)

[21] Peebles P.J.E.: *Principles of Physical Cosmology //* Princeton Univ.Press, (1993)

[22] Petrosian V., Bouvier A., Ryde F.: Gamma-ray Bursts as Cosmological Tools // arXiv:0909.5051

(2009)

[23] Raikov A. A., Orlov V. V. and Beketov O. B.: Non-homogeneities in the spatial distribution of gamma-ray bursts // Astrophysics, 53, 396 (2010)

[24] Raikov A. A. and Orlov V. V.: Method of pairwise separations and its astronomical applications // Mon. Not. Roy. Astron. Soc. 418, 2558 (2011)

[25] Ripa J. & Shafieloo A.: Update on Testing Isotropic Universe Using Properties of Gamma-Ray Bursts // e-Print arXiv:1809.03973 (2018)

[26] Rueda J. A. et al.: GRB 170817A-GW170817-AT 2017gfo and the observations of NS-NS, NS-WD and WD-WD mergers // JCAP, e-Print arXiv:1802.10027 (2018)

[27] Sandage A.: Practical cosmology: Inventing the past. In: Binggeli, Buser, R. (eds.) The Deep Universe // pp. 1–232. Springer, Berlin (1995)

[28] Shirokov S.I. et al.: Large-Scale Fluctuations in the Number Density of Galaxies in Independent Surveys of Deep Fields // Astronomy Reports, Vol. 60, No. 6, 563 (2016)

[29] Shirokov S.I., Raikov A.A. and Baryshev Yu.V.: Spatial Distribution of Gamma-Ray Burst Sources // Astrophysics, Vol. 60, No. 4 (2017)

[30] Shirokov S.I., Raikov A.A.: Spatial Distribution of GRB with Known Redshifts // in Proceedings of The International Conference "SN 1987A, Quark Phase Transition in Compact Objects and Multimessenger Astronomy", Russia, Terskol (BNO INR RAS), Nizhnij Arkhyz (SAO RAS). – P.157 (2018)

[31] Sokolov I.V., et al.: Clustering of galaxies around the GRB 021004 sight-line at z 0:5. // in Proceedings of the International Workshop on Quark Phase Transition in Compact Objects and Multimessenger Astronomy: Neutrino Signals, Supernovae and Gamma-Ray Bursts, Russia, Nizhnij Arkhyz (SAO), KBR, Terskol (BNO). – P.111 (2016)

[32] Sokolov V.V., et al.: The core collapse supernovae, gamma-ray bursts and SN 1987A. // in Proceedings of the International Conference "SN 1987A, Quark Phase Transition in Compact Objects and Multimessenger Astronomy", Russia, Terskol (BNO INR RAS), Nizhnij Arkhyz (SAO RAS). – P.190 (2018)

[33] Strata G. et al.: THESEUS: a key space mission concept for Multi-Messenger Astrophysics // e-Print arXiv:1712.08153 (2018)

[34] Wang F.Y. et al.: Gamma-ray burst cosmology // New Astronomy Reviews, V.67, P.1 (2015)

[35] Wei Jun-Jie and Wu Xue-Feng.: Gamma-ray burst cosmology: Hubble diagram and star formation history. // Int.J.Mod.Phys.D. V.26. No.02. 1730002. (2017)

[36] Zhang Fu-Wen et al.: Cosmological Time Dilation in Durations of Swift Long Gamma-ray Bursts // Astroph.J.Lett., 778:L11 (5pp) (2013)

The multi-aperture survey telescope for the INF project

A. Shugarov[1], M. Nalivkin[1], I. Savanov[1,*], S. Naroenkov[1]

[1] *Institute of Astronomy of the Russian Academy of Science, Moscow, Russia;*

shugarov@inasan.ru

Abstract   INF (INASAN Near Earth Objects Finder) project is a dedicated network of robotic telescopes to detect 10 m asteroids coming in the Near Earth Space. The main features of the project are short cadence time (1 h) of all-sky survey and moderate limiting magnitude (19^m) without filters, possibility of carrying out the additional scientific program. The INF multiaperture telescope consists of 8 VT-78d telescopes on fast mount. The VT-78d telescope provides unique combination of parameters: aperture of 250 mm, fast focal ratio F/1.58, large field of view (10 deg diameter, 78.5 sq. deg) and D_{80} image quality of 5 arcsec. The INF total field of view is 574 sq. deg (298 Mpixels) with 5.2 arcsec/pixel scale. The key features of INF for NEO observation program is the ability to find nearby small objects of size >10 m not included into existing catalogues at a distance less than 0.01 a.u., follow them to determine their orbit and report about potential impact to the Earth quickly (in few hours). INF can detect 10 m asteroid at a distance of 0.5-2.2 million kilometers what corresponds to approaching time of 9-40 hours for typical NEO speed of 15 km/s. The warning time, e.g. the time after preliminary orbit determination until possible impact will be in a range from few hours up to one day. In case of multiple sites operation (worldwide) INF can detect most of the dangerous asteroids with a size of >10 m coming from the night sky. According to our estimates INF will discover about 7330 NEOs of 10 m size in 5 years in case of every day operation (8 hours per night).

Keywords: Near Earth Objects, Wide Field Telescopes

1. Introduction

In recent years many countries have begun work on the development of systems for the detection and tracking of dangerous Near Earth Objects (NEOs). The majority (~90 %) of all large (>1 km) potentially hazardous objects has been revealed in the framework of Space Guard Program implemented in the United States. In the next decade the majority of >100 m NEOs will be discovered by large aperture survey telescopes such as Zwicky Transient Facility (ZTF), Catalina Sky Survey, Panoramic Survey Telescope & Rapid Response System (Pan-STARRS) and Large Synoptic Survey Telescope (LSST).

The situation is different with the prospect of detecting smaller bodies with sizes between 10 m and 100 m. The number of potentially hazardous bodies of 10 m sizes is estimated to be 10^8 pieces [1], the rate of their collisions with Earth is about one event per 10 years, smaller bodies have fallen annually. The problem of exhaustive detection of these bodies at long distance which provides the aforementioned warning times will not be solved for at least a few decades. It is more realistic to discover these bodies in the Near Earth Space and to provide alerts about possible collisions with Earth.

The ideal system capable of detecting 10 m class NEOs should have:
- short cadence time (< 1 h);
- limiting magnitude of 19^m and fainter to detect 10 m NEOs at a reasonable distance;
- reasonable angular resolution of a telescope to prevent contamination.

Asteroid Terrestrial-Impact Last Alert System (ATLAS) is an example of successful system designed to detect 30-50 m impactors about one week in advance coming from the night sky, but this system is not efficient enough to detect good share of 10 m NEOs because of survey rate (a cadence time of about 1 day).

The ground-based wide-angle camera array (GWAC) is a set of ground-based instruments in the framework of the SVOM Chinese – French space mission dedicated to detecting gamma-ray bursts (GRBs) [2]. GWAC is designed to comprise 36 cameras of 18 cm aperture each with a totally covered area of more than 5000 deg^2 in one shot. GWAC will monitor the sky to catch the prompt optical emission of GRBs. Besides monitoring of GRBs, GWAC has potential to search NEOs and operate as "last alert system" to provide alerts about possible collisions of asteroid with Earth. The GWAC system will be very fast but not sensitive enough to detect 10 m class NEOs at reasonable distance.

INASAN suggests the INF (INASAN Near Earth Objects Finder) project that was optimized for detection of 10 m class asteroids coming in the Near Earth Space. The worldwide network of about 10 INF telescopes will provide 24 h of operation. In this case the system will ensure completeness of detection and warning time from few hours up to one day.

Position of ATLAS, GWAC, INF and some other survey telescopes on survey merit diagram is shown in Fig. 1. INF seems to be efficient instrument to detect 10 m class NEOs because of optimal combination of cadence time and sensitivity.
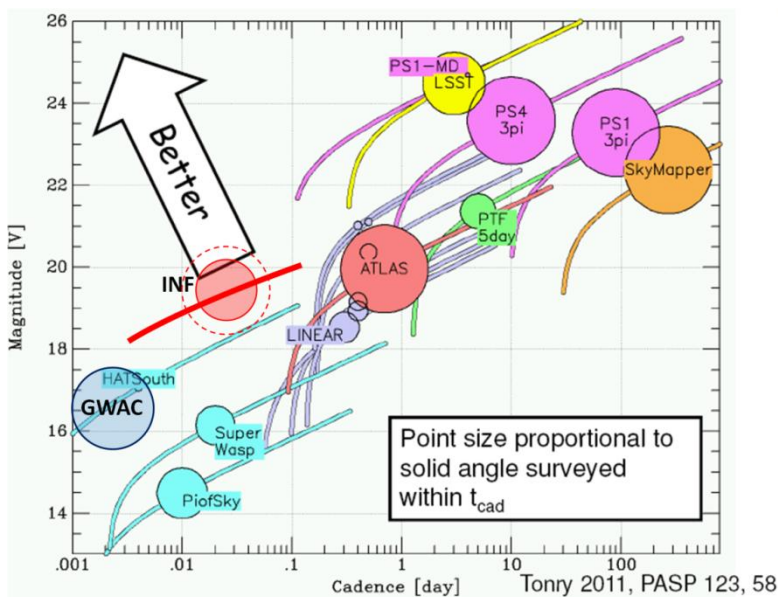
Fig1. *INF on survey merit diagram.*

Beside detection of 10 m class NEOs, INF will be useful for many others scientific goals, such as:

- Discovery and characterization of Near Earth Asteroids and Main Belt asteroids
- Search for new comets
- Monitoring, discovery and characterization of space debris
- Study of

- o transiting exoplanets
- o variable stars
- o young and active stars
- o supernovae
- o gamma-ray bursts
- o AGN / QSO variations
- o microlensing events
- Gravitational wave sources

2. INF and VT-78d telescope

The INF multiaperture telescope (Fig. 2) consists of eight VT-78d telescopes at one fast-track mount ASA DDM160. The main parameters of single VT-78d telescope and multiaperture INF telescope (8 tubes) are presented in Tables 1 and 2 respectively.

For fast repointing INF will be installed in a "shell type" dome.

Fig2. INF multiaperture telescope: 8 x VT-78d telescopes on ASA DDM160 mount.

Table1. Main parameters of the VT-78d telescope

Parameter	Value
Entrance pupil diameter	250 mm
Effective diameter	212 mm
Effective focal length	395 mm

F-ratio	F/1.58
Field of view angular diameter	10 deg
Field of view linear diameter	69.5 mm
Scale	1.915 μm/arcsec
Spectral range, nm	450-850 nm
D_{80} in integral light, center-edge	8-10 μm 4-5 arcsec
Maximum distortion at 550 nm	0.45 %

Table2. Main parameters and all-sky (20000 sq. deg) survey efficiency of the INF telescope (8x tubes)

Parameter	Value
Detector of single tube	CMOS GSENSE6060BSI 6k × 6k, 10 μm pixel
Pixel format	12k × 24k
Number of pixels	298 Mpixel
Pixel scale	5.2 arcsec/pix
Field of view	17.6 × 35.2 deg 574 sq. deg
Readout time	< 0.25 s
All-sky survey @ 10 s exposure	10 min @ 18.3^m
All-sky survey @ 30 s exposure	20 min @ 18.9^m
All-sky survey @ 100 s exposure	1 h @ 19.4^m

The VT-78d telescope is a new generation wide field telescope designed by V. Terebizh (INASAN patent №162010 (RU)). The telescope provides a unique combination of 250 mm aperture, 10 deg field of view and 5 arcsec image quality. The VT-78d optic (Figs. 3, 4) consists of simple optical elements, all surfaces are spherical, simple glass is used.
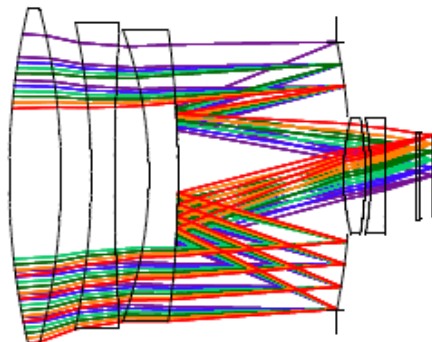
Fig3. *VT-78d optical layout.*

Baffle   First lens   Secondary mirror   Detector

Main mirror   Focuser
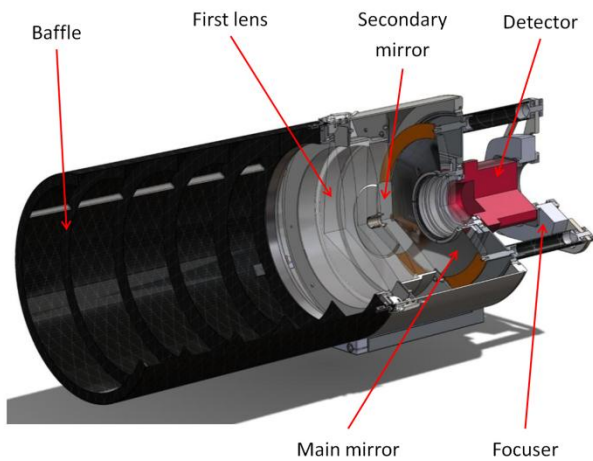
Fig4. *VT-78d mechanical layout.*
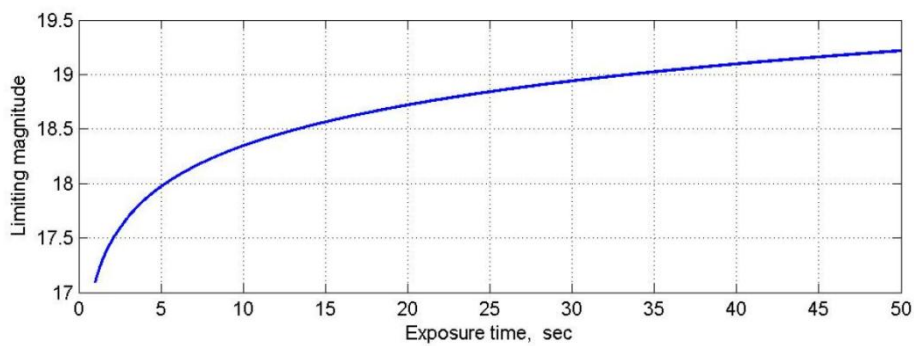
Fig5. *VT-78d limiting magnitude (SNR = 7) vs exposure time.*

The telescope was designed to be used with the cost-effective CMOS detector GSENSE6060BSI (6k × 6k, 10 μm pixel) with electronic shutter. The CMOS-camera NEVA6060 with 4 Hz frame rate is planned to be used. For specific scientific tasks [3,4] the short series of frames can be taken with frame rate of up to 44 Hz.

The telescope limiting magnitude versus exposure time is shown in Fig. 5. Calculation was done for atmosphere FWHM quality of 1.5 arcsec, sky background of 20.5 mag/arcsec^2 and bandwidth of 500 nm.

All tubes of INF multiaperture telescope can be aligned by special mechanism to look at one field in order to perform multicolor photometry or to improve telescope sensitivity and sampling.

In case of all tubes looking at one field (71 sq. deg) the limiting magnitude will be about 20.4^m for 100 s exposure without filters at good observation conditions (low background light).

It is possible to put a filter change mechanism with one specific filter for each telescope. In this case it will be possible to do 8-bands photometry with a limiting magnitude of 18.4^m for 100 s exposure.

3. INF system performance

One of the main characteristics of a NEO discovery system is a visibility zone, e.g. the volume where NEOs of a given size (10 m) can be detected [5].

To calculate NEOs visibility zones the following parameters should be taken into account:
- the size and albedo of the NEO, phase angle, distance to the Sun and observer;
- the main characteristics of a telescope and detector;
- the background illumination, i.e. sky background and scattered light in a telescope;
- exposure time;
- NEO proper motion.

For night-time hemisphere the value of sky background in a range of 20.5-21 mag/arcsec^2 was taken. For the day-time hemisphere we use the values in a range of 20.5-18 mag/arcsec^2 for the NEO-Earth-Sun angle between 90 deg and 70 deg, which means the observation during twilight and/or close to horizon. For the NEO-Earth-Sun angles less than 70 deg the distance of NEO detection drops down very quickly because of phase angle and background light. To take into account the effect of star contamination because of pixel scale and scattered light inside INF multi-lens optical system we increase the sky background by 1 mag/arcsec^2.

Fig. 6 illustrates the INF performance to detect asteroids of 10 m size with the 60 s exposure time. The Earth coordinates are (0,0) and those of the Sun are (0, about -150). Isophote bands (green and blue) of constant SNR are shown with a 3 unit increment. A separate pink isophote is given for SNR = 9 which corresponds to a reliable detection.

You can see that INF provides reliable detection of NEOs approaching the Earth from solid angle of 2 π sr (night sky) at a distance of 0.5-2.2 million km from the Earth. The asteroid with typical approaching speed of 15 km/s crosses this distance in 9-40 hours. For NEOs with large proper motion the detection distance will be shorter.

For exhausting detection of NEOs it is necessary to install few telescopes at different location both in the northern and southern hemispheres of the Earth. We can say that in one night INF will detect practically every asteroids coming inside its visibility zones, getting enough measurements to calculate preliminary orbit and provide the alert about potentially

hazardous objects. To determine the orbit of dangerous NEOs and to calculate the entrance point into Earth atmosphere the follow-up telescopes with better sensitivity and angular resolution should be used. The warning time for typical 10 m size asteroid will be in a range of few hours up to one day.
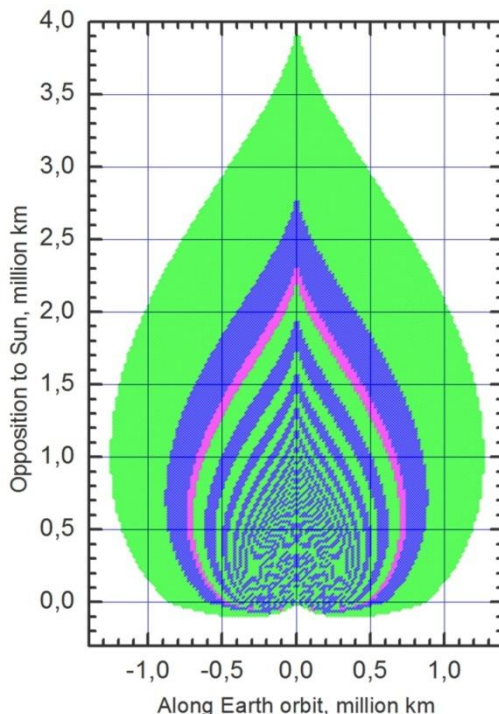
Fig6. *Visibility zone of 10 m NEOs for INF project with 60 s exposure time. The SNR is shown by color coding (green and blue) isophotes with 3 unit increment, the pink isophote shows SNR = 9. The Earth coordinates are (0,0), the Sun is at (0,-150).*

An important question is how many NEOs will be detected by INF in 5 years. To estimate the number we constructed a population of small virtual NEOs. We used the Granvik-Bottke-Morbidelli model [6]. According to the Granvik-Bottke-Morbidelli model, the number of Near Earth Asteroids with H < 25^m is estimated as 0.9 million.

We estimated the number of asteroids accessible for observations with INF in the following way. For each virtual asteroid we integrated asteroid motion for 5 years and estimated the conditions of visibility of the asteroid from the observatory B18 (Peak Terskol, Russia) in the sky. The solution of numerical equations of motion of asteroids was carried out by the Everhart integrator of 17 orders, the model of forces included perturbations from the planets, the Sun and the Moon. We counted asteroids whose visual magnitude is less than 19.7^m, and altitude is more than 15 degrees above horizon at the night time.

According to our estimates the INF will discover ~7330 NEOs in 5 years in case of every day operation (8 hours per night) with a limiting magnitude of 19.7^m. Model distribution of discovered NEOs over the sky is shown in Fig. 9.
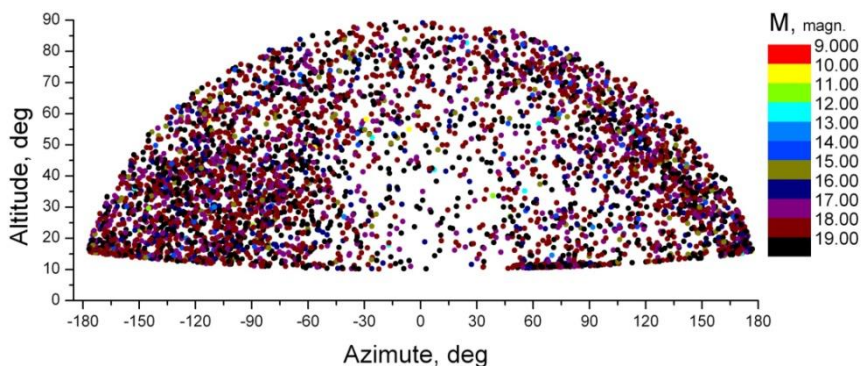
Fig7. *Distribution of possible NEO on (Az-Alt) plane that could be detected by INF.*

2.4. Combed visibility zones for INF and SODA projects

The Chelyabinsk event of February 15, 2013 has clearly shown that the collision of a rather small body of a size about 17 m with Earth at a populate area may cause significant damage. Chelyabinsk asteroid coming to the Earth from the day sky could not be discovered by any ground-based or Near Earth Space telescopes because of unfavorable phase angle and light scattering [7]. The only way to detect these bodies reasonably well beforehand is to put a telescope relatively far from the Earth.

The project of Space system SODA (System of Observation of Day-time Asteroids) was proposed [8] for exhaustive detection of decameter (and larger) bodies approaching the Earth from the Sun direction (Chelyabinsk type meteoroids). The main idea of the mission is to put one or two spacecrafts equipped with medium-size (30 cm) wide field telescopes with pre-aperture active mirrors into the vicinity of L1 point of the Sun-Earth system. This position is very comfortable for detecting asteroids coming from the Sun direction due to relatively short distance between a telescope and an asteroid and optimal phase angle.

In Fig. 8 the visibility zone of 10 m NEOs with 0.15 albedo is shown for INF project with the 60 s exposure time and for SODA project with the 4 s exposure time. The blue doted isophote shows a confident (SNR = 9) detection zone for INF project and the red doted one for SODA project. SODA project was unable to observe asteroids close and behind the Earth because of light scattering from the Earth and the Moon. INF project can operate only at a night hemisphere. You can see that INF and SODA projects complement each other to provide detection of asteroids coming from all directions with the   warning time from few hours up to one day.
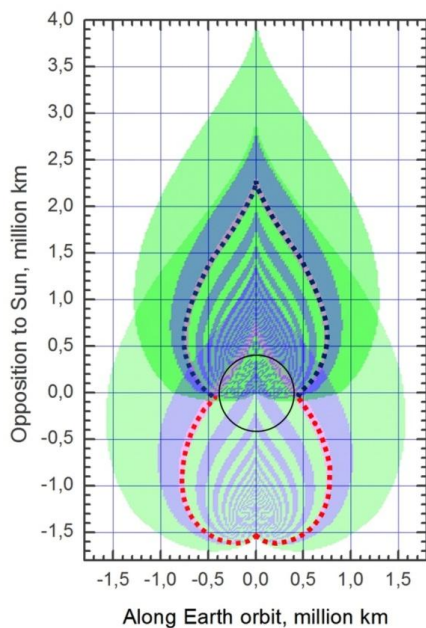
Fig8. *Combined visibility zone of 10 m NEOs for ground-based INF project (blue dotted) and space-based SODA project (red dotted) located at L1 point of the Sun-Earth system (0,-1.5). The SNR is shown by color coding (green and blue) isophotes with 3 unit increment, the pink isophote shows SNR = 9. The Earth coordinates are (0,0), the Sun is at (0,-150), the Moon orbit is indicated by the black circle.*

Fig9. *INF prototype drawing, 2 x VT-78d telescopes on ASA DDM85PRO mount.*

4. INF prototype

INASAN is finishing construction of a prototype of the INF multiaperture telescope. The prototype consists of 2 identical wide-field telescopes VT-78d (Fig. 9) equipped with 4k×4k

CCD cameras on a fast-track mount. First light is expected in 2019. The INF prototype consists of:

- 2 x VT-78d telescopes, 2 x FLI ML16803 CCD cameras;
- 2 x FLI Atlas focusers, ASA DDM85PRO mount;
- ScopeDome 3m full robotic dome;
- control computer and equipment;
- observation planning software;
- data processing software.

5. Conclusion

The Chelyabinsk event changed our priorities in the asteroid and comet hazard problem. We understand that it is necessary to create special facilities to detect decameter size bodies coming both from day and night sky.

INF can operate as "a last alert system" to provide alerts about possible collisions of small asteroids with Earth. In case of multiple sites operation (worldwide) INF can detect most of the dangerous asteroids of a size of >10 m size coming from night sky with the warning time from few hours up to one day. We believe that combination of ground based (INF, ATLAS, GWAC) and Space based (SODA) projects is a proper way to provide realistic warning system against small decameter size impactors.

References

[1] Emel'yanenko, V. V. & Naroenkov, S. A., Dynamical features of hazardous near-Earth objects. 2015, Astrophysical Bulletin, 70, 342, DOI: 10.1134/S199034131503013X

[2] Motch, C et all, The SVOM mission. 2017, Astronomische Nachrichten, 338, 9-10, p. 978-983, DOI: 10.1002/asna.201713415

[3] Beskin, G., et al., Astronomy and Astrophysics Supplement, v.138, p.589-590, 1999

[4] Beskin, Grigory; Bondar, Sergey; Karpov, Sergey; Plokhotnichenko, Vladimir; Guarnieri, Adriano; Bartolini, Corrado; Greco, Giuseppe; Piccioni, Adalberto; Shearer, Andrew. "From TORTORA to MegaTORTORA-Results and Prospects of Search for Fast Optical Transients", 2010, Advances in Astronomy, 2010, article id. 171569, DOI: 10.1155/2010/171569

[5] Shugarov, A. S., Simulation of the detection zone of dangerous celestial bodies for space-based systems. 2013, Solar System Research, 47, 296, DOI: 10.1134/S0038094613040187

[6] Granvik M., Morbidelli A., Jedicke R., Bolin B., et.all, (2018). Debiased orbit and absolute-magnitude distributions for near-Earth objects. Icarus, 312, 181–207

[7] Shustov, B. M., Shugarov, A. S., Naroenkov, S. A., & Prokhorov, M. E., Astronomical aspects of cosmic threats: new problems and approaches to asteroid-comet hazard following the Chelyabinsk event of February 15, 2013. 2015, Astronomy Reports, 59, 983, DOI: 10.1134/S1063772915100066

[8] Shugarov, A., Shustov, B., & Naroenkov, S., System of observation of day-time asteroids (SODA). 2018, Open Astronomy, 27, 132, DOI: 10.1515/astro-2018-0023

The field galaxies clustering in GRB lines of sight based on observations with BTA and other telescopes

Ilya V. Sokolov[1,*], Alberto J. Castro-Tirado[2], Azamat F. Valeev[3], Ilya A. Solovyev[4], Olga P. Zhelenkova[3], Oleg V. Verkhodanov[3]

[1]Terskol Branch of Institute of Astronomy of RAS, Moscow, Russia;

ilia.v.sokolov@gmail.com

[2]Instituto de Astrofísica de Andalucía (IAA-CSIC), P.O. Box 03004, E-18080 Granada, Spain

[3]Special Astrophysical Observatory of RAS, Nizhnij Arkhyz, Russia

[4]Saint-Petersburg State University, SaintPetersburg, Russia

Abstract The characteristic signs of the clustering of field galaxies were detected in the direction to gamma-ray bursts (GRBs). All accessible signs of such clustering in the lines of sight and near the location of GRB021004 were tested. The data from observations with BTA/SCORPIO, HST/ACS, VLT/UVES and from the cluster catalog SDSS-III were used. The works on photometric redshifts were reviewed.

Keywords: Gamma-Ray Bursts, Clusters, BTA Observations

1. Introduction

GRBs with large redshift z are good cosmological probes. They reveal clusters of galaxies on the line of sight both spectroscopically and photometrically. In this connection, mention should be made here of the article "GRBs as an instrument for testing cosmological models" by Shirokov S. I., Raikov A. A., Baryshev Yu. V., Sokolov V. V., and Vlasyuk V. V. in these Proceedings. In fact, this is also the case in a recent article [1] (see Figures 1, 2 and others there). Below, in the subsequent sections of our paper, we have reviewed also other works on the same topic, emphasizing the relevance of research in this direction.

As a concrete example, we also use here our research on the GRB 021004 field, which we began immediately after the discovery of this burst [2] (see also references there) because in interpreting the results of our observations of this GRB field we used the (new then) photometric redshifts method [3] (see also Ilya V. Sokolov's diploma on the same topic). Here we will specifically mention the application of the same method to similar problems in the study of the distribution of galaxies in the direction of distant cosmological objects.

The study using the photometric redshifts method of clusters of galaxies is also discussed in [5]. Here, the authors present the Massive and Distant Clusters of WISE Survey (MaDCoWS), a search for galaxy clusters at $0.7 < z < 1.5$ based upon data from the Wide-field Infrared Survey Explorer (WISE) mission. A total of 1723 of the detections from the WISE – Pan-STARRS sample have also been observed with the Spitzer Space Telescope, providing photometric redshifts and richnesses, and an additional 64 detections within the WISE – SuperCOSMOS

region also have photometric redshifts and richnesses. Spectroscopic redshifts for 38 MaDCoWS clusters with IRAC photometry demonstrate that the photometric redshifts have an uncertainty of $\sigma z /(1+z) \sim 0.036$. A comparison of photometric and spectral z is shown in Figs.13 and 14 of [5].

Thus, in article [5], the possibility of detecting transitions to homogeneity using photometric redshift catalogs was studied. The method is based on measuring the fractality of the projected galaxy distribution, using angular distances, and relies only on observable quantities. It thus provides a way to test the Cosmological Principle in a model-independent unbiased way. The method was tested on different synthetic inhomogeneous catalogs, and shown that it is capable of discriminating some *fractal models* with relatively large fractal dimensions, in spite of the loss of information due to the radial projection. Also studied the influence of the redshift bin width, photometric redshift errors, bias, non-linear clustering, and surveyed area, on the angular homogeneity index in the ΛCDM cosmology. The level to which an upcoming galaxy survey will be able to constrain the transition to homogeneity will depend mainly on the total surveyed area and the compactness of the surveyed region. In particular, a Dark Energy Survey [5] – like survey should be able to easily discriminate certain fractal models with fractal dimensions.

This method will have relevant applications for upcoming large photometric redshift surveys, such as Dark Energy Survey or the Large Synoptic Survey Telescope (LSST). The same photo-z method is used in [6]. So, the photo-z method is a standard approach for estimating the redshifts of galaxies when only photometric information is available. In Figure 3 of paper [6] a representative test set performance is shown as a scatter plot and marginal distributions of 192000 spectroscopic vs. photometric redshifts. So, the photometrically derived z is also used in recent works [6, 7], where galaxy clusters on $z \sim 1$ are investigated.

2. Observational cosmology and GRBs afterglow monitoring using the photo-z method

The characteristic signs of the clustering of field galaxies were detected in the direction to GRB 021004. The results are set out in the series of articles [3] and [2, 8]. It is about the study of BTA, Hubble, Spitzer GRB 021004 deep field and on the clustering of galaxies around the GRB sight-line and on the excess density of field galaxies near $z \sim 0.56$ around the GRB 021004 position. All accessible signs of such clustering in the line of sights and near the location of the GRB were tested. The data from observations with BTA/SCORPIO, HST/ACS, VLT/UVES and from the cluster catalog SDSS-III were used.

We test for reliability any signatures of field galaxies clustering in the GRB 021004 line of sight:

The first signature is the GRB 021004 field photometric redshifts distribution based on the BTA observations with a peak near $z \sim 0.56$ estimated from multicolor photometry in the GRB direction.

The second signature is the Mg II 2796/2803Å absorption doublet at $z \approx 0.56$ in the VLT/UVES spectra obtained for the GRB 021004 afterglow.

The third signature is the galaxy clustering in a larger ($\sim 3 \times 3$ degrees) area around GRB 021004 with an effective peak near $z \sim 0.56$ for both the spectral and photometric redshift distributions obtained from the Baryon Oscillation Spectroscopic Survey (BOSS), which is a part of the Sloan Digital Sky Survey III (SDSS-III).

And a possibility of an inhomogeneity (related with the galaxy clustering) near the

GRB 021004 direction can be also confirmed by an inhomogeneity in cosmic microwave background related with the Sunyaev-Zeldovich effect. From catalogs data the size of the whole inhomogeneity in distribution of the galaxy cluster with the peak near $z \approx 0.56$ was also estimated as ~6-8 degrees.

In connection with our research, we would like to emphasize here the main observational features of GRBs noted in the literature after 1998.

So, the general characteristics of GRBs are as follows:

- Classification of the events by duration: ~ 0.2s (25%), ~ 30s (75%).
- Short and very intensive events in the high energy range.
- Counterparts of all bursts can be observed in all ranges of electromagnetic radiation (X, UV, opt, IR, radio)

Cosmological origin. After 1998, GRBs are distant and very distant (with measured z~10) extragalactic sources related with relativistic collapse of massive stars cores… (Though before 1998 it was supposed that GRBs are the explosions on the surface of neutron stars in the Galaxy.)
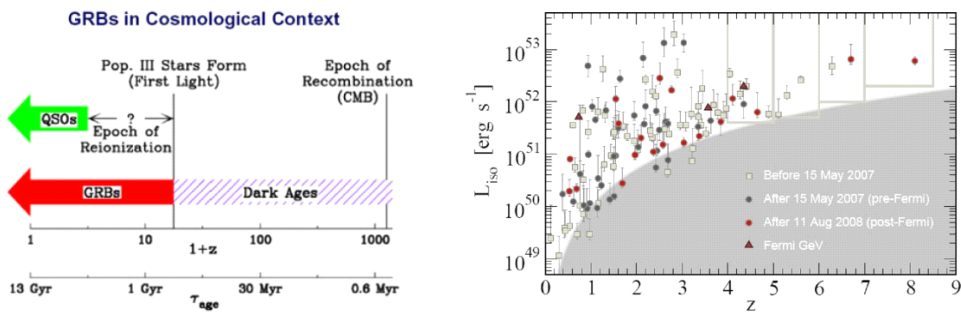
Fig1. Left: GRBs in cosmological context. Right: from [9] — The Liso luminosity-redshift distribution of 119 Swift GRBs. Squares represent 63 GRBs used in [11], with 56 found subsequently: before (grey circles) and after (red circles) the start of Fermi. Three Fermi-LAT GeV bursts (triangles) are shown (but not used in our analysis; see also [1] and references therein).

It is assumed that uniformity of the Universe on cosmological scales is the *fundamental* assumption of the standard cosmology that should be fulfilled even for such distant sources as GRBs. Now it is the most distant objects with measured redshifts z </~ 10 [1], [10].

In 1997-2002, there were studies [2] of GRB fields centered on the host galaxies of GRB 970508, GRB 971214, GRB 980613, GRB 980703, GRB 990123, GRB 991208, GRB 000926, GRB 021004 + investigation of surroundings of radio-source RC J0311+0507 of sizes ~ 4′×4′ (see Table 1 in [2]). The observations were carried out on the 6-m Special Astrophysical Observatory telescope using the BTA/SCORPIO instrument, and these data where supplemented with data obtained with other instruments. SDSS survey was also used. SDSS survey has a limiting magnitude of about 22, and the catalog includes photometric red-shift estimations as well as spectral red-shifts for brighter objects.

So, one of the goals of this work is to point out what can be obtained with 6-m telescope (and others) in these challenging and actual tasks, supplementing these studies with other instruments' data. And the main thing for us here is the clustering of field galaxies near GRB lines of sight.

3. The study of irregularities in the spatial distribution of distant galaxies by the method of photometric redshifts in the direction of GRBs

The GRB 021004 field: *The first signature* of the field galaxies clustering is the distribution of *photometric* redshifts in the BTA GRB 021004 field (of size of ~ 4′×4′) with a peak near z ~ 0.56, determined from the *multi-band BVRI photometry* of the field galaxies the direction of this GRB 021004 + HST/ACS data.
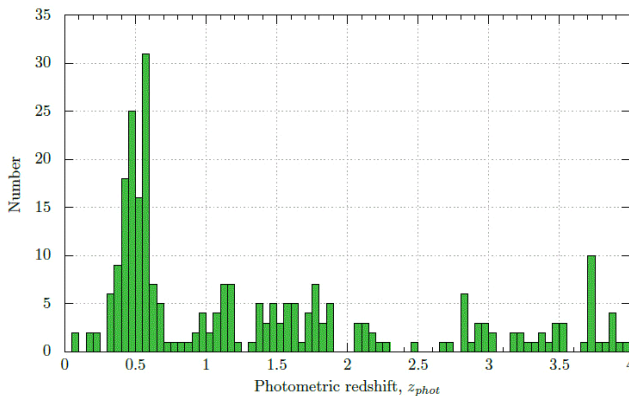
Fig2. *The photometric redshift distribution for 246 objects with the peak at z ≈ 0.56 based on BTA BV RI data [2, 9].*

The method of the photometry of GRB 021004 field is described in detail in our papers [2, 9]. We used the GRB021004 field, which was obtained as a part of GRB afterglow observations program on BTA (see Table 1 in [2, 9]). This field has exposure times of about one hour in each of the BVRI optical bands. The catalog of galaxies, extracted from this field of size 4'x4' includes 935 objects with the signal-to-noise ratio > 3. The following limiting magnitudes: 26.9 (B), 27.2 (V), 26.0 (Rc) and 25.5 (I). We also made sure our results are consisted with HST ACS data and data acquired with HST ACS camera in F475W (24.5), F606W (26.5) and F814W (25.5) bands. So, the photometric redshifts of GRB021004 field galaxies was estimated from the multicolor photometry and the accuracy of these redshifts is about 10%, which is high enough for statistical studies of the properties of distant objects.

The main idea of the photometric redshift estimation is as follows: an objects' multicolor photometry may be considered as a low-resolution spectrum that is used to estimate redshift [2], [12]. In practice, we estimated the photometric redshifts for the extended objects of our sample using the Hyperz software package [13]. The input data for Hyperz were: the apparent magnitudes of the objects in four bands, the internal extinction law (we used the law by Calzetti et al. [14] for starburst galaxies, which is most commonly used for studies similar to our own), the redshift range in which the solution is sought (we considered z from 0 to 4).

The filter transmission curves of HST ACS optical bands F475W, F606W. F814W and BTA BVRI optical bands were used.

So, the method is based on finding the best fit of template spectra (see in [2]), it is crucial to the initial model spectra. For ten of the brightest galaxies in the GRB 021004 field we find that model spectra assigned to these galaxies are in good agreement to HST ACS data, which due to angular resolution of the images reveals the structure of these objects [2]. The field also contains four X-ray sources, for which we estimate redshift. For spatial distribution of field

galaxies we find a large inhomogeneity at z ~ 0.57. (see Figure 2). We emphasize here again that the template spectra of various galaxy types were used in this photometric redshift calculation.

Table1. Redshifts for objects in the GRB21004 field. r_{SDSS} is the r-filter stellar magnitudes from the SDSS catalog, R_{BTA} is the R-filter stellar magnitude from BTA observations, z_{SDSS} is the photometric redshift from the SDSS catalog, z_{SpSDSS} is the spectroscopic redshift from the SDSS catalog, z_{BTA} is the photometric redshift obtained from BTA observations. z_{Err} is the SDSS redshift error, *Prob* is the BTA redshift probability, *Type* is the spectrum type, *M* is the absolute stellar magnitude.

N	r_{SDSS}	R_{BTA}	z_{SDSS}	z_{SpSDSS}	z_{BTA}	$zErr$	Prob	Type	M
1	21.25	21.61	0.384	0.342	0.435	0.051	82.150	E	-19.350
2	23.46	22.34	–	0.622	0.995	–	47.310	Burst	-21.800
4	22.18	22.16	0.425	0.332	0.420	0.116	79.220	E	-18.480
5	20.87	20.60	0.398	0.581	0.410	0.099	92.530	S0	-20.010
6	21.84	21.81	0.538	0.517	0.650	0.049	2.210	Burst	-20.460
7	20.99	20.64	0.407	0.441	0.390	0.050	71.600	S0	-19.970
8	20.68	20.66	0.251	0.176	0.200	0.132	97.980	Sa	-18.270
9	20.61	20.42	0.358	0.275	0.305	0.087	98.160	Burst	-19.380
10	21.64	21.77	–	0.633	3.140	–	96.550	E	-24.130
11	21.30	21.20	0.601	0.508	0.445	0.066	97.750	E	-19.720
12	21.25	21.30	0.421	0.312	1.635	0.125	23.630	Burst	-24.360
13	21.47	22.35	0.153	0.347	0.440	0.074	73.120	Sa	-18.640
14	21.56	21.63	0.483	0.444	0.115	0.091	98.950	Burst	-15.450
15	21.38	20.78	0.755	0.631	0.525	0.066	73.850	E	-20.930
16	20.00	19.99	0.310	0.564	0.290	0.063	99.420	Burst	-19.850
17	21.97	21.76	0.497	0.530	0.465	0.078	87.750	Burst	-19.300
18	20.78	20.82	0.459	0.603	0.405	0.058	50.330	E	-19.750
20	21.76	22.34	0.371	0.328	0.455	0.045	80.380	S0	-18.630
21	21.31	21.42	0.747	0.603	1.130	0.042	0.000	Burst	-22.720
22	21.38	21.41	0.609	0.675	0.405	0.088	98.440	E	-19.240
23	21.89	21.51	0.502	0.146	0.420	0.123	84.200	Sa	-19.170
24	20.91	21.05	0.388	0.420	0.440	0.049	49.290	E	-19.910
25	21.96	22.10	0.413	0.512	0.355	0.061	72.790	Burst	-17.930
26	21.27	20.98	0.474	0.543	0.660	0.097	99.000	Burst	-21.280
27	21.25	21.81	0.436	0.515	0.400	0.063	93.860	Burst	-18.920
28	22.05	21.20	–	0.670	0.695	–	96.540	Burst	-21.580
29	25.30	24.53	0.664	0.790	0.480	0.151	42.830	E	-16.790
35	20.69	20.61	0.440	0.281	0.255	0.120	98.630	E	-18.730
41	20.64	20.54	0.403	0.581	0.395	0.070	77.230	E	-20.110
42	20.95	21.02	0.503	0.537	0.350	0.097	95.490	S0	-19.300
43	19.06	19.01	0.301	0.325	0.260	0.028	90.410	Sa	-20.440
44	20.50	20.42	0.413	0.171	0.255	0.148	92.470	E	-18.760
50	21.62	21.68	0.407	0.436	0.340	0.097	86.800	E	-18.690
51	21.85	21.83	0.673	0.827	0.650	0.093	28.910	Burst	-20.550
52	22.10	21.80	0.120	0.023	1.605	0.089	0.020	Burst	-24.200
55	21.34	22.10	–	0.178	0.440	–	76.270	Sa	-18.890
58	21.99	21.56	0.534	0.685	0.450	0.055	95.600	Burst	-19.360
59	21.89	21.65	0.467	0.513	0.550	0.034	37.430	Burst	-20.050
61	22.67	22.61	0.594	0.723	0.715	0.093	90.770	Burst	-20.000
62	22.29	22.01	0.521	0.567	1.770	0.038	2.850	Burst	-23.450
70	20.41	20.44	0.319	0.335	0.150	0.095	85.840	Burst	-17.770
82	21.03	21.54	0.373	0.288	2.650	0.184	99.990	Burst	-23.410
83	21.69	22.05	0.099	0.090	0.095	0.062	97.530	Burst	-15.530
93	21.71	22.16	0.525	0.479	0.340	0.087	86.130	E	-18.210
94	22.05	21.83	0.465	0.413	0.345	0.082	95.950	S0	-18.520
99	22.62	22.04	–	0.323	0.200	–	99.980	S0	-16.710

Paper [14] on the VLT/UVES of GRB 021004 afterglow spectra shows three parts of the UVES spectrum of GRB 021004 afterglow with the doublet Mg II 2796/2803.   So, here we have **The second signature** – the absorption doublet Mg II 2796/2803Å at the redshift $z \approx 0.56$ detected in the same VLT/UVES spectrum of the GRB 021004 afterglow of this GRB, i.e. on the line of sight of the GRB. Totally the following was detected there:

Mg II doublet at z= 2.3295 [GRB],

Mg II doublet at z= 1.6020,

Mg II doublet at z= 0.570 (identified also in SAO).

And here (on BTA) we have also the same doublet (with the same spacing between components) is outlined, but at z = 0.570.

Analogous cases were observed by other authors and for other GRBs. For example, see [15] on the clustering of galaxies around GRB sight-lines. In Introduction of their paper it is said that:

- There is evidence of an overdensity of strong intervening MgII absorption line systems distributed along the lines of sight towards GRB afterglows relative to quasar sight-lines. If this excess is real, one should also expect an overdensity of field galaxies around GRB sight-lines, as strong MgII tends to trace these sources.
- And in spectra by A. J. Castro-Tirado et al. [14] for GRB 021004 afterglow such MgII absorption line systems are as many as 3.

Considering the redshift ranges $0.37 < z < 2.27$ of the SDSS survey, an excess of strong intervening MgII systems was found along the 10 GRB lines of sight observed by VLT-UVES of a factor of ~ 2 compared to QSO lines of sight [16].

But we see ourselves the 3-d system with z≈0.57 in our BTA GRB 021004 afterglow spectra, though this MgII absorption at z=0.5550 (near Al II 1670 at z=1.6026) was first identified.

See also the above-mentioned study of GRB 021004 optical afterglow with the 8.2m VLT (UVES & ISAAC) between 10 and 14 hours after the onset of the event [14].

The paper also analyzed the distribution of matter around the progenitor star of GRB 021004 as well as the properties of its host galaxy with high-resolution echelle as well as near-infrared spectroscopy. Observations were taken by the 8.2m Very Large Telescope with the Ultraviolet and Visual Echelle spectrograph (UVES) and the Infrared Spectrometer And Array Camera (ISAAC) between 10 and 14 hours after the onset of the event.

And, at last, the ***third signature***, related to this already well-studied field around GRB 021004: on the clustering of galaxies in a larger area (>/~ 3×3 sq. degrees) around GRB 021004 with the effective peak near z ~ 0.56, detected from distributions of spectral and ***photometric redshifts*** from the Baryon Oscillation Spectroscopic Survey (BOSS), which is a part of the Sloan Digital Sky Survey III (SDSS-III).

Distributions over photometric redshifts in the fields of ~6-8 degrees near $z \approx 0.56$ were also studied by data from 6 catalogs (see Figure 3):

1) redMaPPer DR8 cluster catalog [17] (Rykoff et al., AJ 785, 104, 2014),

2) Group catalogues of the local universe [18] (Saulder et al., A&A 596, A14, 2016),

3) Newly rich galaxy clusters identified in SDSS-DR12 [19] (Wen et al., AJ 807, 178, 2015),

4) Northern Optical Cluster Survey [20] (Gal et al., AJ 137, 2981, 2009),

5) Richness of galaxy clusters [21] (Oguri, MNRAS 444, 147, 2014),

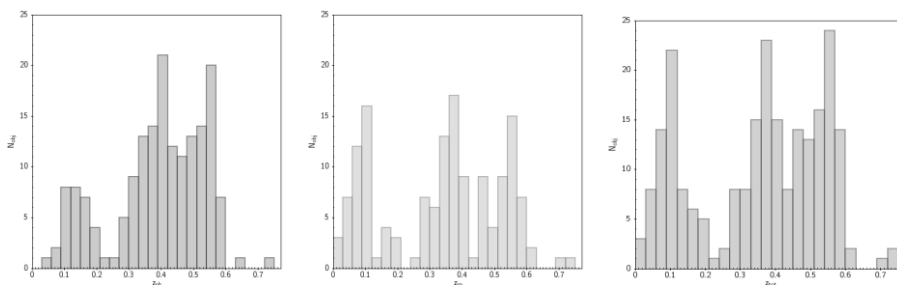6) Flux- and volume-limited groups for SDSS galaxies [22] (Tempel et al., A&A 566, A1, 2014).

Fig3. *The data from of 6 catalogs: the size of the whole irregularity is ~ 6–8 degrees in the distribution of galaxy clusters with the peak near z ≈ 0.56 was also estimated.*

So, the presence of a cluster near z ≈ 0.56 does not contradict the spectroscopy of the GRB021004 afterglow and one galaxy of this cluster turned out to be at the GRB line of sight at least… This could be determined if the spectroscopy with БТА & HST or narrow-band observations of the area of the host galaxy were carried out. Most probably, the irregularity with z ~ 0.57 in the direction to GRB021004 is a part of a huge supercluster and the study of the GRB 021004 area confirms the presence of an irregularity at z=0.57.

Then the origin of other systems of absorption lines (z*abs*) in spectra of this and other afterglows becomes understandable: for more distant clusters it is not a single galaxy, but the whole cluster that gets to the spectrograph slit. That is why the lines of this doublet are stronger at high z.

A possibility of inhomogeneity (a galaxy clustering) near the GRB 021004 direction can be also confirmed by an *inhomogeneity* in cosmic microwave background (CMB) related with the Sunyaev-Zeldovich effect. From CMB catalogs data *the size* of the whole inhomogeneity in distribution of the galaxy cluster with the peak near z ≈ 0.56 was also estimated as ~6-8 degrees [23]. Thus, the distribution of GRBs from catalogs of the BATSE and BeppoSAX space observatories relative to the cosmic microwave background (CMB) data by Planck space mission is studied. Three methods were applied for the data analysis:

1) a histogram of CMB signal values in GRB directions,

2) mosaic correlation maps calculated for GRB locations and CMB distribution,

3) calculation of an average response in the area of "an average population GRB" on the CMB map.

A correlation between GRB locations and CMB fluctuations was detected which can be interpreted as systematic effects in the process of observations. Besides, in averaged areas of CMB maps, *a difference between distributions of average fluctuations for short and long GRBs was detected*, which can be caused by different natures of these events.

The CMB fluctuations in direction of GRBs were also studied in the paper [23] on statistics of the Planck CMB signal in direction of gamma-ray bursts from the BATSE and BeppoSAX catalogs. See also [24] on the optical identifications of high-redshift galaxy clusters from Planck Sunyaev-Zeldovich survey, which presents the results of optical identifications and spectroscopic redshifts measurements for galaxy clusters from 2-nd Planck catalogue of Sunyaev-Zeldovich sources (PSZ2), located at high redshifts, z ~ 0.7–0.9. The paper used the data of optical observations obtained with the Russian-Turkish 1.5-m telescope (RTT150), the Sayan observatory 1.6-m telescope, the Calar Alto 3.5-m telescope and the 6-m SAO RAS telescope. Spectroscopic redshift measurements were obtained for seven galaxy clusters, including one cluster, PSZ2 G126:57+51:61, from the cosmological sample of PSZ2 catalogue.

In central regions of two clusters, PSZ2 G069:39+68:05 and PSZ2 G087:39-34:58, the strong gravitationally lensed background galaxies are found, one of them at the redshift z ~ 4.262. The data presented below roughly double the number of known galaxy clusters in the second Planck catalogue of Sunyaev-Zeldovich sources at high redshifts, z ~ 0.8.

The giant ring-like structures at 0.78 < z < 0.86, formed by GRBs was also mentioned in [25], where a giant ring-like structure at 0.78<z<0.86 displayed by GRBs was detected.

So, the clustering of galaxies (and around GRB sight-lines) are discovered and investigated in detail in very many papers already – see, e.g., in [26]. Following the detection of GRB 161017A by Swift (Troja et al. GCNC 20064), *Fermi* (Hui and Meegan, GCNC 20068) and *Lomonosov* (Sadovnichy et al. GCNC 20075), we observed the optical afterglow (Yurkov et al. GCNC 20063; Breeveld and Troja, GCNC 20074) with the 10.4m Gran Telescopio Canarias (GTC) at the Spanish island of La Palma, starting at 05:59 UT on Oct 18 (i.e. 12.1 hr post-burst), covering a combined range of 3800-10000 A. The reddest spectrum (convering the range between 7350 and 10000 A at a resolution of 2500) shows the strong Mg II doublet at a redshift z = 2.0127, consistent with the value reported by de Ugarte Postigo et al. (GCNC 20069). We also identify, in the bluest spectrum, other absorption lines (eg. SiII, FeII) and the two intervening systems reported on their GTC (+OSIRIS) R1000B spectrum taken 1.3 hr earlier than us.

Mg II doublet at z= 0.916
Mg II doublet at z= 1.370
Mg II doublet at z= 2.0127 [GRB]

4. Conclusions

Thus, the study of the GRB 021004 field confirms the presence of a cluster at z=0.57 also.

Then the origin of other absorption line systems (zabs) in spectra of this and other afterglows becomes clear [27]. And for more distant galaxies it is not a single galaxy, but the whole cluster gets to the spectrograph slit. That is why the lines of this doublet (and other lines also) are stronger at higher z. All these systems can be related to analogous clusters at *large z*, as is observed for a long time in direction to QSOs. See also [28], [29] where the galaxy clusters in the range $0.2 \lesssim z \lesssim 0.9$ were found and quantifying the suppression of the (un)-obscured star formation in galaxy cluster cores at $0.2 \lesssim z \lesssim 0.9$ studied.

We note here also that only direct optical identification of neutrino and gravitational events can confirm or disprove a particular model of their source, as was in the case with identification, and subsequent choice of a theoretical model for GRB sources. Until 1998, it was believed that these are explosions in the Galaxy on the surface of neutron stars. After 1998, it turned out that these are still extragalactic sources (z ≤ 10) associated with supernova explosions and the relativistic collapse of the nuclei of massive stars...

See also the report by Alberto J. Castro-Tirado, Vladimir V. Sokolov and Sergey S. Guziy "Gamma-ray bursts: Historical afterglows and early-time observations" in Proceedings of the International Conference [30], which discusses the GRB afterglows (GRB 920723 and 920925C) prior to the Afterglow Era that started in 1997. There it is shown how we used observations obtained with the 6-meter BTA in Zelenchuk (Russia) and the 10.4-m GTC in La Palma (Spain) for the study of GRB afterglows and their host galaxies. Moreover, when completed with our BOOTES Global Network of 0.6-meter robotic telescopes, this result had completed studying the early phases starting seconds after the trigger. Since the discovery of the afterglows to GRBs in 1997, much has been advanced in the field, with several hundreds of

counterparts in the last 20 yr in all the electromagnetic range from radio to gamma-rays, ending up with the detection of gravitational waves associated to a short-duration GRB in 2017 (GRB 170817/GW 170817).

The new Era of Gravitational Wave Astronomy was discussed at the previous (third) conference "The multi-messenger astronomy: gamma-ray bursts, search for electromagnetic counterparts to neutrino events and gravitational waves" (7-14 October 2018). See the talk by A.J.Castro-Tirado [31] on "The monitoring of gamma-ray burst afterglows and search for optical counterparts to neutrino events and gravitational wave signals".

This talk emphasized that "the new Era of Gravitational Wave Astronomy has just been opened thanks to the detection of the first electromagnetic counterpart to GW 170817 and will discuss the implications of the short-duration GRB associated to it, just before the opening of the forthcoming O3 LIGO-Virgo run in 2019."

References

[1]   Tomoya Kinugawa, Yuichi Harikane, Katsuaki Asano, "Long gamma-ray burst rate at very high redshift",   arXiv:1901.03516 and all references therein.

[2]   Sokolov Ilya V., Castro-Tirado A.J., Verkhodanov O.V., Zhelenkova O.P., Baryshev Yu.V. "Clustering of galaxies around the GRB 021004 sight-line at z ~ 0.5", in "Proceedings of the International Workshop on Quark Phase Transition in Compact Objects and Multimessenger Astronomy: Neutrino Signals, Supernovae and Gamma-Ray Bursts", Russia, Nizhnij Arkhyz (SAO RAS), Terskol (BNO INR RAS), October, 7 - 14, 2015, Publishing house "Sneg", Pyatigorsk, 2016, pp. 111-120

[3]   Yu. V. Baryshev, Ilya V. Sokolov, Alex S. Moskvitin et al., "Study of Faint Galaxies in the Field of GRB 021004", Astrophysical Bulletin, 65, 311 (2010)

[4]   D. Alonso et al., "Measuring the transition to homogeneity with photometric redshift surveys" , arXiv:1312.0861

[5]   Anthony H. Gonzalez, Daniel P. Gettings, Mark Brodwin, et al., "Galaxy Clusters at z~1 The Massive and Distant Clusters of WISE Survey. I: Survey Overview and a Catalog of >2000 Galaxy Clusters at z~1", arXiv:1809.06820

[6]   Kristen Menou, "Morpho-Photometric Redshifts", arXiv:1811.06374, submitted   in MNRAS.

[7]   Jasleen Matharu, Adam Muzzin, Gabriel B. Brammer, et al., "HST/WFC3 grism observations of z ~ 1 clusters: The cluster vs. field stellar mass-size relation and evidence for size growth of quiescent galaxies from minor mergers", arXiv:1811.06548

[8]   Ilya V. Sokolov, Oskar J.A. Bravo Calle, and Yu.V. Baryshev , "Study of BTA, Hubble, and Spitzer GRB 021004 deep field", in "Gamma–ray Bursts: 15 Years of GRB Afterglows – Progenitors, Environments and Host Galaxies from the Nearby to the Early Universe" (A.J. Castro-Tirado, J.Gorosabel and I.H. Park (eds)), EAS Publications Series, 61 (2013) 435-437 (2013).

[9]   I. V. Sokolov, A. J. Castro-Tirado, O. P. Zhelenkova, I. A. Solovyev, O. V. Verkhodanov, and V. V. Sokolov. "The Excess Density of Field Galaxies near z ~ 0.56 around the Gamma-Ray Burst GRB021004 Position", (Astrophysical Bulletin, Vol. 73, No. 2, 2018 p.111 and see in arXiv:1805.07082).

[10] Matthew D. Kistler, Hasan Yuksel, John F. Beacom, Andrew M. Hopkins, J. Stuart B. Wyithe, "The Star Formation Rate in the Reionization Era as Indicated by Gamma-ray Bursts", Astrophys.J.705:L104-L108,2009,   arXiv:0906.0590

[11] Matthew D. Kistler, Hasan Yuksel, John F. Beacom, Andrew M. Hopkins, J. Stuart B. Wyithe , "The Star Formation Rate in the Reionization Era as Indicated by Gamma-ray Bursts", Astrophys.J.705:L104-L108,2009, arXiv:0906.0590

[12] G. E. Prochter, J. X. Prochaska, and S. M. Burles, Astrophys. J. 639, 766 (2006).

[13] S. D. Vergani, P. Petitjean, C. Ledoux, et al., Astron. and Astrophys. 503, 771 (2009).

[14] A. J. Castro-Tirado, P. Møller, G. Garc´ıa-Segura, et al., "GRB 021004: Tomography of a gamma-ray burst progenitor and its host galaxy", Astron. and Astrophys. 517, A61 (2010), arXiv1004.1131

[15] Vladimir Sudilovsky, Jochen Greiner, Arne Rau, Mara Salvato, Sandra Savaglio, Susanna D. Vergani, et al., Clustering of galaxies around GRB sight-lines, arXiv:1302.6362

[16] Vergani, S. D., Petitjean, P., Ledoux, C. et al. MgII absorbers along GRB lines of sight observed with VLT-UVES, 2009, A&A, 503, 771 (arXiv:0906.3269)

[17] Rykoff et al., AJ 785, 104 (2014)

[18] Saulder et al., A&A 596, A14 (2016)

[19] Wen et al., AJ 807, 178 (2015),

[20] Gal et al., AJ 137, 2981 (2009),

[21] Oguri, MNRAS 444, 147 (2014),

[22] Tempel et al., A&A 566, A1 (2014).

[23] M.L.Khabibullina, O.V.Verkhodanov, V.V.Sokolov, Astrophysical Bulletin, 2014, No 69, Vol.4, Statistics of the Planck CMB signal in direction of gamma-ray bursts from the BATSE and BeppoSAX catalogs) arXiv:1406.6480, Astrophysical Bulletin, 2014, No 69, Vol.4

[24] R. A. Burenin, I. F. Bikmaev, I. M. Khamitov, I. A. Zaznobin, G. A. Khorunzhev, M. V. Eselevich, V. L. Afanasyev, S. N. Dodonov, J. A. Rubiño-Martín, N. Aghanim, R. A. Sunyaev arXiv:1801.04464 Optical identifications of high-redshift galaxy clusters from Planck Sunyaev-Zeldovich survey,

[25] Balazs, et al., arXiv:1507.00675, Accepted for publication in MNRAS,

[26] GCN CIRCULAR 20077, GRB 161017A: GTC additional spectroscopy and refined redshift DATE: 16/10/18 18:18:16 GMT (12.1 hr post-burst, A. J. Castro-Tirado (IAA-CSIC), A. F. Valeev, V. V. Sokolov et al.]

[27] Susanna D. Vergani et al.: MgII absorbers along GRB lines of sight observed with VLT-UVES, A&A 503, 771 (2009)

[28] Andrews et al., "Galaxy clusters in the line of sight to background quasars. III. Multi-object spectroscopy", The Astrophysical Journal, vol. 774, iss.1. arXiv:1306.6117

[29] L. Rodríguez-Muñoz, G. Rodighiero, C. Mancini, et al. "Quantifying the suppression of the (un)-obscured star formation in galaxy cluster cores at $0.2 \lesssim z \lesssim 0.9$", arXiv:1812.08804, submitted to MNRAS

[30] Alberto J. Castro-Tirado, Vladimir V. Sokolov and Sergey S. Guziy "Gamma-ray bursts: Historical afterglows and early-time observations, pp. 41-50 in Proceedings of the International Conference SN 1987A (2-8 July 2017), "Quark Phase Transition in Compact Objects and Multimessenger Astronomy", http://www.sao.ru/hq/grb/conf_2017/proceedings.html

[31] A.J.Castro-Tirado (Instituto de Astrofisica de Andalucia IAA-CSIC, Granada, Spain). "The monitoring of gamma-ray burst afterglows and search for optical counterparts to neutrino events and gravitational wave signals". (see the site https://www.sao.ru/hq/grb/conf_2018/program.html

Vertical structure of accretion discs in LMXB

A. Tavleev[1,*], K. Malanchev[2], G. Lipunova[2]

[1]Faculty of Physics M.V.Lomonosov Moscow State University, Leninskie Gory, Moscow, 119991 Russia; tavleev.as15@physics.msu.ru

[2]M.V.Lomonosov Moscow State University, Sternberg Astronomical Institute, Universitetsky pr. 13,Moscow, 119234, Russia

Abstract   A low-mass X-ray binary (LMXB) is a binary system where one of the components is either a neutron star or a black hole. The other component (donor, usually a main sequence star) fills its Roche lobe and therefore looses mass to the compact object. We calculate the vertical structure of an accretion disc formed around the compact object. We develop a flexible numerical code, which allows us to change the equation of state, opacity law, and chemical composition. Our calculations can improve the accuracy of the modeling of LMXB outbursts.

Keywords: Accretion, Accretion Discs, Low-Mass X-Ray Binaries, LMXB, X-Ray, X-Ray Bursts, Vertical Structure of Accretion Discs

1. Introduction

Flares of LMXBs are among the brightest transient sources in the X-ray sky. To model X-ray bursts in LMXBs, one has to solve the equation of non-stationary disc accretion (see, for example, [1]). To solve this equation, a relation between physical parameters of the disc, for example, the energy flux and surface density, should be provided. Such a relation can be obtained by solving equations of vertical structure and finding dependencies of the pressure, surface density, energy flux, and temperature on the vertical coordinate.

Considering different physical conditions and processes in discs, we can construct so-called S-curves [2], namely, the dependencies of the radiation flux on the surface density, and study an instability driving outbursts of LMXBs.

Up to now, the structure of accretion discs was calculated by numerical methods in many works. For example, the vertical and radial structure of an accretion disc was calculated in [3].

In [4], the vertical structure was calculated, introducing Π-parameters (see below) and using analytical formulas for the opacity. We offer a more advanced and more flexible code, which uses modern opacities and is intended to be publicity open.

2 Model of the vertical structure

The equations of the accretion discs vertical structure are (see, e. g., [3], [4], and [5]):

$$\frac{1}{\rho}\frac{dP}{dz} = -\omega_K^2 z \ , \tag{1}$$

$$\frac{d\Sigma}{dz} = -2\rho \quad , \tag{2}$$

$$\frac{dT}{dz} = -\frac{3\varkappa_R \rho}{4ac}\frac{Q}{T^3} \; , \tag{3}$$

$$\frac{dQ}{dz} = \frac{3}{2}\omega_K \omega_{r\varphi} \quad , \tag{4}$$

$$z \in [0, z_0]$$

Here, Eq. (1) is the hydrostatic equilibrium equation with the pressure P, density ρ, Keplerian angular velocity $\omega_K^2 = GM/r^3$; Eq. (2) is, in fact, a definition of the surface density Σ as a function of the vertical coordinate z; Eq. (3) gives the temperature gradient in the case of radiative energy transfer in the Eddington approximation, where $\varkappa_R$ is the Rosseland mean opacity, Q is the radiation flux, a is the radiation constant; Eq. (4) is an equation of viscous heating, where $w_{r\varphi}$ is a component of the viscous stress tensor. The vertical coordinate z changes from zero (the plane of symmetry) to z_0, the semithickness of disc.

This system should be supplemented by an equation of state and law of viscosity:

$$\rho = f(P, T), \; w_{r\varphi} = \alpha P.$$

We use the Shakura-Sunyaev α-prescription for viscosity [6], where α is the turbulence parameter.

The code in Python 3 was developed to solve system (1–4) numerically. Input parameters are: the mass of the central body M, radius r, radiation flux F (or effective temperature T_{eff}) at this radius, type of opacity, turbulent parameter α.

The opacity coefficient $\varkappa_R$ is determined in the code by analytical formulas or by tabular values. In particular, we use MESA [7] for interpolating tabular opacities (opacity tables from [8], [9], and [10]). An example of opacity coefficient in the disc at one location is shown in Fig.1 (the right panel). At a fixed radius of the disc the opacity coefficient changes with temperature and density.

Boundary conditions for equations (1-4) are:

$$\Sigma(z_0) = 0,$$

$$Q(z_0) = Q_0 = \sigma_{SB} T_{eff}^4$$

$$T(z_0) = T_{eff}$$

$$P(z_0) = P_0$$

The program integrates the equations of vertical structure and performs an optimization task to find the values of free parameter z_0, for which the condition at the symmetry plane of the disc is fulfilled:
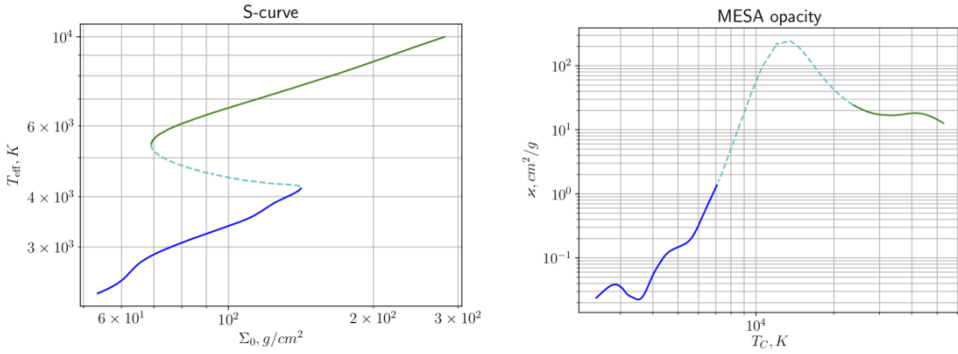
$$Q(0) = 0.$$

Fig1. *The left panel shows the S-curve for r = 10¹¹ cm, α = 0.5, and M = 6M⊙. The right panel shows an example of opacity provided by MESA, calculated for the same range of parameters. Same colors on both panels show the same parameters. Region of thermal instability is indicated by the dashed line.*

3 Testing the code

The vertical structure (Eqs. 1–4) with the Kramers formula for opacity has been previously calculated in [4], where the dimensionless Π-parameters were introduced:

$$\Pi_1 = \frac{\omega_K^2 z_0^2 \mu}{\mathcal{R} T_c} \; , \quad \Pi_2 = \frac{\Sigma_0}{2 z_0 \rho_c} \; ,$$

$$\Pi_3 = \frac{3}{4} \frac{\alpha \omega_K R T_c \Sigma_0}{Q_0 \mu} \quad , \quad \Pi_4 = \frac{3}{32} \left(\frac{T_{eff}}{T_c} \right)^4 \Sigma_0 \varkappa_c \; .$$

Here T_c, ρ_c, and $\varkappa_c$ are the temperature, density, and opacity coefficient at the symmetry plane of disc. In our code we obtain the values of Π that are in good agreement with the values calculated in [4] (see Table 1).

Table 1: *Comparison of Π at r = 10¹¹ cm, α = 0.5, M = 6M⊙, T_eff = 2300K, ΔΠ — difference between the values from [4] and those calculated in our code.*

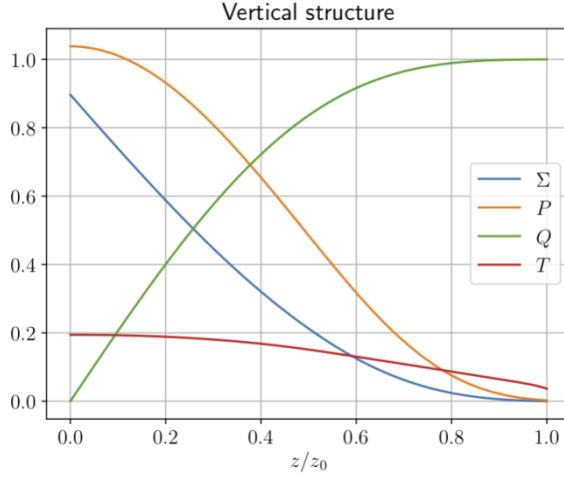|	**Our code**	ΔΠ
Π_1	5.7928	0.0028
Π_2	0.5373	0.0002
Π_3	1.1298	0.0002
Π_4	0.3994	0.0016

Fig2. *Calculated vertical structure for r = 10^{11} cm, α = 0.5, M = $6M_\odot$, T_{eff} = 10_4K. All quantities are normalized to their characteristic values (see Eqs. (5)).*

4 Results

We show an example of the vertical structure calculated by our code in Fig. 2. This structure is obtained for $r = 10^{11}$ cm, α = 0.5, $M = 6M_\odot$, and $T_{\text{eff}} = 10^4$K. Opacities provided by MESA are used. All quantities are normalized to their characteristic values:

$$Q' = Q_0, \quad \Sigma' = \frac{28Q_0}{2\alpha z_0^2 \omega_K^3}, \quad P' = \frac{4Q_0}{3\alpha z_0 \omega_K} \ , \qquad T' = \frac{\mu}{\Re}\omega_K^2 z_0^2 \tag{5}$$

We obtain the half-thickness of the disc $z_0 = 5.1 \cdot 10^9$ cm ($z_0/r = 0.069$).

The S-curve calculated for the same parameters of the disc if shown in the left panel of Fig1.

5. Summary

We are developing a modern flexible code to calculate the vertical structure of accretion discs for a wide range of parameters. Much effort is put into the code ability to easily change the opacity, chemical composition, and equation of state. The code is intended to be publicity available in the future.

Acknowledgements

References

[1]   J.-M. Hameury, K. Menou, G. Dubus, J.-P. Lasota, and J.-M. Hure. MNRAS, 298:1048–1060, August 1998.

[2] F. Meyer and E. Meyer-Hofmeister. A&A, 104:L10, 1981.

[3] F. Meyer and E. Meyer-Hofmeister. A&A, 106:34–42, February 1982.

[4] N. A. Ketsaris and N. I. Shakura. Astronomical and Astrophysical Transactions, 15:193, 1998.

[5] N. I. Shakura, G. V. Lipunova, K. L. Malanchev, V. V. Zhuravlev, D. N. Razdoburdin, P. K. Abolmasov, A. Chashkina, K. A. Postnov, A. Yu Kochetkova, and L. Hjalmarsdotter. Accretion flows in astrophysics. New York, New York, 2018.

[6] N. I. Shakura and R. A. Sunyaev. A&A, 24:337–355, 1973.

[7] B. Paxton, L. Bildsten, A. Dotter, F. Herwig, P. Lesaffre, and F. Timmes. ApJS, 192:3, January 2011.

[8] J. W. Ferguson, D. R. Alexander, F. Allard, T. Barman, J. G. Bodnarik, P. H. Hauschildt, A. Heffner-Wong, and A. Tamanai. ApJ, 623:585–596, April 2005.

[9] C. A. Iglesias and F. J. Rogers. ApJ, 412:752–760, August 1993.

[10] C. A. Iglesias and F. J. Rogers. ApJ, 464:943, June 1996.

The Konus-Wind observations of gamma-ray bursts with known redshifts

A. Tsvetkova[*], D. Frederiks, D. Svinkin, S. Golenetskii, A. Lysenko, M. Ulanov, R. Aptekar

Ioffe Institute, Politekhnicheskaya 26, St. Petersburg 194021, Russia;
  tsvetkova@mail.ioffe.ru

Abstract   We present the results of a systematic study of 166 gamma-ray bursts (GRBs) with reliable redshift estimates detected in the triggered mode of the Konus-Wind (KW) experiment. The sample covers the period from 1997 February to 2018 October and represents the largest set of cosmological GRBs studied to date over a broad energy band. For these bursts, we derived the durations, the spectral lags, the results of spectral fits with two model functions, the total energy fluences, and the peak energy fluxes, the rest-frame, isotropic-equivalent energy and peak luminosity, and the collimation-corrected values of the energetics for 32 GRBs with reasonably-constrained jet breaks. We consider the behavior of the rest-frame GRB parameters in the hardness-duration and hardness-intensity planes, and confirm the "Amati" and "Yonetoku" relations for Type II GRBs. The correction for the jet collimation does not improve these correlations for the KW sample. We discuss the influence of instrumental selection effects on the GRB parameter distributions and estimate the KW GRB detection horizon. Accounting for the instrumental bias, we estimate the KW GRB luminosity evolution, luminosity and isotropic-energy functions, and the evolution of the GRB formation rate.

Keywords: Gamma-Ray Bursts, Redshift

1. Instrumentation and the burst sample

KW is a gamma-ray spectrometer designed to study temporal and spectral characteristics of GRBs, solar flares, soft gamma repeater bursts, and other transient phenomena over a wide energy range from ~ 20 keV to ~ 10 MeV (at present). It consists of two identical omnidirectional NaI(Tl) detectors, mounted on opposite faces of the rotationally stabilized Wind spacecraft, which observe the entire celestial sphere. In interplanetary space far outside the Earth's magnetosphere, KW has the advantages over Earth-orbiting GRB monitors of continuous coverage, uninterrupted by Earth occultation, and a steady background, undistorted by passages through Earths trapped radiation, and subject only to occasional solar particle events. is expected that authors will submit carefully written and proofread material. Careful checking for spelling and grammatical errors should be performed.

The sample comprises 150 GRBs with reliable redshift estimates detected by KW in the triggered mode from the beginning of the afterglow era in 1997 to the middle of 2016 (Tsvetkova et al. 2017), supplemented by 16 GRBs detected by KW recently, and represents the largest set of cosmological GRBs studied to date over a broad energy band. Among these GRBs, 14 bursts (or 8%) belong to the Type I (merger origin, short/hard) GRB population and the others are Type II (collapsar origin, long/soft) bursts (see Svinkin et al. (2016) for the KW GRB classification details).

2. Analyses and results

We derived the durations $T100$, $T90$, and $T50$ (the total burst duration and the time intervals that contain 5% to 95% and 25% to 75% of the total burst count fluence, respectively), and the spectral lags, quantitative measures of spectral evolution often seen in long GRBs, when the emission in a soft detector band peaks later or has a longer decay relative to a hard band; a positive spectral lag corresponds to the delay of the softer emission. Figure 1 presents the $T50$, $T90$, and $T100$ observer- and rest-frame distributions. We note that the observer-frame energy band 80–1200 keV, in which the durations are calculated, corresponds to multiple energy bands in the source-frame thus introducing a variable energy-dependant factor which must be accounted for when analyzing the rest-frame durations. The same considerations apply to the spectral lags.

For each burst from our sample, two time intervals were selected for spectral analysis: time-averaged fits were performed over the interval closest to $T100$ (hereafter the TI spectrum); the peak spectrum corresponds to the time when the peak count rate (PCR) is reached. Each spectrum was fitted by two spectral models. The first model is the Band function (hereafter BAND; Band et al. 1993), and the second spectral model is an exponentially cutoff power-law (CPL). In the only case where both "curved" models result in ill-constrained fits (GRB 080413B), a simple power-law (PL) function was used. All the spectral models were normalized to the energy flux (F) in the 10 keV– 10 MeV range (observer frame). The best-fit spectral model (the BEST model) was chosen based on the difference in χ^2 between the CPL and the BAND fits. The criterion for accepting a model with a single additional parameter is a change in χ^2 of at least 6 ($\Delta\chi^2 \equiv \chi^2_{CPL} - \chi^2_{BAND} > 6$). We found BAND to be the BEST model for 61 TI and 56 peak spectra. The remaining spectra (with the exception of GRB 080413B) were best fitted by CPL. Figure 2 shows the distributions of peak energies E_p. The TI spectrum E_p ($E_{p,i}$) distributions for both spectral models peak around 250 keV, while the peak spectrum E_p ($E_{p,p}$) distributions peak around 300 keV.

Figure 3 shows $E_{p,i}$ as a function of the burst durations T_{90} in the observer and rest frames. In the observer frame the KW Type I GRBs are typically harder and shorter than Type II bursts, which is consistent with the classification obtained from the hardness-duration distribution, and this tendency shows no dependence on the burst redshift. In the cosmological rest frame this pattern remains practically unchanged for GRBs at $z \lesssim 1.7$ but it appears to be less distinct when the whole sample is considered. Although in the rest frame Type I GRBs are still shorter than Type II GRBs, their rest-frame E_p, clustered around 1 MeV, are superseded by those of a significant fraction of the Type II population. We note, however, that the derived rest-frame durations are affected by a variable energy-dependant factor and the KW rest-frame E_p are subject to the observational bias thus an interpretation of the rest-frame hardness-duration distribution should be done with care.

From the BEST spectral models we calculated the 10 keV–10 MeV energy fluences (S) and the peak energy fluxes ($Fpeak$) on three time scales: 1024 ms, 64 ms, and $(1 + z)64$ ms (the GRB rest-frame 64 ms scale). Based on the GRB redshifts, which span the range $0.1 \leq z \leq 5$, we estimated the rest-frame, isotropic-equivalent energies (E_{iso}) and peak luminosities (L_{iso}) in the rest-frame bolometric range 1 keV–$(1 + z)10$ MeV. For 32 GRBs with reasonably constrained jet break times (t_{jet}) we derived the collimation-corrected values of the energetics.

3. KW selection effects and GRB detection horizon

Figure 4 shows the KW GRB distributions in the z–E_{iso}, z–L_{iso}, and z–$E_{p,z}$ diagrams[k]. The region in the z–L_{iso} plane above the limit defined by the bolometric flux $F_{lim} \sim 1 \times 10^{-6}$ erg cm^{-2} s^{-1} may be considered free from the selection bias. In the z–E_{iso} plane, the selection-free region corresponds to the bolometric fluence $S_{lim} \gtrsim 3 \times 10^{-6}$ erg cm^{-2}. The detector sensitivity drops rapidly as Ep (the peak energy in νF_ν spectrum) approaches the lower boundary of the KW band, and this results in a lack of bursts below the rest-frame limit $\approx (1+z)^2 \cdot 25$ keV in the z - $E_{p,z}$ plane.

Accounting for the KW trigger sensitivity to the GRB incident angle, its light-curve shape, and the shape of the energy spectrum, we estimated the KW detection horizon for each burst from the sample as a redshift z_{max}, at which the GRB peak count rate in the trigger energy band ($\sim$80–300 keV) drops below the trigger threshold (9σ) on both trigger time scales (140 ms and 1 s). The most distant GRB horizon for the KW sample ($z_{max} \approx 16.6$) is reached for the ultra-luminous GRB 110918A (Frederiks et al. 2013) at observed $z = 0.981$. At $z \approx 16.6$ the age of the Universe amounts to only $\sim$ 230 Myr, i.e. a burst which occurred close to the end of the cosmic Dark Ages could still trigger the KW detectors, and a thorough temporal and spectral analysis in a wide observer-frame energy range could be performed.

A common approach to estimate the GRB detection horizon is to find a redshift $z_{max,L}$, at which the limiting isotropic luminosity $L_{iso,lim} = 4\pi D_L^2 \times F_{lim}$, defined by the "monolithic" F_{lim} estimated for the whole sample, starts to exceed the GRB L_{iso}. We found that for both Type I and Type II GRBs z_{max} are distributed narrowly around $z_{max,L}$ corresponding to the bolometric $F_{lim} = 1 \times 10^{-6}$ erg cm^{-2} s^{-1}.

4. GRB Luminosity and Isotropic-energy functions, GRB Formation Rate

To estimate the GRB luminosity function (LF), isotropic energy release function (EF), and the cosmic GRB formation rate (GRBFR) for the KW Type II bursts we used the non-parametric Lynden-Bell C^- method (Lynden-Bell 1971) further advanced by Efron & Petrosian (1992) (the EP method); the details of our calculations are described in Tsvetkova et al. (2017). Applying the EP method to the z–L_{iso} plane and using the functional form of the evolution $(z) = (1 + z)$, we found the luminosity evolution significance $\tau_0 \sim 1.7\sigma$, and estimated the luminosity evolution index $\delta_L = 1.7^{+0.9}_{-0.9}$. Applying the same method to the z–E_{iso} plane, we found $\delta_E = 1.1^{+1.5}_{-0.7}$ ($\tau_0 \sim 1.6\sigma$). Thus, the estimated E_{iso} and L_{iso} evolutions are comparable.

Then, using the C^- method, we obtained evolution-free cumulative LF and EF, $\psi(L')$ and $\psi(E')$ (Figure 5), where $L' = L_{iso}/(1 + z)^{\delta_L}$ and $E' = E_{iso}/(1 + z)^{\delta_E}$, and fitted the distributions with a broken power-law (BPL) function and with the exponentially-cutoff PL (CPL). The derived BPL slopes of LF and EF are close to each other, both for the dim ($\alpha_1 \sim$ −0.5) and bright ($\alpha_2 \sim -1$) segments; also, these indices are roughly consistent with the LF and EF slopes obtained in Yonetoku et al. (2004) and Wu et al. (2012). When compared to BPL, the CPL fit to (L') results in a considerably worse quality. Conversely, the cutoff PL fits (E')

---

[k] We use A_z notation for rest-frame GRB parameters.

better ($\Delta\chi^2 \sim 5.5$), with the PL slope ~ -0.35 and the cutoff energy $E'_{cut} \gtrsim 10^{54}$ erg. The existence of a sharp cutoff of the GRB isotropic energy distribution around $\sim 1 - 3 \times 10^{54}$ erg was suggested recently by Atteia et al. (2017). We also estimated the LF and EF not accounting for the evolution, and found them very similar in shape to (L') and (E').

The GRBFR (Figure 5), estimated using the EP method from the evolution-corrected z–L' distribution, exceeds the star formation rate (SFR) at $z < 1$ and nearly traces the SFR at higher redshifts; the same behavior is noted for the GRBFRs estimated using both the evolution-corrected z–E' and the non-corrected z–E_{iso} distributions. The low-z GRBFR excess over SFR is in agreement with the results reported in Yu et al. (2015) and Petrosian et al. (2015). Meanwhile, the only GRBFR that traces the SFR in the whole KW GRB redshift range is the one derived from the z–L_{iso} distribution (i.e. not accounting for the luminosity evolution).

5. Hardness-intensity correlations

We tested the KW GRB characteristics against E_p–S and E_p–F_{peak} correlations in the observer frame, and Ep,z–Eiso ("Amati", Amati et al. 2002) and $E_{p,z}$–L_{iso} ("Yonetoku", Yonetoku et al. 2004) correlations in the rest frame. For the subsamples of Type I and Type II KW GRBs both the Amati and Yonetoku correlations improve considerably when moving from the observer frame to the GRB rest frame, with only marginal changes in the slopes. The derived slopes of the Amati and Yonetoku relations for Type II GRBs are ~0.47 and ~0.49, respectively. These values are in agreement with Amati et al. (2002), Yonetoku et al. (2004). For 30 KW Type II GRBs with reliable t_{jet}, accounting for the jet collimation neither improves the significance of the correlations nor reduces the dispersion of the points around the best-fit relations. The slopes we obtained for the collimated Amati and Yonetoku relations are steeper compared to those of the non-collimated versions.

The lower boundaries of both the Amati and Yonetoku relations (Figure 6) are defined by GRBs with moderate-to-high detection significance, so the instrumental biases do not affect the correlations from this edge of the distributions. Meanwhile, all outliers in the relations lie *above* the upper boundaries of the 90% prediction intervals (PIs) of the relations. Since these bursts were detected at lower significance, with the increased number of GRB redshift observations, one could expect a "smear" of the correlations due to more hard-spectrum/less-energetic GRB detections. Thus, using the KW sample, we confirm a finding of Heussaff et al. (2013) that the lower right boundary of the Amati correlation (the lack of luminous soft GRBs) is an intrinsic GRB property, while the top left boundary may be due to selection effects. For the KW sample, this conclusion may also be extended to the Yonetoku correlation.

The $E_{p,z}$–E_{iso} and $E_{p,z}$–L_{iso} correlations for the Type I bursts are less significant when compared to those for Type II GRBs, and they are characterized by less steep slopes. Meanwhile, the rest-frame E_p of Type I GRBs shows only a weak (if any) dependence on the burst energy below $E_{iso} \sim 10^{52}$ erg (Figure 6), and the same is true for the $E_{p,z}$–L_{iso} relation at $L_{iso} \lesssim 5\times10^{52}$ erg s^{-1}. Above these limits the slopes of both relations for Type I GRBs are similar to those for Type II GRBs. As one can see from the Figure, all KW Type I bursts are hard-spectrum/low-isotropic- energy outliers in the Amati relation for Type II GRBs. In the $E_{p,z}$–L_{iso} plane this pattern is less distinct; at luminosities above $L_{iso} \sim 10^{52}$ erg s^{-1} the Type I bursts nearly follow the upper boundary of the Type II GRB Yonetoku relation.

6. Conclusions

We hope this work will encourage further investigations of GRB physical properties and will contribute to other related studies. Plots of the GRB light curves and spectral fits can be found at the Ioffe Web site[1]. This work was supported by RSF (grant 17-12-01378).

References

[1]   Amati, L., Frontera, F., Tavani, M., et al. 2002, A&A, **390**, 81

[2]   Atteia, J.-L., Heussaff, V., Dezalay, J.-P., et al. 2017, ApJ, **837**, 119

[3]   Band, D., Matteson, J., Ford, L., et al. 1993, ApJ, **413**, 281

[4]   Efron, B., & Petrosian, V. 1992, ApJ, **399**, 345

[5]   Frederiks, D. D., Hurley, K., Svinkin, D. S., et al. 2013, ApJ, **779**, 151

[6]   Heussaff, V., Atteia, J.-L., & Zolnierowski, Y. 2013, A&A, **557**, A100

[7]   Lynden-Bell, D. 1971, MNRAS, **155**, 95

[8]   Petrosian, V., Kitanidis, E., & Kocevski, D. 2015, ApJ, **806**, 44

[9]   Svinkin, D. S., Frederiks, D. D., Aptekar, R. L., et al. 2016, ApJS, **224**, 10

[10]   Tsvetkova, A., Frederiks, D., Golenetskii, S., et al. 2017, ApJ, **850**, 161

[11]   Wu, S.-W., Xu, D., Zhang, F.-W., & Wei, D.-M. 2012, MNRAS, **423**, 2627

[12]   Yonetoku, D., Murakami, T., Nakamura, T., et al. 2004, ApJ, **609**, 935

[13]   Yu, H., Wang, F. Y., Dai, Z. G., & Cheng, K. S. 2015, ApJS, **218**, 13

---

[1] http://www.ioffe.ru/LEA/zGRBs/triggered/

The Helicon-I and Konus-UF gamma-ray burst experiments

M. V. Ulanov[*], R. L. Aptekar, S. V. Golenetskii, D. D. Frederiks,
D. S. Svinkin, A. E. Tsvetkova

Ioffe Institute, St.-Petersburg, Russia; ulanov@mail.ioffe.ru

Abstract   We present Konus-UF and Helicon-I, the future space-based experiments designed to study temporal and spectral characteristics of gamma-ray bursts, solar flares, soft gamma-repeater bursts, and other transient phenomena over a wide energy range from 10 keV to 15 MeV. The instruments will be mounted onboard the World Space Observatory–Ultraviolet (WSO-UV) and the InterhelioProbe spacecraft, respectively. The spacecraft orbits are going to be far from the Earth's magnetosphere, which enables nearly uninterrupted observations of the entire sky under stable background conditions.

Keywords: Gamma-Spectrometer, Gamma-Ray Bursts, Soft Gamma-Repeaters

1. Introduction

Study of cosmic gamma-ray bursts (GRBs) and soft gamma-repeaters (SGRs) remains one of the most important tasks in modern astrophysics, despite several decades of observations and theoretical studies. The progenitors, formation and evolution of such sources remain the subject of modern experimental and theoretical researches around the world [1].

The Konus-UF and Helicon-I experiments are planned to study hard X-ray and gamma radiation from gamma-ray bursts, soft gamma-repeaters and solar flares in a wide energy range from 10 keV to 15 MeV with a high temporal resolution.

2. The Instruments

The Konus-UF instrument (Fig. 1) consists of two identical gamma-ray detector units and an electronics unit that provides data buffering, power supply and interface with on-board spacecraft systems. Each detector will be mounted on the opposite sides of the World Space Observatory–Ultraviolet (WSO-UV) [2] so the instrument will observe the whole sky (Fig. 2).

The Helicon-I instrument is a single gamma-ray detector similar to the Konus-UF one, containing all power and interfaces circuits within the unit. The instrument will be mounted onboard InterhelioProbe [3] spacecraft.

The Konus-UF and Helicon-I detectors consist of Nal(Tl) scintillation crystals with a diameter of 130 mm and a height of 75 mm, placed in a thin-walled aluminum container with a beryllium entrance window. The scintillation crystal is viewed with a photomultiplier tube through a 16 mm thick high transparency lead glass, which is used to screen gamma radiation scattered by the structures of the spacecraft. The detector effective area is about 80–160 cm^2 depending on the photon energy and the incidence angle of the radiation. The spectral resolution is ~ 8% on the ^{137}Cs line (662 keV), and the burst sensitivity is about of 10^{-7} erg/cm^2.

The entrance beryllium window allows to effectively observe soft gamma rays, the transparency of the entrance window for photons with an energy of 20 keV is about 95%.
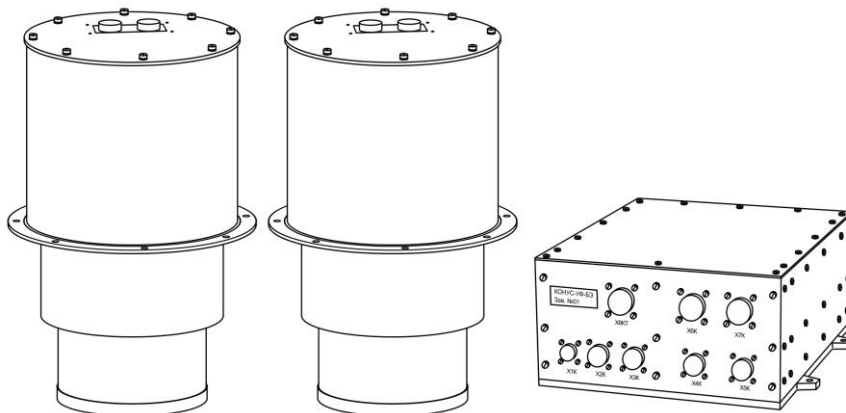

Fig1. The Konus-UF instrument consists of two identical detector units (Konus-UF-DS1, Konus-UF-DS2) and an electronics unit (Konus-UF-BE).
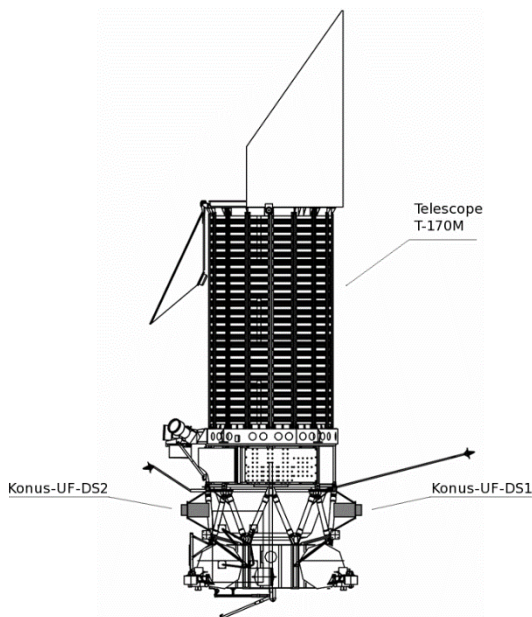

Fig2. Arrangement of the Konus-UF detectors onboard the WSO-UV spacecraft.
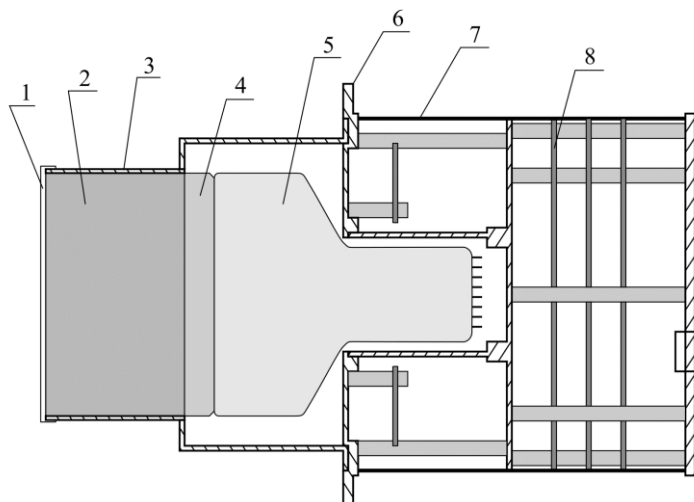
Fig3. Cross-section of the detector: 1 – beryllium entrance window, 2 – NaI(Tl) scintillator, 3 – aluminum housing, 4 – lead glass, 5 – photomultiplier tube, 6 – mounting flange, 7 – outer rim, 8 – electronics PCBs.

The WSO-UV observatory will be placed into geosynchronous orbit ($R = 42000$ km) with an inclination of 51.6°, while InterhelioProbe mission will consist of two identical spacecraft operating in the interplanetary space. Both orbits will allow continuous long-term observations uninterrupted by Earth occultation, and under conditions of a steady background undistorted by Van Allen radiation belts.

A high orbit will also allow to localize the GRB source using triangulation method with a high accuracy.

3. Observation program

The main objective of the Konus-UF and Helicon-I experiments is to observe cosmic gamma-ray bursts (GRBs), soft gamma-repeaters (SGRs), and solar flares. Such transients have a wide range of time scales from a few milliseconds (short GRBs and SGRs) to 1000 seconds (solar flares and long GRBs) and intensity range from 1 ph/cm^2 s (short GRBs and SGRs) to 10^7 ph/cm^2 s (SGR giant flares). The proposed instrument parameters and observation program will allow detailed analysis of time profiles and energy spectra of such transients.

The instruments operate in two main modes: waiting mode and triggered mode. In the waiting mode, time histories (light curves) are continuously recorded in 22 energy channels with a resolution of 1 s and multichannel spectra in 256 quasilogarithmic energy channels with an accumulation time of 60 s.

When the count rate in a certain energy channel exceeds a threshold above the background on one of two fixed timescales, 1 s or 100 ms, the instrument switches into the triggered mode. Two different conditions are used, since there are two different types of GRBs, which differ in duration and hardness of gamma-radiation [4].

In the triggered mode, time histories are recorded with a varying resolution of 2–64 ms in 22

energy channels, along with multichannel spectra with an accumulation time of 64–2048 ms. The total time history duration in triggered mode is 115 s, including the prehistory with duration of 2 s and a time resolution of 2 ms.

To study fine temporal structure of transients and accurate localization via triangulation, it is preferable to use the time-tagged event (TTE) photon registration mode. In the proposed experiments, operating in the triggered mode using TTE registration of individual photons, the amount of output data will be comparable to the amount of data using the traditional high-resolution time history and spectral data structures. The number of photons recorded by the detector with the most powerful GRBs is about 10^6, which requires about 3 MB of data in the case of double-byte time code with a time resolution of 1 μs and 256 energy steps.

During the waiting mode TTE in high-energy channels can also reduce the required data volumes, since the intensity of high-energy photons is low because the instruments will not be exposed to charged particles from the Van Allen radiation belts.

4. Conclusion

The proposed instruments will be a continuation of a series of Konus experiments, held at the Ioffe Institute for more than 40 years [5]. The instrument will contribute to the field of multi-messenger astrophysics, in particular in observation of short GRBs – the main targets of LIGO/Virgo gravitational wave observatories.

According to the results of more than 24 years of continuous observations in the Konus-Wind experiment [6] in interplanetary space, under similar conditions, the expected number of recorded GRBs is about 200 per year, which leads to the average daily amount of data about 100 MB per day.

References

[1]   Gehrels N, Ramirez-Ruiz E, Fox DB. "Gamma-Ray Bursts in the Swift Era" Annu. Rev. Astron. Astrophys. 2009; 47, pp. 567–617

[2]   Sachkov M, Shustov B, Gómez de Castro AI. "WSO-UV project" Adv. Space Res. 2014; 53, pp. 990–995

[3]   Kuznetsov VD et al. "The Sun and heliosphere explorer – the Interhelioprobe mission" Geomagnetism and Aeronomy. 2016; 56 pp. 781–841

[4]   Svinkin DS et al. "The Second Konus-Wind Catalog of Short Gamma-Ray Bursts" Astrophys. J. Suppl. 2016; 224, id. 10

[5]   Aptekar RL et al "Cosmic gamma-ray bursts and soft gamma-repeaters – observations and modeling of the extreme astrophysical phenomena" Phys. Usp., accepted DOI: 10.3367/UFNe.2018.11.038488

[6]   Aptekar RL et al. "Konus-W gamma-ray burst experiment for the GGS WIND spacecraft" Space Sci. Rev. 1995; 71, pp. 265–271

Multi-messenger astronomy: the alert observations of gamma-ray bursts afterglows, supernovae and search for optical counterparts to neutrino events and gravitational waves

Vlasyuk V.V.[*], Sokolov V.V.

Special Astrophysical Observatory of RAS, Nizhnij Arkhyz, Russia; vvlas@sao.ru

Abstract On the strategy for the all SAO telescopes for the study and monitoring of afterglows of cosmic gamma-ray bursts (GRBs), optical identification of sources of gravitational waves and neutrino signals from supernovae, fast radio bursts (FRB). We plan to carry out (to continue) follow-up observations of localization areas (identification) of newly-discovered gamma-ray bursts, neutrino and gravitational signals, and supernovae (in the mode of Target of Opportunity Observation). The telescopes: BTA, Zeiss-2000 (TB INASAN), Zeiss-100 (SAO RAS) in the modes of photometry, spectroscopy, fast photometry and polarimetry. Alerts from missions Swift, Fermi, INTEGRAL, Lomonosov and others. The aim of the search for optical/electromagnetic components with SCORPIO and MANIA at BTA is the sources (related to GRBs) of neutrino and gravitational waves (GW events) detected by LIGO (Laser Interferometer Gravitational-wave Observatory) and Virgo.

Keywords: Gamma-Ray Bursts Afterglow, Neutrino Signals, Gravitational Signals

1. Introduction

In the early 21st century there appeared new challenges for the ground-based astronomy. These include:

- gamma-ray bursts observed in 1978-1997;
- gravitational wave signals. The signal GW150914 was detected on September, 14, 2015, by two detectors LIGO in Hanford and Livingston with 7 msec separation. But the error box is too large – about 1000 sq.deg, so, there was no identification yet. The event GW170104 has similar values. Last events were modeled by coupling of NS;
- neutrino events: SN1987A is the only reliable event so far, but the international projects ICECUBE, ANTARES , etc. are going on;
- FRB – Fast Radio Bursts discovered in 2007, with the 64-m Parks 13-beam radio telescope [3]. There was the first identification with a radio galaxy at z=0.5).

See Proceedings of the International Workshop "Quark Phase Transition in Compact Objects and Multimessenger Astronomy: Neutrino Signals, Supernovae and Gamma-Ray Bursts" held by SAO RAS and BNO INR RAS in 2015 [1] (https://www.sao.ru/hq/grb/conf_2015/proceedings.html) and Proceedings of the International Conference "SN 1987A, Quark Phase Transition in Compact Objects and Multimessenger Astronomy" held by BNO INR RAS and SAO RAS in 2017 [2] (https://www.sao.ru/hq/grb/conf_2017/proceedings.html).

2. Observations in SAO RAS

Reliable identification demands optical identification.
The rates of expected events are as follows:
1. Gamma-Ray Bursts – 2-3 per week
2. Gravitational events (3 or 4 during the recent 1.5 years)
3. Neutrino events (several ones per year)
4. Fast Radio Bursts – less than 10 so far.

Observations are possible only in the ToO (Target of Opportunity) mode.
How can Special Astrophysical Observatory of RAS meet the challenge today?
We have a rather wide range of available ground-based facilities:
- BTA + complexes of spectroscopy, photometry, and fast photopolarimetry (Figs.1,2,3,4);
- Zeiss-1000 + a CCD photometer (the field of 7′) and the low-resolution spectrograph (Figs.5, 6).
- MiniMegaTORTORA – a multi-channel wide-angle complex of subsecond temporal resolution (the FOV about of 900 sq.deg.)
- Zeiss-2000 of Terskol Branch of INASAN + a CCD photometer (FOV - 11′) + a moderate-resolution spectrograph
- ShMT+ CCD photometers (the FOV of 9′ and 20′)
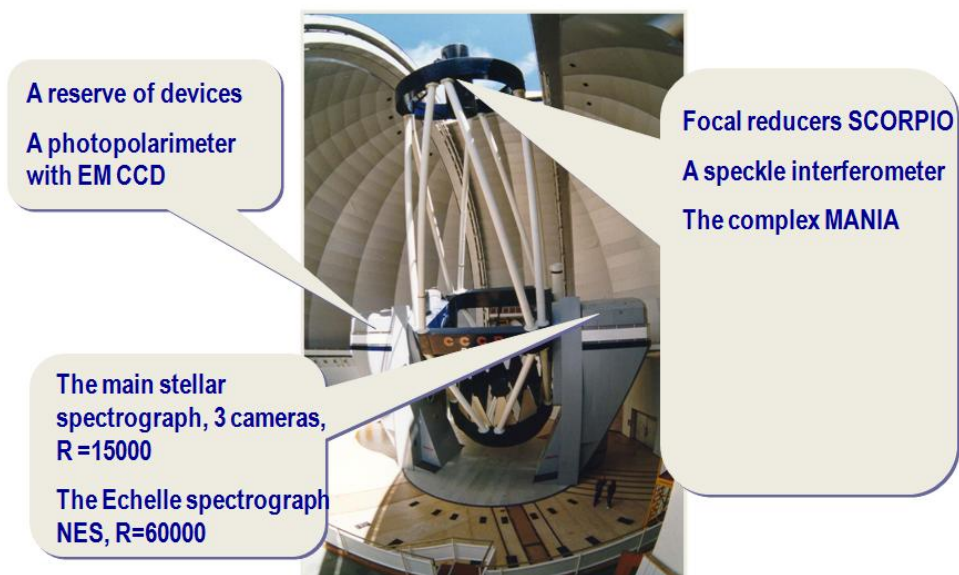
Fig1. *The 6-meter telescope and its main devices.*

Fig2. *Layout of the Spectral Camera with Optical Reducer for Photometrical and Interferometrical Observations (SCORPIO).*
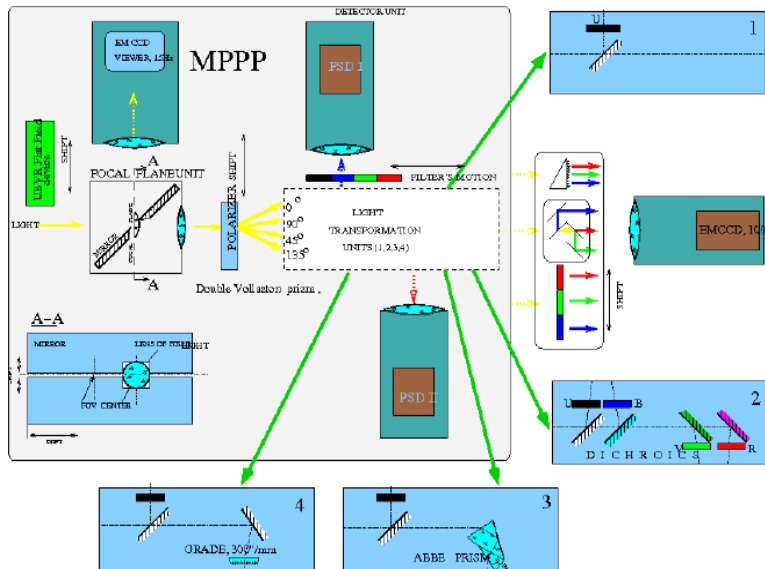

Fig3. *The complexe for studying fast variability in the BTA Primary Focus (PF). MANIA for studying microsecond variations. Scheduled in the BTA about 10-15 nights per year. Performance capabilities: wide-band photometry (up 1 microsec) and polarimetry, low-resolution spectroscopy.*
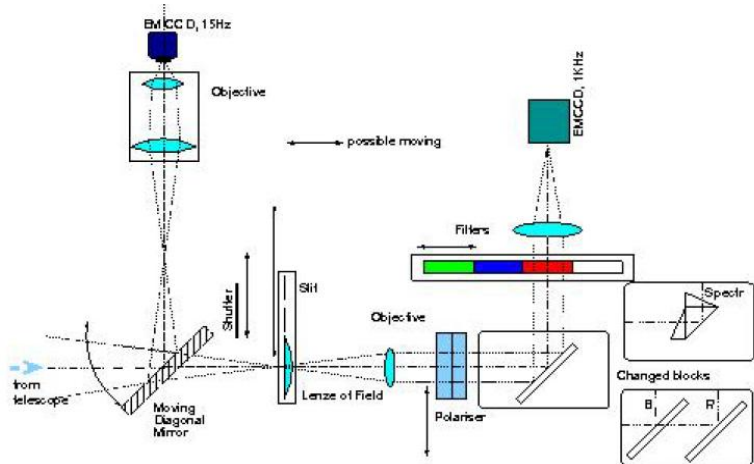
Fig4. *The complex for studying fast variability in the BTA Nasmith-1 (N-1) focus. N-1: a complex in "hot standby": it will operate in the second half of 2018. Can be started up during several minutes. It includes the EM CCD with the temporal resolution till 1 msec. Performance capabilities: wide-band photometry and polarimetry.*

Fig5. *Small SAO's telescopes. Top left: general view of the domes. Right: the 1-meter telescope Zeiss-1000. Bottom left: the 60-cm telescope.*

Fig6*. Equipment of the 1m telescope: a CCD photometer with 2048x2048px by 13.5 microns. The field of view is 7'.
The limit stellar magnitude is 23.5 mag. The medium-band photometry in UBVRI filters + narrow-band filters.*

SAO also uses the multi-channel wide-angle telescope of high temporal resolution Mini-MegaTORTORA since 2014. Performance capabilities are as follows: 9 channels with the field of view of 100 sq.deg., the threshold of magnitude – about 11.5 st.magn. during 0.1s or 15 st.magn. during 60s.   There is a project of extending the system. See also Fig. 1 in the paper "Search and study of optical transients with Mini-MegaTORTORA" by N.V. Orekhova et al. in these Proceedings.

Also some equipment is planned for the nearest future:
- a photopolarimeter in Nasmith-1 ("hot standby"),
- a fast photopolarimeter of the 1m telescope,
- a complex of small telescopes with the fields of 1°.

But we need large-aperture telescopes with large fields and gigapixel CCD detectors.

3. The study of Gamma-Ray Bursts (GRB) in SAO RAS

Gamma-ray bursts are the brightest transient sources. The multiband observations of GRBs (after 1997) confirm that a considerable part of so called "long" GRBs is related with collapse of short-lived massive stars.

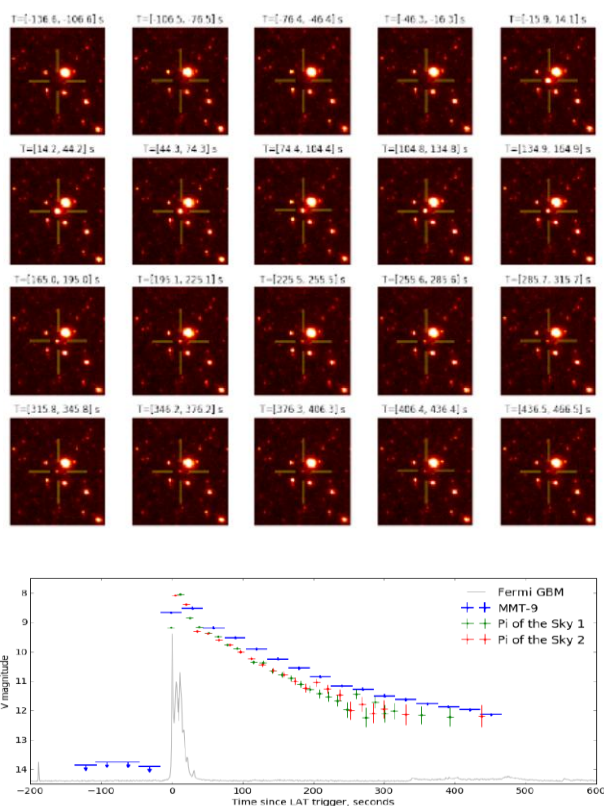Fig.7 shows the MMT study of the gamma-ray burst GRB160625B.

Fig7. *The MMT study of GRB160625B. Operation by a precursor at -180 sec. The study in the field of 30x30°. Texp=30sec. The lag of optics in comparison with gamma-rays is about 3 sec. Top: optical images. Bottom: time diagram.*

4. Some results of our team

4.1. The study of the GRB 021004 field

The results of the field galaxies clustering in GRB lines of sight based on the BTA observations and with other instruments are presented in the paper "The field galaxies clustering in GRB lines of sight based on observations with BTA and other telescopes" by I.V. Sokolov, A.J. Castro-Tirado, I.A. Solovyev, O.V. Verkhodanov, O.P. Zhelenkova, and V.V. Sokolov in these Proceedings.

The characteristic signs of the clustering of field galaxies were detected in the direction to the gamma-ray burst GRB 021004.

All accessible signs of such clustering in the line of sights and near the location of GRB021004 were tested.

The data from observations with BTA/SCORPIO, HST/ACS, VLT/UVES and from the cluster catalog SDSS-III were used.

On the excess density of field galaxies near z ~ 0.56 around the GRB 021004 position

We test for reliability any signatures of field galaxies clustering in the GRB 021004 line of sight.

The first signature is the GRB 021004 field photometric redshifts distribution based on the BTA observations with a peak near z ~ 0.56 estimated from multicolor photometry in the GRB direction.

The second signature is the Mg II 2796/2803Å absorption doublet at z ≈ 0.56 in VLT/UVES spectra obtained for the GRB 021004 afterglow.

The third signature is the galaxy clustering in a larger (~ 3×3 degrees) area around GRB 021004 with an effective peak near z ~ 0.56 for both the spectral and photometric redshift distributions obtained from the Baryon Oscillation Spectroscopic Survey (BOSS), which is a part of the Sloan Digital Sky Survey III (SDSS-III).

A possibility of inhomogeneity (a galaxy clustering) near the GRB 021004 direction can be also confirmed by an *inhomogeneity* in cosmic microwave background related with the Sunyaev-Zeldovich effect.

From catalogs data, *the size* of the whole inhomogeneity in distribution of the galaxy cluster with the peak near z ≈ 0.56 was also estimated as ~6-8 degrees

It is also well proven that long-duration GRBs are associated with the core collapse of very massive stars.

Similarly to core collapse SNe, the collapse of massive stellar iron cores results in the formation of a compact object (collapsar), accompanied by the high-velocity ejection of a large fraction of a progenitor star mass at relativistic speed producing a series of internal shocks giving rise to the GRB itself.

Namely, the determination of distance to SNe and GRBs resulting from collapse of compact objects of stellar mass becomes the main observational task in determining a basic parameter: **the total energy release related to such events**.

The collapse of the massive stellar cores maybe connected with the quark phase transition in the compact objects, which leads to neutrino, gravitational and photon signals from the core collapse SNe (like SN1987A) and GRBs.

It is also obvious that for low and intermediate redshifts, the sky distribution of electromagnetic and neutrino signals associated with the core-collapses can be nonisotropic, **showing the clustering of galaxies** in which the formation of compact objects occurs due to evolution of massive stars.

5. Prospects

TASK:

THE STUDY AND MONITORING of sources of cosmic gamma-ray bursts, *identification* of sources of gravitational waves and neutrino signals from supernovae, fast radio bursts.

We plan to carry out (to continue) follow-up observations of localization areas *(identification)* of newly-discovered gamma-ray bursts, neutrino and gravitational signals, and supernovae (in the mode of "Target of opportunity Observations" (ToO)).

The telescopes: BTA, Zeiss-2000 (TB INASAN), Zeiss-1000 (SAO RAS) in the modes of photometry, spectroscopy, fast photometry and polarimetry.

Alerts : from missions*Swift, Fermi, INTEGRAL, Lomonosov and others.*

The alerts from the MiniMegaTORTORA system (SAO RAS) are possible.

In addition, we aim at the search for optical/electromagnetic components (related to GRBs) sources of neutrino and gravitational waves (GW events) detected by LIGO (Laser

Interferometer Gravitational-wave Observatory) and Virgo.

6. International cooperation

The works as a part of program in an international observational collaboration:

1. In optical:

 with teams from the German-Spanish Observatory Calar Alto (Spain, 2.2 and 3.5 m for imaging and spectroscopy),

observatory La Palma (Spain, the telescopes of 1-2m for photometry, 4.2m and 10.4m GTC for photometry and spectroscopy),

the Observatory Nainital (the 1.0m telescope, the 1.3m telescope Devasthal for imaging),

 In near IR range the telescope AZT-24 (MAO RAS, Campe-Imperatore, Italy).

2. Radio observations will be fulfilled with the 30-meter radio telescope IRAM (Spain), the 32-meter telescopes of IAA RAS and with the telescope GMRT (India).

It is proposed to combine the observations with the robotic telescopes of the MASTER-II network of the MASTER Net (Moscow, Kislovodsk, Amur, Urals, Spain, Argentina, South Africa).

7. The strategy of study.

 Alert signals from space gamma-raymissions, neutrino observatories (we are interested in ICECUBE and KAMIOKANDE), LIGO&VIRGO.

Fast radio bursts – for the time being the search is made with the Parks 64m telescope (the Southern sky).

It is planned to start searching for FRBs with RATAN-600.

It is possible to use the data from MiniMegaTORTORA.

Stage 1: IDENTIFICATION (the specification of coordinates with the 1m and 2m telescopes in the photometry mode, for very large error boxes – the identification with MiniMegaTORTORA) and prompt transfer of coordinates to BTA and other telescopes.

Stage 2: STUDY (photometry in BVRcIc bands with 1-2m telescopes up to R~22, with BTA – spectroscopy of objects brighter than R~22 in the range 350-950 nm for determining z of the source and obtaining absorptions on the line of sight, resolution (depending on the source brightness), fast photometry and polarimetry with the complex of fast variability in the first minutes and hours after the burst, then – photometry with the deep limit up to R~25).

CRITICAL – photopolarimetry for determination of the collapse geometry, the expected polarization is of order of 10%.

Stage 3: BTA low-resolution PHOTOMETRY and SPECTROSCOPY of different phases of the source evolution – the appearance of the second peak in luminosity, spectral features of supernovae.

In conclusion we would like also to emphasize here that since GRBs are detected at more and more distant cosmological distances with redshifts more than 9.2, this poses additional new questions which are of outmost importance for observational cosmology.

What are the redshifts at which the sky distribution of GRBs becomes homogeneous?

And what are the redshifts where such bursts (which are related now with collapse of compact objects of stellar mass) are unobservable already?

THE PROBLEM

This strategy does well for identification of sources with good error boxes. Here our

advantage is the fast reaction and geographic location.

In case of neutrino and gravitational signals, data of fast radio bursts, the coordinate precision is not sufficient yet; the telescopes with large fields and good limits are necessary.

In the West: the operating PAN-STARRS and SkyMapper, DEC, etc.

Coming soon: the 8.4-m Large Synoptic Survey Telescope (LSST).

8. Our plans for the future

1. The project off a new large-aperture telescope with large field (this is not decided yet).
2. New equipment for BTA: a spectrophotometer of the IR range (is being made)
3. Manufacturing of a series of effective moderate-resolution spectrographs for telescopes of the 2m class (a prototype is being used with AZT33IK of ISTP RAS).
4. Creation of a photometer-polarimeter for the 1m telescope (is planned for 2017-2018)
5. Creation of a network of small telescopes (up to 6 items with D=0.5-0.6m and the field of view about 1 sq.deg.) equipped with CCD photometers with large cameras (up to 4Kx4K elements).

Tasks: the monitoring in fields about 1 degree, photometry of bright sources.

The project starts in Summer 2017, observations – in 2018.

8.1. A telescope of new Russian technology (TNRT)

The prototype – the 4.1m telescope VISTA ESO

The main tasks: the study of transient sources: GRB, SN, neutron events, deep surveys in wide fields, etc.

The project status: preliminary, under discussion.

Time of creation: 2018-2023.

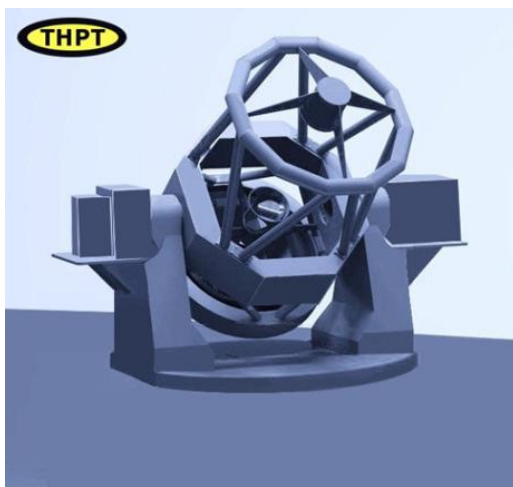The TNRT design is shown in Fig.8. Some TNRT equipment is presented in Figs. 9, 10.

Fig8. TNRT design

The main characteristics of the telescope
- Alt-azimuthal mounting
- Optical layout – quasi Ritchey-Chretién
- Diameter of the main mirror – about 3.5(4) m
- MM material – sitall CO-115M (Zerodur)
- Focuses: Cassegrain, 2 (4) Nasmith
- Spectral range: 0.35 – 1.7 (2.5) microns
- Angular resolution (optical)   - not worse than 0.”5
- The operational field - 2° (3 °)
- It is expected that there will be systems of active optics of MM, a system of wave front adaptation in a small field.
- Implementation of the technology of spraying high-effective reflecting coatings with R up to 97% in a wide range.
- Equipment: Cassegrain for photometry in wide fields: mosaics up to 20kx20k px (optics) and 8K×8K (IR), Nasmiths – for integral field spectrograph and scanning Faby-Perot interferometer, multi-object spectrograph for 300-500 objects.
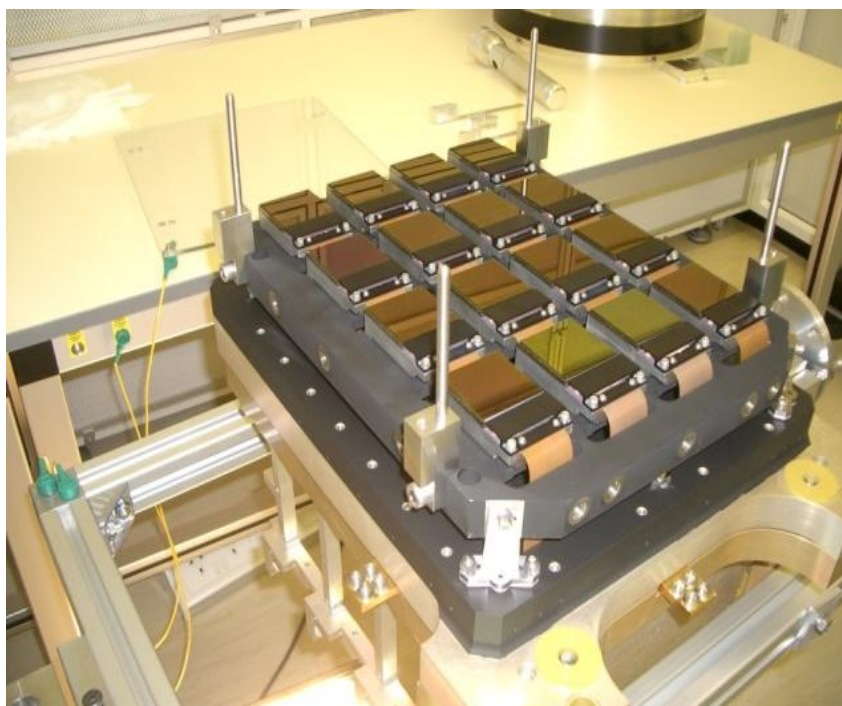
Fig9. *TNRT: a view of the large-field IR camera. Size of the field of view: up to 1° × 1°. Scale: 0.3 – 0.5 arcsec/px. The set of filters: Wideband J, H, K; medium-band (FWHM ~200-300 A). Detector: mosaic HAWAII-2 Location : the Nasmith focus*

Fig10. Technical groundwork for TNRT: photodetector with a mosaic sensor

8.2. Complex of the 0.5-m robotic telescopes at SAO RAS

A complex of 0.5-meter robotic telescopes is being in constructed in SAO RAS. Some views of the process are presented in Figs. 11,12.

Fig11. Construction of the complex. Left: September 2017. Right: December 2017.

Fig12. *One robotic telescope.*

The main scientific goals are as follows:

- GRB: small robotic telescopes detect optical signal, measure it's parameters and within few seconds pass data to 6-m for detailed studies.
- FRB: synchronous observations with RATAN-600 (expecting rate – 8 ev per year).
- Photometrical studies of exoplanets and magnetic stars.
- Alert observations of SNs, Novae, CV, QSO, NEO etc
- Observational programs: students, teachers etc

Conclusion.

- For reliable identification of transients (from gamma-ray, radio, neutrino and gravitational) it is necessary to carry out optical observations
- Equipment of SAO and other telescopes in whole is ready for observations of transient sources of a new class.
- Successful implementation of the projects demands a wide international cooperation and implementation of plans of development of instrument base.

References

[7] "Proceedings of the International Workshop on Quark Phase Transition in Compact Objects and Multimessenger Astronomy: Neutrino Signals, Supernovae and Gamma-Ray Bursts", Russia, Nizhnij Arkhyz (SAO RAS), Terskol (BNO INR RAS), October, 7 - 14, 2015, Publishing house "Sneg", Pyatigorsk, 2016.

[8] Proceedings of The International Conference "SN 1987A, Quark Phase Transition in Compact Objects and Multimessenger Astronomy", Russia, Terskol (BNO INR RAS), Nizhnij Arkhyz (SAO RAS), 2-8 July 2017, INR RAS, Moscow, 2018 .

[9] Thornton et al, 2013, Nature

The origin of GW170817

Grzegorz Wiktorowicz[1,2]

[1]National Astronomical Observatories, Chinese Academy of Sciences, Beijing 100101,
China; gwiktoro@astrouw.edu.pl

[2]School of Astronomy & Space Science, University of the Chinese Academy of Sciences,
Beijing 100012, China

Abstract   The first double neutron star merger was observed by LIGO/Virgo collaboration on August 17, 2017 (GW170817). The possible formation scenarios include isolated (classical) binary evolution, dynamical formation in globular, or nuclear clusters, and other more exotic scenarios like the involvement of quark stars. Here we present the recent simulated results aimed at formation of a binary compact object with a special attention put to GW170817 progenitors. All tested formation scenarios give merger rates far below the observational estimated ones. The highest merger rate is predicted for isolated binary evolution which is still 2 orders of magnitude too small. The scenario involving quark stars shows even worse comparison, but may potentially explain other observational features of GW170817. The results tell us that one of the options is possible: either the only observation is just a statistical coincidence, our understanding of stellar and binary physics is incomplete, or we are missing some important non-canonical formation scenario.

1. Introduction

Recently, several double compact object mergers have been observed by LIGO-Virgo collaboration (Abbott et al. 2017). Among them there is only one merger of two neutron stars, GW170817 (Abbott et al. 2018), the rest being double black hole mergers. Up to now, none mixed mergers (a neutron star with a black hole) have been observed.

Double neutron star mergers potentially have much more progenitors, because neutron stars typically originate from lighter stars, which are more abundant on the zero-age main-sequence. However, double black hole mergers give much more significant signal and, as a result, were statistically predicted to be observed more frequently (Belczynski et. all 2016). Except GW170817, the locations of mergers are not known precisely.

Although black holes detected in the Milky Way have mass in the range $\sim$5-15 solar masses, these detected in merging double compact objects have masses between 7 and 50 times higher than the Sun (only 25% of them have masses below 15 solar masses). This contrast motivated a search for different formation scenarios of black holes in the merging double compact objects, than these found for galactic black holes, which are predominantly components of low-mass X-ray binaries.   For example, it was suggested that compact objects in these systems may originate from primordial black holes (e.g. Hawking 1971), or

populations III stars (e.g. Madau & Rees 2001). Double neutron star mergers, although being a minority among detected gravitational wave sources, are much better for analysis, because such problems are omitted (all neutron stars have very similar masses between 1-2 solar masses, Lattimer 2012). Additionally, the double neutron star merger produces simultaneously electromagnetic radiation, which allows for multi-messenger observations (e.g. Abbott et al 2017b, Evans et al. 2017).

2. Merger rate estimations for GW170817

GW170817 (also known as GRB170817, or AT2017gfo) is the first observed merger of double neutron stars (Abbott et al. 2017). The parameters estimated on the base of its gravitational wave emission are the chirp mass ($M_{chirp} = 1.188 M_{Sun}$) and mass ratio ($q = M_2/M_1 > 0.7$). It is localized on the outskirts of the old elliptical galaxy NGC 4993. The galaxy probably had an episode of star formation 3-7 Gyr ago (Troja et al. 2017). Belczynski at al. (2018) assumed the metallicity to be sub-solar ($Z = 50\% Z_{Sun}$).

Three main formation scenarios are considered in the context of double neutron star mergers. The first one is the isolated (classical) binary evolution (e.g. Lipunov et al. 1997, Belczynski et al. 2016, Stevenson et al. 2017), which occurs in the galactic disks where interactions between stars are rare (however see Klencki et al. 2017). Various models were calculated and compared in the contact of double neutron star merger by Chruslinska et al. (2018). Other scenario predicts a formation of merging double neutron stars in globular clusters (e.g. Portegies Zwart et al. 2004, Askar et al. 2017). Stars and binaries in such environment experience many interactions during which binaries are formed, altered, or destroyed. Neutron stars before the merger might have been a part of a few tens of significant interaction before the close double neutron star was formed. A very similar is a situation in nuclear clusters where dynamical interaction may lead to formation of GW170817 progenitors (e.g. Arca-Sedda et al. 2017).

Belczynski et al. (2018) performed a comparison between merger rate estimations based on these main formation channels and the merger rate obtained from the observation of GW170817. Specifically, they performed simulations of isolated binary evolution using the population synthesis code Startrack (Belczynski 2002, 2008) and simulations of a dynamical formation of double neutron star merger progenitors using Monte Carlo code MOCCA (Giersz et al. 2013, Hypki & Giersz 2013) for globular and nuclear clusters.

The models tend to provide rates which are significantly lower than predicted from observations (see Table 1). Therefore, Belczynski et al. (2018) in their study used combinations of parameters which maximize the rates in particular channels using earlier works of Chruslinska et al. (2018) and Askar et al. (2017). Please note, that not the same parameters give highest rates in different formation channels.

The results of Belczynski et al. (2018) are presented in Table 1. Estimations based on observations (LIGO/Virgo; 90% credibility; Abbott at al. 2017) are provided for comparison. Three synthetic models refer to isolated (classical) evolution, dynamical formation in globular clusters, and dynamical formation in nuclear clusters. Estimations marked as pessimistic, realistic, and optimistic depict the lower, average and upper estimates for LIGO/Virgo results. For synthetic models these columns refer to estimates calculated for a burst star formation 10 Gyr ago (pessimistic), 5 Gyr ago (realistic), and 1 Gyr ago (optimistic).

Table1. *Local double neutron star merger rates [yr $^{-1}$] (within D=100 Mpc^3) after Belczynski et al. (2018)*

Model	pessimistic	realistic	optimistic
LIGO/Virgo	0.3	1.5	4.7
classical binaries	8×10^{-3}	1×10^{-2}	5×10^{-2}
globular clusters	2×10^{-5}	5×10^{-5}	2×10^{-4}
nuclear clusters	7×10^{-6}	1×10^{-5}	1×10^{-4}

Although simulations of double neutron stars show good agreement with Galactic populations of binary pulsars, or rates of gamma ray bursts (Chruslinska et al. 2017), the merger rates of double neutron stars are far below the estimates based on the observation of GW170817. The comparison shows (Table 1) that isolated evolution provides merger rates that are closest to the LIGO/Virgo rates, but still about 2 orders of magnitude smaller. Interestingly, isolated binary evolution correctly predicts merger rates of double black holes (e.g. Belczynski et al. 2016).

We note that all observations are subject to uncertainties due to beaming, unknown emission mechanisms, and low statistics, which may, potentially, change the comparison in favor of the simulations. Additionally, it is possible that NGC 4993 experienced a recent star formation episode (300-400 Myr ago; Palmese et al. 2017). If true, it will significantly increase synthetic merger rates, because double compact objects merge more effectively in young stellar environments.

3. Quark stars merger

The existence of stars built partially or totally from deconfined quarks was predicted theoretically. The former are called twin-stars (e.g. Alford et al. 2013), whereas the latter are possible in the context of the so-called two-families scenario (e.g. Drago et al. 2014, Wiktorowicz et al. 2017). The two-families scenario shows a promising framework to explain all phenomena connected with the GW170817 event (De Pietri et al. in prep).

In order to obtain predictions for the merger rates within the two-families scenario, it was assumed that the transition from a hadronic star to a quark star occurs at a conversion mass of $M_{max}^{H} = 1.5 - 1.6 M_{Sun}$ (Wiktorowicz et al. 2017). The results from simulations (De Pietri et al. in prep) show the prevalence of mixed mergers (hadronic star with a quark star) for low mass ration (but within observational estimated range for GW170817: $0.7 < q < 0.85$). The merger rate is $2 \times 10^{-4} yr^{-1}$ in the volume limited by a sphere with a radius of 100 Mpc (for a comparison with Belczynski et al. 2018). Although higher than estimates of merger rates for two hadronic stars or two quark stars, this estimate is more than 4 orders of magnitude below the merger rates estimated on the base of the observations of GW170817. We note that for higher mass ratios ($q > 0.85$) two hadrons stars give higher merger rates (up to 6.4×10^{-3} than a mixed merger, or double quark star merger.

4. Conclusions

All tested formation scenarios give merger rates far below the observationally estimated rate for the GW170817 event. Among tested model, the most promising is the isolated (classical)

binary evolution in the field, which, nevertheless, gives merger rates about 100 times smaller than inferred from LIGO observations.

If GW170817 is not just a statistical coincidence and next observational runs will confirm the actual merger rate estimates, we will know that our understanding of stellar physics in at least one of the main formation channels is incomplete, or some of the exotic or currently unknown scenarios give much higher merger rates of double neutron stars.

An example of such a less canonical scenario is a merger of a star built of hadrons with a star composed of quarks. We showed that for merger similar to GW170817 and with low mass ratios ($0.7 < q < 0.85$) the merger rate of such mixed mergers is higher than for neutron stars. Nonetheless, the merger rate (about $10^{-4} yr^{-1}$ within a distance of 100 Mpc) is still much smaller than these inferred from observations (a few per year within a distance of 100 Mpc).

Acknowledgments

References

[1] Abbott et al. GW170817: Observation of Gravitational Waves from a Binary Neutron Star Inspiral, Physical Review Letters, Volume 119, Issue 16, id.161101, 2017a. http://adsabs.harvard.edu/abs/2017PhRvL.119p1101A

[2] Abbott et al. Multi-messenger Observations of a Binary Neutron Star Merger. The Astrophysical Journal Letters, Volume 848, Issue 2, article id. L12, 59 pp. 2017b. http://adsabs.harvard.edu/abs/2017ApJ...848L..12A

[3] Abbott et al. GWTC-1: A Gravitational-Wave Transient Catalog of Compact Binary Mergers Observed by LIGO and Virgo during the First and Second Observing Runs. eprint arXiv:1811.12907, 2018. http://adsabs.harvard.edu/abs/2018arXiv181112907T

[4] Belczynski et al. The first gravitational-wave source from the isolated evolution of two stars in the 40-100 solar mass range. Nature, Volume 534, Issue 7608, pp. 512-515 2016. http://adsabs.harvard.edu/abs/2016Natur.534..512B

[5] Belczynski et al. The origin of the first neutron star - neutron star merger. Astronomy & Astrophysics, Volume 615, id.A91, 13 pp. 2018. http://adsabs.harvard.edu/abs/2018A%26A...615A..91B

[6] Lipunov, V. M.; Postnov, K. A.; Prokhorov, M. E. Black holes and gravitational waves: Possibilities for simultaneous detection using first-generation laser interferometers. Astronomy Letters, Volume 23, Issue 4, July 1997, pp.492-497; Pis'ma v Astronomicheskii Zhurnal, Vol. 23, p. 563, 1997. http://adsabs.harvard.edu/abs/1997AstL...23..492L

[7] Stevenson et al. Formation of the first three gravitational-wave observations through isolated binary evolution. Nature Communications, Volume 8, id. 14906, 2017. http://adsabs.harvard.edu/abs/2017NatCo...814906S

[8] Klencki et al. Dynamical formation of black hole low-mass X-ray binaries in the field: an alternative to the common envelope. Monthly Notices of the Royal Astronomical Society, Volume 469, Issue 3, p.3088-3101, 2017. http://adsabs.harvard.edu/abs/2017MNRAS.469.3088K

[9]   Chruslinska et al. Double neutron stars: merger rates revisited. Monthly Notices of the Royal Astronomical Society, Volume 474, Issue 3, p.2937-2958, 2018. http://adsabs.harvard.edu/abs/2018MNRAS.474.2937C

[10]   Portegies Zwart et al. Formation of massive black holes through runaway collisions in dense young star clusters. Nature, Volume 428, Issue 6984, pp. 724-726, 2004. http://adsabs.harvard.edu/abs/2004Natur.428..724P

[11]   Askar et al. MOCCA-SURVEY Database - I. Coalescing binary black holes originating from globular clusters. Monthly Notices of the Royal Astronomical Society: Letters, Volume 464, Issue 1, p.L36-L40. 2017.   http://adsabs.harvard.edu/abs/2017MNRAS.464L..36A

[12]   Arca-Sedda et al. The MEGaN project - I. Missing formation of massive nuclear clusters and tidal disruption events by star clusters-massive black hole interactions. Monthly Notices of the Royal Astronomical Society, Volume 471, Issue 1, p.478-490. 2017. http://adsabs.harvard.edu/abs/2017MNRAS.471..478A

[13]   Hawking S. Gravitationally collapsed objects of very low mass. Monthly Notices of the Royal Astronomical Society, Vol. 152, p. 75, 1971. http://adsabs.harvard.edu/abs/1971MNRAS.152...75H

[14]   Madau & Rees, Massive Black Holes as Population III Remnants. The Astrophysical Journal, Volume 551, Issue 1, pp. L27-L30, 2001.   http://adsabs.harvard.edu/abs/2001ApJ...551L..27M

[15]   Lattimer J.M., The Nuclear Equation of State and Neutron Star Masses. Annual Review of Nuclear and Particle Science, vol. 62, issue 1, pp. 485-515, 2012. http://adsabs.harvard.edu/abs/2012ARNPS..62..485L

[16]   Evans et al. Swift and NuSTAR observations of GW170817: Detection of a blue kilonova. Science, Volume 358, Issue 6370, pp. 1565-1570, 2017. http://adsabs.harvard.edu/abs/2017Sci...358.1565E

[17]   Troja et al. The X-ray counterpart to the gravitational-wave event GW170817. Nature, Volume 551, Issue 7678, pp. 71-74, 2017. http://adsabs.harvard.edu/abs/2017Natur.551...71T

[18]   Belczynski et al. A Comprehensive Study of Binary Compact Objects as Gravitational Wave Sources: Evolutionary Channels, Rates, and Physical Properties. The Astrophysical Journal, Volume 572, Issue 1, pp. 407-431, 2002. http://adsabs.harvard.edu/abs/2002ApJ...572..407B

[19]   Belczynski et al. Compact Object Modeling with the StarTrack Population Synthesis Code. The Astrophysical Journal Supplement Series, Volume 174, Issue 1, pp. 223-260, 2008. http://adsabs.harvard.edu/abs/2008ApJS..174..223B

[20]   Giersz et al. MOCCA code for star cluster simulations - II. Comparison with N-body simulations. Monthly Notices of the Royal Astronomical Society, Volume 431, Issue 3, p.2184-2199, 2013. http://adsabs.harvard.edu/abs/2013MNRAS.431.2184G

[21]   Hypki & Giersz, MOCCA code for star cluster simulations - I. Blue stragglers, first results. Monthly Notices of the Royal Astronomical Society, Volume 429, Issue 2, p.1221-1243, 2013. http://adsabs.harvard.edu/abs/2013MNRAS.429.1221H

[22]   Palmese et al. Evidence for Dynamically Driven Formation of the GW170817 Neutron Star Binary in NGC 4993. The Astrophysical Journal Letters, Volume 849, Issue 2, article id. L34, 8 pp., 2017. http://adsabs.harvard.edu/abs/2017ApJ...849L..34P

[23]   Alford et al. Generic conditions for stable hybrid stars. Physical Review D, vol. 88, Issue 8, id. 083013, 2013.   http://adsabs.harvard.edu/abs/2013PhRvD..88h3013A

[24] Drago et al. Can very compact and very massive neutron stars both exist? Physical Review D, Volume 89, Issue 4, id.043014, 2014.   http://adsabs.harvard.edu/abs/2014PhRvD..89d3014D

[25] Wiktorowicz et al. Strange Quark Stars in Binaries: Formation Rates, Mergers, and Explosive Phenomena. The Astrophysical Journal, Volume 846, Issue 2, article id. 163, 10 pp., 2017. http://adsabs.harvard.edu/abs/2017ApJ...846..163W

The observations of GRB afterglows and the plan to search for optical counterparts of gravitational wave events

Liping Xin[1,*], Xuhui Han[1], Jianyan Wei[1], Jing Wang[2], Yulei Qiu[1], Chao Wu[1], Huali Li[1], Xianggao Wang[2]

[1]*National astronomical observatories, Chinese Academy of Sciences, Beijing, China;*

xlp@nao.cas.cn

[2]*Guangxi University, Nanning, China*

Abstract   Here we give an overview of the follow-up campaign of the gamma-ray bursts. And then we give an introduction about GWAC project which is aiming to detect the prompt emission with high-cadence photometry and large field of view monitoring. Besides, we also present our plan to search for the associated counterparts of gravitational wave events in the optical during the O3 run.

Keywords: Gamma-ray Burst, Gravitational Wave, Afterglow, Optical Counterpart, Follow-up Observations

1. Introduction

Gamma-ray bursts are the intensive flashes in high-energy in the deep universe. It consists of two classes, one is long-duration, soft spectral burst, the other is the short-duration, hard burst, separated by the duration of two seconds for their high-energy prompt emission. It is expected that there is afterglow emission in multi-wavelength for both types of gamma-ray bursts. A large fraction of GRB X-ray afterglows shows that there is a very steep decay attributed to the curvature effect and followed by a shallow-decay phase. After that, the afterglow would evolve into the normal decay phase, which is interpreted to be caused by the interactions between the relativistic shock and medium around a GRBs. About 90% of X-ray afterglow emission of GRBs were detected by Swift XRT (e.g. [5]) and about 50% of optical afterglow were detected by telescopes all over the world. The successful detection of multi-wavelength afterglows could provide fruitful information of GRB science, including the high precise localization, the inner physics of relativistic jets, distance, and burst environment, etc. On the other hand, only a few GRBs were detected successfully in the optical band during their prompt emission. Nevertheless, these successful observations of prompt emission have revolutionized much of our knowledge on the GRB science. Taking the naked-eye burst GRB 080319B as an example, it is the brightest GRB up to now, whose peak magnitude during the prompt emission is as high as ~5.3 magnitude in the visible band (e.g. [1]). The non-delayed and high temporal resolution observations of prompt optical emission of GRB 080319B by several ground-based wide-field optical monitor systems, including Pi of the sky and TORTORA (e.g. [1]), make the burst possible for revealing the detailed structure of optical emission, shedding light on the behavior of the burst internal engine (e.g. [3]). With these observations, people are able to study the effect of environment (e.g. [4]) and the

radiation mechanism in the inner area of relativistic jets (e.g. [2]).

At least for a friction of short bursts, people believe that they are related to the gravitational events, as a result of the merger of a binary of neutron-black hole or neutron star-neutron star. One of the promising counterpart in the optical is the kilonova/macronova, which is emission powered by radioactive decays of r-process nuclei and it is one of the most promising electromagnetic counterparts of gravitational wave sources (e.g. [22]). Up to now, only several kilonova candidates were found by modeling multi-wavelength light curves of GRB afterglows (e.g. [23]), except for one case, AT2017gfo (e.g. [14]), which was confirmed to be associated to GW170817 and GRB 170817A.

Here we give an overview of the GRB follow-up observations by the TNT telescope in China. In the second part, we give an introduction about the GWAC project which is aiming at detecting the prompt emission with high-cadence photometry and large field of view monitoring. Finally, we present our plan to search for the associated optical counterparts of gravitational waves by follow-up observations.

2. TNT to follow-up the Swift GRBs

TNT is the Tsinghua University-NAOC 0.8m telescope, which is located at Xinglong station (e.g. [6]), northeast of Beijing with a distance of about 120 kilometers. As one of most primary observing stations of National Astronomical Observatories, Chinese Academy of Sciences (NAOC) (IAU code: 327, coordinates: 40°23′39″ N, 117°34′30″ E), the average altitude of the Xinglong station is bout 900m. The mean and media seeing values of the Xinglong station are 1.9 arcsec and 1.7 arcsec, respectively. There are more than 100 photometric nights and about 230 observable nights per year on average. The sky brightness is about 21.1 mag/arcsec^2 in V band at the zenith. Xinglong station has more than 8 telescopes with aperture larger than 0.5 meters, including the 2.16m optical telescope (e.g. [17]).

A PI 1340*1300 CCD is equipped for TNT. The focal ratio of TNT is f/10, giving a field of view of 11.4*11.1 arcminutes. The pixel scale is 0.52 arcsecond. A set of the Johnson-cousin filters UBVRI are equipped for this photometry system. A rapid follow-up system is developed for observations of GRB afterglows for TNT telescope (e.g. [7]). With this system, more than 130 Swift GRBs have been followed and the optical afterglows have been detected for about 50% of these observed GRBs.
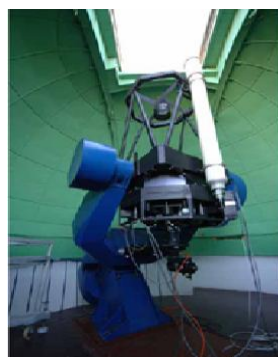

Fig1. *Left: The bird's eye view of the Xinglong observatory, China. Right: The 0.8m TNT optical telescope. Adapted from the website of Xinglong station (e.g. [6])*

When a GRB alert is received, TNT could start the multi-band follow-up observation in 1-2 min since the burst trigger with a pre-defined strategy. In case that the optical afterglow of a GRB is detected and its emission is brighter than 16 magnitude in R band, a low-resolution spectroscope observation by the 2.16m telescope would be requested. The typical delay time for the follow-up observations by the 2.16m telescope is 10-30 min. As done for GRB 140629A (e.g. [8]), the brightness of about 15.3 mag was measured by TNT at the time of about 500 sec after the burst. After a request, a spectroscopic observation was obtained by the Xinglong 2.16m telescope at about one hour after the burst time. The redshift of z=2.275 was derived based upon some absorption lines (e.g. [8]), such as CIV λ 1549. After the joint analysis by modeling the optical and X-ray afterglows in the framework of standard synchrotron external shock model (e.g. [9]), the main sciences for GRB 140629A in the following are derived:

1) It follows the standard forward shock model in the thin shell case.
2) The ambient density around the GRB is 60 ± 9 cm^{-3}.
3) The opening angle of jet is very narrow, which is about 0.04 radian.
4) The GRB radiating efficiency is as low as 0.24%, likely indicating a baryonic-dominated ejecta of this GRB.
5) It does not follow the Ghirlanda relation (e.g. [10]) confidently, but fully agrees with Liang relation (e.g. [11]).

3. GWAC to measure the prompt optical emission

In order to measure the temporal properties of the prompt optical emission and the afterglow of all kinds of GRBs at very early phase, an observation system with a very fast slewing or very angle monitoring shall be employed. GWAC (Ground-based Wide Angle Cameras), after its fully setup, would have a capability to monitor ~5000 square degrees of the sky in the cadence of 15 seconds. As a key part of facilities of the future Chinese-French space mission SVOM (Space-based multiband astronomical Variable Objects Monitor, e.g. [14]), the full system of GWAC consists of 10 units. One unit consists of one mount and four cameras. The diameter of each camera is 18cm. Four cameras are mounted in each mount. The magnitude limit is V~16.5 mag with an exposure time of 10 seconds in the moonless night, and V~15.5 mag in the full moon phase. 4k*4k e2V CCD is equipped for each camera, giving a pixel scale of 11.7 arcsec. No filter is equipped in order to increase the detection sensitivity.

The prototype of GWAC was set at Xinglong station, near the dome of the TNT telescope. At present, three units are running normally every night. With the support of a powerful database, a real-time pipeline for short-duration transient detection is developed for GWAC system based on the catalog crossmatch from the object catalog obtained from GWAC observed stacking image and Astronomical distributed catalogs, such as the USNO B1.0 catalog and Gaia dr2 catalog.

Two 60cm optical telescopes with a field of view of 19 arcmin for each and one 30cm optical telescope with a field of view of 1.9 square degrees are also setup in the same dome of GWAC in order to make fast and multi-wavelength follow-up for any transient candidates detected by GWAC. With these follow-ups, it is more easy for people to valid the transients, to measure their higher precise locations, and to obtain the color changes and to monitor the evolution of light curves. Besides, these successful follow-ups also provide alert for scientists to decide whether spectroscopic follow-up observation by the 2.16m telescope and others is needed. More detailed description was presented (e.g. [13]).

Fig2. *GWAC and its follow-up telescope, including two 60 cm telescopes and one 30 cm telescope. Currently, all these are set at Xinglong station, NAOC, China,*

Besides, an automatic follow-up system is also developed for GWAC system to detect the afterglow of GRBs triggered by Swift and Fermi, though there are still no positive detections for GRB afterglows up to now. However, with optimization of the system including hardware and software, the science is believed to be on the way.

4. Search for the optical counterparts from GRBs to GWs

During the O1 and O2 observation campaigns, only one gravitational event GW170817 (Abbott, B. P., et al., 2017) was originated from the merger of binary neutron stars and its counterpart GRB 170817A (e.g. [15]) in high energy was found by the space observatories Fermi and Integral. And its optical counterpart kilonova AT2017gfo (e.g. [14]) was also detected by variety of telescopes in the worldwide. Apart from this one, other gravitational events were considered to be results of the merger of binary of black holes (BBH). During the O1 and O2 epochs, nine BBH gravitational wave events (e.g. [13]) in total were followed by the prototype of GWAC, Mini-GWAC. Particularly, GW151226 was the only one and the first event for Mini-GWAC to search for any possible optical counterparts related to the gravitational events. Eight other GW events were observed by our system during the O2 run as shown in Fig 3. The typical upper limit for all observations for Mini-GWAC was 11-12 magnitude in R band. It is noted that among these follow-ups, the observations by Mini-GWAC for GW170104 started soon in minutes after the alert, and about 2 hours after the event. The sky coverage of GW170104 by Mini-GWAC was about 84.4% of probability which was the largest probability coverage in shortest latency for all observations in the worldwide.

No credible optical transient was found in our images during the O1 and O2 runs. There might be two reasons. One is the nature of these GW events. Nine GW events observed by our system were originated from the merger of binary of black holes. The electromagnetic counterparts from BBH is highly uncertain (e.g. [18], [19], [20], [21]). Secondly, the sensitivity of the mini-GWAC telescopes was not enough to detect relatively faint transients such as the kilonova emission like AT2017gfo (e.g. [14]).

The optimization is going on, we will utilize the GWAC system to search for the kilonova-like transients during the O3 run. The diameter of the GWAC camera is 18cm, compared to that of D=7cm for Mini-GWAC, the detection sensitivity could be increased to V~16mag in a single frame. Since the brightness of AT2017gfo evolves with 1 magnitude per day during its peak time, it is not advantage to search these relatively slowly fading transients

in very short cadence of 15 seconds. The image stacking would increase the sensitivity of GWAC to about V~18mag (e.g. [13]), which increases the possibility to detect optical counterparts of GW events.
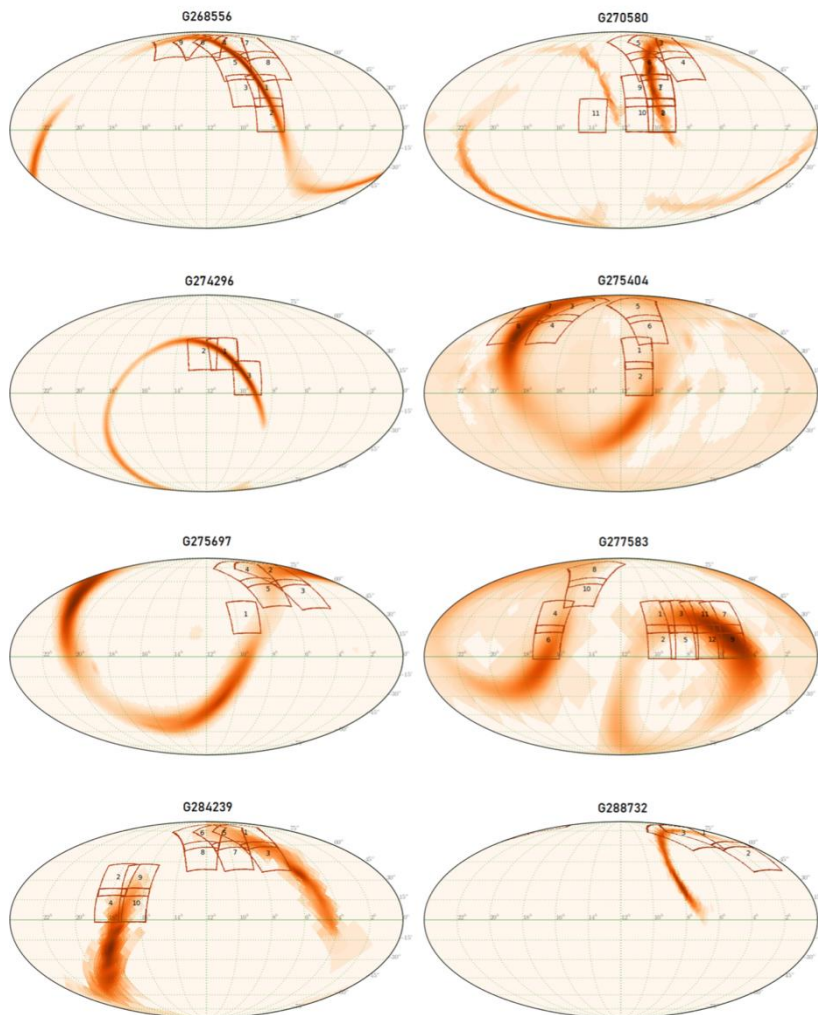

Fig 3. *The skymaps of the eight gravitational wave events followed by GWAC system during O2 run, adapted from [13]. All observation grids are shown with the red squares each of them identified with a grid ID.*

5. Conclusion

Here we present an overview of the follow-up of GRBs mainly carried out by the 0.8m Tsinghua and National astronomical observation telescope (TNT) in China. The follow-up campaign mainly focuses on the well localized GRBs triggered by Swift for more than 12 years since 2006. The follow-up observations to search for the optical counterparts from

gravitational wave events during the O1 and O2 runs are also briefly presented. Furthermore, we also introduce our next plan for the follow-up observations of gravitational wave events detected by LIGO/Virgo during the O3 run.

Acknowledgements

References

[1] Racusin J.~L., et al., "Broadband observations of the naked-eye γ-ray burst GRB080319B", 2008, Nature, 455, 183

[2] Siyao Xu and Zhao Li., "Prompt optical emission from gamma-ray bursts with multiple timescale variability of central engine activities", 2014, RAA, 14,411

[3] Beskin, G.; Karpov, S.; Bondar, S.; Greco, G.; Guarnieri, A.; Bartolini, C.; Piccioni, A. "Fast Optical Variability of a Naked-eye Burst—Manifestation of the Periodic Activity of an Internal Engine", 2010, ApJ, 719,10

[4] Cui, Xiao-Hong; Li, Zhuo; Xin, Li-Ping, "Delayed onset and fast rise of prompt optical-UV emission from gamma-ray bursts in molecular clouds", 2013, RAA, 13,57

[5] Gehrels, et al., "The Swift Gamma-Ray Burst Mission",2004, 611,1005

[6] The website for Xinglong observatory, www.xinglong-naoc.org

[7] Zheng, Wei-Kang; Deng, Jin-Song; Zhai, Meng; Xin, Li-Ping; Qiu, Yu-Lei; Wang, Jing; Lu, Xiao-Meng; Wei, Jian-Yan; Hu, Jing-Yao, "A GRB Follow-up System at the Xinglong Observatory and Detection of the High-Redshift GRB 060927", 2008, CHJAA, 8, 693

[8] Xin, Li-Ping; Zhong, Shu-Qing; Liang, En-Wei; Wang, Jing; Liu, Hao; Zhang, Tian-Meng; Huang, Xiao-Li; Li, Hua-Li; Qiu, Yu-Lei; Han, Xu-Hui; Wei, Jian-Yan, "Photometric and Spectroscopic Observations of GRB 140629A", 2018, ApJ, 860,8

[9] Sari, Re'em; Piran, Tsvi; Narayan, Ramesh, "Spectra and Light Curves of Gamma-Ray Burst Afterglows", 1998, ApJ, 497,1

[10] Ghirlanda, Giancarlo; Ghisellini, Gabriele; Lazzati, Davide, "The Collimation-corrected Gamma-Ray Burst Energies Correlate with the Peak Energy of Their vFv Spectrum", 2004, ApJ, 616,331

[11] Liang, En-Wei; Lin, Ting-Ting; Lü, Jing; Lu, Rui-Jing; Zhang, Jin; Zhang, Bing, " A Tight L_{iso}-$E_{p,z}$-Γ_0 Correlation of Gamma-Ray bursts", 2015, 813,116

[12] Wei, J.; Cordier, B., et al., "The Deep and Transient Universe in the SVOM Era: New Challenges and Opportunities - Scientific prospects of the SVOM mission", 2016, arXiv161006892

[13] Turpin, D.; Wu, C.; Han, X. H.; Xin, L. P.; Antier, S.; Leroy, N.; Cao, L.; Cai, H. B.; Cordier, B.; Deng, J. S.; Dong, W. L.; Feng, Q. C.; Huang, L.; Jia, L.; Klotz, A.; Lachaud, C.; Li, H. L.; Liang, E. W.; Liu, S. F.; Lu, X. M.; Meng, X. M.; Qiu, Y. L.; Wang, H. J.; Wang, J.; Wang, S.;

Wang, X. G.; Wei, J. Y.; Wu, B. B.; Xiao, Y. J.; Xu, D. W.; Xu, Y.; Yang, Y. G.; Zhang, P. P.; Zhang, R. S.; Zhang, S. N.; Zheng, Y. T.; Zou, S. C., "The Mini-GWAC optical follow-up of the gravitational wave alerts: results froom the O2 campaign and prospects for the upcoming O3 run", 2019, arXiv:1902.08476

[14] Villar, V.A., Guillochon, J., Berger, E., et al., 2017, ApJ, 851, L21

[15] Goldstein, A., Veres, P., Burns, E., Briggs, M. S., et al., 2017, ApJ, 848, L14

[16] Abbott, B. P., Abbott, R., Abbott, T. D., et al., 2017a, PRL, 119, 161101

[17] Zhou Fan, Huijuan Wang, Xiaojun Jiang, Hong Wu, Hongbin Li, Yang Huang, Dawei Xu, Zhongwen Hu, Yinan Zhu, Jianfeng Wang, Stefanie Komossa, and Xiaoming Zhang., "The Xinglong 2.16-m Telescope: Current Instruments and Scientific Projects", 2016, Publications of the Astronomical Society of the Pacific, 128, 969

[18] Loeb, Abraham, "Electromagnetic Counterparts to Black Hole Mergers Detected by LIGO", 2016, ApJ, 819,21

[19] Bing Zhang, "Mergers of Charged Black Holes: Gravitational-wave Events, Short Gamma-Ray Bursts, and Fast Radio Bursts", 2016, ApJ, 827,31

[20] Perna, Rosalba; Lazzati, Davide; Giacomazzo, Bruno, "Short Gamma-Ray Bursts from the Merger of Two Black Holes", 2016, ApJ, 821,18

[21] de Mink, S. E.; King, A. "Electromagnetic Signals Following Stellar-mass Black Hole Mergers", 2017, ApJ, 839,7

[22] Tanaka M., 2016, AdAst, 2016, 634197

[23] Guillochon, James; Parrent, Jerod; Kelley, Luke Zoltan; Margutti, Raffaella, "An Open Catalog for Supernova Data", 2017, ApJ, 835,64